

# **SYNTHESIS AND CHARACTERIZATION OF REDUCED GRAPHENE OXIDE, METAL OXIDE/HYDROXIDE AND POLYANILINE NANOCOMPOSITES FOR SUPERCAPACITOR APPLICATION**

**Thesis**

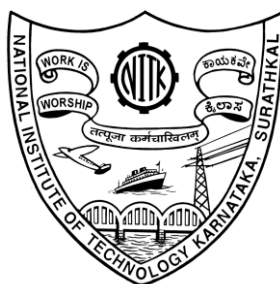
Submitted in partial fulfilment of the requirements for the degree of

**DOCTOR OF PHILOSOPHY**

by

**ARANGANATHAN V**

**(Reg. No.148033CY14F04)**



**DEPARTMENT OF CHEMISTRY**

**NATIONAL INSTITUTE OF TECHNOLOGY KARNATAKA,**

**SURATHKAL, MANGALORE - 575 025**

**MAY, 2020**



## DECLARATION

I hereby declare that the Research Thesis entitled “SYNTHESIS AND CHARACTERIZATION OF REDUCED GRAPHENE OXIDE, METAL OXIDE/HYDROXIDE AND POLYANILINE NANOCOMPOSITES FOR SUPERCAPACITOR APPLICATION” which is being submitted to the **National Institute of Technology Karnataka, Surathkal** in partial fulfillment of the requirements for the award of the degree of **Doctor of Philosophy** in Chemistry is a **bonafide report of the research work carried out by me**. The material contained in this Research Thesis has not been submitted to any other university or Institute for the award of any degree.

ARANGANATHAN V

148033CY14F04

Department of Chemistry

Place: NITK – Surathkal

Date:





## **CERTIFICATE**

This is to certify that the Research Thesis entitled “SYNTHESIS AND CHARACTERIZATION OF REDUCED GRAPHENE OXIDE, METAL OXIDE/HYDROXIDE AND POLYANILINE NANOCOMPOSITES FOR SUPERCAPACITOR APPLICATION” submitted by **Mr. Aranganathan V (Register Number: 148033CY14F04)** as the record of the research work carried out by him, is accepted as the Research Thesis submission in partial fulfillment of the requirements for the award of degree **Doctor of Philosophy**.

Research Guide

(Dr. A. Nityananda Shetty)

Chairman – DRPC



## **ACKNOWLEDGEMENT**

It's my immense happiness to express my heartfelt gratitude to Dr. A. Nityananda Shetty, Professor, Department of Chemistry, NITK for having taken me under his wings as his research student, motivating me to pass through obstacles, mentoring me, supporting me when I am broken, sharing his scintillating thoughts that have driven me to progress well with research; and most importantly for being an elderly friend. It is to be recorded that without his able guidance it is indeed would have not been possible to culminate my Ph.D. My research progress assessment committee members Dr. Keyur Raval, Assistant Professor, Department of Chemical Engineering and Dr. Darshak R. Drivedi, Associate Professor, Department of Chemistry, NITK merit my deepest gratitude for assessing my research time to time, enlightening me with their technical suggestions and motivations right through my entire research period.

I thank the Heads of the Department (present and past), all the faculty members of Department of Chemistry for their support. I also extend my acknowledgement to all the non-teaching staffs of Chemistry Department from whom I have received helps one way or the other, which were important right along the way.

I would like place a special acknowledgment to my colleague Mr. Prakashaiah for his constant, technical helps which made essential part of my research work without whose support it would have been impossible to finish my research.

It would be unfair if I fail to recognize Ms. Medhashree H, Dr. Subramanya Byndoor and Dr. Raghavendra Prasad J, NITK, from whom I have received key helps that made me to comprehend my research field better and in turn motivated to flourish further in the research. The timely help by Mr. J. Suresh and Mr. Gopinath, Tech Science, Chennai and characterization facility extended by Metallurgical and Material Engineering, and DST PURSE, Mangalore University are sincerely acknowledged.

It's my joy to extend my gratitude to my friends cum colleagues, Mr. Venkatadri Tekuri, Mr. Momidi Bharath Kumar, Dr. Kshama Shetty, Mr. Gururaj Acharya M, my batch mates and all the research scholars of the Chemistry Department NITK, for their timely help and motivations. The stipend provided by NITK is sincerely acknowledged.

Last but definitely not least I would like to thank my lovely parents and siblings for their limitless love, cheers, motivation and support, that made my back bone straight and chin up.

**ARANGANATHAN V**



## ABSTRACT

The research thesis entitled “**Synthesis and characterization of reduced graphene oxide, metal oxide/hydroxide and polyaniline nanocomposites for supercapacitor application**” presents the synthesis, structural characterization and electrochemical characterization of reduced graphene oxide/metal oxide/polyaniline nanocomposites. Two different metal oxides, namely, copper oxide and vanadium pentoxide and a metal hydroxide, namely, nickel hydroxide were used to synthesize three sets of nanocomposites with reduced graphene oxide (rGO) and polyaniline (PANI) by insitu single step chemical methods by varying the weight percentages of each of the constituents. The synthesized nanocomposites were reduced graphene oxide/copper oxide/polyaniline nanocomposites (GCP), reduced graphene oxide/vanadium pentoxide/polyaniline nanocomposites (GVP) and reduced graphene oxide/nickel hydroxide/polyaniline nanocomposites (GNP). The structures of the nanocomposites were characterized by powder-XRD, FT-IR spectroscopy, X-ray photon spectroscopy, energy dispersive spectroscopy, field emission scanning electron microscopy and Raman spectroscopy. The electrochemical characterizations of the synthesized nanocomposites were carried out in a two electrode system, by cyclic voltammetry, galvanostatic charge/discharge studies and electrochemical impedance spectroscopy in the presence of aqueous electrolytes. The magnetic effect to improve the electrochemical performance of antiferromagnetic GNP nanocomposites were also studied under different magnetic fields. The electrochemical results obtained for all the three sets of nanocomposites are highly impressive. Among the three sets of nanocomposites synthesized, the nanocomposite G14NP with a weight percentage composition of rGO14%: Ni(OH)<sub>2</sub>14%: PANI72%, exhibited a highest specific capacitance of 602.40 F g<sup>-1</sup>, specific capacity of 722.88 C g<sup>-1</sup>, an energy density of 120.48 W h kg<sup>-1</sup> and a power density of 2584.83 W kg<sup>-1</sup> with 1 M sulfuric acid as the electrolyte, at a current density of 1 A g<sup>-1</sup>. The G14NP retains 75% of its initial specific capacitance up to 16500 cycles. With one nanocomposite, which exhibited highest electrochemical performance, from each of the three series of nanocomposites, the practical application as secondary power source was demonstrated.

**Keywords:** supercapacitors, specific capacitance, energy density, power density.



# CONTENTS

**DECLARATION**

**CERTIFICATE**

**ACKNOWLEDGEMENT**

**ABSTRACT**

**CONTENTS** **I**

**LIST OF FIGURES** **VII**

**LIST OF TABLES** **XVII**

**NOMENCLATURES** **XX**

**LIST OF SYMBOLS** **XXI**

**CHAPTER – 1** **1**

**1.1. INTRODUCTION** **1**

**1.2. BATTERIES VERSUS FUEL CELLS VERSUS ELECTROCHEMICAL  
CAPACITORS** **3**

**1.3. CONSTRUCTION OF A SUPERCAPACITOR** **7**

**1.4. CLASSIFICATIONS AND WORKING OF SUPERCAPACITORS** **8**

**1.4.1. Electrical-double layer supercapacitors (EDLS)** **9**

1.4.1.1. Working of EDLS **10**

**1.4.2. Pseudo capacitors** **11**

1.4.2.1. Working of pseudocapacitors **12**

1.4.3. Hybrid supercapacitors	13
<b>1.5. ELECTROLYTES USED IN SUPERCAPACITORS</b>	<b>14</b>
1.5.1. Aqueous electrolytes	14
1.5.2. Organic electrolytes	15
1.5.3. Ionic liquids (ILs)	16
<b>1.6. DEFINITIONS INVOLVED IN SUPERCAPACITANCE</b>	<b>17</b>
1.6.1. Capacitance ( <i>C</i> )	17
1.6.2. Cycle Life	18
1.6.3. Specific energy, energy density and efficiency	18
1.6.4. Power density ( <i>P</i> )	19
<b>1.7. ELECTRODE MATERIALS</b>	<b>20</b>
1.7.1. Carbon materials	20
1.7.2. Graphene	22
1.7.2.1. Advantages	22
1.7.2.2. Limitations	23
1.7.2.3. Remedies	23
1.7.3. Reduced graphene oxide (rGO)	23
1.7.4. Faradaic materials	24
1.7.4.1. Metal/ Metal oxides/hydroxides	25
1.7.4.2. Conducting polymers	27
<b>1.8. APPLICATIONS</b>	<b>31</b>
1.8.1. Present applications	31
1.8.2. Future applications	32
1.8.2.1. Industrial applications	33
1.8.2.2. Electric utility applications	33
1.8.2.3. Automotive applications	33
<b>1.9. LITERATURE REVIEW</b>	<b>35</b>
<b>1.10. SCOPE AND OBJECTIVES</b>	<b>43</b>



<b>1.10.1. Scope of the proposed work</b>	<b>43</b>
<b>1.10.2. Objectives</b>	<b>44</b>
<b>1.11. FRAMEWORK OF THE THESIS</b>	<b>44</b>
<b>CHAPTER – 2</b>	<b>47</b>
<b>2. MATERIALS AND METHODS</b>	<b>47</b>
<b>2.1. MATERIALS</b>	<b>47</b>
<b>2.2. SYNTHESSES</b>	<b>47</b>
<b>2.2.1. Synthesis of graphite oxide (GO)</b>	<b>47</b>
<b>2.2.2. Synthesis of rGO</b>	<b>47</b>
<b>2.2.3. Synthesis of PANI</b>	<b>48</b>
<b>2.2.4. Synthesis of reduced graphene oxide/copper oxide/ polyaniline (GCP)         nanocomposite using H<sub>2</sub>SO<sub>4</sub> as dopant</b>	<b>48</b>
<b>2.2.5. Synthesis of GCP composites using glacial acetic acid as dopant</b>	<b>49</b>
<b>2.2.6. Synthesis of reduced graphene oxide/ vanadium pentoxide/         polyaniline ternary nanocomposites (GVP)</b>	<b>49</b>
<b>2.2.7. Synthesis of reduced graphene oxide/nickel hydroxide/polyaniline         nanocomposite (GNP) using glacial acetic acid as dopant</b>	<b>50</b>
<b>2.2.8. Synthesis of GNP nanocomposite using methane sulphonic acid as         dopant</b>	<b>51</b>
<b>2.3. PREPARATION OF WORKING ELECTRODES</b>	<b>51</b>
<b>2.3.1. Fabrication of magnetic supercapacitor cell</b>	<b>52</b>
<b>2.4. CHARACTERIZATIONS AND MEASUREMENTS</b>	<b>52</b>
<b>2.4.1. Structural and surface characterizations</b>	<b>52</b>
2.4.1.1. XRD studies	52
2.4.1.2. FT-IR spectroscopy	53
2.4.1.3. X-ray photoelectron spectroscopy	53
2.4.1.4. Raman spectroscopy	54

2.4.1.5. FESEM and EDS analyses	54
<b>2.4.2. Electrochemical characterization</b>	<b>54</b>
2.4.2.1. Cyclic voltammetry (CV)	55
2.4.2.2. Galvanostatic Charge/discharge	55
2.4.2.3. Electrochemical impedance spectroscopy (EIS)	56
<b>CHAPTER – 3</b>	<b>59</b>
<b>3. RESULTS AND DISCUSSION</b>	<b>59</b>
<b>REDUCED GRAPHENE OXIDE, COPPER OXIDE AND POLYANILINE (GCP) NANOCOMPOSITE</b>	<b>59</b>
<b>3.1. GCP WITH H<sub>2</sub>SO<sub>4</sub> AS DOPANT</b>	<b>60</b>
<b>3.1.1. Structural characterization</b>	<b>60</b>
3.1.1.1. X-ray diffraction analysis	60
3.1.1.2. FT-IR spectra	61
3.1.1.3. SEM analyses	62
<b>3.1.2. Electrochemical analysis</b>	<b>63</b>
3.1.2.1. Cyclic voltammetry (CV) studies	64
3.1.2.2. Galvanostatic charge/discharge (GCD) studies	66
3.1.2.3. Electrochemical impedance spectroscopic (EIS) studies	72
<b>3.2. GCP WITH GLACIAL ACETIC ACID AS DOPANT</b>	<b>77</b>
<b>3.2.1. Structural characterization</b>	<b>77</b>
3.2.1.1. X-ray diffraction analysis	77
3.2.1.2. FT-IR spectra	78
3.2.1.3. Raman spectra	80
3.2.1.4. XPS	81
3.2.1.5. FE-SEM	84
<b>3.2.2. Electrochemical characterizations</b>	<b>85</b>
3.2.2.1. CV studies	86
3.2.2.2. GCD studies	87

3.2.2.3. EIS studies	96
<b>3.3. REDUCED GRAPHENE OXIDE, VANADIUM PENTOXIDE AND POLYANILINE TERNARY NANOCOMPOSITES</b>	<b>102</b>
<b>3.3.1. Structural characterizations</b>	<b>102</b>
3.3.1.1. X-ray diffraction studies	102
3.3.1.2. FT-IR spectrum	103
3.3.1.3. Raman spectrum	104
3.3.1.4. FE-SEM analyses	104
3.3.1.5. XPS analysis	105
<b>3.3.2. Electrochemical characterizations</b>	<b>107</b>
3.3.2.1. CV studies	108
3.3.2.2. GCD studies	109
3.3.2.3. EIS studies	116
<b>REDUCED GRAPHENE OXIDE, NICKEL HYDROXIDE AND POLYANILINE NANOCOMPOSITES</b>	<b>121</b>
<b>3.4. GNP WITH GLACIAL ACETIC ACID AS DOPANT</b>	<b>121</b>
<b>3.4.1. Structural characterizations</b>	<b>121</b>
3.4.1.1. X-ray diffraction analysis	121
3.4.1.2. FT-IR spectrum	122
3.4.1.3. Raman spectrum	123
3.4.1.4. XPS	124
3.4.1.5. FE-SEM and EDS	125
<b>3.4.2. Electrochemical characterization</b>	<b>126</b>
3.4.2.1. CV studies	127
3.4.2.2. GCD studies	128
3.4.2.3. EIS studies	136
<b>3.5. EFFECT OF MAGNETIC FIELD IN ELECTROCHEMICAL PERFORMANCES OF REDUCED GRAPHENE OXIDE, NICKEL HYDROXIDE, AND POLYANILINE NANOCOMPOSITE</b>	<b>139</b>
<b>3.5.1. Electrochemical characterizations</b>	<b>140</b>

3.5.1.1. CV studies	146
3.5.1.2. GCD studies	147
3.5.1.3. EIS studies	151
<b>3.6. GNP WITH METHANE SULPHONIC ACID AS DOPANT</b>	<b>156</b>
<b>3.6.1. Structural characterization</b>	<b>156</b>
3.6.1.1. XRD studies	156
3.6.1.2. FE-SEM analyses	156
<b>3.6.2. Electrochemical characterizations</b>	<b>158</b>
3.6.2.1. CV studies	159
3.6.2.2. GCD studies	160
3.6.2.3. EIS studies	169
<b>3.7. COMPARISON OF ELECTROCHEMICAL PERFORMANCES OF GCP-300, G12CP, GVP80, G11NP AND G14NP</b>	<b>172</b>
<b>CHAPTER – 4</b>	<b>175</b>
<b>SUMMARY AND CONCLUSIONS</b>	<b>175</b>
<b>4.1. SUMMARY</b>	<b>175</b>
<b>4.2. CONCLUSIONS</b>	<b>176</b>
<b>4.3. SCOPE FOR FUTURE WORK</b>	<b>176</b>
<b>REFERENCES</b>	<b>177</b>
<b>LIST OF PUBLICATIONS</b>	<b>201</b>
<b>CURRICULUM VITAE</b>	<b>203</b>

## LIST OF FIGURES

<b>Fig. No</b>	<b>Caption</b>	<b>Page No.</b>
1.1	Schematic representation of charge storage process via (a) electrochemical double layer capacitance (b) pseudo capacitance. Adapted from MRS Bull., 2 Copyright Materials Research Society (2011).	2
1.2	Representation of a battery (Daniell cell) showing the key features of battery operation and the requirements on electron and ion conduction.	4
1.3	Representation of (a) supercapacitor, illustrating the energy storage in the electric double layers at the electrode-electrolyte interfaces, and (b) a fuel cell showing the continuous supply of reactants (hydrogen at the anode and oxygen at the cathode) and redox reactions in the cell.	4
1.4	Simplified Ragone plot of the energy storage domains for the various electrochemical energy conversion systems compared to an internal combustion engine and turbines and conventional capacitors.	6
1.5	Theoretical specific energies ( $\text{kW h ton}^{-1}$ ) and energy densities ( $\text{kW h /m}^3$ ) of various rechargeable battery systems compared to fuels, such as gasoline, natural gas, and hydrogen.	6
1.6	Representation of a single-cell double-layer capacitor and illustration of the potential drop at the electrode/electrolyte interface	8
1.7	Schematic representation of EDLS mechanism	10
1.8	Schematic representation of pseudo capacitance mechanism	12

<b>1.9</b>	Schematic representation of EDLC and pseudo capacitance mechanism	13
<b>2.1</b>	The schematic representation of the synthesis route of GCP nanocomposite	48
<b>2.2</b>	Pictorial representation of reduced graphene oxide, vanadium pentoxide and polyaniline ternary nanocomposites (GVP).	49
<b>2.3</b>	The schematic representation of the synthesis route of GNP nanocomposite	50
<b>2.4</b>	(a, b, c) SEM images of fabricated carbon fabric, d) Pictorial representation of supercapacitor cell setup.	51
<b>2.5</b>	Photographs of (a) fabricated supercapacitor device (b) arrangement magnets for the application of magnetic field.	52
<b>3.1</b>	X-ray diffraction patterns of graphene oxide (GO), reduced graphene oxide (rGO), polyaniline (PANI), and reduced graphene oxide/copper oxide/polyaniline nanocomposite (GCP)	60
<b>3.2</b>	FT–IR spectra of GO, rGO, PANI and GCP.	61
<b>3.3</b>	(a) and (b) SEM images of GCP nanocomposite.	62
<b>3.4</b>	ED spectrum (EDS) of GCP nanocomposite.	63
<b>3.5</b>	Cyclic voltammograms (CV curves) of GCP ternary nanocomposites of different weight ratios at a scan rate of 5 mV s <sup>-1</sup> .	65
<b>3.6</b>	CV curves of G <sub>25</sub> mg: Cu <sub>2</sub> O/CuO <sub>50</sub> mg: P <sub>300</sub> mg (GCP-300) at different scan rates.	65

<b>3.7</b>	CV curves of GCP-300, CP, GC and GP at a scan rate of 5 mV s <sup>-1</sup> .	66
<b>3.8</b>	GCD curves of GCPs of different weight ratio of PANI at a current density of 0.25 A g <sup>-1</sup> .	67
<b>3.9</b>	Galvanostatic charge discharge curves of GCP – 300 composite of weight ratio 300 mg of PANI at current densities of 0.25, 0.5, 1, 2, and 3 A g <sup>-1</sup> .	68
<b>3.10</b>	Galvanostatic charge/ discharge curves of GCP-300, CP, GC, and GP at 0.25 A g <sup>-1</sup> .	70
<b>3.11</b>	Plot of specific capacitance versus number of cycles.	71
<b>3.12</b>	Ragone plots of GCP-300, CP, GC and GP at current densities of 0.25, 0.5, 1, 2 and 3 A g <sup>-1</sup> respectively. Inset shows magnified portion of CP and GC.	71
<b>3.13</b>	Nyquist plot of GCP-300, CP, GC and GP composites. The inset depicts the magnified portion of GCP-300 and GP at high frequency.	73
<b>3.14</b>	The original and fitted EIS data of GCP-300 with knee frequency and circuit.	74
<b>3.15</b>	Bode plots of GCP-300, CP, GC and GP.	75
<b>3.16</b>	a) X-ray diffraction patterns of reduced graphene oxide/copper oxide/polyaniline nanocomposite (GCP); b) X-ray diffraction patterns of copper oxide/polyaniline (CP), reduced graphene oxide/copper oxide (GC), reduced graphene oxide/polyaniline (GP) binary composites.	77

<b>3.17</b>	a) FT–IR spectra of copper oxide/polyaniline (CP), reduced graphene oxide/copper oxide (GC), reduced graphene oxide/polyaniline (GP) binary composites and reduced graphene oxide/copper oxide/polyaniline ternary nanocomposite (GCP).	79
<b>3.18</b>	Raman spectra of graphite oxide (GO), reduced graphene oxide (rGO), polyaniline (PANI) and GCP.	80
<b>3.19</b>	a) Survey XPS spectrum of GCP, b-e) core level spectra of C 1s, N 1s, O 1s, Cu 2p 3/2, f) Cu 3p Auger electron spectra and core level spectra of g) Cu 3p h) Cu 3s.	82
<b>3.20</b>	(a) and (b) The FE-SEM images of the GCP nanocomposites.	84
<b>3.21</b>	(a) Cyclic voltammograms of G12CP, GC43P, GCP80, CP, GC and GP at a scan rate of 5 mV s <sup>-1</sup> ; (b) Cyclic voltammograms of composites G12CP at different scan rates.	86
<b>3.22</b>	GCD curves of composites (a) with different weight percentages of PANI at a current density of 0.25 A g <sup>-1</sup> ; (b) with different weight percentages of copper oxide at a current density of 0.25 A g <sup>-1</sup> ; (c) with different weight percentages of rGO at a current density of 0.25 A g <sup>-1</sup> ; (d) GCD curves of composites G12CP at current densities ranging from 0.25 to 10 A g <sup>-1</sup> ; (e) GCD curves of G12CP, GC43P, GCP80, CP, GC and CP at a current density of 0.25 A g <sup>-1</sup> ; (f) Plot of specific capacitances of nanocomposites synthesized at a current density of 0.25 A g <sup>-1</sup> vs weight percentages of rGO, copper oxide and PANI.	89
<b>3.23</b>	(a) Plots of specific capacitance versus current densities of composites G12CP, GC43P, GCP80, CP, GC and GP (with the inset of same plot of G12CP till current density of 10 A g <sup>-1</sup> ); (b) Ragone plots of composites G12CP, GC43P, GCP80, CP, GC and	93



GP from current density from 0.25 to 3 A g<sup>-1</sup> (with the inset of same plot of G12CP at current densities from 0.25 to 10 A g<sup>-1</sup>); (c) Plots of retention of capacitance versus number of cycles of composites G12CP, GC43P, GCP80; (d) Nyquist plots before and after 5000 cycles (with the inset of a table of resistance values) (e and f) The as-fabricated supercapacitors energizing red and yellow light emitting diodes.

- 3.24** Comparison of energy density and power density of G12CP with energy densities of lithium ion batteries. 94
- 3.25** (a) Cyclic voltammograms of bare carbon cloths at scan rates of 100, 80, 50, 30, 10, 5 mV s<sup>-1</sup>. (b) GCD curves of carbon cloths at applied currents of 0.5 mA, 1 mA, 2 mA, and 3 mA. 95
- 3.26** (a) Nyquist plots of G12CP, GC43P, GCP80, CP, GC and GP; (b) Nyquist plot of a nanocomposite CP with Arc 1 and Arc 2; (c) Equivalent circuit fitment of G12CP with the equivalent circuit (EC) at the inset; (d) Bode plots of G12CP, GC43P, GCP80, CP, GC and GP with the table of  $f_0$  and  $\tau_0$  values; (e) Bode magnitude plots of G12CP, GC43P, GCP80, CP, GC and GP; (f) Plots of capacitance versus log frequency of G12CP, GC43P, GCP80, CP, GC and GP. 96
- 3.27** (a) X-ray diffraction pattern of GVP (b) FT-IR spectra of GVP (c) Raman spectra of GVP (d-f) FE-SEM images of GVP at different magnifications. 103
- 3.28** (a-c) FE-SEM images of GVP nanocomposites; and (e-f) with distinct labels of PANI, rGO, V<sub>2</sub>O<sub>5</sub> nanoparticles, nanochannels and their marked dimensions. 105
- 3.29** (a) The XPS survey spectrum of GVP, core level spectra of (b) C 1s (c) N 1s (d) O 1s and V 2p. 106

<b>3.30</b>	(a) Cyclic voltammograms (CV curves) of composites GVP82, GV44P and G16VP at a scan rate of 5 mV s <sup>-1</sup> (b) CV curves of GVP82 at different scan rates (c) Charge/discharge curves (CD curves) of composites GVP82, GV44P and G16VP at a current density of 1 A g <sup>-1</sup> (d) Charge/discharge curves (CD curves) of composite GVP82 at different current densities.	108
<b>3.31</b>	(a) Plots of specific capacitance versus current density (b) Ragone plots of composites GVP82, GV44P and G16VP (c) Comparison of energy densities of GVP82 with Li-ion batteries (d) Plot of percentage retention of specific capacitance versus number of cycles of composite GVP82 (CV curves obtained after 4500, 9000 and 1300 cycles at 400 mV s <sup>-1</sup> at the inset) (e) Nyquist plots of GVP82 before and after 13000 cycles.	112
<b>3.32</b>	(a-d) GVP82 super capacitor device energizing green, blue, red color LEDs and a DC motor.	113
<b>3.33</b>	The circuit of DC-DC SCC.	114
<b>3.34</b>	(a) The real time DC-DC SCC with GVP82 incorporated in the circuit (b – f) The digital oscilloscope reading of GVP82 on applying 2 V.	115
<b>3.35</b>	(a) Nyquist plots of composites GVP82, GV44P and G16VP (b) Equivalent circuit fitment for the Nyquist plot of GVP82 (c) Bode phase angle plots (d) Bode magnitude plots (e) Plots of capacitance versus log frequency of composites GVP82, GV44P and G16VP.	117
<b>3.36</b>	XRD pattern of GNP.	122
<b>3.37</b>	FT-IR spectrum of are reduced graphene oxide/Ni(OH) <sub>2</sub> /polyaniline (GNP).	122

<b>3.38</b>	Raman spectrum of reduced graphene oxide/Ni(OH) <sub>2</sub> /polyaniline (GNP).	123
<b>3.39</b>	a) Survey spectrum of GNP b) core level spectra of Ni 2p c) core level spectra of O 1s, d) C 1s and e) N 1s.	124
<b>3.40</b>	(a - c) FE-SEM images of GNP at different magnifications.	126
<b>3.41</b>	(a) Cyclic Voltammograms (CV curves) of composites GNP80, GN24P and G11NP at a scan rate of 5 mV s <sup>-1</sup> (b) CV curves of G11NP at different scan rates.	128
<b>3.42</b>	(a) CD curves of composites GNP80, GN24P and G11NP at a current density of 1 A g <sup>-1</sup> (b) CD curves of G11NP at different current densities.	129
<b>3.43</b>	(a) Plots of specific capacitance versus current densities (b) Ragone plots of composites GNP80, GN24P, and G11NP (c) Plot of retention of specific capacitance versus number of cycles of G11NP (d) comparison of energy density and power density of Li-ion batteries with energy density and power density of G11NP obtained after 5000, 10000 and 15000 cycles.	131
<b>3.44</b>	(a) CV curves of G11NP at a scan rate of 5 mV s <sup>-1</sup> (b) CD curves of G11NP at a current density of 1 A g <sup>-1</sup> (c) Plots of specific capacitance versus current densities of G11NP (d) Ragone plots of G11NP , after subjecting into different number of cycles.	133
<b>3.45</b>	(a) Nyquist plots (b) Bode magnitude plots (c) Plots of capacitance versus log frequency plots (d) Bode phase angle plots, of G11NP after subjecting into different number of cycles.	135
<b>3.46</b>	The as-fabricated GNP composite device lighting up blue, green, orange, and red LEDs.	136

<b>3.47</b>	(a) Nyquist plots of composites GNP80, GN24P and G11NP; (b) Equivalent circuit fitment of G11NP with the equivalent circuit in the inset; (c) Bode magnitude plots; (d) Plots capacitance versus log frequency; (e) Bode phase angle plots, of composites GNP80, GN24P and G11NP.	137
<b>3.48</b>	(a) CV curves at a scan rate of 5 mV s <sup>-1</sup> (b) CD curves at a current density of 0.25 A g <sup>-1</sup> (c) Nyquist plots, of GN24P.	141
<b>3.49</b>	(a) CV curves at a scan rate of 5 mV s <sup>-1</sup> (b) CD curves at a current density of 0.25 A g <sup>-1</sup> (c) Nyquist plots, of GN31P.	142
<b>3.50</b>	(a) CV curves at a scan rate of 5 mV s <sup>-1</sup> (b) CD curves at a current density of 0.25 A g <sup>-1</sup> (c) Nyquist plots, of GN38P	143
<b>3.51</b>	(a) CV curves at a scan rate of 5 mV s <sup>-1</sup> (b) CD curves at a current density of 0.25 A g <sup>-1</sup> (c) Nyquist plots, of GN43P.	144
<b>3.52</b>	(a) CV curves at a scan rate of 5 mV s <sup>-1</sup> (b) CD curves at a current density of 0.25 A g <sup>-1</sup> (c) Nyquist plots, of GN51P	145
<b>3.53</b>	Plot of magnetic susceptibility versus weight percentage of Ni(OH) <sub>2</sub> .	146
<b>3.54</b>	(a) CV curves of GN48P at different magnetic fields at a scan rate of 5 mV s <sup>-1</sup> (b) CV curves of GN48P at a magnetic field of 625 μT at different scan rates (c) CD curves of GN48P at different magnetic fields at a current density of 0.25 A g <sup>-1</sup> (d) CD curves of GN48P at a magnetic field of 625 μT and at different current densities.	147
<b>3.55</b>	(a) Plots of specific capacitance versus current densities (b) Ragone plots and (c) Plots of coulombic efficiency versus current densities of GN48P at different applied magnetic fields (d) Plots	149

of percentage retention of capacitance versus number of cycles of GN48P at an applied magnetic field of 625  $\mu\text{T}$  with an inset of CV curves obtained after every 1000 cycles upto 5000 cycles (e) Comparison of Nyquist plots obtained before and after the cyclic studies with an inset of table showing the equivalent circuit parameters values.

- 3.56** (a) Nyquist plots of GN48P at different magnetic fields (b) 152  
Circuit fitment of GN48P with the equivalent circuit in the inset  
(c) Bode magnitude plots of GN48P at 0 T and 625  $\mu\text{T}$  (d)  
Admittance plots of GN48P at 0 T and 625  $\mu\text{T}$  (e) Plots of  
capacitance versus log frequency of GN48P at 0 T and 625  $\mu\text{T}$   
(f) Bode phase angle plots of GN48P at 0 T and 625  $\mu\text{T}$ .
- 3.57** XRD pattern of GNP synthesized using MSA as dopant. 156
- 3.58** (a-d) FE-SEM images of GNP synthesized using MSA as dopant 158  
(e) EDS of GNP with a spot from which the spectra were  
recorded.
- 3.59** The CV curves of (a) GNP73, GN35P and G14NP at a scan rate 159  
of 5  $\text{mV s}^{-1}$ , (b) G14NP at different scan rates, CD curves of (c)  
GNP73, GN35P and G14NP at a current density of 1  $\text{A g}^{-1}$ , (d)  
G14NP at different current densities.
- 3.60** (a) Plots of specific capacitance versus current density of 162  
GNP77, GN35P and G14NP; (b) Ragone plots of GNP77,  
GN35P and G14NP; (c) Plot of retention of specific capacitance  
versus number of cycles of cycles.
- 3.61** (a) CV curves (b) CD curves (c) Plots of specific capacitance 164  
versus current density (d) Ragone plot (e) Plots of coulombic  
efficiency versus current density, of G14NP after different  
number of cycles

<b>3.62</b>	(a) Nyquist plots, (b) Bode phase angel plot, (c) Bode magnitude plot, d) Plots of series resistance versus log frequency (e) Plots of capacitance versus log frequency, of G14NP before and after 4500, 7000, 11500 and 16500 cycles.	166
<b>3.63</b>	The G14NP energizing (a) LED of blue (~2 V) and green (~1.7 V) color at a time (b) Two DC motors at a time.	168
<b>3.64</b>	(a) Nyquist plots (b) Equivalent circuit fitment on Nyquist plot of G14NP (c) Bode phase angle plots (d) Bode magnitude plots (e) Plots of capacitance versus log of frequency, of nanocomposites GNP77, GN35P and G14NP.	169

## LIST OF TABLES

<b>Table No</b>	<b>Caption</b>	<b>Page No.</b>
1.1	Performance comparison between supercapacitor and Li-ion batteries (Courtesy of Maxwell Technologies, Inc.).	7
1.2	Classification of supercapacitors and their electrode materials	9
1.3	Theoretical pseudo capacitance and conductivity of selected metal oxides	25
1.4	Summary of the different types of supercapacitor devices	30
1.5	Few of the early reported similar work.	35
3.1	The elements present with corresponding weight and atomic percentages.	63
3.2	The compositions and the notations of nanocomposites synthesized.	64
3.3	The specific capacitance values of GCP composites with different weight ratio of PANI at a current density of $0.25 \text{ A g}^{-1}$ .	68
3.4	Specific capacitance of GCP-300 and corresponding binary composites at a current density of $0.25 \text{ A g}^{-1}$ .	71
3.5	Magnitudes of $f_0$ and $\tau_0$ .	76
3.6	The nomenclature used for the GCP composites of different composition and their respective percentages of the constituents.	85
3.7	The electrochemical parameters of different GCP composites synthesized at a current density of $0.25 \text{ A g}^{-1}$ .	88

<b>3.8</b>	The electrochemical parameters of nanocomposites G12CP, CP, GC and GP at a current density of $0.25 \text{ A g}^{-1}$ .	92
<b>3.9</b>	Equivalent circuit fitment parameters of nanocomposites G12CP, GC43P, GCP80 and binary composites CP, GC and GP.	97
<b>3.10</b>	Comparison of obtained results of G12CP with reported similar systems.	99
<b>3.11</b>	The weight percentages of GVP composites and their nomenclature.	107
<b>3.12</b>	The electrochemical parameters GVP composites.	110
<b>3.13</b>	Comparison electrochemical results of GVP82 with similar work.	118
<b>3.14</b>	The nomenclatures of the GNP composites	127
<b>3.15</b>	The electrochemical parameters of the composites at a current density of $1 \text{ A g}^{-1}$	130
<b>3.16</b>	Electrochemical parameters of G11NP before cycling, after 5000, 10000 and 15000 cycles.	133
<b>3.17</b>	The electrical parameters of G11NP after subjecting into different number of cycles.	134
<b>3.18</b>	The electrochemical parameters of GN48P at different magnetic fields at $0.25 \text{ A g}^{-1}$ .	148
<b>3.19</b>	The impedance parameters in the absence and in the presence of magnetic field.	153
<b>3.20</b>	Comparison of obtained results of GN48P under a magnetic field $625 \mu\text{T}$ with reported similar systems.	155



<b>3.21</b>	The elements present with corresponding weight and atomic percentages.	158
<b>3.22</b>	The nomenclatures of the GNP composites	158
<b>3.23</b>	The electrochemical parameters of GNP composites at a current density of $1 \text{ A g}^{-1}$ .	161
<b>3.24</b>	Electrochemical parameters of G14NP after different number of cycles.	163
<b>3.25</b>	The electrical parameters of G14NP after subjecting into different number of cycles.	167
<b>3.26</b>	Comparison of the results of G11NP and G14NP supercapacitor with the reported similar systems.	170
<b>3.27</b>	The comparison of electrochemical performances of GCP-300, G12CP, GVP80, G11NP and G14NP.	173
<b>3.28</b>	The results obtained for as GN48P composite at an applied magnetic field of $625 \mu\text{T}$ and without magnetic field.	174

## NOMENCLATURES

2EL	Two electrode system
3EL	Three electrode system
APS	Ammonium persulfate
CPE	Constant phase element
CV	Cyclic voltammetry
CV curves	Cyclic voltammograms
EDLC	Electrical double layer capacitance
EDLS	Electrical double layer supercapacitor
ES	Electrochemical supercapacitor
EIS	Electrochemical impedance spectroscopy
EDS	Energy dispersive spectrum
ESR	Equivalent series resistance
FE-SEM	Field emission scanning electron microscopy
FT-IR	Fourier transform Infra-Red
FWHM	Full width half maximum
GCD	Galvanostatic charge/discharge
GCD curves	Galvanostatic charge/discharge curves
GCP	Reduced graphene oxide/Copper oxide/ Polyaniline nanocomposite
GNP	Reduced graphene oxide/Nickel hydroxide/ Polyaniline nanocomposite
GO	Graphene oxide
GVP	Reduced graphene oxide/Vanadium pentoxide/ Polyaniline nanocomposite
JCPDS	Joint committee on powder diffraction standards
OCP	Open circuit potential
PANI	Polyaniline
PEDOT: PSS	Poly(3,4-ethylenedioxythiophene)-poly(styrenesulfonate)
rGO	Reduced graphene oxide
XRD	X-ray Diffraction
XPS	X-ray Photoelectron Spectroscopy

## LIST OF SYMBOLS

$C$	Capacitance
$R_{ct}$	Charge transfer resistance
$H$	Coulombic efficiency
$Q$ or CPE	Constant phase element
$C_{dl}$	Electric double layer capacitance
$E$	Energy density
$R_{leak}$	Leakage resistance
$P$	Power density
$\tau_0$	Relaxation time
$R_s$	Solution resistance
$C_s$	Specific capacitance
$Q$	Specific capacity
$T$	Time constant



## CHAPTER – 1

### 1.1. INTRODUCTION

The production of energy from non-renewable energy sources like fossil fuel reserves, leading to worse CO<sub>2</sub> emissions, is known to cause worst climatic change and global warming. The non-renewable energy resources are at their prime utilization and are forecasted to be exhausted in the near future. Therefore, unquestionably, the environmental pollution and energy crisis are the two most pressing problems of human kind today. To prevent environment from worst climatic changes caused by global warming and to preserve the non-renewable energy sources, energy need to be harvested from renewable energy sources.

Harnessing renewable energy sources such as the solar energy and the wind energy are the appropriate primary considerations as substituents for fossil fuels, to enable sustainable energy production. However, unreliable by nature, they are diffuse and intermittent. Therefore, the harvested energy has to be stored in an efficient mode. Energy storage devices such as batteries are capable of storing large quantities of energy and providing energy for consumer devices and vehicles. However, they usually suffer from poor power density. Therefore, batteries are usually oversized and heavy weight, resulting in increased vehicle load and reduced efficiency.

To meet the future thriving energy demand, the development of low-cost, lightweight, flexible, eco-friendly and high performance energy storage systems that can store energy efficiently and deliver it on demand are paramount. Thus, intense worldwide research has been focused on developing sustainable energy storage and conversion devices. As the performances of these devices implicitly depend on the properties of the electrode materials used in fabricating such devices, advancement in nanomaterials technology plays a pivotal role in constructing such devices (Kumar and Baek 2014).

Dealing with energy storage and its delivery in time would largely encounter supercapacitors, due to their high power density (fast charge-discharge rate), excellent long cyclic stability, low weight and operational security in comparison with other

secondary batteries. Hence rudimentary knowledge of supercapacitors and their advancement would be of fine step in marching ahead with sustainable energy storage and their applications. Supercapacitor can be defined as a “*device that stores electrical energy in the electrical double layer formed at the interface between an electrolytic solution and an electronic conductor*”. The term applies to charged carbon- carbon systems as well as carbon battery electrode and conducting polymer electrode combinations, sometimes called ultracapacitors, supercapacitors or hybrid capacitors (Winter and Brodd 2004).

Like batteries, electrochemical supercapacitors store and deliver electrical energy, but through different mechanisms. While batteries do it chemically (faradaic reaction), supercapacitors fabricated with carbonaceous materials store electricity physically by separating the positive and negative charges (non-faradaic). Typically, the energy is stored by the formation of electrical double-layers on the surfaces of both negative and positive electrodes through rapid ion adsorption, called as electrical double layer capacitance (EDLC); and by the fast and reversible faradic charge transfer processes (surface oxidation–reduction reactions) on or near the electrode surface, called as pseudo capacitance. A combination of the above can store and release electric energy by nanoscopic charge separation at the interfaces between the electrode and the electrolyte as illustrated in Fig. 1.1.

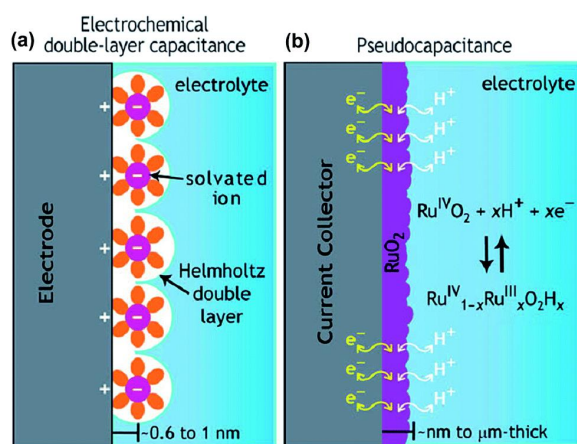


**Fig. 1.1** Schematic representation of charge storage process via (a) electrochemical double layer capacitance and (b) pseudo capacitance. Adapted from MRS Bull., 2 Copyright Materials Research Society (2011).

In general, the carbon-based electrode materials with high specific surface area, are used as electrode materials in electrical double layer capacitors and electroactive materials such as transition metal oxides and electrically conducting polymers are used in pseudo capacitors. A combination of the above two mechanisms could form high performance supercapacitors, which is a cost-effective solution for applications where durability and reliability of the storage devices become paramount. In addition, electrical double layer capacitors are believed to provide clean energy with almost zero waste emission before the disposal of these devices (Kumar and Baek 2014).

## **1.2. BATTERIES VERSUS FUEL CELLS VERSUS ELECTROCHEMICAL CAPACITORS**

Systems for electrochemical energy storage and conversion include batteries, fuel cells and supercapacitors. Despite of their different energy storage and conversion mechanisms, there are “electrochemical similarities” of these three systems. Common features are that the energy-providing processes take place at the electrode/electrolyte interface and that electron and ion transport are separated. Fig. 1.2 and 1.3 show the basic operation mechanisms of the three systems. Batteries, fuel cells and supercapacitors, all consist of two electrodes in contact with an electrolyte solution.

In batteries and fuel cells, electrical energy is generated by conversion of chemical energy via redox reactions at the anode and cathode. As reactions at the anode usually take place at lower electrode potentials than at the cathode, the terms negative and positive electrode (indicated as minus and plus poles) are used. The more negative electrode is designated as the anode, whereas the more positive electrode is designated as the cathode. The difference between batteries and fuel cells is related to the locations of energy storage and conversion. Batteries are closed systems, with the anode and cathode being the charge-transfer medium and taking an active role in the redox reaction as “active masses”. In other words, energy storage and conversion occur in the same compartment.

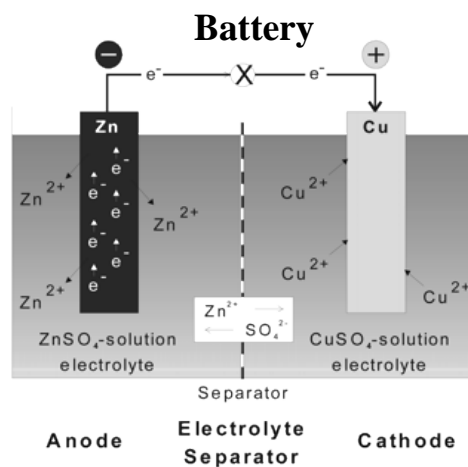


**Fig. 1.2** Representation of a battery (Daniell cell) showing the key features of battery operation and the requirements on electron and ion conduction.

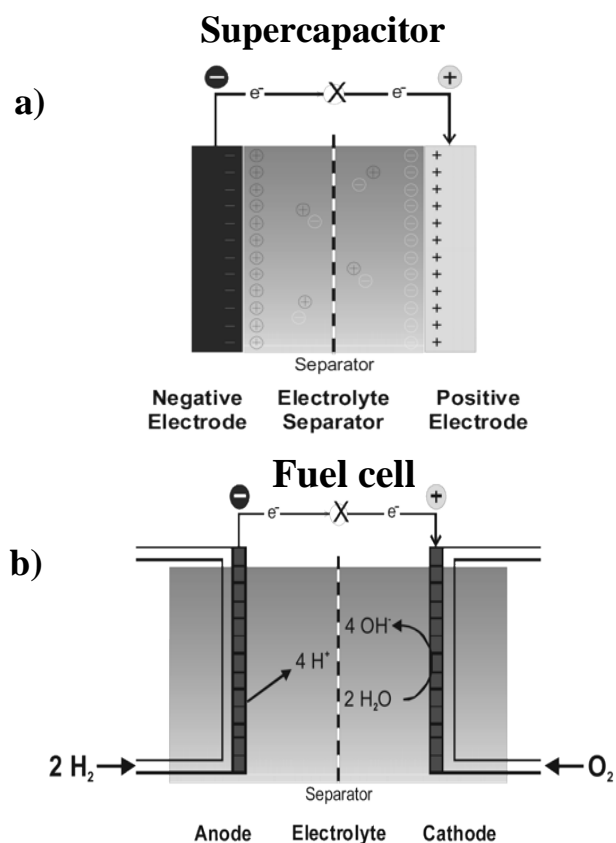


**Fig. 1.3** Representation of (a) supercapacitor, illustrating the energy storage in the electric double layers at the electrode-electrolyte interfaces, and (b) a fuel cell showing the continuous supply of reactants (hydrogen at the anode and oxygen at the cathode) and redox reactions in the cell.



Fuel cells are open systems, in which the anode and cathode are just charge-transfer media and the active masses undergoing the redox reaction are delivered from outside the cell, either from the environment (for example, oxygen from air) or from a tank, (for example, fuels such as hydrogen and hydrocarbons). Energy storage (in the tank) and energy conversion (in the fuel cell) are thus locally separated.

The supercapacitors having electrode materials made of carbonaceous materials, energy may not be delivered via redox reactions and thus the use of the terms anode and cathode may not be appropriate but are in common usage. By orientation of electrolyte ions at the electrode/electrolyte interface, so-called electrical double layers (EDLs) are formed and released, which results in a parallel movement of electrons in the external wire, that is, in the energy-delivering process.

The most promising future markets for fuel cells and supercapacitors are in the same application sector as batteries. In other words, supercapacitor and fuel cell developments aim to compete with, or even to replace, batteries in several application areas. Thus, fuel cells, which originally were intended to replace combustion engines and combustion power sources due to possible higher energy conversion efficiencies and lower environmental impacts, are now under development to replace batteries to power cellular telephones and notebook computers and for stationary energy storage.

The terms “specific energy” ( $\text{W h kg}^{-1}$ ) is used to express the energy contents of a system, whereas the rate at which the energy is observed/delivered is expressed as “specific power” (in  $\text{W kg}^{-1}$ ). To compare the power and energy capabilities, a representation known as the Ragone plot has been developed. A simplified Ragone plot (Fig. 1.4) discloses that fuel cells can be considered to be high-energy systems, whereas supercapacitors are considered to be high-power systems. Batteries have intermediate power and energy characteristics.

There are some overlaps in the energies and powers of supercapacitors or fuel cells, with those of batteries. Indeed, batteries with thin film electrodes exhibit power characteristics similar to those of supercapacitors. Finally, Fig. 1.4 also shows that no single electrochemical power source can match the characteristics of the internal combustion engine.

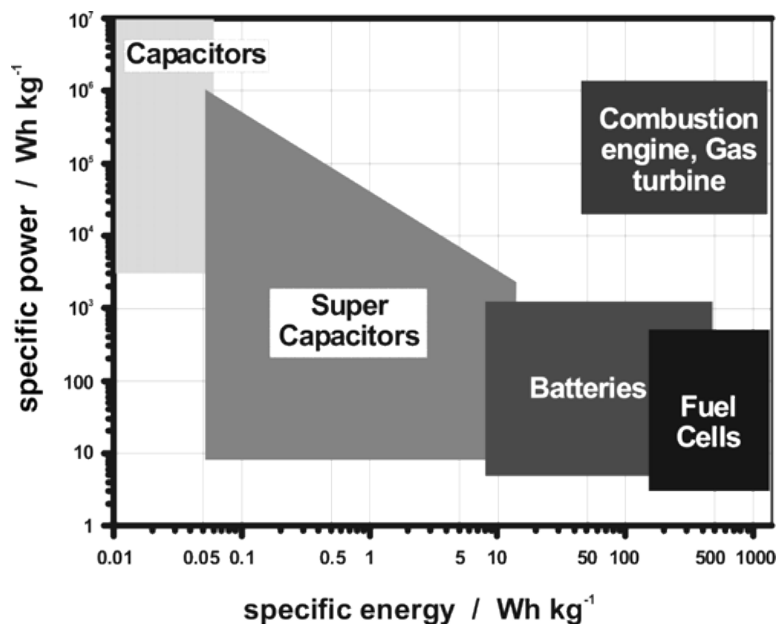


**Fig. 1.4** Simplified Ragone plot of the energy storage domains for the various electrochemical energy conversion systems compared to an internal combustion engine and turbines and conventional capacitors.

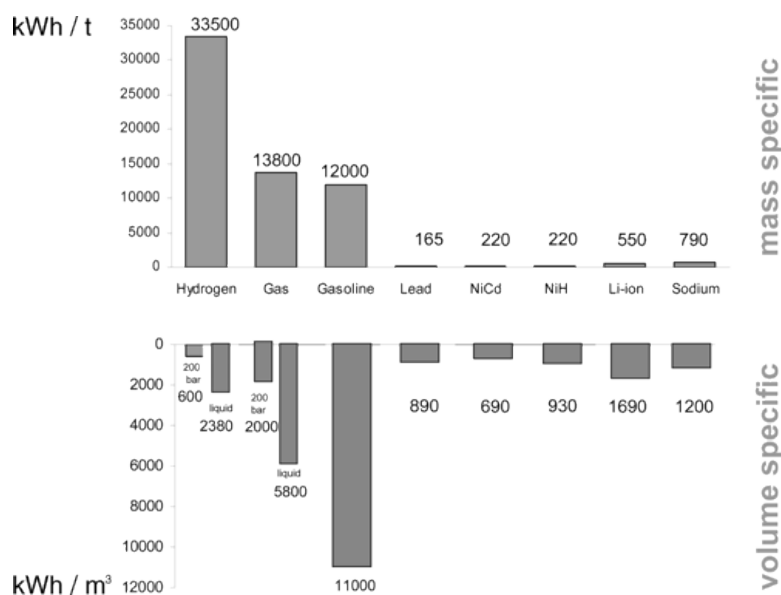


**Fig. 1.5** Theoretical specific energies  $[(\text{kW h}) \text{ton}^{-1}]$  and energy densities  $[(\text{kW h})/\text{m}^3]$  of various rechargeable battery systems compared to fuels, such as gasoline, natural gas, and hydrogen.

*“High power and high energy, the competitive behaviors in comparison to combustion engines and gas turbines, can best be achieved when the available electrochemical power systems are combined”.* In such hybrid electrochemical power

systems, supercapacitors would provide high power and the batteries and fuel cells would deliver high energy. Fig. 1.5 shows the theoretical specific energies ( $\text{kW h t}^{-1}$ ) and energy densities ( $\text{kW h}/\text{m}^3$ ) of various rechargeable battery systems in comparison with fuels, such as gasoline, natural gas and hydrogen. The inferiority of batteries is evident (Winter and Brodd 2004). The performance comparisons between supercapacitor and Li-ion batteries are listed in Table 1.1.

**Table 1.1** Performance comparison between supercapacitor and Li-ion batteries (Courtesy of Maxwell Technologies, Inc.) (Gidwani et al. 2014).

Function	Supercapacitor	Lithium-ion batteries
Charge time	1–10 seconds	0.1 - 1 h
Cycle life	1 million	500 and higher
Cell voltage	2.3 to 2.75 V	3.6 to 3.7 V
Specific energy (W h/kg)	5 (typical)	100–200
Specific power (W/kg)	Up to 10,000	1,000 to 3,000
Cost per W h	\$20 (typical)	\$0.50-\$1.00(large system)
Service life (in vehicle)	10 to 15 years	5 to 10 years
Charge temperature	–40 to 65°C (–40 to 149°F)	0 to 45°C (32°to 113°F)
Discharge temperature	–40 to 65°C (–40 to 149°F)	–20 to 60°C (–4 to 140°F)

### 1.3. CONSTRUCTION OF A SUPERCAPACITOR

An electrochemical supercapacitor (ES) is a charge-storage device similar to batteries in design and manufacturing. As shown in Fig. 1.6, an ES consists of two electrodes, an electrolyte and a separator that electrically isolates the two electrodes. The most important component in an ES is the electrode material. In general, the electrodes of ES are fabricated from nanoscale materials that have high surface area and high porosity. It can be seen from Fig. 1.6 that charges can be stored and separated at the interface between the electrodes made of conductive solid particles (such as carbon particles, metal oxide particles or conducting polymers) and the electrolyte. This interface can be treated as a capacitor with an electrical double-layer capacitance, which can be expressed by the following equation

$$C = \frac{\epsilon_r}{4\pi d} A \quad (1.1)$$

where  $A$  is the area of the electrode surface, which for a supercapacitor should be the active surface of the electrode porous layer,  $\epsilon_r$  is the dielectric constant of the medium (electrolyte), which will be equal to 1 for a vacuum and larger than 1 for all other materials, including gases and  $d$  is the effective thickness of the electrical double layer.

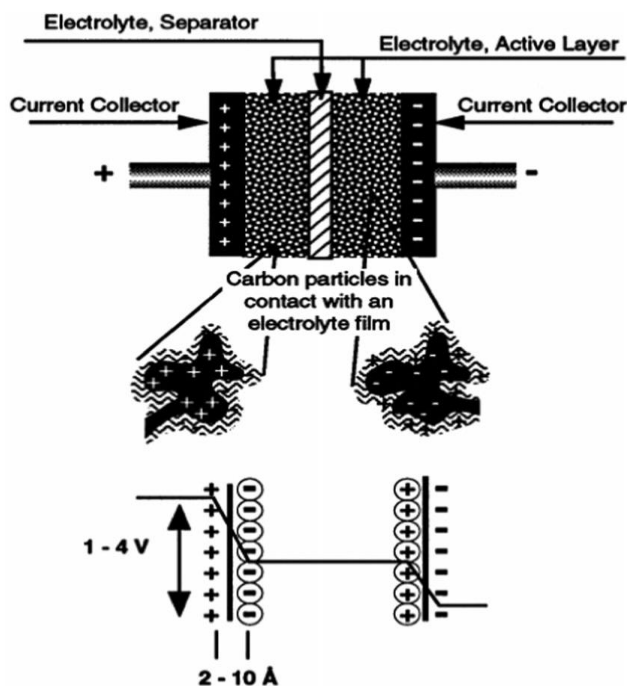


**Fig. 1.6** Representation of a single-cell double-layer capacitor and illustration of the potential drop at the electrode/electrolyte interface (Wang et al. 2012a).

#### 1.4. CLASSIFICATIONS AND WORKING OF SUPERCAPACITORS

Electrochemical supercapacitors may be distinguished by several criteria such as the electrode material utilized, the electrolyte or the cell design. With respect to electrode materials viz., carbon based, metal oxides and polymeric materials, supercapacitors are classified into three types; (Vangari et al. 2012)

- Electrical-double layer supercapacitors
- Pseudo capacitors
- Hybrid supercapacitors

The classification of supercapacitors and the materials used in them are listed in Table 1.2.

**Table 1.2** Classification of supercapacitors types and their electrode materials (Vangari et al. 2012).

Electric double layer capacitors	<ul style="list-style-type: none"> <li>➤ Carbon aerogels</li> <li>➤ Activated carbon</li> <li>➤ Carbon nanotubes</li> <li>➤ Carbon nanosheets</li> </ul>
Pseudo capacitors	<ul style="list-style-type: none"> <li>➤ Metal oxides</li> <li>➤ Conducting polymers</li> </ul>
Hybrid capacitors <ul style="list-style-type: none"> <li>▪ Asymmetric</li> <li>▪ Composite</li> <li>▪ Battery type</li> </ul>	<ul style="list-style-type: none"> <li>➤ Carbon materials, Conducting polymers</li> <li>➤ Carbon materials, metal oxides</li> </ul>

#### 1.4.1. Electrical-double layer supercapacitors (EDLS)

It is an energy storage device with both the electrodes made of carbonaceous materials separated by an insulator. It stores the energy charge by non-faradaic process and there is no charge transfer at the electrode-electrolyte interface. Carbon nanomaterials are unique structures with large surface area, high chemical, mechanical stability and excellent electrical conductivity (Chen et al. 2014).

Electrochemical double-layer capacitance (EDLC), results from the electrical double-layer formed at the interface of electrode surface and electrolyte. That is, the depletion of the oppositely charged species stores the energy at the electrode/electrolyte interface, which is a non-faradaic process. The specific capacitance of an EDLS is calculated as

$$C = \frac{\epsilon_r \epsilon_0 A}{d} \quad (1.2)$$

where  $\epsilon_r$  is the relative permittivity of the medium in the electrical double-layer,  $\epsilon_0$  is the permittivity of vacuum,  $A$  is the specific surface area of the electrode and  $d$  is the effective thickness of the electrical double-layer (Zhi et al. 2013).

## 1.4.1.1. Working of EDLS

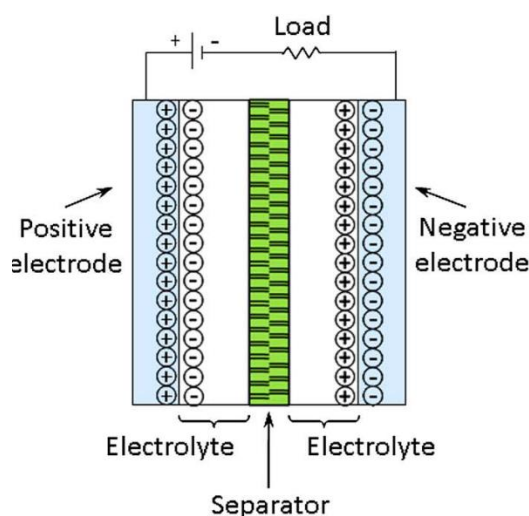


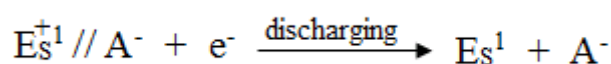
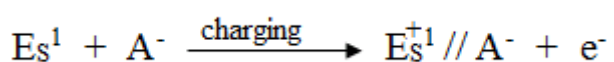
**Fig. 1.7** Schematic representation of EDLS mechanism (Vangari et al. 2012).

The capacitance generated at the electrolyte/electrode interface in an EDLS is associated with an electrode potential dependent accumulation of electrostatic charge at the interface. The mechanism for the production of capacitance by the electrical double layer involves reversible electrostatic adsorption of electrolytic ions on the electrode materials which generally possess electrochemical stability and high specific surface area (Simon et al. 2014). As shown in Fig. 1.7, this electrical double-layer capacitance emerges from electrode material particles, such as at the interface between the carbon particles and electrolyte, where an excess or a deficit of electric charges is accumulated on the electrode surfaces and electrolyte ions with counter balancing the charge built up on the electrolyte side in order to meet electroneutrality. During the process of charging, the electrons travel from the negative electrode to the positive electrode through an external load. Within the electrolyte, cations move towards the negative electrode while anions move towards the positive electrode. During discharge, the reverse processes take place.

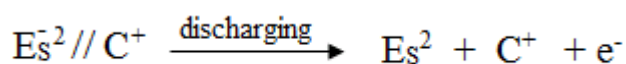
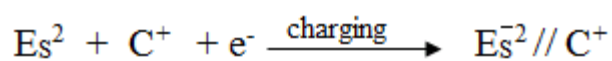
In this type of electrochemical supercapacitors, no charge transfers across the electrode/ electrolyte interface and no net ion exchanges occur between the electrode and the electrolyte. This implies that the electrolyte concentration remains constant during the charging and discharging processes. In this way, energy is stored in the double-layer interface.

If the two electrode surfaces can be expressed as  $E_s^1$  and  $E_s^2$ , an anion as  $A^-$ , a cation as  $C^+$ , and the electrode/ electrolyte interface as //, the electrochemical processes for charging and discharging can be expressed as per the following equations:

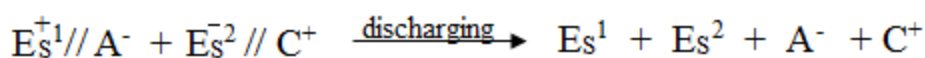
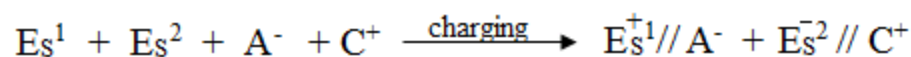
On one electrode (say, a positive one):



On the other electrode (say, a negative one):



And the overall charging and discharging process can be expressed as



### 1.4.2. Pseudo capacitors

Pseudo capacitors store the charge by the faradaic charge transfer occurring at the electrode/electrolyte interface. It has high specific capacitance and high energy density than the EDLS. Transition metal oxides and conducting polymers are examples of pseudo capacitors or redox capacitors.

Pseudo capacitance originates from the redox reaction of the electrode material with the electrolyte. The accumulation of electrons at the electrode is a faradaic process and the electrons produced by the redox reaction are, transferred across the electrolyte/electrode interface. The theoretical pseudo capacitance of metal oxide can be calculated as

$$C = \frac{nF}{MV} \quad (1.3)$$

where  $n$  is the mean number of the electrons transferred in the redox reaction,  $F$  is the Faraday constant,  $M$  is the molar mass of the metal oxide and  $V$  is the operating voltage window.

#### 1.4.2.1. Working of pseudocapacitors

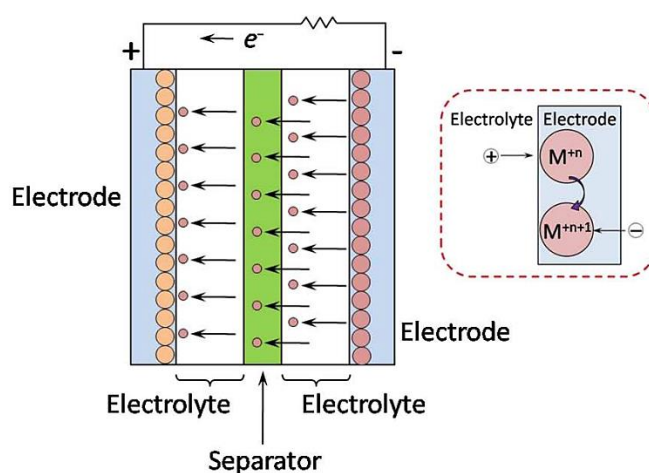


**Fig. 1.8** Schematic representation of pseudo capacitance mechanism (Vangari et al. 2012).

Faradaic supercapacitors (FS) or pseudo capacitors are different from electrostatic or EDLS. A schematic representation of pseudo capacitance mechanism is shown in Fig. 1.8. When a potential is applied to a faradaic supercapacitor, fast and reversible faradaic reactions (redox reactions) take place on the electrode materials and involve the passage of charge across the double layer, similar to the charging and discharging processes that occur in batteries, resulting in faradaic current passing through the supercapacitor cell. Materials undergoing such redox reactions include conducting polymers such as polyaniline (PANI) and metal oxides, such as  $\text{RuO}_2$ ,  $\text{MnO}_2$ , and  $\text{Co}_3\text{O}_4$ . Three types of faradaic processes occur at faradaic supercapacitor electrodes: reversible adsorption (for example, adsorption of hydrogen on the surface of platinum or gold), redox reactions of transition metal oxides (e.g.  $\text{RuO}_2$ ) and reversible electrochemical doping–dedoping in conductive polymer based electrodes. It has been demonstrated that these faradaic electrochemical processes not only extend the working voltage but also increase the specific capacitance of the supercapacitors. Since the electrochemical processes occur both on the surface and in the bulk near the surface of the solid electrode, a faradaic supercapacitor exhibits far larger capacitance



values and energy densities than an EDLS. As reported by Conway et al. (1999) the capacitance of a FS can be 10–100 times higher than the electrostatic capacitance of an EDLS. However, a FS usually suffers from relatively lower power density than an EDLS because faradaic processes are normally slower than non-faradaic processes. Moreover, as the redox reactions occur at the electrode, faradaic supercapacitors often lack stability during cycling, similar to batteries (Wang et al. 2012a).

### 1.4.3. Hybrid supercapacitors

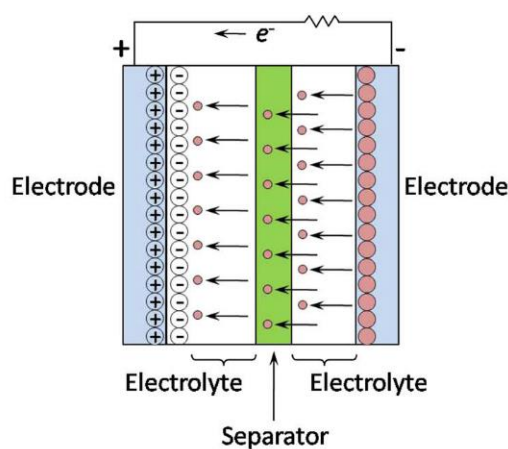


**Fig. 1.9** Schematic representation of combined operation of EDLC and pseudo capacitance mechanisms.

Materials used in hybrid type supercapacitors are composite materials, which involve the combinations of carbon materials with either metal oxides or conducting polymers or with both, thereby incorporating the aspects of both EDLC and pseudo capacitance.

It is worth mentioning that hybrid electrochemical supercapacitor with an asymmetrical electrode configuration (e.g. one electrode consisting of carbonaceous material while the other consisting of faradaic capacitance material) have been extensively studied lately to capitalize on the advantages of both the electrode materials in improving the overall cell voltage, energy and power densities. A schematic representation of combined operation of EDLC and pseudo capacitance mechanisms is shown in Fig. 1.9. In this kind of hybrid supercapacitor, both electrical double-layer capacitance and faradaic capacitance mechanisms occur simultaneously, but one of

them plays a greater role. In both mechanisms, large surface area, appropriate pore size distribution and high conductivity are essential characters of the electrode materials to achieve large capacitance (Wang et al. 2012a).

Regardless of the materials for supercapacitor electrodes, combining different materials to form composites should be an important approach because the individual substances in the composites can have a synergistic effect through minimizing the particle size, enhancing the specific surface area, inducing the porosity, preventing the particles from agglomerating, facilitating the electron and proton conduction, expanding the active sites, extending the potential window, protecting the active materials from mechanical degradation, improving the cycling stability and providing the extra pseudo capacitance. As a result, the composites can overcome the drawbacks of the individual substances and embody the advantages of all the constituents. But it is worth to point out that the reverse effects may also take place in the process of making composites. Consequently, there should be a compromise among the composition of individual substances and an optimized molar ratio of constituents for every composite material (Wang et al. 2012a).

## **1.5. ELECTROLYTES USED IN SUPERCAPACITORS**

As shown in Fig. 1.6, besides the two electrodes, the electrolyte, which resides inside the separator as well as inside the active material layers, is also one of the most important ES components. The requirements for an electrolyte in ES include: wide voltage window, high electrochemical stability, high ionic concentration, low solvated ionic radius, low resistivity, low viscosity, low volatility, low toxicity, low cost and availability at high purity (Wang et al. 2012a).

The electrolyte used in an ES can be classified into three types: aqueous electrolytes, organic electrolytes and ionic liquids (ILs).

### **1.5.1. Aqueous electrolytes**

The aqueous electrolytes (such as aqueous solutions of  $\text{H}_2\text{SO}_4$ ,  $\text{KOH}$ ,  $\text{Na}_2\text{SO}_4$  and  $\text{NH}_4\text{Cl}$ , etc.) can provide a higher ionic concentration and lower resistance than those of organic electrolytes. ES containing aqueous electrolyte may display higher

capacitance and higher power than those with organic electrolytes, probably due to the higher ionic concentration and the smaller ionic radius. In addition, aqueous electrolytes can be prepared and utilized with ease, while organic ones need strict processes and conditions to obtain ultra-pure electrolytes.

However, the biggest limitation of aqueous electrolytes is their narrow potential window as low as  $\sim 1.2$  V, much lower than those of organic electrolytes. Due to their narrow potential window aqueous electrolytes possess serious limitation in improving both the energy and power densities (Wang et al. 2012a).

In order to avoid the electrolyte depletion problems during the charging of ES, the electrolyte concentration has to be high. If the electrolyte reservoir is too small compared to the huge surface area of the electrodes, performance of the capacitor is reduced. This problem is particularly important for organic electrolytes where the solubility of the salts may be low. Zheng and Jow found, however, that concentrations higher than 0.2 molar are sufficient (Kötz and Carlen 2000).

### **1.5.2. Organic electrolytes**

Organic electrolytes can provide a potential window as high as 3.5 V, in comparison with aqueous electrolytes. This is the promising merit of organic electrolytes over aqueous electrolytes. Among the organic electrolytes, acetonitrile and propylene carbonate (PC) are the most widely used solvents. Acetonitrile can dissolve larger amounts of salts than other organic solvents, but suffers from environmental and toxic problems. PC-based electrolytes are eco-friendly and can offer a wide potential window, a wide range of operating temperature and good electrical conductivity. Besides, organic salts such as tetraethylammonium tetrafluoroborate, tetraethylphosphonium tetrafluoroborate and triethylmethylammonium tetrafluoroborate (TEMABF<sub>4</sub>) have also been used in ES electrolytes. Salts with asymmetric structures possess lower crystal-lattice energy and increased solubility (Wang et al. 2012a).

#### *Disadvantages*

However, the water content in organic electrolytes must be maintained less than 3–5 ppm. Otherwise, the ES's potential will be significantly reduced (Wang et al. 2012a).

Compared to a concentrated aqueous electrolyte the electrical resistance of the organic electrolytes is higher by a factor of at least 20, typically by a factor of 50. The higher electrolyte resistance also affects the equivalent distributed resistance of the electrode material and consequently reduces the maximum usable power ( $P$ ), which is calculated according to equation 1.4.

$$P = \frac{U^2}{4R} \quad (1.4)$$

where  $R$  is the total effective series resistance (ESR) and  $U$  is the cell voltage. However, the part of the reduction in power is compensated by the higher cell potential, which is achievable with organic electrolytes (Kötz and Carlen 2000).

### 1.5.3. Ionic liquids (ILs)

A molten salt, obtained by providing heat to the salt to counter balance the lattice energy of the salt, is called the ionic liquid (IL). ILs can exist in liquid form at the desired temperatures. Their characteristic properties make them promising to be used in ES as electrolytes. These properties are low vapor pressure, high thermal and chemical stability, low flammability, wide stable electrochemical potential window ranging from 2 to 6 V, typically about 4.5 V and electric conductivity in the range of 10 mS cm<sup>-1</sup>. Since ILs are solvent-free, there is no solvation shell in ILs and thus they can offer a well identified ion size.

The most commonly used ILs in ES as electrolyte are imidazolium, pyrrolidinium and asymmetric aliphatic quaternary ammonium salts with anions such as tetrafluoroborate, trifluoromethanesulfonate, bis(trifluoromethanesulfonyl)imide, bis(fluorosulfonyl)imide or hexafluorophosphate. Room temperature ILs are usually quaternary ammonium salts like tetralkylammonium [R<sub>4</sub>N]<sup>+</sup> and cyclic amines like aromatic pyridinium, imidazolium, saturated piperidinium and pyrrolidinium. Low temperature ILs based on sulfonium [R<sub>3</sub>S]<sup>+</sup> and phosphonium [R<sub>4</sub>P]<sup>+</sup> cations are also explored in the literature (Wang et al. 2012a).

To overcome the issue of inadequate electrical conductivity of ILs, particularly below room temperature, a dilution of ILs with organic solvents (such as acetonitrile, propylene carbonate or  $\gamma$ -butyrolactone) might be beneficial. For example, ionic liquids mixed with the commonly used PC/TEMABF<sub>4</sub> electrolytes improves the conductivity and therefore higher capacity and enhanced low-temperature power density. However, this approach may lead to other issues like safety, toxicity, flammability, narrow temperature regimes and so on. Furthermore, to achieve a high wettability of electrodes by ILs, the interface properties of electrode–ionic liquids need to be optimized (Wang et al. 2012a).

## 1.6. DEFINITIONS INVOLVED IN SUPERCAPACITANCE

### 1.6.1. Capacitance (C)

The capacitance ( $C$ ) of a supercapacitor is an intrinsic property, measured in Farad (F) and is the amount of electrical charge  $Q$  (in Coulomb) effectively stored in the supercapacitor, when it is charged at the rated voltage  $V_R$ , according to the following equation: (Conte 2010)

$$C = \frac{Q}{V_R} \quad (1.5)$$

The standardized method to measure the capacitance is using the ‘constant current discharge method’ and is based on the discharge curve. In this method, the capacitance is calculated using the following equation: (Conte 2010)

$$C = \frac{I(t_2 - t_1)}{(V_1 - V_2)} \quad (1.6)$$

where  $I$  (in A) is the discharge current,  $t_2 - t_1$  is difference in discharge time, and  $V_1 - V_2$  gives the potential window used. This method has been mostly based on the assumption that the discharge behavior of the supercapacitor remains linear. The values of  $V_1$  and  $V_2$  can differ from various procedures and standards, and can be stated as a fixed quotient of the rated voltage.

The method used to minimize the potential differences due to nonlinearity of the discharge behavior is the ‘energy conversion capacitance method’ and is based on the following (1.7) energy equation:(Conte 2010)

$$C = \frac{2E}{V_2^2 - V_1^2} \quad (1.7)$$

where,  $E$  is the amount of energy discharged effectively in Joule (J), when the supercapacitor potential changes from  $V_1$  to  $V_2$ . In this case, these voltages can be fixed values of the rated voltage (Conte 2010).

### **1.6.2. Cycle Life**

It is generally believed that supercapacitors do not show appreciable deterioration over a long period of time and under hundreds of thousands of charge/discharge cycles, even if it is fully discharged at a potential near to zero. In reality this is true for the EDLC, but it is not the case of supercapacitor, in which faradic processes store energy. The ageing of supercapacitors is pertaining to a variety of processes, which depend on the supercapacitor design and the operating conditions, and electrode material used in fabricating the supercapacitor.

A critical aspect in the cycle life determination is the definition of the end of life criteria. Some characteristics such as, capacitance, equivalent series resistance (ESR) and operating potential window of the supercapacitor change significantly and can be used to state the end of the life. Cycle life test procedures are normally based on a constant current profile. The supercapacitors are charged and discharged at constant current between the rated voltage and a defined end-of discharge voltage arbitrary selected, as a percentage of the rated voltage (normally, one-half or one-third of the rated voltage). Periodically, after a defined number of complete charge/discharge cycles, the basic characteristics of the SC are measured and the variations are estimated. The measurement is terminated whenever the capacitance (or the energy) decreases for at least 20 or 30% with respect of the initial one (Kötz and Carlen 2000).

### **1.6.3. Specific energy, energy density and efficiency**

The amount of energy stored in a capacitor per volume of a capacitor is called as its energy density. Energy density is measured volumetrically (per unit of volume) in watt-

hours per liter (Wh L<sup>-1</sup>) and gravimetrically (per unit of mass) in watt-hours per kilogram (Wh kg<sup>-1</sup>) (Zhi et al. 2013). The electrical energy ( $E_{\max}$ ) stored or energy density of a supercapacitor is calculated by: (Conte 2010)

$$E_{\max} = \frac{1}{2} C V_R^2 \quad (1.8)$$

where,  $C$  is the capacitance and  $V_R$  is the rated voltage. Practically, the complete discharge up to a voltage equal to zero is impossible and therefore, a useable energy content is the energy delivered when the supercapacitor is discharged in a defined manner (e.g. at constant current or at constant power) from the rated voltage  $V_R$  up to  $1/2 V_R$ .

The energy efficiency (%) is the ratio of the energy delivered by a supercapacitor to the energy that was supplied to it during a defined cycle. The specific energy and specific power can be obtained by dividing the measured value of energy and power with the overall weight of the supercapacitor (Conte 2010).

#### 1.6.4. Power density ( $P$ )

Power density is the measure of rate/speed at which energy can be delivered to/absorbed from the load. Power density is calculated either gravimetrically in kilowatts per kilogram (kW kg<sup>-1</sup>) or volumetrically in kilowatts per liter (kW L<sup>-1</sup>). The power density can be calculated using equation 2.7.

$$P = \frac{E}{t_d} \quad (1.9)$$

where, the  $E$  is the energy density (W h kg<sup>-1</sup>) and  $t_d$  is the discharge time in hour.

The maximum power ( $P_{\max}$ ) is calculated by the formula (Zhi et al. 2013):

$$P_{\max} = \frac{V^2}{4R} \quad (1.10)$$

$V$  is the voltage applied and  $R$  is the equivalent series resistance (ESR) of the device at a given condition.

## 1.7. ELECTRODE MATERIALS

The key performance parameters of supercapacitors are specific capacitance (normalized by electrode mass, volume or area), energy density, power density, rate capability (retained capacitance at a high current loading) and cyclic stability. In order to increase the energy density and power density of a supercapacitor, it is necessary to increase the specific capacitance ( $C_s$ ) and the operating potential window (V) as well as reduce the equivalent series resistance (ESR). For EDLS, the maximum operating voltage window (V) is mainly dependent on the electrolyte used, which is limited by the stability of the electrolyte. One of the current research trends in supercapacitors is to develop non-aqueous electrolytes with wide potential window.

Ideal electrode materials are required to possess (Zhi et al. 2013):

- High specific surface area (governs the specific capacitance).
- Controlled porosity (affects the specific capacitance and the rate capability).
- High electronic conductivity (crucial for the rate capability and the power density).
- Desirable electroactive sites (governs pseudo capacitance).
- High thermal stability and chemical stability (affect the cyclic stability).
- Low costs of raw materials and manufacturing.

### 1.7.1. Carbon materials

Carbon materials are promising electrode materials for large scale production and to be used as commercial supercapacitor electrode materials due to their advantages such as high abundance, lower cost, easy processing, non-toxicity, higher specific surface area, good electrical conductivity, high chemical stability and wide operating temperature range. Carbon-based supercapacitors store energy by EDLC mechanism, have excellent cyclic stability and long cycle life (durability) as the electrode undergoes no chemical change during the charge/discharge processes (Zhi et al. 2013).

The carbonaceous materials store charges at the electrochemical double-layer formed at the electrode/electrolyte interface, rather than storing them in the bulk of the capacitive material. Therefore, the capacitance majorly depends on the surface area accessible to the electrolyte ions. The factors that govern their energy storage performance are specific surface area, pore-size distribution, electrical conductivity and



surface functionality. Among these, specific surface area and pore-size distribution are the two most essential factors affecting the performance of carbonaceous materials.

As suggested by Conway et al. (1999) the carbonaceous material for EDLS must have three properties:

- High specific areas, in the order of  $1000 \text{ m}^2 \text{ g}^{-1}$ ,
- Good intra- and inter-particle conductivity in porous matrices,
- Good electrolyte accessibility to the intra-pore space of carbon materials.

Therefore, the process of selecting supercapacitor electrode materials, obtaining a high and accessible specific surface area, with good electrical conductivity is essential (Wang et al. 2012a).

*Zero-dimensional (0-D) carbon nanoparticles:* 0-D carbon particles are round-shaped particles with an aspect ratio close to 1. 0-D carbon particles mainly include ultrafine activated carbon (AC), carbon nanospheres and mesoporous carbon. They possess high specific area ( $\sim 3000 \text{ m}^2 \text{ g}^{-1}$  for AC). More importantly, the pore content and size distribution can be tailored, which makes them suitable for supporting material for metal oxides, for the supercapacitor electrodes.

*One-dimensional (1-D) carbon nanostructures:* 1-D nanostructures are the fiber-shaped materials like carbon nanotubes (CNT), carbon nanofibers (CNF) and carbon nanocoils. They have high aspect ratio and good electronic transport properties, which is anticipated to facilitate the kinetics of the electrochemical reactions.

*Two-dimensional (2-D) nanosheets:* 2-D nanostructures are the sheet-shaped materials with a high aspect ratio. Graphene, graphene oxide (GO) are the examples of the 2-D carbon nanosheets. Graphene and GO exhibit great mechanical strength, excellent electronic conductivity and high specific surface area, which are essential properties for supercapacitor electrodes. For example, the theoretical surface area of single layer graphene is  $2756 \text{ m}^2 \text{ g}^{-1}$  with a charge mobility of  $200\,000 \text{ cm}^2 \text{ V}^{-1} \text{ s}^{-1}$ .

*Three-dimensional (3-D) porous architectures:* 3-D architectures are made of low dimensional building blocks. 3-D porous carbon nano-architectures used in the supercapacitor electrodes are mainly carbon nanofoams or sponges as they have high

specific surface area, large area of electrolyte – electrode interface and continuous electron transport path (Zhi et al. 2013).

### 1.7.2. Graphene

Graphene, a two-dimensional all-sp<sup>2</sup> hybridized carbon, is an excellent electrode material for supercapacitors due to its high mechanical strength, high theoretical specific area, excellent charge carrier mobility, ability to withstand a high current density up to 108 A/cm<sup>2</sup> and chemical stability. Graphene has wide applications in catalysis, field effect transistors, sensors, energy storage, conversion, etc., The synthesis of graphene involves various techniques like mechanical cleaving (exfoliation) and chemical exfoliation of graphite, chemical synthesis and thermal chemical vapor deposition (CVD), unzipping nanotube and microwave synthesis. The choice of synthetic route depends upon the size and purity of the graphene desired for specific applications (Bhuyan et al. 2016). Graphene sheets are very hydrophobic and tend to form agglomerates easily and irreversibly in aqueous solution in the absence of dispersing reagents, through the  $\pi$ - $\pi$  stacking and van der Waals interactions (Ates 2016). The theoretical capacitance of a single graphene sheet when the complete surface area ( $\sim 2756 \text{ m}^2\text{g}^{-1}$ ) is utilized is  $550 \text{ F g}^{-1}$ . (Zhao et al. 2012).

#### 1.7.2.1. Advantages

- The consideration of graphene in energy storage originates from its abundance, low production cost, processability, chemical stability, excellent electrical conductivity, high thermal stability, wide potential windows, good capacitance and eco-friendliness.
- The graphene exhibits a very large electrochemically active surface area, which is the most notable feature as it determines the capacitance. Crumpled silk like structure of graphene with large interlayer spacing allows the easy access of electrolyte ions to form electrical double layers.
- Oxygenated form of graphene namely graphene oxide (GO) is an important precursor for preparing graphene sheets on a large scale. The major advantage of GO is that it can be easily dispersed in water due to the presence of many polar oxygen-containing functional groups at its edges and basal planes. These negatively charged oxygen-containing functional groups can, not only be used as nucleation sites to

adsorb precursors of conducting polymers and metal oxides onto the GO sheets via electrostatic force, but can also be used to modify their surfaces chemically and electrochemically and to attach or convert them to other useful functional groups required for anchoring or dispersing foreign moieties on graphene sheets.

- In addition, it is believed that these groups will greatly influence the electrochemical performance in terms of the heterogeneous electron transfer.

Therefore, graphene is generally considered as an ideal building block in synthesizing the composite materials and can be an electrode material for the next generation electrochemical supercapacitors, when coupled with a variety of compounds such as conducting polymers, metals and metal oxides etc., (Kumar and Baek 2014).

#### 1.7.2.2. *Limitations*

- The maximum capacitance is restricted by the active electrode surface area and the pore size distribution (typically  $0.15\text{--}0.4\text{ F m}^{-2}$ , or  $\sim 150\text{ F g}^{-1}$  for carbon). Overall, the energy densities of commercial carbon-based EDLSs are typically  $3\text{--}5\text{ W h kg}^{-1}$ , which are much lower than that of an electrochemical battery ( $30\text{--}40\text{ W h kg}^{-1}$  for a lead acid battery and  $10\text{--}250\text{ W h kg}^{-1}$  for a lithium-ion battery). Such low energy densities cannot fulfill the requirement of energy storage devices for vehicles, wind farms and solar power plants (Zhi et al. 2013).

#### 1.7.2.3. *Remedies*

- In order to improve the specific capacitance and the energy density, transition metal oxides and conducting polymers are being studied as supporting materials to be composited with graphene for supercapacitor electrodes.
- The studied metal oxides include  $\text{RuO}_2$ ,  $\text{MnO}_2$ ,  $\text{NiO}$ ,  $\text{Co}_3\text{O}_4$ ,  $\text{SnO}_2$ ,  $\text{ZnO}$ ,  $\text{TiO}_2$ ,  $\text{V}_2\text{O}_5$ ,  $\text{CuO}$ ,  $\text{Fe}_2\text{O}_3$ ,  $\text{WO}_3$ , etc., and conducting polymers include polyaniline (PANI), polypyrrole (PPy), etc., In particular, some metal oxides show excellent pseudo capacitance, unlike a lithium battery in which the ions are deeply intercalated in the materials lattice (Zhi et al. 2013).

### 1.7.3. **Reduced graphene oxide (rGO)**

The reduced form of graphene oxide (GO) with a few unreduced oxygen containing functional groups is called as reduced graphene oxide (rGO) (Bianco et al.

2013). The reduction process includes, chemical reduction method using reducing agents like sodium borohydride, hydrazine hydrate, etc., reduction by heat treatment, reduction using micro wave radiations, hydrothermal method, etc., (Zhao et al. 2012; Johra and Jung 2015). The chemical and mechanical properties of rGO is similar to that of graphene which is with no oxygen containing functional groups. The layer properties of reduced graphene oxide can be controlled when it is composited using an appropriated spacer which could deter the rGO layers from restacking. The advantage rGO over the graphene is that, the synthesis of rGO is facile than that of graphene, as the graphene synthesis requires sophisticated instruments and conditions whereas the synthesis of rGO can be carried out even at a laboratory condition without specific setup which makes the rGO more feasible and economic than that of graphene.

The graphite oxide is an oxidized product of graphite, the oxidation of which is carried out using strong oxidizing agents like potassium permanganate and sodium nitrite with concentrated sulphuric acid, commonly known as Hummers method (Hummers and Offeman 1958). A modified version of Hummers method is also in practice which involves the use of phosphoric acid instead of sodium nitrite along with sulphuric acid (Marcano et al. 2010). The graphene oxide is a product that is obtained by exfoliation of graphite oxide. The exfoliation of graphite oxide is generally carried out by ultrasound sonication (Peng et al. 2011) which disrupts the stacked layers of honeycomb lattices, thereby causing the loose packing and widening the d-spacing. The hydrophilicity of graphene oxide (Compton and Nguyen 2010) makes it more dispersible in water, which is favorable for the synthesis of metal oxides and conducting polymers on it.

#### **1.7.4. Faradaic materials**

The carbon materials mentioned above are with limited specific capacitance, typically in the range of 10–50  $\mu\text{F cm}^{-2}$  for a real electrode surface. The capacitance of faradaic materials may be 10–100 times greater than that of non-faradic materials. Therefore, supercapacitors made of faradaic (redox) active materials are suitable for the next generation of electrochemical supercapacitors. They not only store charges in the double layer, like EDLS electrodes, but also undergo fast and reversible surface redox reactions (faradaic reactions), producing high specific capacitance. Therefore,

substantial attempts have been made lately to develop electrode materials with pseudo capacitance. This kind of materials are generally classified into two types: (Wang et al. 2012a)

- Electroactive metal oxides
- Conducting polymers

#### 1.7.4.1. Metal/ Metal oxides/hydroxides

In general, metal oxides can provide higher energy density for supercapacitor than conventional carbon materials and better electrochemical stability than polymer materials. They not only store energy electrostatically like carbonaceous materials but also by electrochemical faradaic reactions between electrode materials and electrolytic ions within appropriate potential windows.

The prerequisites for metal oxides to be used in supercapacitors as electrode materials are:

- The metal oxides should be electrically conductive,
- The metals of metal oxides should be able to exist in two or more oxidation states that coexist over a continuous range with no phase changes involving irreversible modifications of a three-dimensional structure,
- The protons should freely intercalate into the metal oxide lattice on reduction (and out of the lattice on oxidation), allowing facile interconversion of  $O_2 \leftrightarrow 2OH^-$  (Wang et al. 2012a).

**Table 1.3** Theoretical pseudo capacitance and conductivity of few selected metal oxides (Zhi et al. 2013).

Metal oxide	Electrolyte	Charge storage reaction	Theoretical capacitance (F g <sup>-1</sup> )	Conductivity (S cm <sup>-1</sup> )	Ref.
MnO <sub>2</sub>	Na <sub>2</sub> SO <sub>4</sub>	$MnO_2 + M^+ + e^- \rightarrow MMnO_2$ (M could be H <sup>+</sup> , Li <sup>+</sup> , Na <sup>+</sup> , K <sup>+</sup> )	1380 (0.9 V)	10 <sup>-5</sup> to 10 <sup>-6</sup>	(Toupin et al. 2004) (Bélanger et al. 2008)
NiO	KOH, NaOH	$NiO + OH^- \rightarrow NiOOH + e^-$	2584 (0.5 V)	0.01 to 0.32	(Nandy et al. 2009) (Kong et al. 2011)

Co <sub>3</sub> O <sub>4</sub>	KOH, NaOH	$\text{Co}_3\text{O}_4 + \text{OH}^- + \text{H}_2\text{O} \rightarrow$ $3\text{CoOOH} + \text{e}^-$ $\text{CoOOH} + \text{OH}^- \rightarrow$ $\text{CoO}_2 + \text{H}_2\text{O} + \text{e}^-$	3560 (0.45 V)	10 <sup>-4</sup> to 10 <sup>-2</sup>	(Hamdani et al. 2010) (Rakhi et al. 2012) (Yuan et al. 2012)
RuO <sub>2</sub> , xH <sub>2</sub> O	H <sub>2</sub> SO <sub>4</sub> , Na <sub>2</sub> SO <sub>4</sub>	$\text{RuO}_2 + x\text{H}^+ + x\text{e}^- \rightarrow \text{RuO}_{2-x},$ $(\text{OH})_x \quad (0 < x < 2)$	1200–2200 (1.23 V)	103 for poly-crystalline, and ~1 for amorphous	(Hu et al. 2004) (Adeyemo et al. 2011)

Table 1.3, lists the theoretical capacitances of few metal oxides and their charge storage reactions. It can be seen that the transition metal oxide electrodes possess higher theoretical specific capacitance than the carbon electrodes. Several reports have indicated that bare metal oxide electrodes can deliver large specific capacitance and high energy density at a slow scan rate or at a low current density. For example, the electrodeposited NiO thin film electrode exhibited a specific capacitance of 1776 F g<sup>-1</sup> in 1 M KOH electrolyte at a scan rate of 1 mV s<sup>-1</sup>. However, only 23% of capacitance was retained when the scan rate was increased from 1 mV s<sup>-1</sup> to 100 mV s<sup>-1</sup>. Therefore, metal oxides may not be employed alone as the supercapacitor electrodes for practical purpose due to the following drawbacks (Zhi et al. 2013).

#### Limitations

- The electrical conductivity of most metal oxides except for RuO<sub>2</sub> is very low. The high resistivities of metal oxides increase the intrinsic resistances of the electrodes and especially cause a large ohmic loss at a high current density. Thus, the power density and the rate capability become poor.
- The strain developed in the pure metal oxide during the charge–discharge processes produces cracks in electrode, leading to poor cyclic stability.
- The surface area, porosity and its distribution are difficult to tailor in metal oxides (Zhi et al. 2013).

#### 1.7.4.2. Conducting polymers

Conducting polymers (CPs) possess many advantages like low cost, low environmental impact, high conductivity in a doped state, high potential window, high energy storage capacity, porosity, reversibility and adjustable redox activity through chemical modifications that make them suitable materials for supercapacitor. Conducting polymers offer capacitive behavior through the faradaic process. On oxidation the ions are transferred to the back bone of the polymers and on reduction the ions are transferred back to the electrolyte from the backbone; these redox reactions occur throughout the entire bulk of the conducting polymers, and not just on their surfaces. As the charging and discharging reactions do not involve any structural alterations like phase changes, the processes are highly reversible.

Conducting polymers can be positively or negatively charged with ion insertion in the polymer matrix to increase electronic conductivity. They can cause oxidation or reduction reactions, which generate delocalized ‘n’ electrons on the polymer chains. The oxidation/reduction processes of these polymers are termed as ‘doping/dedoping’. The positively-charged polymers, introduced by oxidation on the repeating units of polymer chains, are termed as ‘p-doped’, while negatively-charged polymers generated by reduction are termed as ‘n-doped’. The potentials of these doping processes are determined by the electronic states of  $\pi$  – electrons.

Conducting polymers-based electrochemical supercapacitor systems have three configurations:

*Type I (symmetric).* This type of supercapacitor is called as a p–p supercapacitor in which both electrodes possess the same p-dopable polymer. When fully charged, one electrode is in the full p-doped (positive) state and the other in the uncharged state.

*Type II (asymmetric).* This type is a p–p’ supercapacitor. Two different p-dopable polymers with a different range of oxidation and reduction electro activities are used, such as polypyrrole/polythiophene.

*Type III (symmetric).* This is an n–p type supercapacitor. Electrodes use the same polymer which can be both p- and n-doped in the same molecule, such as poly(3-fluorophenyl)thiophene. The type III is considered as a significant advance in

conducting polymers based supercapacitors in terms of materials design and the stored energy density.

The commonly used conducting polymers in supercapacitor applications are polyaniline (PANI), polypyrrol (PPy), polythiophene (PTh) and their corresponding derivatives. PANI and PPy can only be p-doped as their n-doping potentials are much lower than the reduction potential of common electrolyte solutions. As PANI requires a proton for proper charging and discharging, a protic solvent, an acidic solution or a protic ionic liquid is required. It seems that all conducting polymers can only work (supplying charges) within a strict potential window. Beyond this strict potential range, the polymer may be degraded at more positive potential and at a more negative potential the polymer may be switched to an insulating state (un-doped state). Hence, the selection of a suitable potential range for ES performance is crucial (Wang et al. 2012a).

#### *1.7.4.2.1. Polyaniline (PANI)*

PANI is an important and highly promising electrode material for energy storage applications. Due to its multiple redox states, PANI possesses the highest theoretical pseudo capacitance ( $\sim 2000 \text{ F g}^{-1}$ ) among all the other conducting polymers like polypyrrole (PPy), polythiophene (PT) and poly(3,4-ethylenedioxythiophene) (PEDOT). And this high pseudo capacitance originates from its fast and reversible faradic redox reactions (Kumar and Baek 2014).

- PANI has high pseudo capacitance, light weight, low cost, controllable electrical conductivity, high energy density, eco-friendliness and facile synthesis. It also has high electrical conductivity in doped states ( $\sim 100\text{-}10,000 \text{ S m}^{-1}$ ) and ease of fabrication for largescale devices. Moreover, it exhibits excellent specific capacitance in the range typically between 500 and 3400  $\text{F g}^{-1}$ , depending on the synthesis conditions, which is substantially higher than that of conventional carbonaceous electrodes ( $\sim 100\text{-}200 \text{ F g}^{-1}$ ) and comparable to pseudocapacitive metal oxides (Pan et al. 2016).
- PANI has the merits of acid–base doping–dedoping chemistry which is responsible for its unique electronic and redox properties (Kumar and Baek 2014).

#### *Compatibility of PANI with graphene oxide*



- The oxygenated groups like epoxides, hydroxyl groups and carboxyl functional groups present in graphene oxide's (GO) basal planes and edges, make it compatible with polymers and has been widely used to fabricate polymer-based nanocomposites because of its extraordinary structure and strong hydrophilicity.
- The carboxyl groups present in GO could link to the nitrogen atoms in the PANI backbone, providing doping for the interaction in addition to bonding, thus avoiding the need of an additional dopant.
- During the oxidative polymerization of PANI in the presence of GO, aniline oxidizes to PANI and simultaneously removal of oxygen occurs where GO is reduced to graphene thereby creating a good conducting network.
- The PANI can also act as a spacer by limiting the re-aggregation sheets of graphene, graphene oxide and reduced graphene oxide, thereby enhancing the specific surface area. Thus, the composite of GO/rGO and PANI can produce high electrochemical capacitance and longer charge/discharge cycle life than that are possible with GO/rGO and PANI individually (Kumar and Baek 2014).

#### *Limitations*

- PANI is brittle and has poor cycling stability, which severely hamper its potential application in energy storage (Kumar and Baek 2014).
- PANI undergoes large volumetric expansion and contraction during charge/discharge process as a result of ion doping and dedoping. This volumetric change leads to structural breakdown and thus causing fast capacitance decay of conducting polymers. Therefore, most of the PANI based supercapacitor electrodes retain less than 50% of the initial capacitance after about 1000 charge/discharge cycles. And this cycling instability limits its application in the development of high performance supercapacitors (Pan et al. 2016).
- Conducting polymers exhibit poor electric conductivity in the reduced state (at more negative potentials) and thereby, producing a low capacitance. Therefore, they are usually employed as the positive electrodes with a negative electrode made from another material such as carbon (Wang et al. 2012a).

#### *Remedies*

- In order to improve PANI's cycling stability, PANI can be composited with the other energy storage materials like carbonaceous materials (graphene, carbon nanotube or carbon nanofibers) and metal oxides/hydroxides (Chao et al.2012).
- Composites of PANI with graphene derivatives are promising because graphene is an excellent substrate to host the active polymer and can produce good cyclic stability. Besides, dramatic improvements in their energy storage performances can be achieved due to the synergistic effect between the two components.
- The high doping/dedoping rate of PANI during charge/discharge cycles can also increase the electrochemical capacitance of carbonaceous material composited with it (Kumar and Baek 2014).

The merits and limitations of different supercapacitor electrode materials are summarized in Table 1.4.

**Table 1.4** Summary of the different types of supercapacitor devices (Zhi et al. 2013).

Type of supercapacitor		Electrode material	Charge storage mechanism	Merits	Limitations
Electrical double layer supercapacitor (EDLS)		Carbon	Electrical double layer (EDL), non-Faradaic process	Good cycling stability and good rate capability	Low specific capacitance, low energy density
Pseudo capacitor		Redox metal oxide or redox polymer	Redox reaction, Faradaic process	High specific capacitance, relatively high energy density and relatively high power density.	Relatively low rate capability.
Hybrid capacitor	Asymmetric hybrid	Anode: faradaic materials, cathode: carbon	Anode: redox reaction, cathode:EDL	High energy density, high power density and good cycle stability	High cost and requires electrode material capacity match.
	Symmetric composite Hybrid	Redox metal oxide/carbon or redox polymer/carbon	Redox reaction plus EDL	High energy density, moderate cost and moderate stability.	
	Battery like hybrid	Anode: Li-insertion material, cathode: carbon	Anode: Lithiation/delithiation cathode: EDL	High energy density.	

## 1.8. APPLICATIONS

### 1.8.1. Present applications

The most of the electrochemical capacitors sold nowadays is used in consumer electronic products, where they mainly serve as backup sources for memories, microcomputers, system boards and clocks. In these applications, the supercapacitors provide power to critical electrical units or consumers, in case of power outages due to disconnection or turn-off of the primary source, contact problems due to vibration or shocks or a drop of the system voltage due to switching-in of other heavy loads. Some typical applications are:

- *Video recorders, TV satellite receivers:* Backup of TV-channel setting, recording times and clock time. The backup is provided for a duration of hours to weeks.
- *Car audio system, taxi meter:* Backup of radio station memory, taxi fare programs and accumulated fare data while the car-radio or the taxi meter is taken out of the car or the car battery is disconnected. Backup for a few hours to a few days.
- *Alarm clock radios, process controllers, home bakery, coffee machines:* Protects clocks and programmed functions from getting lost in case of temporary power outage. Backup for minute to hour.
- Photo and video cameras, programmable pocket calculators, electronic agendas and organizers and mobile phones. The backup is provided during the replacement of the batteries for seconds to minute. In many of those applications, the cost of an electrochemical capacitor is lower or comparable to the costs of a rechargeable battery. The most important benefits of electrochemical capacitors are the longer lifetime, the larger cycling capability, the possibility of fast recharging, and the environmental compatibility.

Another series of applications of the supercapacitors are their use as the main power source. The supercapacitor delivers one or several large current pulses from several milliseconds to several seconds duration. Later, the supercapacitors are recharged by a power supply of low power rating.

Typical applications are:

- *Toys*: Toy cars with ‘rechargeable motors’ contain a supercapacitor which can be recharged from a battery- or mains-powered charger. The charging takes about ten seconds and power is supplied to the car for several tens of seconds. Due to compactness and low weight the cars can accelerate very fast.
- *Fail-safe positioning*: The electrochemical capacitors provide the power for open or close positioning in case of power failures. In the past, mostly spring systems have been used. The use of electric actuators with electrochemical capacitors allows to make smaller, cheaper and faster systems.
- *Starter applications*: The electrochemical capacitors are the main part of the pulse power for starting off, e.g. diesel locomotives. It is charged within ~1 min from lead-acid batteries. It allows to start the diesel engine at very low temperature (Siberia). The size of the battery system may be reduced by up to 50%. Since the pulse currents drawn from the batteries are much smaller, the lives of the batteries double.

In a third type of applications the electrochemical capacitors are used as alternating power sources, e.g. on a day-night basis. During the day the electric load is supplied by power sources like solar cells, which also recharge the electrochemical capacitors. During the night the power is delivered by the electrochemical capacitors.

- *Solar watch*: After being completely charged the electrochemical capacitors may feed the watch for several days. The watch does not need any battery replacement during its lifetime.
- *Solar lanterns, road marking lanterns, lighting of time-tables at bus stop, illumination of parking meters, traffic warning signals*: the combination of solar panels, LEDs instead of incandescent bulbs and supercapacitors make a reliable system with a long lifetime and no needs for maintenance.

The huge number of charge-discharge cycles, the long lifetime, the large temperature range, the high cycling efficiency and the low self-discharge makes electrochemical capacitors very suitable for this type of applications (Kötz and Carlen 2000).

### **1.8.2. Future applications**

The new applications areas for supercapacitors are in the following sectors:

- Industrial applications
- Electric utility applications

➤ Automotive applications

Most of these applications require high power storage systems which may be eventually coupled with a high energy storage system. The basic idea is to use the most appropriate technology for each function to be performed, considering both technical and economic aspects. Each application's analysis needs to clearly identify technical requirements and costs for design evaluation.

*1.8.2.1. Industrial applications*

In the industrial, residential and business building sectors, there are increasing demands for storage systems for energy back-up and for improving energy efficiency of systems used in carrying and elevating masses. The most interesting applications are the uninterruptible power supply systems (UPS) and the integration of storage systems in civil and industrial movers, such as elevators and cranes.

*1.8.2.2. Electric utility applications*

Progress in supercapacitor systems has made them suitable for high power applications with growing interest from electric utilities, which are looking to these devices for performance improvement and reliability in a variety of areas, with much higher power levels and with voltage up to 600 V. The key features of supercapacitors are extremely appealing for a variety of applications in electricity grids: fast response time in millisecond, high energy efficiency (more than 95%), high power density and long calendar and cycle life. Various functions can be then performed by supercapacitor devices like voltage regulator and smart grids.

*1.8.2.3. Automotive applications*

In the transport sector, the use of SC devices has been proposed for a variety of vehicles and transport systems from small ones (light-duty commercial and passenger cars) up to heavy-duty systems, such as, trucks, buses, trams up to trains. The proposed applications for these devices range from very low energy content for very high power services (engine starts) up to more energy-intensive service in hybrid vehicle configurations combining conventional thermal engines and even more advanced electrical generators such as the fuel cells.

*Electric and hybrid vehicles*

In case of electric and hybrid electric vehicles, supercapacitor devices can be usefully applied to carry out different functions: peak power storage for acceleration and recovery of energy during braking/deceleration, peak shaving of peak demands on batteries, cost reduction of electricity generators, such as fuel cells, by optimal sharing of power size according to the duty cycles.

*The advantages of using supercapacitor are various:*

- The energy efficiency of the vehicle may be improved because there is a better charge capacity of supercapacitor with respect to battery at high charge rates.
- The cost per power unit of electrical generators, as fuel cells, is significantly higher than that of supercapacitor, allowing for a power downsizing and cost reduction in drivetrain production.

In general, for such applications, the overall energy content and power for supercapacitor devices may vary from 50 up to 2,000 W h, depending on the configuration with or without batteries and the size of the vehicle.

*Heavy duty and large transport systems*

Supercapacitor applications have been also proposed in very large transport system as hybrid transit buses, trolley buses, trams and trains in order to improve energy efficiency and minimize braking failure in both cases with or without feeding lines (Conte 2010).

## 1.9. LITERATURE REVIEW

The composites containing both faradaic and non-faradaic materials, particularly 2D carbon materials, metal oxides and conducting polymers, particularly polyaniline, for their application in supercapacitors as electrode materials were surveyed. The survey results of some of the recent works on such electrode materials are presented in Table 1.5.

**Table 1.5** Few of the early reported similar work.

Components	Method of preparation	Electrode system used	Electrochemical characteristics				Ref.	
			$C_s$ (F g <sup>-1</sup> )		Cyclic stability at current density	$P$ (W kg <sup>-1</sup> )		$E$ (W h kg <sup>-1</sup> )
			Corresponding binary composites	Ternary composites				
Graphene, SnO <sub>2</sub> and polypyrrole	One – pot synthesis	3 EL	Graphene and SnO <sub>2</sub> – 80.2	616 at 1 mV s <sup>-1</sup> in 1 M H <sub>2</sub> SO <sub>4</sub>	No obvious decay even after 1000 cycles at 1 A g <sup>-1</sup> .	9973.26	19.4	(Wang et al. 2012b)
rGO, MoO <sub>3</sub> and PANI	One – step method	3EL	<b>MoO<sub>3</sub> and PANI</b> 261 in 1 M H <sub>2</sub> SO <sub>4</sub> 273 in 1 M Na <sub>2</sub> SO <sub>4</sub>	553 at 1 mV s <sup>-1</sup> in 1 M H <sub>2</sub> SO <sub>4</sub>	Retains 86.6% of the initial capacitance after 200 cycles in 1 M H <sub>2</sub> SO <sub>4</sub>	10294.5 in 1 M H <sub>2</sub> SO <sub>4</sub>	28.6 in 1 M H <sub>2</sub> SO <sub>4</sub>	(Xia et al. 2012b)
			<b>rGO and PANI</b> 295 in 1 M H <sub>2</sub> SO <sub>4</sub> 270 in 1 M Na <sub>2</sub> SO <sub>4</sub>	363 at 1 mV s <sup>-1</sup> in 1 M Na <sub>2</sub> SO <sub>4</sub>	Retains 73.4% of the initial capacitance after	3993.8 in 1 M Na <sub>2</sub> SO <sub>4</sub>	13.3 in 1 M Na <sub>2</sub> SO <sub>4</sub>	

					200 cycles in 1M Na <sub>2</sub> SO <sub>4</sub>				
Graphene(G), Fe <sub>2</sub> O <sub>3</sub> (F) and PANI(P)	Two – step process	3EL	G-198 F-33 P-58	GF-96 FP-87 GP-678	638 at 1 mV s <sup>-1</sup> in 1 M KOH	Retains 92% of the initial capacitance after 5000 cycles at current density of 0.2 A g <sup>-1</sup>	4407	17	(Xia et al. 2012a)
Graphene, MnFe <sub>2</sub> O <sub>4</sub> and PANI	Two – step process	3EL	–		454.8 at 1 mV s <sup>-1</sup> in 1 M KOH	Retains 76.4% of the initial capacitance after 5000 cycles at current density of 2 A g <sup>-1</sup>	5218	56.97	(Xiong et al. 2014a)
Graphene(G), cobalt ferrite(C) and PANI(P)	Two-step process	2EL & 3EL	Two Electrode system C-39.4, P-24.6 G-171.5, CG-183.2 CP-30, GP-578.8		1133.3 at 1 mV s <sup>-1</sup> in 1 M KOH (Three electrode)	Retains 96.6% of the initial capacitance after 5000 cycles at current density of 2 A g <sup>-1</sup>	3776.1	21.5	(Xiong et al. 2014b)
			Three electrode system C-52.5, P-34.1		716.4 at 1 mV s <sup>-1</sup> in 1 M KOH (Two electrode)				



			G-218.7, CG-254.5 CP-48.3, GP-615.3						
GO, MnO <sub>2</sub> and PANI	Two-step process	3EL	MnO <sub>2</sub> -150	GO and MnO <sub>2</sub> -162 GO and PANI-20	412 in 1 M Na <sub>2</sub> SO <sub>4</sub>	Retains 97% of the initial capacitance after 5000 at current density 0.25 A g <sup>-1</sup>	–	–	(Han et al. 2015)
Graphene, MnO <sub>2</sub> and PANI	In situ, oxidative polymerization and hydrothermal method	3EL	Graphene and MnO <sub>2</sub> – 54		395 at 10 mA g <sup>-1</sup> in 1 M H <sub>2</sub> SO <sub>4</sub>	Retains 92% of the initial capacitance after 1200 cycles at current density 100 mV s <sup>-1</sup>	–	–	(Mu et al. 2014)
Graphene, MoO <sub>3</sub> and poly(p-phenylene diamine)	Two step method	3EL & 2EL	–		1042.6 at 1 A g <sup>-1</sup> in 1 M H <sub>2</sub> SO <sub>4</sub> (Three electrode system)	Retains 86.7% of the initial capacitance after 3000 cycles at current density 12 A g <sup>-1</sup>	3263 (Three electrode system)	6.8 (Three electrode system)	(Li et al. 2015a)

				418.5 at 1 A g <sup>-1</sup> in 1 M H <sub>2</sub> SO <sub>4</sub> (Two electrode system)		325 (Two electrode system)	24.5 (Two electrode system)	
Graphene, SnO <sub>2</sub> and PANI	One-pot method	3EL	Graphene and SnO <sub>2</sub> -45 PANI-467.9	913.4 at 5 mV s <sup>-1</sup> in 1 M H <sub>2</sub> SO <sub>4</sub>	Retains 90.8% of the initial capacitance after 1000 cycles at current density of 1.2 A g <sup>-1</sup>	–	–	(Jin and Jia 2015)
Graphene, SnO <sub>2</sub> and PANI	Two step method	3EL	–	729 at 3.5 A g <sup>-1</sup> in 1 M H <sub>2</sub> SO <sub>4</sub>  1012 at 4 A g <sup>-1</sup> in 1 M Na <sub>2</sub> SO <sub>4</sub>	Retains 84.4% of the initial capacitance after 1500 cycles at current density of 3.5 A g <sup>-1</sup> in 1 M H <sub>2</sub> SO <sub>4</sub>  Retains 91% of the initial capacitance after 1500 cycles at current density of 4 A g <sup>-1</sup> 1 M Na <sub>2</sub> SO <sub>4</sub>	–	–	(Nguyen and Shim 2015)

Graphene, SnO <sub>2</sub> and poly (p-phenylene diamine)	One-pot method	3EL	–	777.5 at 5mV s <sup>-1</sup> in 1M H <sub>2</sub> SO <sub>4</sub>	Retains 97.8% of the initial capacitance after 2000 cycles at scan rate 5mVs <sup>-1</sup> .	–	–	(Li et al. 2015b)
Graphene, MoO <sub>3</sub> and PANI	One step in situ polymerization	3EL	PANI-336 and Graphe-472	734 at 10 mV s <sup>-1</sup> in 1 M H <sub>2</sub> SO <sub>4</sub>	Retains 92.4% of the initial capacitance after 1000 cycles at current density of 1 A g <sup>-1</sup> .	1678.99	55.5	(Das et al. 2015)
Activated carbon, MnO <sub>2</sub> and PANI	Two step method	3EL	Activated carbon-126.7 Activated carbon and MnO <sub>2</sub> -161.7	245 in 0.5 M Na <sub>2</sub> SO <sub>4</sub>	Retains 85% of the initial capacitance after 1000 cycles at current density 1 A g <sup>-1</sup> .	–	–	(Chen et al. 2016b)
GO, pristine graphene (PG) and PANI (P)	Two step method	3EL	GO and PG-10.2 GO and P-282.6	793.7 at 1 A g <sup>-1</sup> in 2 M H <sub>2</sub> SO <sub>4</sub>	Retains 80% of the initial capacitance after 1000 cycles at current density 1 A g <sup>-1</sup> .	9906	41	(Zhang et al. 2016a)
Graphene, Au and PANI	In Situ polymerization combined with	3EL	–	572 at 0.1 A g <sup>-1</sup> in 2 M H <sub>2</sub> SO <sub>4</sub>	Retains 88.54% of the initial capacitance after	–	–	(Wang et al. 2016b)

	hydrothermal method				10,000 cycles at current density of 5 A g <sup>-1</sup>			
Graphene, Co <sub>3</sub> O <sub>4</sub> and PANI	In Situ polymerization combined with hydrothermal method	3EL	–	1247 at 1 A g <sup>-1</sup> in 6 M KOH	No obvious decay even after 3500 cycles at 1 A g <sup>-1</sup>	190	90	(Lin et al. 2016)
PEDOT: PSS, NiFe <sub>2</sub> O <sub>4</sub> and rGO	One step method	3EL	NiFe <sub>2</sub> O <sub>4</sub> and graphene-300	1090 at 0.5 A g <sup>-1</sup> in acetonitrile containing 1 M LiClO <sub>4</sub>	94% retention after 950 cycles at 0.5A g <sup>-1</sup>	–	660	(Hareesh et al. 2016)
GO, TiO <sub>2</sub> and PANI	In situ polymerization of PANI on Graphene oxide and TiO <sub>2</sub>	3EL	–	464 at 0.62 A g <sup>-1</sup> in 1 M HCl	Retains 86.5% of the initial capacitance after 2000 cycles at current density 12.4 A g <sup>-1</sup>	3720	34	(Wang et al. 2016a)
Graphene, NiO and poly(aniline-	In situ polymerization combined with	3EL	–	562 at 0.5 A g <sup>-1</sup> in 1 M H <sub>2</sub> SO <sub>4</sub>	Retains 76.3% of the initial capacitance after	–	–	(Ji et al. 2016)

CO-m-aminophenol)	hydrothermal method				800 cycles at current density 2 A g <sup>-1</sup>			
rGO, CuO and PANI	In situ polymerization combined with hydrothermal method	3EL	rGO – 113.6 rGO and PANI – 343.4	634 in 1 M Na <sub>2</sub> SO <sub>4</sub> 1 A g <sup>-1</sup>	Retains 97.4% of the initial capacitance after 1000 cycles at current density 1 A g <sup>-1</sup>	114.2	126.8	(Zhu et al. 2016)
Graphene, Ag <sub>2</sub> O and PANI	In situ polymerization	3EL	Graphene and Ag <sub>2</sub> O – 70	1572 at 0.05 A g <sup>-1</sup> in 6 M KOH	Retains 85% of the initial capacitance after 3000 cycles at current density 0.05 A g <sup>-1</sup>	–	–	(Usman et al. 2016)
rGO, CuO-Cu(OH) <sub>2</sub> and polypyrrole (PPy)	Two step method	3EL & 2EL	GO/PPy – 500 rGO/PPy – 685.5 GO/PPy/CuO – Cu(OH) <sub>2</sub> – 750	Three electrode system 997 at 10 A g <sup>-1</sup> in 0.5 M Na <sub>2</sub> SO <sub>4</sub>	–	–	–	(Asen and Shahrokhian 2017a)
			–	Two electrode system 225 10 A g <sup>-1</sup> in 0.5 M Na <sub>2</sub> SO <sub>4</sub>	Retains 90% of the initial capacitance after 2000 cycles at current density 10 A g <sup>-1</sup>	20	8000	

rGO, Fe <sub>2</sub> O <sub>3</sub> and PANI	One step method	3EL	–	283.4 at 1 A g <sup>-1</sup> in	Retains 78% of the initial capacitance after 5000 cycles	47.7	550	(Mondal et al. 2017)
rGO, NiO and PANI	Two step method	3EL	–	638.1 at 1 mV s <sup>-1</sup>	Retains 91% of the initial capacitance after 5000 cycles at 500 mA g <sup>-1</sup>	–	–	(Bai et al. 2017)

It is seen from the Table 1.5 that the ternary composites have exhibited higher performances than those of their binary composites.

## **1.10. SCOPE AND OBJECTIVES**

### **1.10.1. Scope of the proposed work**

It is a known fact that the available energy storage devices are unable to meet the requirements of efficient energy storage, as they are suffering from their own limitation like low energy density, low power density, etc. Hence, having a long term vision, supporting the prevailing research scenario on energy storage and marching ahead towards its betterment in terms of modifying, combining and developing effective energy storage material is essential.

Though varieties of energy storing electrode materials are available, graphene, metal oxides and polyaniline are with extraordinary qualities to be used as electrode materials in energy storage devices. But each of them and their binary combinations suffers from some serious limitations, which bring their energy storing properties down. Hence making a super capacitive material by integrating all the merits of them would be of wise notion.

It is proposed to develop composite electrodes for the supercapacitors, containing carbon, transition metal oxide and conducting polymers, which combine the merits and mitigates the shortcomings of the three individual components. In such carbon nanostructure, metal oxide/hydroxide and conducting polymer ternary composite electrodes, the carbon nanostructures not only serve as the physical support to metal oxides but also provide the channels for charge transport. The high electronic conductivity of carbon nanostructures benefits to the rate capability and power density at a large charge/discharge current. The metal oxides and conducting polymers are the main sources that store the charge and in turn the energy. The electro activities of metal oxides and conducting polymers contribute to high specific capacitance and high energy density of the carbon nanostructure, metal oxide/hydroxide and conducting polymer ternary composite electrodes. A synergistic effect on the electrochemical properties could be expected and the materials cost can be reduced. The composition of the constituents, microstructure and physical properties of carbon/metal oxide/conducting polymer ternary composites govern the performance of the supercapacitor electrodes. The electrode porosity, electronic conductivity, pore size distribution and specific

surface area affect the cell performance and would be better tailored by the combined effect of carbon nanostructure, metal oxide/hydroxide and conducting polymer when synthesized in the form of ternary composites.

### **1.10.2.Objectives**

Based on the literature review and the understanding gained from it the following objectives are fixed.

- To synthesize nanocomposites of reduced graphene oxide, transition metal oxide/hydroxide and polyaniline by facile in-situ one step chemical method, using different acid dopants.
- To characterize the structure and surface morphology of thus prepared electrode materials.
- To study their electrochemical properties by cyclic voltammetry, galvanostatic charge discharge and electrochemical impedance spectroscopy.
- To study the effect of magnetic field in improving the energy storage of the composite material containing antiferromagnetic material.

## **1.11. FRAMEWORK OF THE THESIS**

The entire research work in this thesis has been presented in four chapters. The overview of each chapter as follows:

**Chapter 1** introduces the various electrochemical energy storage devices and explains the merits and limitations of them. Details of supercapacitors, their definitions, classifications, design, working principle, electrode materials and electrolyte used in them, the merits and limitations of electrode materials and electrolytes and applications are also discussed. A detailed literature survey of 2D carbonaceous material/ metal oxide/conducting polymer composite materials followed by the motivations and targeted objectives of the present work are presented.

**Chapter 2** presents the various chemicals and materials used for the synthesis, synthetic method of two different metal oxide and a metal hydroxide containing nanocomposites, fabrication techniques of supercapacitor cell and techniques used for structural characterizations and electrochemical characterizations.



**Chapter 3** presents the structural characterizations and electrochemical characterizations results of three nanocomposites namely GCP, GVP and GNP followed by the discussion on obtained results.

**Chapter 4** summarizes the work carried out and the important findings obtained from the electrochemical results exhibited by the nanocomposites GCP, GVP and GNP. It also presents the major conclusions drawn from the results and the scope for the future research.



---

## CHAPTER – 2

### 2. MATERIALS AND METHODS

#### 2.1. MATERIALS

All chemicals used were of analytical grade, procured from commercial suppliers, and used without any further purifications. The chemicals used were: copper sulphate pentahydrate ( $\text{CuSO}_4 \cdot 5\text{H}_2\text{O}$ ), nickel sulphate hexahydrate ( $\text{NiSO}_4 \cdot 6\text{H}_2\text{O}$ ), vanadyl sulphate ( $\text{VOSO}_4$ ), aniline, ammonium persulphate (APS), hydrazine hydrate ( $\text{N}_2\text{H}_4 \cdot \text{H}_2\text{O}$ ), sodium hydroxide pellets (NaOH), graphite powder, potassium permanganate ( $\text{KMnO}_4$ ), sodium nitrite ( $\text{NaNO}_2$ ), glacial acetic acid ( $\text{CH}_3\text{COOH}$ ), phosphoric acid ( $\text{H}_3\text{PO}_4$ ), hydrogen peroxide ( $\text{H}_2\text{O}_2$ ), sodium sulphate anhydrous ( $\text{Na}_2\text{SO}_4$ ), methane sulphonic acid ( $\text{CH}_3\text{SO}_3\text{H}$ ) (MSA) and sulphuric acid ( $\text{H}_2\text{SO}_4$ ).

#### 2.2. SYNTHESSES

##### 2.2.1. Synthesis of graphite oxide (GO)

The GO was synthesized by following reported modified Hummer's method (Marcano et al. 2010). In the synthesis, 1 g of graphite powder was added to a mixture of 40 mL of conc.  $\text{H}_2\text{SO}_4$  and 10 mL of conc.  $\text{H}_3\text{PO}_4$ , taken in a 500 mL beaker. Then 1 g of  $\text{NaNO}_2$  was added and the content was stirred at 50 °C, and during the stirring 6 g of  $\text{KMnO}_4$  was added slowly, little at a time. The stirring and heating were continued for 12 h. After 12 h the reaction product was slowly transferred into a 1 L beaker containing ice cubes with constant stirring using a glass rod and 30 mL of 6%  $\text{H}_2\text{O}_2$  was added and stirred well. Eventually the product was washed several times with distilled water, centrifuged and dried.

##### 2.2.2. Synthesis of rGO

In the synthesis of rGO, a dispersion of 25 mg of GO in 50 mL of distilled water was sonicated for 30 min. Then the pH was increased to 14 by adding 2 M NaOH, an appropriate amount of hydrazine hydrate was added and stirred at 90°C for 2 h. The product formed was washed repeatedly with distilled water, alcohol, finally with acetone and dried at room temperature (Ren et al. 2011).

### 2.2.3. Synthesis of PANI

PANI was synthesized by following the reported procedure (Zhang et al. 2002). In the synthesis, 300  $\mu\text{L}$  of aniline was stirred with 150 mL of distilled water for 10 min, to obtain a uniform mixture of aniline and distilled water. Later 600 mg of APS in 50 ml of distilled water was added to aniline/water mixture followed by the addition of 10 mL 2 M  $\text{H}_2\text{SO}_4$ , and the polymerization was continued for 5 h. Finally, the obtained polyaniline was washed several times with distilled water, with acetone and dried at room temperature.

### 2.2.4. Synthesis of reduced graphene oxide/copper oxide/ polyaniline (GCP) nanocomposite using $\text{H}_2\text{SO}_4$ as dopant

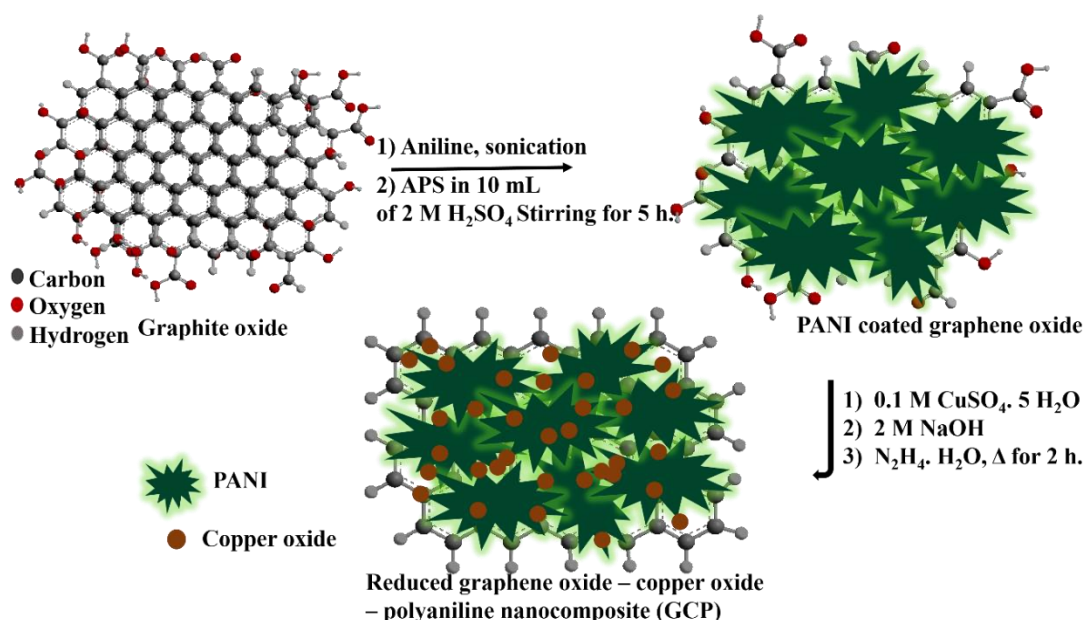


**Fig 2.1** The schematic representation of the synthesis route of GCP nanocomposite

A schematic representation of the synthetic route followed for the synthesis of reduced graphene oxide /copper oxide/polyaniline nanocomposite (GCP) is shown in Fig.2.1. In a typical synthesis of the composite, 35 mg of graphite oxide was sonicated with 8 mL of 0.1 M  $\text{CuSO}_4 \cdot 5\text{H}_2\text{O}$  and 100  $\mu\text{L}$  aniline in 25 mL of distilled water for 15 min. Then 200 mg of APS in 10 mL of 2 M  $\text{H}_2\text{SO}_4$  was added and stirred at room temperature for 5 h, followed by increasing the pH to 14 by using 2 M NaOH and the content was heated at 90  $^\circ\text{C}$  with hydrazine hydrate ( $\text{N}_2\text{H}_4 \cdot \text{H}_2\text{O}$ ) for 2 h. Then the

product was repeatedly washed with distilled water followed by alcohol and finally with acetone and dried at room temperature. The binary composites were synthesized following the same method excluding the third constituent.

### 2.2.5. Synthesis of GCP composites using glacial acetic acid as dopant

35 mg of graphite oxide was sonicated with 100  $\mu\text{L}$  aniline in 25 mL of distilled water for 30 min. Then 200 mg of APS in 10 mL of glacial acetic acid was added and stirred at room temperature for 4 h, 8 mL of 0.1 M  $\text{CuSO}_4 \cdot 5\text{H}_2\text{O}$  was added and stirring was continued for 1 h, followed by changing the pH to 14 by using 2 M NaOH and the content was heated at 90  $^\circ\text{C}$  with hydrazine hydrate ( $\text{N}_2\text{H}_4 \cdot \text{H}_2\text{O}$ ) for 2 h. Then the product was washed several times with distilled water, followed by alcohol and finally with acetone and dried at room temperature. The binary composites were synthesized following same method excluding the third constituent.

### 2.2.6. Synthesis of reduced graphene oxide/ vanadium pentoxide/ polyaniline ternary nanocomposites (GVP)

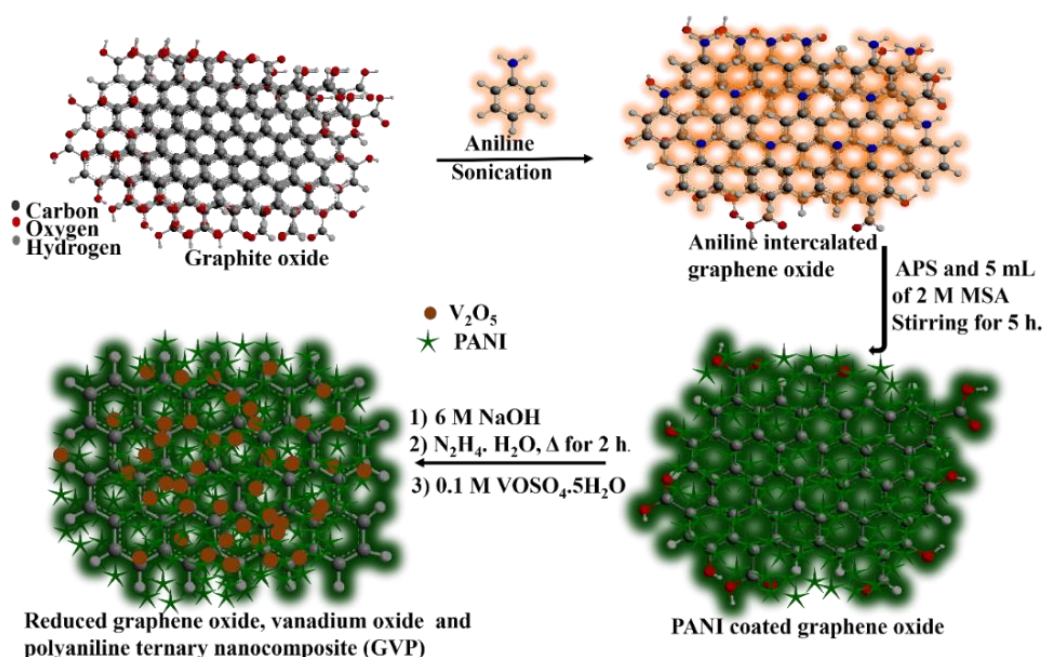


**Fig. 2.2** Pictorial representation of reduced graphene oxide, vanadium pentoxide and polyaniline ternary nanocomposites (GVP).

The pictorial representation of the synthesis of reduced graphene oxide/ vanadium oxide/ polyaniline ternary nanocomposite (GVP) is depicted in Fig. 2.2. In the synthesis of GVP, 35 mg of graphite oxide in 30 mL of distilled water containing 300  $\mu\text{L}$  of

aniline was sonicated for 30 min. 600 mg of APS and 5 mL of 2 M methane sulphonic acid (MSA) were added and the reaction mixture was stirred at room temperature for 5 h. Then, the pH of the reaction mixture was increased to 14 by adding 6 M NaOH. The content was heated with  $\text{N}_2\text{H}_4 \cdot \text{H}_2\text{O}$  at  $90^\circ\text{C}$  for 2 h. At the end, 6.1 mL of 0.1 M vanadyl sulphate ( $\text{VO}\text{SO}_4 \cdot 5\text{H}_2\text{O}$ ) was added and the stirring continued for 15 min at room temperature. The composite obtained was washed multiple times with distilled water, finally with acetone and dried at room temperature.

### 2.2.7. Synthesis of reduced graphene oxide/nickel hydroxide/polyaniline nanocomposite (GNP) using glacial acetic acid as dopant

The schematic representation of the synthesis route of GNP nanocomposite is shown in Fig. 2.3. In the synthesis of the nanocomposite, 35 mg of graphite oxide was sonicated with 300  $\mu\text{L}$  of aniline in 25 mL of distilled water for 30 min. Then 600 mg of APS was added, followed by the addition of 10 mL of glacial acetic acid, stirred at room temperature for 4 h, 6.7 mL of 0.1 M  $\text{NiSO}_4 \cdot 6\text{H}_2\text{O}$  solution was added and the stirring was continued for an hour. The pH of the content was adjusted to 14 by the addition of 6M NaOH. Then the reduction was carried out with  $\text{N}_2\text{H}_4 \cdot \text{H}_2\text{O}$  for 2 h. The obtained product was washed multiple times with distilled water, finally with acetone and dried at room temperature.

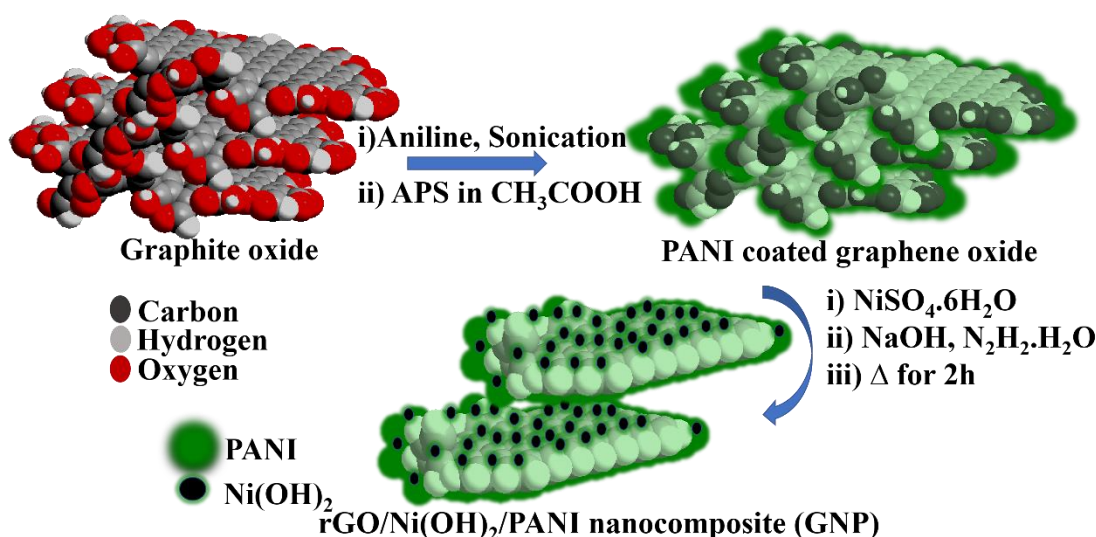


**Fig. 2.3** The schematic representation of the synthesis route of GNP nanocomposite

### 2.2.8. Synthesis of GNP nanocomposite using methane sulphonic acid as dopant

In the synthesis of the nanocomposite, 35 mg of graphite oxide was sonicated with 300  $\mu\text{L}$  of aniline in 25 mL of distilled water for 30 min. Then 600 mg of ammonium persulphate was added, followed by the addition of 5 mL of 2 M MSA, stirred at room temperature for 4 h, 6.7 mL of 0.1 M  $\text{NiSO}_4 \cdot 6\text{H}_2\text{O}$  solution was added and the stirring was continued for an hour. The pH of the content was adjusted to 14 by the addition of 6 M NaOH; and then the reduction was carried out with  $\text{N}_2\text{H}_4 \cdot \text{H}_2\text{O}$  for 2 h. The obtained product was washed multiple times with distilled water, finally with acetone and dried at room temperature.

### 2.3. PREPARATION OF WORKING ELECTRODES

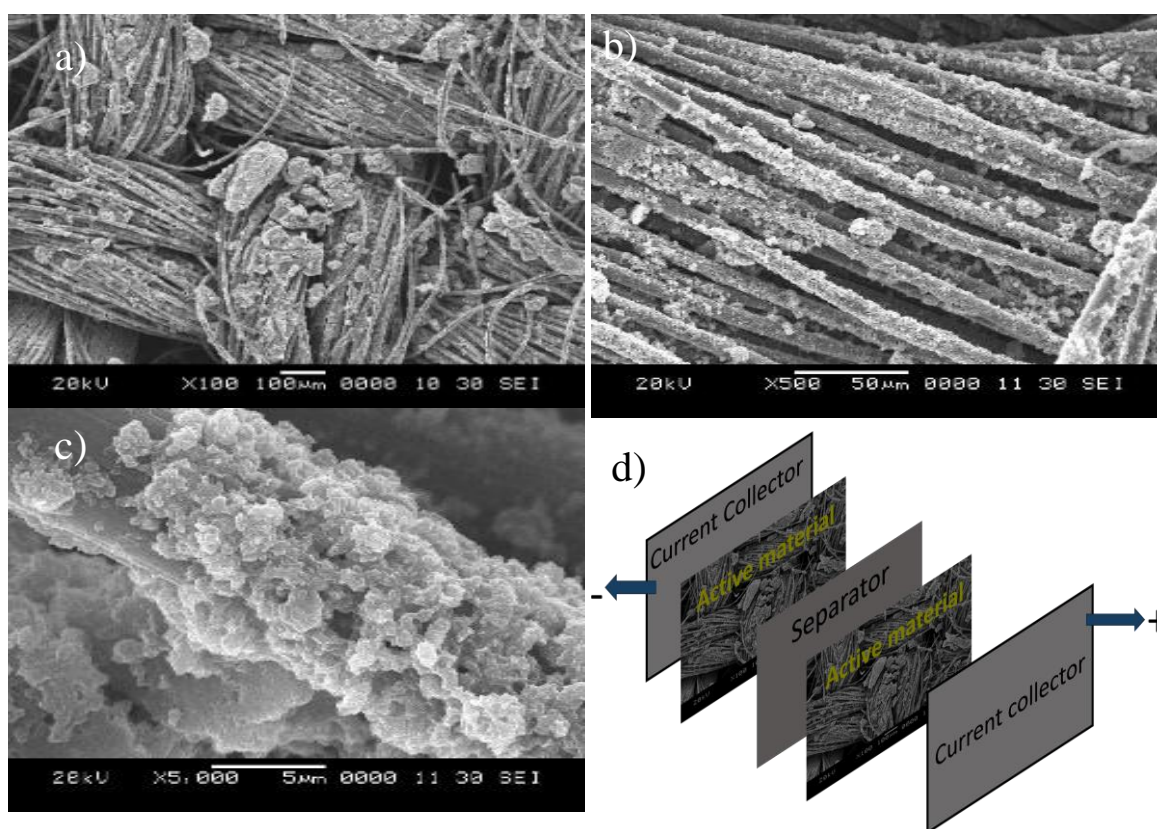


**Fig. 2.4** (a, b, c) SEM images of fabricated carbon fabric, d) Pictorial representation of the supercapacitor cell setup.

The SEM images of carbon fabric coated with as-synthesized nanocomposite are shown in Fig. 2.4 a, b, and c. The pictorial representation of supercapacitor cell setup is shown in fig 2.4 d. The synthesized composite was sonicated with acetone to



get an homogeneous dispersion and without the addition of any binder, drop casted over a pair of 2 cm × 2 cm carbon cloths of same weight, by placing over a hot plate for easy evaporation. The drop-casting was done in such a way that both the carbon clothes gain same quantity of material. A Whatman filter paper (Cat. No-1001 125) of approximately the same dimension of that of the carbon clothes, soaked with the electrolyte were used as dielectric material to separate them from contact and then sandwiched between two stainless steel current collectors.

### 2.3.1. Fabrication of magnetic supercapacitor cell

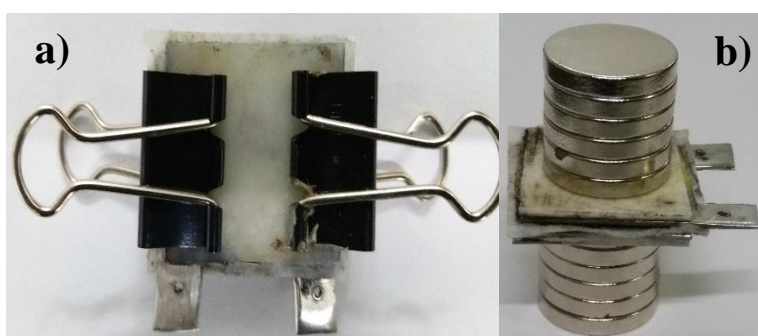


**Fig. 2.5** Photographs of (a) fabricated supercapacitor device (b) arrangement magnets for the application of magnetic field.

The method for the preparation of the electrodes is same as it is described in the section 2.3. The photographs of the fabricated supercapacitor device and the arrangement of the disc magnets to apply the magnetic fields are shown in Fig. 2.5a and 2.5b, respectively. In order to apply the magnetic field, the as prepared supercapacitor cell was sandwiched between pairs of magnets as shown in Fig 2.5b. The magnets used for providing the magnetic fields are nickel coated permanent disc magnets of diameter 18 mm and thickness of 3 mm.

## 2.4. CHARACTERIZATIONS AND MEASUREMENTS

### 2.4.1. Structural and surface characterizations

#### 2.4.1.1. XRD studies

The powder XRD was carried out to arrive at the qualitative confirmations of the nanocomposites synthesized. The qualitative analyses were carried out by comparing diffraction peaks obtained with the JCPDS reference files. The XRD analyses were also informative to confirm the crystallinity of the composite. The XRD



patterns, act as an indicator to confirm the complete reduction of GO to rGO, give information about the loose packing of graphene layers present in composite. The crystalline sizes of constituents present in the composite give the information about the dimensions of the constituents (i. e. micro or nano) which is calculated using Scherrer's equation (Salavati-Niasari and Davar 2009).

$$D = \frac{k\lambda}{\beta \cos \theta} \quad (2.1)$$

where, D is the crystalline size, K is a constant (0.94 assuming that the particles are spherical),  $\lambda$  is the wavelength of the X-ray radiation,  $\beta$  is the full width half maximum intensity of the peak and  $\theta$  is the angle of diffraction. The powder-XRD spectra was recorded using Rigaku instrument of Model-miniflex 600 with a reference Cu K $\alpha$  ( $\lambda=1.54 \text{ \AA}$ ) at 20 kV and 2 mA. The scan rate used was 2 $\theta$  per min.

#### 2.4.1.2. FT-IR spectroscopy

In order to determine the functional groups present in the nanocomposites synthesized FT-IR spectroscopy was used. The IR spectra of composites were recorded using FT-IR spectrometer (Bruker, Model-alpha) by KBr pellet method (4000  $\text{cm}^{-1}$  – 400  $\text{cm}^{-1}$ ) and ATR method (4000  $\text{cm}^{-1}$  – 600  $\text{cm}^{-1}$ ).

#### 2.4.1.3. X-ray photoelectron spectroscopy

XPS is utilized to deduce the exact elemental composition of both surface and the bulk of the material under study (up to few layers). The oxidation states of the metals in their oxides and hydroxides, the functional groups present on rGO and the bonding nature of PANI and the nature of PANI (emeraldine, leucoemeraldine or emeraldine salt) were deduced from the XPS analyses by deconvoluting the characteristic peak obtained. The XPS spectra was recorded using X-ray photoelectron spectroscope (XPS-SPECS) with non-monochromatic Al K $\alpha$  radiations (1486.6 eV) under high vacuum  $5 \times 10^{-9}$  mbar and C 1s peak located at 284.6 eV was used as a reference peak. The survey spectrum was obtained with a pass energy of 70 eV, and for the individual Cu 2p, V2p, Ni2p, O 1s and N 1s peaks a pass energy of 40 eV was used.

#### 2.4.1.4. Raman spectroscopy

Raman spectroscopy is one of the most convenient techniques to characterize graphene materials in non-destructive way and it was recorded to get details of reduction of GO to rGO, density of defect present in rGO, number of graphene layers present in rGO and also for confirming the metal oxide/hydroxide and PANI present in the composite. The ratio of intensity of 2D band to intensity G band ( $I_{2D}/I_G$ ) is the tool that gives information about the layer property of the rGO present. The  $I_{2D}/I_G$  ratio that corresponds to single, double, triple and multilayer graphene structures are  $>1.6$ ,  $\sim 0.8$ ,  $\sim 0.30$  and  $\sim 0.07$ , respectively (Akhavan et al. 2014). The Raman spectra were recorded in Horiba Yvon Jobin microscope of model Labram hr800, at a wavenumber range 400–4000  $\text{cm}^{-1}$  using laser source of wavelength of 532 nm.

#### 2.4.1.5. FESEM and EDS analyses

FESEM is extremely versatile technique capable of providing structural information over a wide range of magnifications. It is used to image the sample surface by scanning it with a high energy beam of electrons in a raster scan pattern. The electrons interact with atoms that make up the sample to produce signals that contain information of surface topography and composition. The FESEM analyses was carried out to get information on the morphology and structure, like particle size distribution and crystallinity of a sample, extent of agglomeration, the atomic arrangements of ternary nanocomposite, particle sizes, pattern of intercalation of metal oxides and PANI nano particles between graphene layers and their homogeneous distribution. The EDS analyses were carried out to find the elements present in the composite. FE-SEM images and EDS analyses were carried out using field emission spectroscope Carl Zeiss of model AG ultra 55.

### 2.4.2. Electrochemical characterization

Cyclic voltammetry, chronopotentiometry (galvanostatic charge/discharge) and electrochemical impedance methods were employed to analyze the newly fabricated supercapacitors in two electrode system using 2 M  $\text{Na}_2\text{SO}_4$ , 0.4 M  $\text{H}_2\text{SO}_4$ , 1 M  $\text{H}_2\text{SO}_4$  as electrolytes. The electrochemical analyses for GNP composites were carried out at in the presence of magnetic field. The different magnetic fields were supplied with Permanent magnets (nickel coated disc magnets) of diameter 18 mm and thickness of

3 mm (Seller – Perfect magnets) were used to apply magnetic field. The Gaussmeter (Polytronic GM 504 with Hall probe (serial No. – G1916)) was used to measure the applied magnetic field strength. The electrochemical analyses were carried out using electrochemical work station IVIUM of model–vertex.

#### 2.4.2.1. Cyclic voltammetry (CV)

The CV analyses were carried out to confirm the redox property, reversibility and rate capability of electrodes made up of synthesized nanocomposites. The potential window used is 1.2 V and the scan rates used were ranging from 5 mV s<sup>-1</sup> to 2 V s<sup>-1</sup>.

#### 2.4.2.2. Galvanostatic Charge/discharge

The charge/discharge behavior of the electrodes was examined by chronopotentiometry method. The potential window used was 1.2 V. GCD analyses were carried out at different current densities. The specific capacitance ( $C_s$ ), the specific capacity ( $Q$ ), equivalent series resistance ( $ESR$ ), energy density ( $E$ ), power density ( $P$ ), coulombic efficiency ( $\eta$ ) and time constant ( $\tau$ ) were calculated using GCD curves. The formulae used for the calculations are given below.

*Specific capacitance* ( $C_s$  in F g<sup>-1</sup>) (Stoller and Ruoff 2010) was calculated using equation 2.2.

$$C_s = \frac{I}{m \frac{dV}{dt}} \quad (2.2)$$

where  $I$  is the constant current (in ampere),  $m$  is the total mass of the two electrodes (in g),  $dV/dt$  (in V s<sup>-1</sup>) is the slope obtained by fitting a straight line to the discharge curve over the range of  $V$  (the voltage at the beginning of discharge after correcting for IR drop).

*Equivalent series resistance* ( $ESR$  in  $\Omega$ ) (Sudhakar et al. 2017) was calculated using equation 2.3.

$$ESR = \frac{iR_{drop}}{2I} \quad (2.3)$$

where, the  $IR_{\text{drop}}$  is the steep potential drop till the point where the linear discharge begins (in V) and  $I$  (in A) is the constant current applied during charge and discharge process.

*Time constant* ( $\tau$ ) (Parlak et al. 2017) was calculated using equation 2.4.

$$\tau = C_T \cdot ESR \quad (2.4)$$

where  $C_T$  is the cell capacitance (in F) and  $ESR$  is equivalent series resistance (in  $\Omega$ ) of the cell.

*Specific capacity* ( $Q$  in  $C \text{ g}^{-1}$ ) (Parlak et al. 2017) was calculated using equation 2.5.

$$Q = C_s \times \Delta V \quad (2.5)$$

where  $C_s$  is specific capacitance obtained ( $F \text{ g}^{-1}$ ) and  $\Delta V$  is the potential window (V) used.

*Energy density* ( $E$  in  $W \text{ h kg}^{-1}$ ) (Sudhakar et al. 2017) was calculated using equation 2.6.

$$E = \frac{1000 \times C_s \times (\Delta V)^2}{2 \times 3600} \quad (2.6)$$

*Power density* ( $P$  in  $W \text{ kg}^{-1}$ ) (Sudhakar et al. 2017) was calculated using equation 2.7.

$$P = \frac{E}{t_d} \times 3600 \quad (2.7)$$

where,  $E$  is energy density and  $t_d$  is discharging time.

*Columbic efficiency* ( $\eta$  in %) (Wang et al. 2015b). was calculated using equation 2.8.

$$\eta = \frac{t_d}{t_c} \times 100 \% \quad (2.8)$$

where,  $t_d$  and  $t_c$  are discharge and charge times in seconds.

#### 2.4.2.3. Electrochemical impedance spectroscopy (EIS)

Electrochemical impedance spectroscopy study was carried out to evaluate the response of electrode material when a low sinusoidal potential of 10 mV was applied in a frequency range of 0.01 Hz to 100 kHz. The impedance spectra were obtained as

Nyquist plots, Bode phase angle plots, Bode impedance or magnitude plots, admittance plots and plots of frequency versus capacitance.

The Nyquist plot gives the information about the capacitive nature of the material, knee frequency (a frequency below which total capacitance of the electrode material obtained), rate capability. The Nyquist plot gives the magnitudes of various resistances involved during the process of energy storage, when fitted with the equivalent circuit.

The Bode phase angle plot gives information about the ideality of the capacitor, relaxation time ( $\tau_0$ ) of the capacitor (relaxation time is the time that a device takes to discharge all of its stored energy with an efficiency of more than 50% of its maximum value). The  $\tau_0$  is calculated using following equation (Li et al. 2016)

$$\tau_0 = \frac{1}{f_0} \quad (2.9)$$

where,  $f_0$  is the critical frequency, corresponding to phase angle of  $-45^\circ$ .

The Bode impedance plot gives the information of the maximum resistance that impede energy storage process. The admittance plot gives information on the maximum conductivity of the material that supports energy storage.

The capacitance versus frequency plots gives the capacitance value when 10 mV applied at different frequency. The capacitance ( $C$ ) is calculated using following equation:

$$C = \frac{-1}{2\pi fz''} \quad (2.10)$$

where,  $f$  is the frequency (Hz) and  $z''$  is the imaginary part of the impedance ( $\Omega$ ) (Wu et al. 2015b).



## CHAPTER – 3

### 3. RESULTS AND DISCUSSION

#### REDUCED GRAPHENE OXIDE, COPPER OXIDE AND POLYANILINE (GCP) NANOCOMPOSITE

The oxides of copper (CuO and Cu<sub>2</sub>O) are p-type semiconductors (Mugwang'a et al. 2012), abundant on earth, inexpensive, facile to synthesis, low toxic, possess oxidation states of +2 and +1, store energy by faradaic redox reaction and thereby act as a pseudocapacitive material with good electrochemical properties. The theoretical specific capacitances of CuO and Cu<sub>2</sub>O are ~1800 F g<sup>-1</sup> (Vidhyadharan et al. 2014) and ~2247.6 F g<sup>-1</sup> (Wan et al. 2017), respectively. These theoretical specific capacitances are close to the theoretical specific capacitance of hydrated RuO<sub>2</sub>, which is known to be with high theoretical specific capacitance of ~2200 F g<sup>-1</sup> (Vidhyadharan et al. 2014). Copper oxides have furnished a high specific capacity when they were fabricated as electrodes for Li-ion batteries (Vidhyadharan et al. 2014). These properties of oxides of copper make them suitable candidates for supercapacitors.

Thus, the nanocomposite comprising of CuO/Cu<sub>2</sub>O, PANI (with high energy and pseudocapacitance) and rGO (with a good conductive matrix, high surface area, long cycle life and an electrical double layer capacitance) is expected to provide promising electrochemical performances when used to fabricate supercapacitor electrode material. The GCP nanocomposites were synthesized by varying the weight percentage of the each of the constituents. The synthetic route for the synthesis of GCP with dopants 1 M H<sub>2</sub>SO<sub>4</sub> and glacial acetic acid were described in section 2.2.2. and 2.2.3, respectively. The sections 3.1 and 3.2 present the structural and electrochemical characterizations of GCP nanocomposites with electrolytes, 2 M Na<sub>2</sub>SO<sub>4</sub> and 0.4 M H<sub>2</sub>SO<sub>4</sub>, respectively.

### 3.1. GCP WITH H<sub>2</sub>SO<sub>4</sub> AS DOPANT

#### 3.1.1. Structural characterization

##### 3.1.1.1. X-ray diffraction analysis

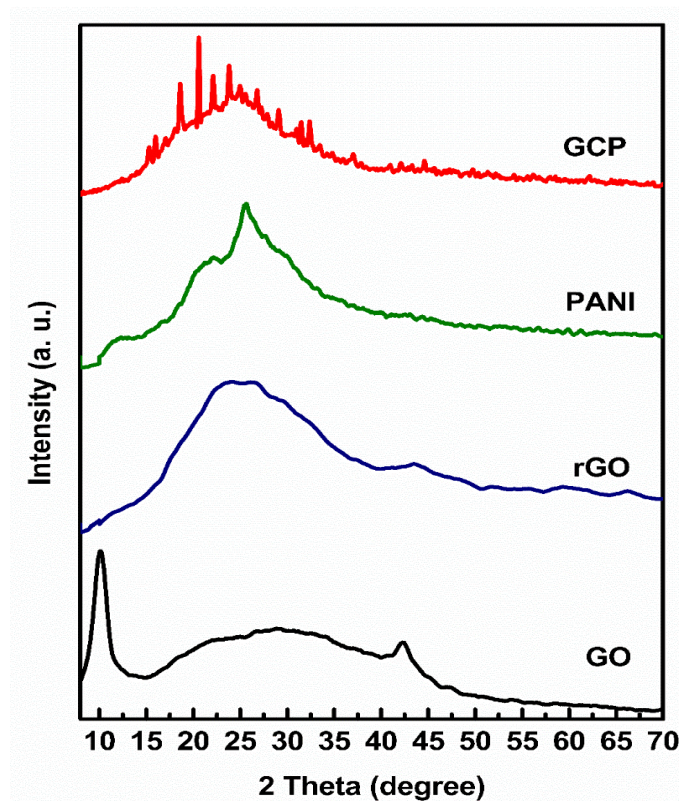


**Fig. 3.1** X-ray diffraction patterns of graphene oxide (GO), reduced graphene oxide (rGO), polyaniline (PANI), and reduced graphene oxide/copper oxide/polyaniline nanocomposite (GCP).

The X-ray diffraction spectra of graphene oxide (GO), reduced graphene oxide (rGO), polyaniline (PANI) and reduced graphene oxide/copper oxide/polyaniline nanocomposite (GCP) are shown in Fig. 3.1. The diffraction peak of GO at 9.95° (001) is due to the intercalation of water molecules and formation of oxygenated functional groups on carbon sheets (Jin and Jia 2015); and the peak at 42° is due to the graphitic structure of GO corresponding to the plane of (100) (JCPDS File No. – 41-1487, 25-0284, and 75-1621). This peak is not observed for the rGO and GCP composite indicating the absence of oxygen containing functional groups in the composite as they are successfully reduced to rGO during the synthesis of ternary composite. The diffraction pattern of GCP composite possesses the peaks of all the three constituents,



showing the efficient intercalation of copper oxide and PANI in between rGO layers. The peaks of GCP and their crystal planes are as follows. Peaks at  $36.80^\circ$  (111) and  $42.20^\circ$  (200) are of cuprous oxide ( $\text{Cu}_2\text{O}$ ) (JCPDS file No. 78–2076), a peak at  $32.41^\circ$  (110) is of  $\text{CuO}$  (JCPDS file No.80–1917) and the remaining peaks at  $19.20^\circ$  (110),  $21.97^\circ$  (021),  $23.27^\circ$  (200),  $26.87^\circ$  (003),  $27.90^\circ$  (210),  $29.14^\circ$  (202),  $31.90^\circ$  (020),  $33.35^\circ$  (120),  $34.06^\circ$  (221),  $37.87^\circ$  (132),  $49.70^\circ$  (025) (JCPDS file No.053–1717 and 053–1891) are of polyaniline. Pure PANI shows peaks at  $21.88^\circ$  (020) and  $25.68^\circ$  (200) (Xia et al. 2012b) and these peaks are shifted considerably to  $19.20^\circ$  (110) and  $23.27^\circ$  (200), and new peaks of polyaniline with different crystalline plane are observed in the case of GCP composite indicating the production of PANI with an assembly of different crystal planes in the composite. The crystalline sizes of the  $\text{CuO}$  and PANI were calculated using Scherrer's equation 2.1 and it was found to be 12.43 nm and 22.92 nm, respectively, indicating the nano dimension of the composite.

#### 3.1.1.2. FT-IR spectra

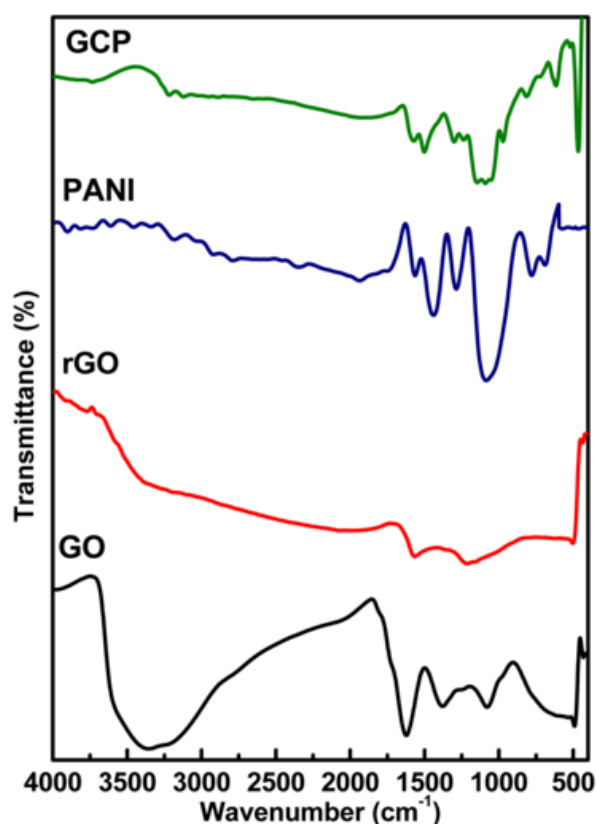


**Fig. 3.2** FT-IR spectra of GO, rGO, PANI and GCP.

The Fig. 3.2 shows the FT-IR spectra of GO, rGO, PANI and GCP. GO shows four peaks at  $1078\text{ cm}^{-1}$ ,  $1382\text{ cm}^{-1}$ ,  $1623\text{ cm}^{-1}$  and  $3361\text{ cm}^{-1}$  of  $-\text{C}-\text{O}-\text{C}-$ ,  $-\text{C}-\text{OH}$ ,  $-\text{C}=\text{O}$  of carboxylic acid (Xu et al. 2010) and  $-\text{OH}$  (Xia et al. 2012b), of water, respectively. None of these peaks are observed in the case of rGO, but the two peaks at  $1565\text{ cm}^{-1}$  and  $1213\text{ cm}^{-1}$ , later of low intensity, are of skeletal  $-\text{C}=\text{C}-$  (Feng et al. 2015) and epoxy ( $-\text{C}-\text{O}$ ) (Midander et al. 2009). PANI exhibits peaks at  $1567\text{ cm}^{-1}$ ,  $1441\text{ cm}^{-1}$ ,  $1284\text{ cm}^{-1}$ ,  $1079\text{ cm}^{-1}$ , and  $780\text{ cm}^{-1}$  correspond to  $\text{C}=\text{C}$  stretching of quinoid and benzenoid ring,  $\text{C}-\text{N}$  stretching vibration,  $\text{C}=\text{N}$  stretching vibration and  $\text{C}-\text{C}$  stretching vibrations, respectively (Jin and Jia 2015). In the case of GCP composite, there are peaks at  $1581\text{ cm}^{-1}$ ,  $1472\text{ cm}^{-1}$ ,  $1376\text{ cm}^{-1}$ ,  $1188\text{ cm}^{-1}$ ,  $1109\text{ cm}^{-1}$  and  $994\text{ cm}^{-1}$ , correspond to  $\text{C}=\text{C}$  stretching of quinoid and benzenoid ring,  $\text{C}-\text{N}$  stretching vibration,  $\text{C}=\text{N}$  stretching vibration,  $-\text{C}-\text{H}$  in plane bending (Pan et al. 2016), and  $-\text{C}-\text{H}$  out of plane bending (Midander et al. 2009), respectively, of PANI. The peak at  $607\text{ cm}^{-1}$  is attributed to  $\text{Cu(I)}-\text{O}$  vibrations in  $\text{Cu}_2\text{O}$  and at  $449\text{ cm}^{-1}$  possibly attributed to  $\text{CuO}$  (Feng et al. 2015), which substantiate the fact that the as synthesized composite has both  $\text{Cu}_2\text{O}$  and  $\text{CuO}$  and corroborate the results obtained in powder-XRD. The above facts indicate integrated synthesis of reduced graphene oxide/copper oxide/polyaniline during in situ single step synthesis.

### 3.1.1.3. SEM analyses

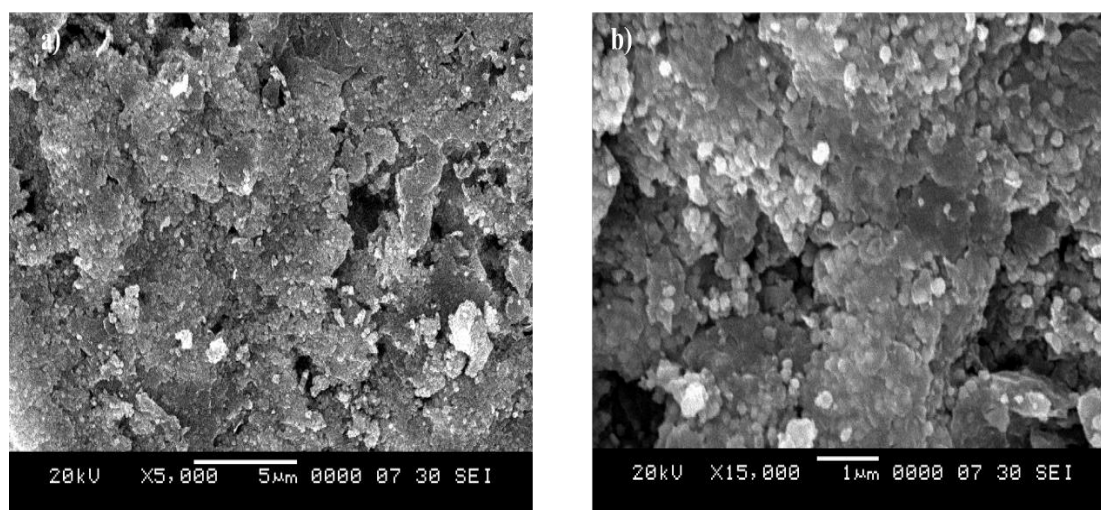


**Fig. 3.3** (a) and (b) SEM images of GCP nanocomposite.

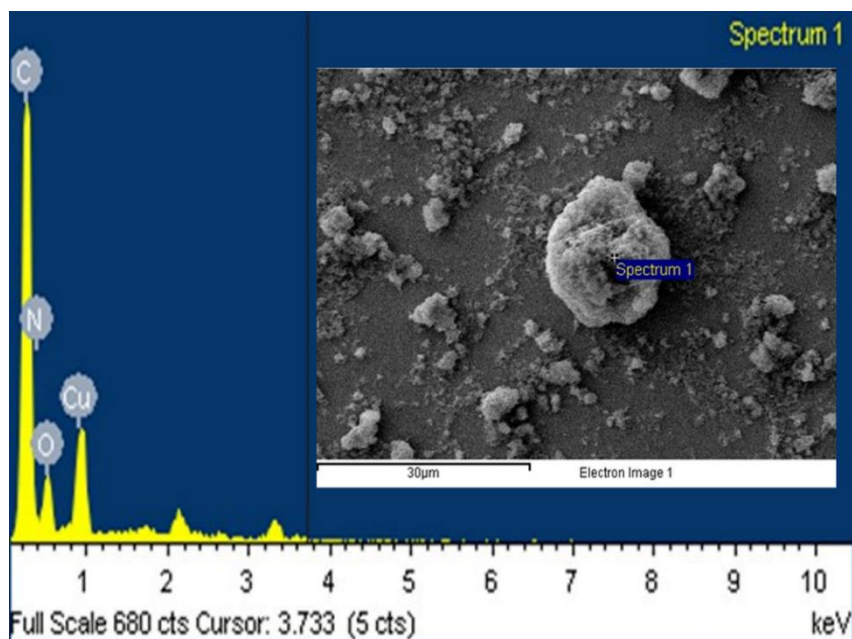


**Fig. 3.4** ED spectrum (EDS) of GCP nanocomposite.

The SEM images of GCP at two different magnifications are shown in Fig. 3.3. The images depict the uniform dispersion of  $\text{Cu}_2\text{O}/\text{CuO}$  nanoparticles over PANI covered reduced graphene oxide layers. The EDS of the GCP surface is shown in Fig. 3.4, with the surface spot on which EDS was recorded, shown in the inset. The surface elemental composition of the as synthesized composite was confirmed by EDS analyses to be C, N, O and Cu with the weight ratios as shown in Table 3.1.

**Table 3.1** The elements present with corresponding weight and atomic percentages.

Elements	Weight %	Atomic %
C	58.73	74.47
N	8.49	9.23
O	11.85	11.28
Cu	20.93	5.02

### 3.1.2. Electrochemical analysis

A series of GCP nanocomposites were synthesized by varying the weight ratio of PANI and a constant weight ratio of copper oxide and rGO. The electrochemical performance of the synthesized GCP nanocomposites were evaluated by cyclic voltammetry and galvanostatic charge discharge studies, using two electrode system

with 2 M Na<sub>2</sub>SO<sub>4</sub> as electrolyte. Among all the composites, the GCP nanocomposite with a composition (wt %) rGO<sub>6.6%</sub>: Cu<sub>2</sub>O/CuO<sub>13.40%</sub>: PANI<sub>80%</sub>, (GCP-300) exhibited higher electrochemical performance. The entire electrochemical observations and discussion are presented in the following sections. The compositions and the nomenclatures of nanocomposites synthesized are presented in Table 3.2.

**Table 3.2** The compositions and the notations of nanocomposites synthesized.

Weight ratio of GCP composites	Weight percentages	Nomenclature
G 25 mg : Cu <sub>2</sub> O/CuO 50 mg : P 100 mg	G <sub>14.28%</sub> : C <sub>28.57%</sub> : P <sub>57.14%</sub>	GCP-100
G 25 mg : Cu <sub>2</sub> O/ CuO 50 mg : P 150 mg	G <sub>11.11%</sub> : C <sub>22.22%</sub> : P <sub>66.66%</sub>	GCP-150
G 25 mg : Cu <sub>2</sub> O/ CuO 50 mg : P 200 mg	G <sub>9.09%</sub> : C <sub>18.18%</sub> : P <sub>72.72%</sub>	GCP-200
G 25 mg : Cu <sub>2</sub> O/ CuO 50 mg : P 250 mg	G <sub>7.69%</sub> : C <sub>15.38%</sub> : P <sub>76.92%</sub>	GCP-250
G 25 mg : Cu <sub>2</sub> O/ CuO 50 mg : P 300 mg	G <sub>6.66%</sub> : C <sub>13.34%</sub> : P <sub>80.00%</sub>	GCP-300
G 25 mg : Cu <sub>2</sub> O/ CuO 50 mg : P 350 mg	G <sub>5.88%</sub> : C <sub>11.76%</sub> : P <sub>82.35%</sub>	GCP-350
G 25 mg : Cu <sub>2</sub> O/CuO 50 mg	G <sub>33.33%</sub> : C <sub>66.66%</sub>	GC
G 25 mg : P 300 mg	G <sub>7.69%</sub> : P <sub>92.30%</sub>	GP
Cu <sub>2</sub> O/CuO 50 mg : P 300 mg	C <sub>14.29%</sub> : P <sub>85.71%</sub>	CP

### 3.1.2.1. Cyclic voltammetry (CV) studies

The CV curves of GCP composites with different weight ratios of PANI, recorded at a scan rate of 5 mV s<sup>-1</sup> in the potential range of 0 – 0.8 V are shown in Fig. 3.5. It can be seen from the figure that the CV curves of the composites with different PANI loading show good distorted rectangularity, indicating the excellent capacitive behavior of the composite electrode material. The presence of redox peaks indicate the faradaic process along with the non-faradaic process in storing energy. The area of the CV curve increases with the increase in PANI weight, indicating the contribution of PANI in storing the energy. The composite with the weight ratio composition of G 25 mg: Cu<sub>2</sub>O/CuO 50 mg: P 300 mg (GCP-300) possesses maximum area, suggesting its high charge storage capacity and superior capacitive behavior compared to other compositions.

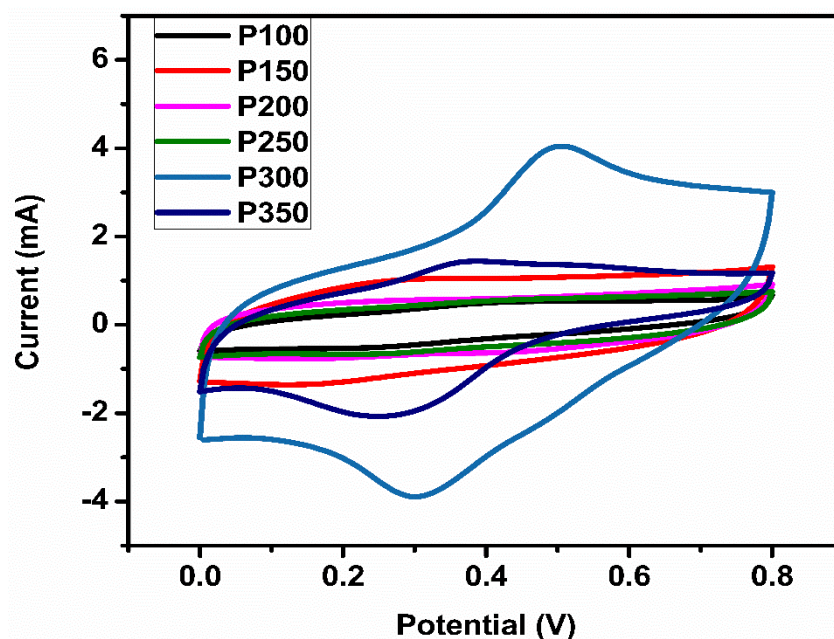


**Fig. 3.5** Cyclic voltammograms (CV curves) of GCP nanocomposites of different weight ratios at a scan rate of  $5 \text{ mV s}^{-1}$ .

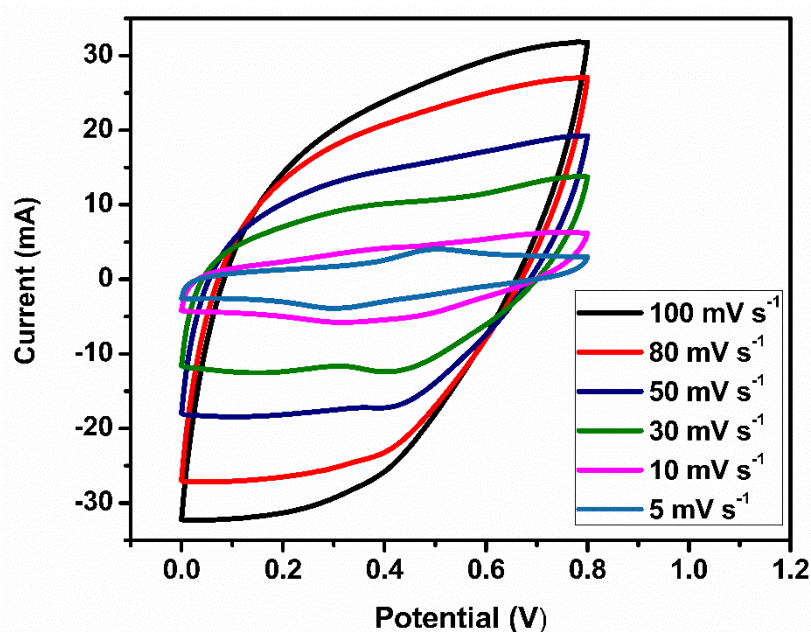


**Fig. 3.6** CV curves of G 25 mg;  $\text{Cu}_2\text{O}/\text{CuO}$  50 mg; P 300 mg (GCP-300) at different scan rates.

CV curves of composite with 300 mg of PANI (GCP-300) at different scan rates, are shown in Fig. 3.6. It is observed from the Fig. 3.6 that at higher scan rates the CV curves do not possess any significance redox peaks, suggesting that the energy

storage is by electrical double layer capacitance. When the scan rate is decreased, at a scan rate of  $5 \text{ mV s}^{-1}$ , there is an appearance of a pair of redox peaks, indicating the emergence of pseudo capacitance. The pseudo capacitance originates from the faradaic reaction of PANI through its redox transition between a semiconducting leucoemeraldine form and a conducting polaronic emeraldine form (Xia et al. 2012b) predominantly; and also between oxides of copper ( $\text{Cu}_2\text{O}$  and  $\text{CuO}$ ) present in the GCP composite.

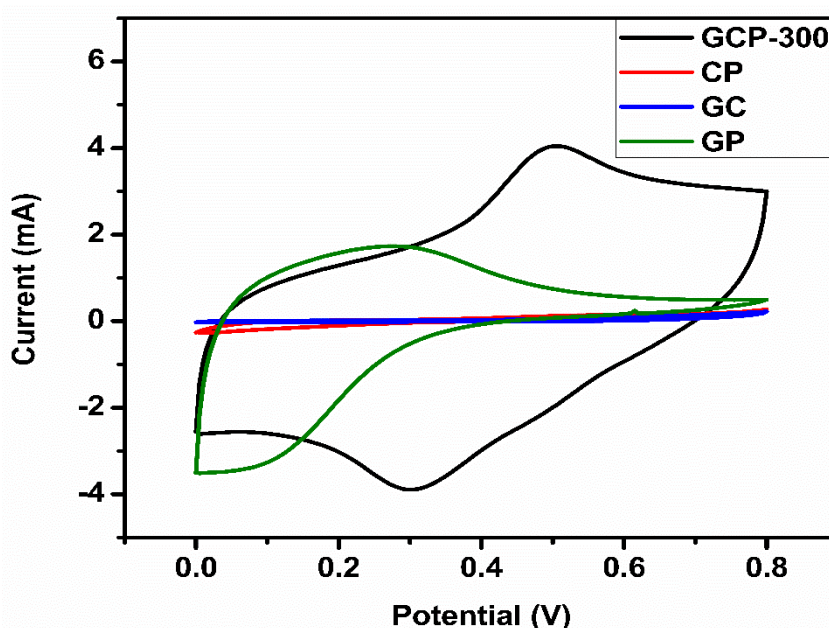


**Fig. 3.7** CV curves of GCP-300, CP, GC and GP at a scan rate of  $5 \text{ mV s}^{-1}$ .

Therefore, it can be inferred that at low scan rate the energy storage is through a combination of faradic and non-faradic processes (Midander et al. 2009). The CV curves of binary combinations of constituents with corresponding weight ratios viz.,  $G_{25\text{mg}}: \text{Cu}_2\text{O}/\text{CuO}_{50\text{mg}}$  (GC),  $G_{25\text{mg}}: P_{300\text{mg}}$  (GP),  $P_{100\text{mg}}: \text{Cu}_2\text{O}/\text{CuO}_{50\text{mg}}$  (CP) and the composite  $G_{25\text{mg}}: \text{Cu}_2\text{O}/\text{CuO}_{50\text{mg}}: P_{300\text{mg}}$  (GCP) at a scan rate of  $5 \text{ mV s}^{-1}$  are shown in Fig. 3.7. The voltammograms show the larger charge storage on GCP over the binary combinations, which can be attributed to the uniform dispersion of PANI particles and  $\text{Cu}_2\text{O}/\text{CuO}$  nano particles on the reduced graphene sheets and their combined effect.

### 3.1.2.2. Galvanostatic charge/discharge (GCD) studies

The preliminary GCD studies on the synthesized composites were carried out at different current densities of  $0.25 \text{ A g}^{-1}$ ,  $0.5 \text{ A g}^{-1}$ ,  $1 \text{ A g}^{-1}$ ,  $2 \text{ A g}^{-1}$  and  $3 \text{ A g}^{-1}$ . The



curves obtained were of equilateral triangle in shape, indicating high reversibility of the electrode material during charge and discharge processes (Han et al. 2014). The rate of charging and discharging was slow at lower current densities; and took longer charge and discharge time compared to the charge/ discharge rate at higher current densities. This can be attributed to the sufficient insertion of  $\text{Na}^+$  ion in the nano-pores created in composite architecture at lower current density and access of electrolyte through composite material during charge and discharge process (Han et al. 2014). The specific capacitance offered by the electrode materials were calculated using the equation (2.2). (Stoller and Ruoff 2010). As the maximum specific capacitance was obtained at  $0.25 \text{ A g}^{-1}$ , the effect of composition of the composites were studied at  $0.25 \text{ A g}^{-1}$ . The galvanostatic charge-discharge curves of GCP composites at different weight ratio compositions, at a current density of  $0.25 \text{ A g}^{-1}$  are shown in Fig. 3.8.

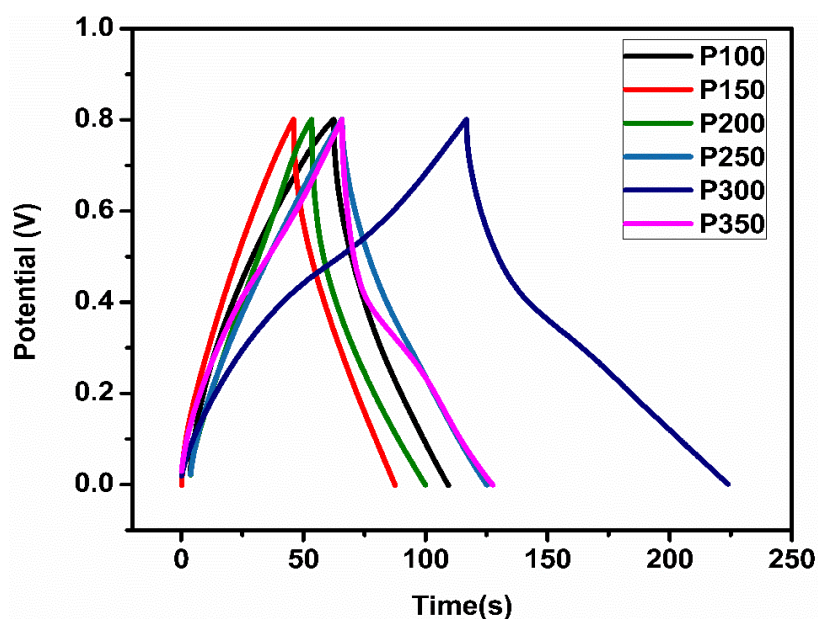


**Fig. 3.8** GCD curves of GCPs of different weight ratio of PANI at a current density of  $0.25 \text{ A g}^{-1}$ .

The specific capacitance is maximum for 300 mg of PANI loading and further increase in the weight of PANI shows a decrease in specific capacitance. This is because, the PANI particles are getting denser with the increase in the weight of PANI in a random way and tend to produce agglomerates and hence, all the produced PANI are not used efficiently (Kannappan et al. 2013). The weight percentage composition of

GCP-300 was determined to be rGO<sub>6.6%</sub>: Cu<sub>2</sub>O/CuO<sub>13.40%</sub>: PANI<sub>80%</sub>. The specific capacitance values of GCP composites with different weight ratios of PANI at a current density of 0.25 A g<sup>-1</sup> are listed in Table 3.3.

**Table 3.3** The specific capacitance values of GCP composites with different weight ratio of PANI at a current density of 0.25 A g<sup>-1</sup>.

Weight ratio of GCP composites	C <sub>s</sub> (F g <sup>-1</sup> )
G 25 mg : Cu <sub>2</sub> O/ CuO 50 mg : P 100 mg	18.11
G 25 mg : Cu <sub>2</sub> O/ CuO 50 mg : P 150 mg	19.28
G 25 mg : Cu <sub>2</sub> O/ CuO 50 mg : P 200 mg	19.68
G 25 mg : Cu <sub>2</sub> O/ CuO 50 mg : P 250 mg	21.92
G 25 mg : Cu <sub>2</sub> O/ CuO 50 mg : P 300 mg	53.30
G 25 mg : Cu <sub>2</sub> O/ CuO 50 mg : P 350 mg	27.74

Since the composite with the polyaniline loading of 300 mg exhibited better performance compared to all other polyaniline weight compositions, the performance of GCP-300 at different current densities (0.25, 0.5, 1, 2 and 3 A g<sup>-1</sup>) were evaluated and the corresponding GCD curves are presented in Fig. 3.9.

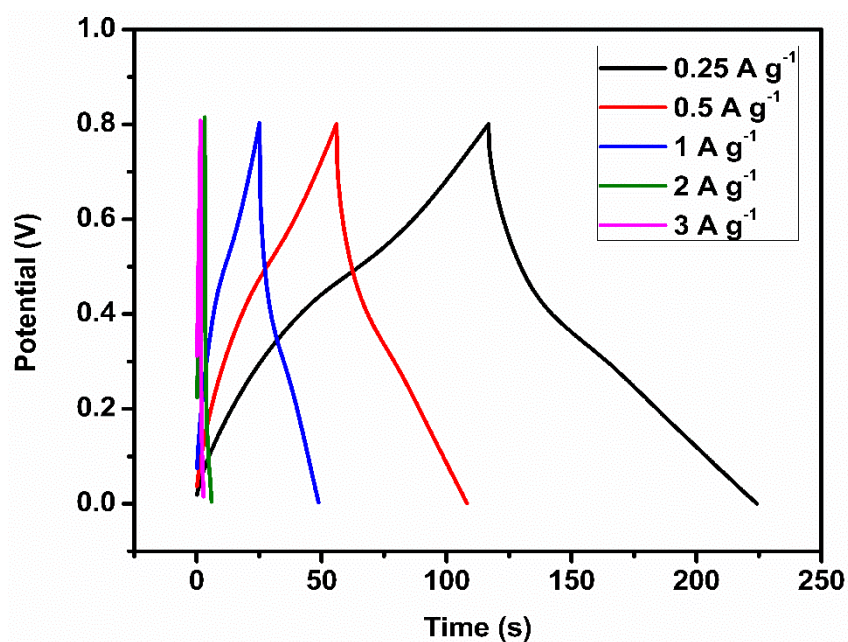


**Fig. 3.9** Galvanostatic charge discharge curves of GCP – 300 composite at different current densities.



The specific capacitance values of GCP – 300 at current densities of 0.25 A g<sup>-1</sup>, 0.5 A g<sup>-1</sup>, 1 A g<sup>-1</sup>, 2 A g<sup>-1</sup> and 3 A g<sup>-1</sup> are 53.29 F g<sup>-1</sup>, 40.64 F g<sup>-1</sup>, 38.40 F g<sup>-1</sup>, 14.07 F g<sup>-1</sup> and 13.80 F g<sup>-1</sup>, respectively. The decrease in specific capacitance with the increase in current density might be due to the lower ionic penetration on the electrode surface at higher current densities (Kannappan et al. 2013). The decrease in the specific capacitance of the cell proportionally with the increasing current densities, is the typical behavior of electrochemical supercapacitors (Li et al. 2011). The CD curves of GCP – 300 and the binary composites with their respective weight ratios at a current density of 0.25 A g<sup>-1</sup> are depicted in Fig.3.10. The superiority of the composite GCP-300, over the binary combinations can be observed from the curves. The equivalent series resistance (*ESR*) of the GP and GCP-300 were calculated using Equation (2.4) (Sudhakar et al. 2017) and the values were found to be 87.89 mΩ and 7.19 mΩ, respectively.

The low resistance value of GCP-300 indicates that the GCP-300 offers less resistance and more charge storage compared to that of binaries. The ohmic loss of GP and GCP-300 are 0.501 V and 0.041 V, respectively (Fig. 3.10). Since GC and CP offered very less specific capacitance, their *ESR* values were left uncalculated. The low *ESR* of GCP-300 is attributed to the low resistances at the interfaces between electrode material/current collector and electrode material/electrolyte (Sahoo and Shim 2017). The specific capacities (*Q*) of GCP – 300 and GP were calculated using the Equation 2.5. The *Q* values are 42.63 C g<sup>-1</sup> and 35.27 C g<sup>-1</sup>, respectively. The specific capacitance values of GCP – 300 and binary composites at a current density of 0.25 A g<sup>-1</sup> are presented in Table 3.4. The high capacitance of GCP – 300 nanocomposite can be attributed to the presence of nanosized PANI, which causes the decrease in charge diffusion distance during the charge/discharge process; and also to the integrated effect of the combination of all the three materials (Usman et al. 2016). It might also be due to the uniformity in the dispersion of Cu<sub>2</sub>O/CuO nano particles and PANI particles over rGO layers which provides an efficient three-dimensional porous structure with short diffusion path length for faster electron transport (Lin et al. 2016). The cyclic stability of GCP – 300 was tested by continuous cyclic voltammetry scans at 200 mV s<sup>-1</sup> up to 5000 cycles.

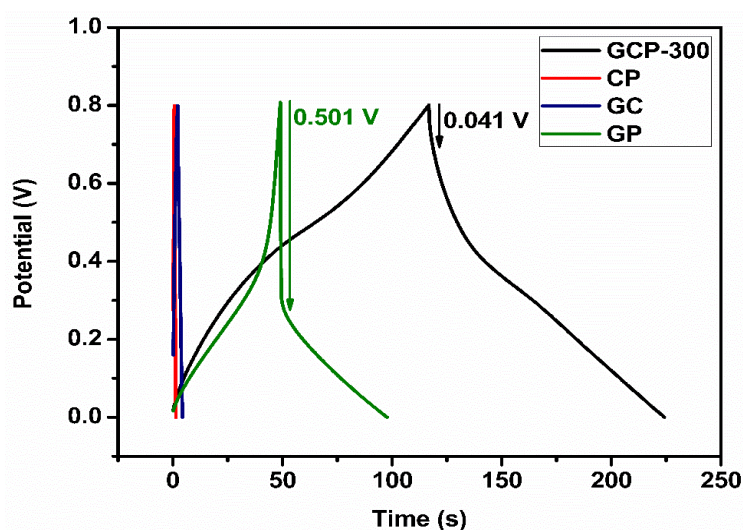


**Fig. 3.10** Galvanostatic charge/ discharge curves of GCP-300, CP, GC, and GP at  $0.25 \text{ A g}^{-1}$ .

**Table 3.4** Specific capacitance of GCP-300 and corresponding binary composites at a current density of  $0.25 \text{ A g}^{-1}$ .

Weight ratios	$C_s \text{ (F g}^{-1}\text{)}$
G 25 mg : Cu <sub>2</sub> O/CuO 50 mg : P 300 mg	53.3
G 25 mg : Cu <sub>2</sub> O/CuO 50 mg	0.71
G 25 mg : P 300 mg	44.09
Cu <sub>2</sub> O/CuO 50 mg : P 300 mg	0.13

From the plot of specific capacitance versus cycle number, which is shown in Fig. 3.11, it is observed that there is only a little deterioration of initial capacitance with the increasing cycle numbers and the GCP-300 retained 97.6% of its initial capacitance up to 5000 cycles, exhibiting a good cyclic stability. This might have emerged from the smaller particle size and larger surface area, which effectively decrease the distance to be traveled for charge transport, providing the faster mass transfer of the electrolyte (Hareesh et al. 2016). The introduction of rGO, can effectively relieve the contraction/expansion of PANI during doping/dedoping process (Mu et al. 2014). Ragone plots of GCP-300, CP, GC and GP at different current densities ( $0.25 - 3 \text{ A g}^{-1}$ ) with the magnified portions of CP and GC in the inset are shown in Fig. 3.12.

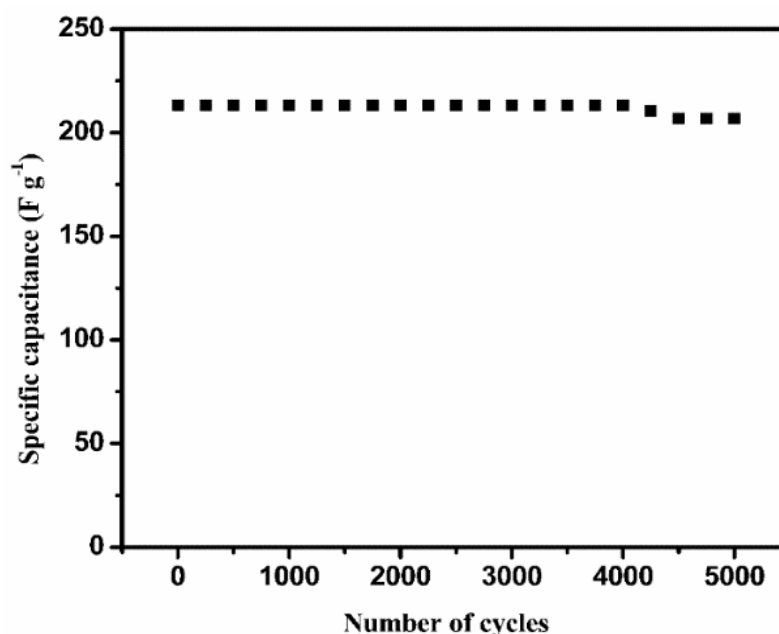


**Fig. 3.11** Plot of specific capacitance versus number of cycles.

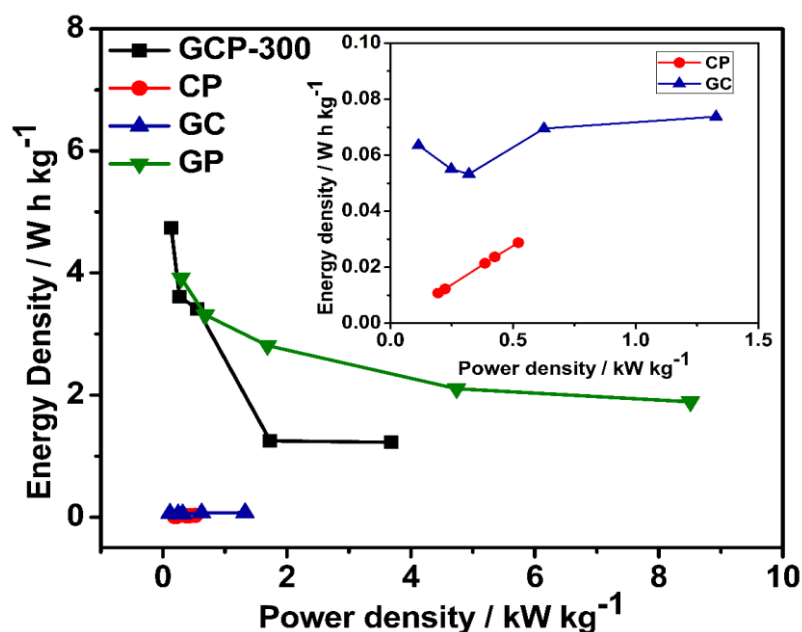


**Fig. 3.12** Ragone plots of GCP-300, CP, GC and GP at different current densities, respectively. Inset shows the magnified portion of the plots of CP and GC.

The energy densities and power densities of the nanocomposites were calculated using Equation 2.6 and 2.7, respectively (Sudhakar et al. 2017). It is observed from the plots that the GCP-300 shows high energy density of  $4.73 \text{ W h kg}^{-1}$  and high power density of  $136.25 \text{ W kg}^{-1}$  at a lower current density of  $0.25 \text{ A g}^{-1}$ ; and also it maintains

an energy density of  $1.22 \text{ W h kg}^{-1}$  and power density of  $3681.5 \text{ W kg}^{-1}$  at higher current density of  $3 \text{ A g}^{-1}$ . The relatively better electrochemical behavior of GCP-300 is attributed to the good interfacial contact between the PANI nanoparticles with rGO through  $\pi$ - $\pi$  interaction, enhancing the utilization of PANI and reducing the diffusion path for electrolyte ions during redox reactions, thereby producing high energy density (Shen et al. 2013). The sustained high-power density at high current density might have originated from the intact structural stability of the composite GCP-300 even at high current density. The columbic efficiencies calculated using Equation 2.8 (Wang et al. 2015b) to be 91.91% and 95.78%. for GCP-300 and GP, respectively.

### 3.1.2.3. Electrochemical impedance spectroscopic (EIS) studies

The Nyquist plots of GCP-300, CP, GC and GP are shown in Fig. 3.13 with the magnified parts of semicircles in the inset. Nyquist plots obtained are with a semicircle over the high frequency region and a linear Warburg portion over the low frequency region, indicating the ideal supercapacitor behavior. The semi-circle with a small diameter and the straight Warburg portion of GCP-300 compared to the Nyquist plots of binary composites, indicate the good conductivity, better ion diffusion and better ion transport (Li et al. 2011) in GCP-300, which make the ternary composite more promising than binary composites.

The magnitude of resistances involved during the process of charge storage were generated from the EIS data by fitting an equivalent circuit (EC) using the software Zsimpwin (version 3.21). The fitment curve and the EC are shown in Fig. 3.14. The equivalent circuit consists of the equivalent series resistance ( $R_s$ ), the double-layer capacitance ( $C_{dl}$ ), the charge transfer resistance ( $R_{ct}$ ), the Warburg resistance ( $W$ ), the leakage resistance ( $R_{leak}$ ), the constant phase element of pseudo capacitance ( $CPE_1$ ) and the constant phase element of mass capacitance ( $CPE_2$ ) (Masarapu et al. 2009; Li and Wei 2012). The equivalent series resistance ( $R_s$ ) comprises of the electrolyte resistance, the ionic resistance of ions moving through the separator, the intrinsic resistance of the active electrode material, and the contact resistance at the interface of active material/current collector.

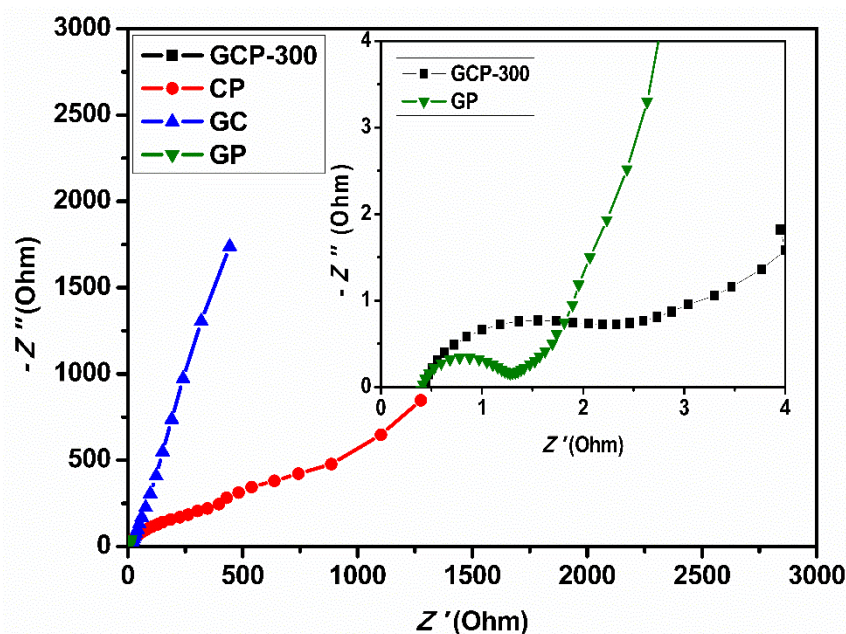


**Fig. 3.13** Nyquist plot of GCP-300, CP, GC and GP composites. The inset depicts the magnified portion of GCP-300 and GP at high frequency.

The low  $R_s$  value of GCP – 300, as shown by the small intercept of the X-axis at high frequency, indicates the good conductivities of active materials and current collectors (Masarapu et al. 2009). The  $R_{ct}$  is the resistance developed across the rGO and the electrolyte; and the lower  $R_{ct}$  value is evident from the smaller diameter of the semicircular capacitive loop (0.934  $\Omega$ ). The  $CPE_1$  is associated with the redox capacitance or pseudo capacitance due to the faradaic reaction of PANI; and also, oxides of copper ( $Cu_2O$  and  $CuO$ ) present in the GCP composite.  $W$  is the Warburg resistance, corresponding to the electrolyte ion diffusion into the electrode material. In simulation analysis, to arrive at the EC,  $CPE (Q)$  is used in the place of ideal capacitive element ( $C$ ) for a better fit of depressed capacitive loops. The depressed semicircles indicate a deviation from the ideal capacitive behavior; and are obtained due to the frequency dispersion arising out of inhomogeneity on the electrode surface in contact with the electrolyte, as a consequence of a porous and non-uniform electrode (Juttner 1990; Dinodi and Shetty 2014).

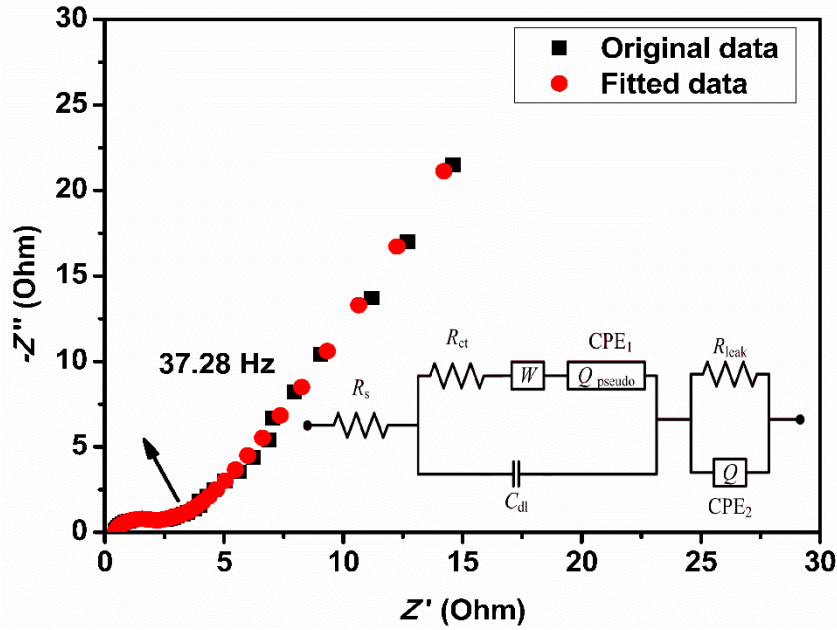


**Fig. 3.14** The original and fitted EIS data of GCP-300 with knee frequency and circuit.

The relation between the real capacitance and the constant phase element after accounting for the frequency dispersion, is expressed as per the Equation 3.1 given below (Dinodi and Shetty 2014):

$$C = Q(\omega_{\max})^{n-1} \quad (3.1)$$

where  $Q$  is the CPE constant,  $\omega_{\max}$  is the frequency at which the imaginary part of the impedance ( $Z''$ ) has a maximum and  $n$  is a CPE exponent or frequency factor which provides a measure of inhomogeneity on the electrode surface. The value of  $n$  is given by  $(-1 \leq n \leq 1)$ , and when  $n = 1$ , CPE behaves like an ideal capacitor. The values of frequency factors obtained are at 0.87 and 0.80 for CPE<sub>1</sub> and CPE<sub>2</sub>, respectively, indicating the moderate capacitive behavior of GCP-300 composites. The steeper Warburg region in the case of GCP-300 indicates the faster ion transport through the electrode material and efficient access of electrolyte ions to the electrode surface (Jaidev et al. 2011).

The frequency dependency of supercapacitors is measured in terms of knee frequency. The knee frequency is the frequency below which the whole capacitance of a supercapacitors is attained (Miao et al. 2016). The knee frequencies of GCP-300, CP, GC and GP are 37.28 Hz, 0.51 Hz, 5.17 Hz and 19.31 Hz, respectively. The ternary

GCP-300 has the highest knee frequency, indicating a far early onset of capacitive behavior of GCP-300 compared to that of binary composites (Miao et al. 2016). Also, the higher knee frequency implies that the electrolyte ions are easily accessible into the pores and hence a better rate performance of GCP-300 electrodes (Brun et al. 2012). These observations are in agreement with the cyclic voltammetry and charge discharge results.

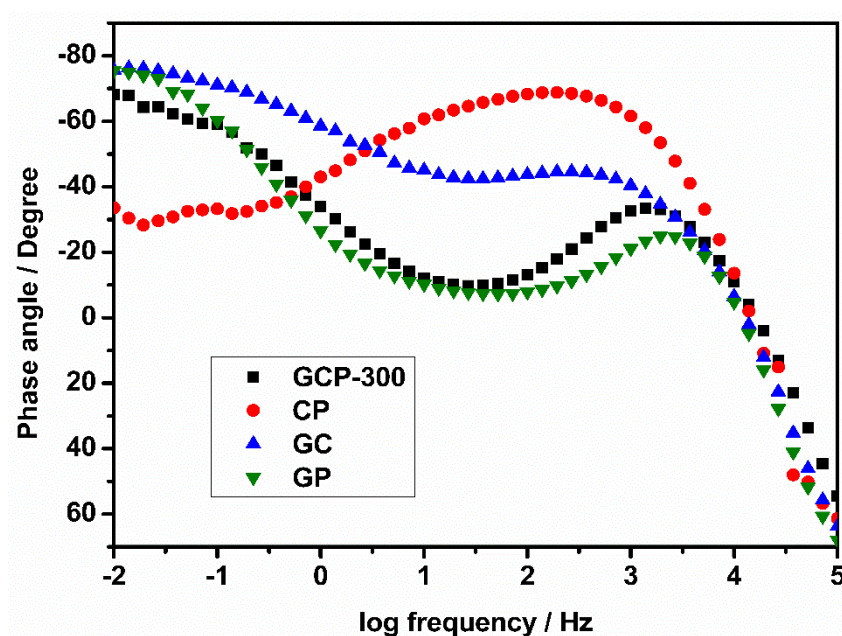


**Fig. 3.15** Bode plots of GCP – 300, CP, GC and GP.

The phase angle Bode plots of GCP – 300 and the binary composites are depicted in Fig. 3.15. The plots present the frequency dependency on phase angle and the frequency corresponds to the phase angle of  $-45^\circ$ , is considered the critical frequency at which the quick response of a super capacitor is determined (Yuan et al. 2011; Sheng et al. 2012a; Pan et al. 2014). At  $-45^\circ$  the resistance and the reactance of the capacitor are equal in magnitude (Sheng et al. 2012a). The critical frequency ( $f_0$ ) that corresponds to the phase angle of  $-45^\circ$  is found to be 4.66 Hz for GCP – 300. The relaxation time ( $\tau_0$ ) gives a measure of the rate of the ionic diffusion in the electrode and the minimum time consumed by the device to discharge all of its energy with an efficiency of more than 50% of its maximum value (Yuan et al. 2011; Pan et al. 2014). The  $\tau_0$  found to be 0.21 s, indicating a fast discharge process. The critical frequencies corresponding to phase angle  $-45^\circ$  and their respective relaxation times are given in

---

Table 3.5. From Table 3.5 it can be observed that the GCP – 300 possesses second highest critical frequency of 4.66 Hz and second lowest relaxation time constant of 0.21 s, which are attributed to the fast response and faster discharge of as fabricated device. The GC possesses the highest critical frequency of 9.03 Hz and lowest relaxation time of 0.11 s, despite having the low specific capacitance, which can be attributed to the high leakage resistance of GC binary composite.

**Table 3.5** Magnitudes of  $f_0$  and  $\tau_0$ .

Composites	$f_0$ (Hz)	$\tau_0$ (s)
<b>GCP-300</b>	4.66	0.21
<b>CP</b>	1.29	0.77
<b>GC</b>	9.03	0.11
<b>GP</b>	3.71	0.26



### 3.2. GCP WITH GLACIAL ACETIC ACID AS DOPANT

#### 3.2.1. Structural characterization

##### 3.2.1.1. X-ray diffraction analysis

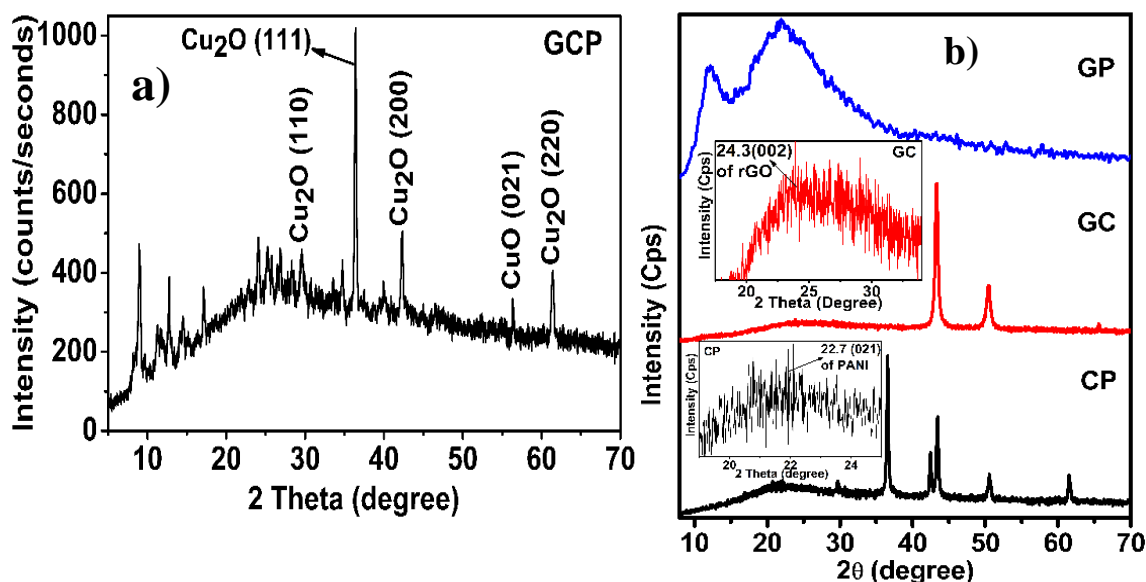


**Fig. 3.16** (a) X-ray diffraction patterns of reduced graphene oxide/copper oxide/polyaniline nanocomposite (GCP); (b) X-ray diffraction patterns of copper oxide/polyaniline (CP), reduced graphene oxide/copper oxide (GC), reduced graphene oxide/polyaniline (GP) binary composites.

The X-ray diffraction patterns of graphene oxide (GO), reduced graphene oxide (rGO) and polyaniline (PANI) are shown in Fig.3.1 and the explanations are also discussed in section 3.1.1. The reduced graphene oxide/copper oxide/polyaniline nanocomposite synthesized using glacial acetic acid as dopant (GCP) is shown in Fig. 3.16a. The broad peak at  $24.19^\circ$  and the additional overlapped peaks corresponding to polyaniline (PANI), distinctly suggest the further increase in interlayer spacing due to the intercalations of PANI between rGO layers (Han et al. 2014). The peaks of GCP and their crystal planes are as follows. Peaks at  $29.61^\circ$  (110),  $36.41^\circ$  (111),  $42.31^\circ$  (200) and  $61.35^\circ$  (220) are of cuprous oxide ( $\text{Cu}_2\text{O}$ ) (JCPDS file No. 78–2076), a peak at  $56.36^\circ$  (021) is of CuO (JCPDS file No. 80–1917) and the remaining peaks at  $23.98^\circ$  (110),  $26.98^\circ$  (003),  $28.34^\circ$  (210),  $30.89^\circ$  (020),  $33.55^\circ$  (120),  $34.73^\circ$  (221),  $39.78^\circ$  (310) (JCPDS file No. 53–1717 and 53–1891) are of polyaniline. The presence of several peaks of polyaniline with different crystalline planes, in the GCP

nanocomposite indicates the production of PANI with an assembly of different crystal planes in the composite. Peaks at  $9.06^\circ$ ,  $11.80^\circ$ ,  $12.76^\circ$ ,  $14.60^\circ$ , and  $17.18^\circ$  on the spectra of GCP are due to the presence of oxygen containing glacial acetic acid that are doped on the polymer backbone of PANI (Veerendra and Sathyanarayana 2005). The crystalline size of the  $\text{Cu}_2\text{O}$ ,  $\text{CuO}$  and PANI were calculated from their respective most intense peaks and they are 36.88 nm, 35.76 nm and 33.27 nm, respectively, indicating that the synthesized nanocomposites are in nanodimensions. The X-ray diffraction patterns of copper oxide/polyaniline (CP), reduced graphene oxide/copper oxide (GC), reduced graphene oxide/polyaniline (GP) are shown in Fig. 3.16b. CP shows peaks at  $22.70^\circ$  (021) corresponds to PANI (JCPDS file No. 53–1891),  $29.74^\circ$  (110),  $36.43^\circ$  (111),  $42.31^\circ$  (200),  $61.53^\circ$  (220) correspond to  $\text{Cu}_2\text{O}$  (JCPDS file No. 78–2076) and peaks at  $43.43^\circ$  (111),  $50.57^\circ$  (200), correspond to Cu (JCPDS file No. 04–0836). GC shows peaks at  $24.31^\circ$  (002) of rGO,  $43.38^\circ$  (111) and  $50.46^\circ$  (200) correspond to Cu (JCPDS file No. - 04-0836). GP shows two peaks, the first broad peak centered at  $12.10^\circ$  shows the presence of oxygen containing acetic acid which was used as dopant and traces of other oxygen containing functional groups left unreduced and the second broad peak centered at  $22.14^\circ$  is due to the well intercalated PANI between rGO layers.

#### 3.2.1.2. FT-IR spectra

The FT-IR spectra of copper oxide/polyaniline (CP), reduced graphene oxide/copper oxide (GC), reduced graphene oxide/polyaniline (GP) binary composites and reduced graphene oxide/copper oxide/polyaniline ternary nanocomposite (GCP) are given in Fig. 3.17. The FT-IR spectra of graphene oxide (GO), reduced graphene oxide (rGO), polyaniline (PANI) are shown in Fig. 3.2 and the explanations are discussed in section 3.1.2. Copper oxide/polyaniline (CP) binary composite shows peaks at  $3388\text{ cm}^{-1}$ ,  $1587\text{ cm}^{-1}$ ,  $1503\text{ cm}^{-1}$ ,  $1396 - 1312\text{ cm}^{-1}$ ,  $1168\text{ cm}^{-1}$ ,  $1046\text{ cm}^{-1}$ ,  $832 - 748\text{ cm}^{-1}$ ,  $695 - 626\text{ cm}^{-1}$ ,  $496 - 413\text{ cm}^{-1}$ , corresponding to  $-\text{OH}$  of water,  $\text{C}=\text{C}$  stretching of quinoid and benzenoid ring,  $\text{C}-\text{N}$  stretching vibration quinoid ring,  $\text{C}-\text{N}$  bending vibration of benzenoid ring (Gopalakrishnan et al. 2014),  $-\text{C}-\text{H}$  in plane bending of aromatic ring,  $-\text{C}-\text{H}$  out plane bending of aromatic ring (Gopalakrishnan et al. 2014),  $\text{Cu}-\text{O}$  stretching vibration in  $\text{Cu}_2\text{O}$  (Gopalakrishnan et al. 2014) and Cu peaks, respectively.

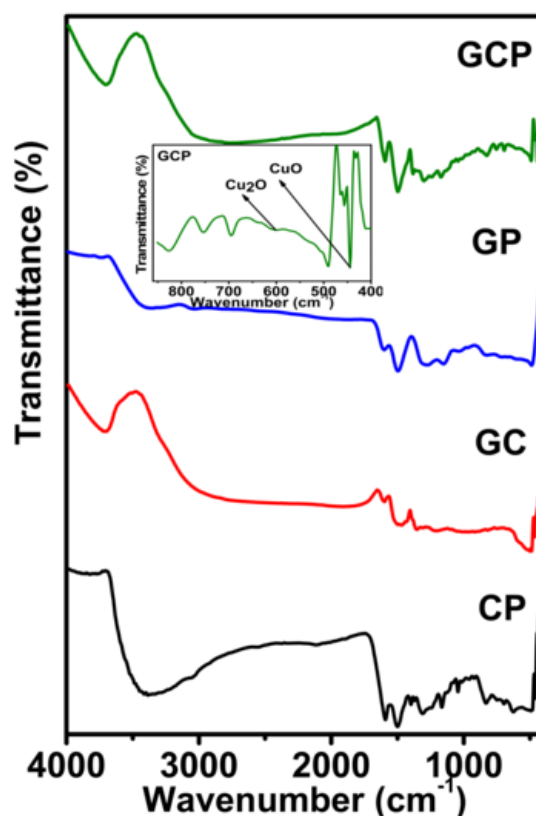


**Fig. 3.17** FT-IR spectra of copper oxide/polyaniline (CP), reduced graphene oxide/copper oxide (GC), reduced graphene oxide/polyaniline (GP) binary composites and reduced graphene oxide/copper oxide/polyaniline ternary nanocomposite (GCP).

Reduced graphene oxide/copper oxide (GC) binary composite shows peaks at  $3708\text{ cm}^{-1}$ ,  $1602\text{ cm}^{-1}$ ,  $1488\text{ cm}^{-1}$ ,  $1358\text{ cm}^{-1}$ ,  $1221\text{ cm}^{-1}$ ,  $496\text{--}429\text{ cm}^{-1}$ , corresponding to  $\text{-OH}$  (Xia et al. 2012b) of water, skeletal  $\text{-C=C-}$ ,  $\text{-C-O-}$  in  $\text{-C-OH}$ ,  $\text{-C-OH}$ , epoxy  $\text{-C-O-}$ , and the rest are of Cu, respectively. Reduced graphene oxide/polyaniline (GP) binary composite show peaks at  $3378\text{ cm}^{-1}$ ,  $1594\text{ cm}^{-1}$ ,  $1489\text{ cm}^{-1}$ ,  $1289\text{ cm}^{-1}$ ,  $1159\text{ cm}^{-1}$ ,  $1041\text{ cm}^{-1}$  and  $831\text{--}711\text{ cm}^{-1}$ , corresponding to  $\text{C=C}$  stretching of quinoid and benzenoid ring,  $\text{C-N}$  stretching vibration of benzenoid ring (Gopalakrishnan et al. 2014),  $\text{C=N}$  stretching vibration,  $\text{-C-H}$  out plane bending of aromatic ring, respectively. In the case of GCP composite, there are peaks at  $1581\text{ cm}^{-1}$ ,  $1472\text{ cm}^{-1}$ ,  $1376\text{ cm}^{-1}$ ,  $1188\text{ cm}^{-1}$ ,  $1109\text{ cm}^{-1}$  and  $994\text{ cm}^{-1}$ , corresponding to  $\text{C=C}$  stretching of quinoid and benzenoid ring,  $\text{C-N}$  stretching vibration,  $\text{C=N}$  stretching vibration,  $\text{-C-H}$  in plane bending (Pan et al. 2016), and  $\text{-C-H}$  out of plane bending (Gopalakrishnan et al. 2014), respectively, corresponding to PANI. The peak at  $607\text{ cm}^{-1}$  is attributed to

Cu(I)–O vibrations in  $\text{Cu}_2\text{O}$  and at  $449\text{ cm}^{-1}$  possibly attributed to  $\text{CuO}$  (Midander et al. 2009), which substantiate the fact that the synthesized composite has both  $\text{Cu}_2\text{O}$  and  $\text{CuO}$ . The IR spectral results corroborate the XRD results. The above facts indicate integrated synthesis of reduced graphene oxide/copper oxide/ polyaniline during in situ single step synthesis.

### 3.2.1.3. Raman spectra

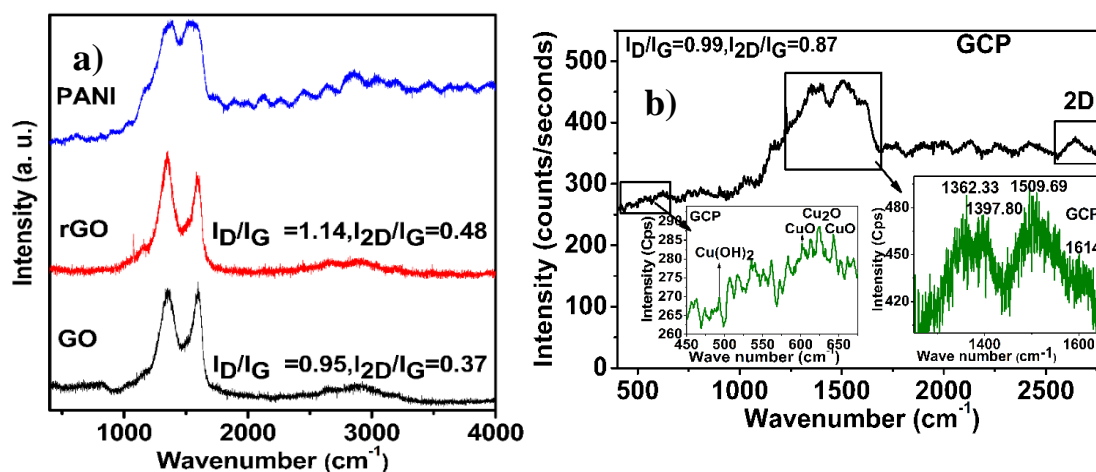


**Fig. 3.18** Raman spectra of graphite oxide (GO), reduced graphene oxide (rGO), polyaniline (PANI) and GCP.

The Raman spectra of graphene oxide (GO), reduced graphene oxide (rGO), polyaniline (PANI) and reduced graphene oxide/copper oxide/polyaniline nanocomposite (GCP) are depicted in Fig. 3.18. It is seen from the figure that the D, G and 2D bands of GO are at  $1355\text{ cm}^{-1}$ ,  $1595\text{ cm}^{-1}$  and  $2642\text{ cm}^{-1}$ , that of rGO are at  $1356\text{ cm}^{-1}$ ,  $1595\text{ cm}^{-1}$  and  $2664\text{ cm}^{-1}$ , and that of GCP are at  $1397\text{ cm}^{-1}$ ,  $1614\text{ cm}^{-1}$  and  $2665\text{ cm}^{-1}$ . An observation on the peak positions of D band of GO, rGO and GCP infers that there is a positive shift in wavenumber from  $1355\text{ cm}^{-1}$  to  $1356\text{ cm}^{-1}$  and to  $1366\text{ cm}^{-1}$  appraising the easy electron transfer enabled between rGO and PANI by the intercalation of PANI in between the rGO layers and their bosom contact (Kotal et al. 2013). The increase in  $I_D/I_G$  ratio from GO to GCP, as depicted in Fig. 3.18b, shows the increase in defects and the reduction of GO to rGO during the synthesis of GCP (Rana and Malik 2012; Mondal et al. 2017). The  $I_{2D}/I_G$  ratios of GO, rGO and GCP are 0.37, 0.48 and 0.87, respectively. The  $I_{2D}/I_G$  ratios of GO and rGO correspond to

multilayer nature and of GCP corresponds to few layer nature honeycomb lattices (Akhavan et al. 2014), attributed to the facts that the intercalation of PANI between the rGO layers may not only serves as a source of pseudo capacitance, but also act as a spacer by increasing the d-spacing of honeycomb lattices of rGO during the synthesis of GCP (Kumar and Baek 2014). The formation of PANI was ascertained by the peaks at  $518.57\text{ cm}^{-1}$ ,  $583.83\text{ cm}^{-1}$ ,  $808.24\text{ cm}^{-1}$ ,  $1170.10\text{ cm}^{-1}$ ,  $1223.71\text{ cm}^{-1}$ ,  $1362.33\text{ cm}^{-1}$ ,  $1506.18\text{ cm}^{-1}$ , and  $1600.00\text{ cm}^{-1}$ , corresponding to phenazine like segments, stretching and bending of out of plane C–H bonds of quinoid rings, bending modes of C–H in benzenoid rings, stretching modes of –C–N in polaronic elements, vibrational semiquinone radicals, stretching vibrations of C=N in quinoid elements, and stretching modes of C=C in quinoid rings, respectively. The presence of copper oxides are substantiated by the peaks at  $492.48\text{ cm}^{-1}$  of  $\text{Cu}(\text{OH})_2$  (Deng et al. 2016),  $601.89\text{ cm}^{-1}$  (Wang et al. 2003) and  $643.17\text{ cm}^{-1}$  of  $\text{CuO}$  (Chen et al. 1995), and at  $623.89\text{ cm}^{-1}$  of  $\text{Cu}_2\text{O}$  (Deng et al. 2016), respectively.

#### 3.2.1.4. XPS

Figures 3.19 (a-h) present the survey XPS spectrum of GCP composite, core level spectra of C, N, O, and Cu. The elements present in the GCP composites are confirmed from survey spectrum as it possesses the characteristic peaks of C, N, O and Cu (Fig. 3.19a). Each of these peaks were deconvoluted by using Gaussian fitment (Peak fit, version – 4.12). The C 1s core level spectrum (Fig. 3.19b) was deconvoluted into five peaks with binding energies of 284.16 eV, 285.07 eV, 286.34 eV, 288.06 eV and 289.69 eV, which are assigned to  $\text{sp}^2$  hybridized carbons of C=C (Arezzo et al. 1994), C–N bonds of polyaniline (Kumar et al. 1990), C–O, C=O of traces of oxygen containing functional groups on reduced graphene oxide which were left unreduced and O–C=O of acetic acid that was used as dopant on the synthesis (Hareesh et al. 2016), respectively.

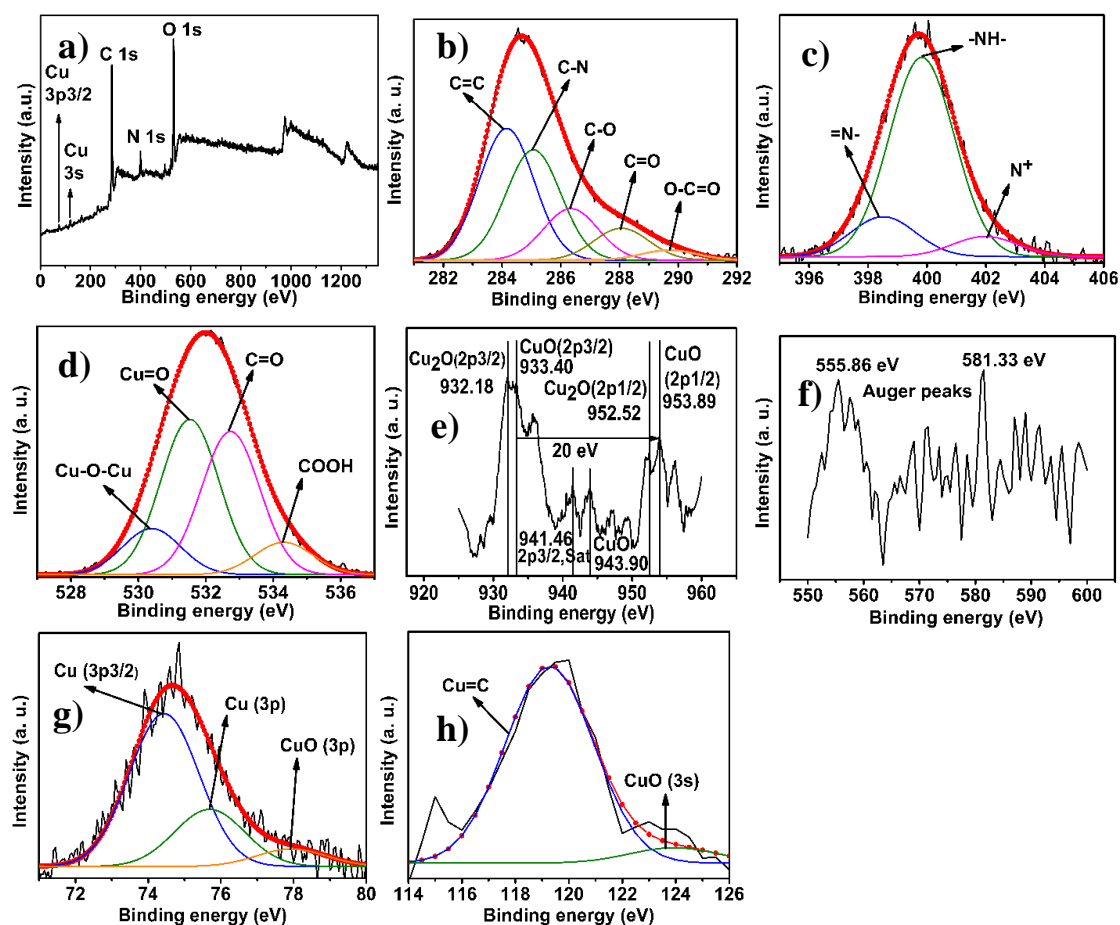


**Fig. 3.19** (a) Survey XPS spectrum of GCP, (b-e) core level spectra of C 1s, N 1s, O 1s, Cu 2p 3/2, (f) Cu 3p Auger electron spectra and core level spectra of (g) Cu 3p (h) Cu 3s.

The N 1s core level spectra (Fig. 3.19c) were deconvoluted into three peaks at binding energies of 398.51 eV, 399.82 eV, and 401.97 eV pertaining to benzenoid amine bonds (=N-) (Kang et al. 1996; Kumar et al. 1990), quinoid imine bonds (-NH-) (Kang et al. 1996) and nitrogen cationic radicals (N<sup>+</sup>) (Kumar et al. 1990) of polyaniline, respectively. The O 1s spectra (Fig. 3.19d) was deconvoluted into four peaks of binding energies 530.39 eV, 531.53 eV, 532.74 eV, and 534.31 eV which correspond to oxygen bonded to cuprous ion (Cu<sup>+</sup>) (McIntyre 1981), oxygen bonded to cupric (Cu<sup>2+</sup>) ion (McIntyre 1981), carbonyl oxygen (C=O) of unreduced oxygen bearing entities, and carboxylic acid groups (Krause and Oliver 1979; Bournel et al. 1996), used as dopants, respectively. The core level spectrum of copper is shown in Fig. 3.19e. It is observed from the spectra that the cuprous oxides (Cu<sub>2</sub>O) has a 2p<sub>3/2</sub>

peak at 932.18 eV and a 2p<sub>1/2</sub> peak at 952.52 eV (Zhao et al. 2011); the cupric oxide has a couple of peaks, a 2p<sub>3/2</sub> peak at 933.40 eV and a 2p<sub>1/2</sub> peak at 953.89 eV (Jolley et al. 1989) with the peak separation of 20.49 eV (Fig. 3.19e). The peak binding energy gap of 20.49 eV substantiates the divalent nature of CuO in the nanocomposite (Li et al. 2014a). The satellite peaks are used to differentiate the Cu metal, CuO and Cu<sub>2</sub>O from each other (Poulston et al. 1996). The CuO is distinguished from Cu<sub>2</sub>O and Cu by having a couple of CuO 2p<sub>3/2</sub> satellite peaks which are flanked between the two major peaks of itself at binding energies of 941.46 eV and 943.90 eV. Each of these two binding energies are at an addition of 8.06 eV and 10.5 eV on the major peaks of CuO 2p<sub>3/2</sub> at 933.40 eV, which are close to ~9 eV of addition reported in the literature (Ghijssen et al. 1988). The presence of two satellite peaks is attributed to the spin orbit splitting of Cu (2p) and Cu (3p) lines (McIntyre and Cook 1975). The satellite peaks are considered to be the feature of materials with d<sup>9</sup> configuration in its ground state and the broad nature of these peaks is attributed to the multiple splitting of 2p<sup>5</sup> 3d<sup>9</sup>, while Cu<sub>2</sub>O 2p<sub>3/2</sub> has no satellite peak (Ghijssen et al. 1988). The presence of Auger peaks and core level spectra of Cu 3p and Cu 3s further corroborates the presence of copper oxides in the composites. There are two Auger peaks of Cu<sub>2</sub>O (Fig. 3.19f) observed at binding energies of 555.36 eV and 581.33 eV, which are converted into kinetic energies of 935 eV and 909 eV using Equation 3.2.

$$KE = h\nu - BE - \varphi_s \quad (3.2)$$

where *KE* is the kinetic energy of an Auger electron, *hν* is the X-ray excitation energy, *BE* is the binding energy and  $\varphi_s$  is the work function of 3.9 eV. The Auger parameter ( $\alpha$ ) of Cu<sub>2</sub>O was calculated using Equation 3.3 (Reitz and Solomon 1998).

$$\alpha = KE(LMM) + BE(2p_{3/2}) \quad (3.3)$$

The values were found to be 1867.32 and 1842.80, which are in good agreement with literature (Barreca et al. 2007). The expected Auger peak is at a kinetic energy of about 919 eV, but the splitting of Auger peak into two peaks, centering at kinetic energies of 935 eV and 909 eV, is attributed to the existence of Cu/Cu<sub>2</sub>O heterogenic interface (Trivich et al. 1978) and the presence of two Cu 2p levels (Schön 1972). A pair of peaks corresponding to Cu (0) 3p<sub>3/2</sub> (Ertl et al. 1980) and 3p (Robert and

Offergeld 1972) are obtained along with a peak of CuO 3p (Robert and Offergeld 1972) with binding energies of 74.43 eV, 75.68 eV and 77.88 eV, respectively, on the deconvolution of the peak for the core-level of 3p<sub>3/2</sub> (Fig. 3.19g). The deconvolution of the peak of Cu 3s core level spectra (Fig. 3.19h) exhibits a peak at a binding energy of 119.28 eV, corresponding to Cu=C bonds (Hawaldar et al. 2012) formed in the synthesized GCP composite. Another peak with the binding energy of 123.93 eV is assigned to CuO 3s (Hawaldar et al. 2012).

### 3.2.1.5. FE-SEM

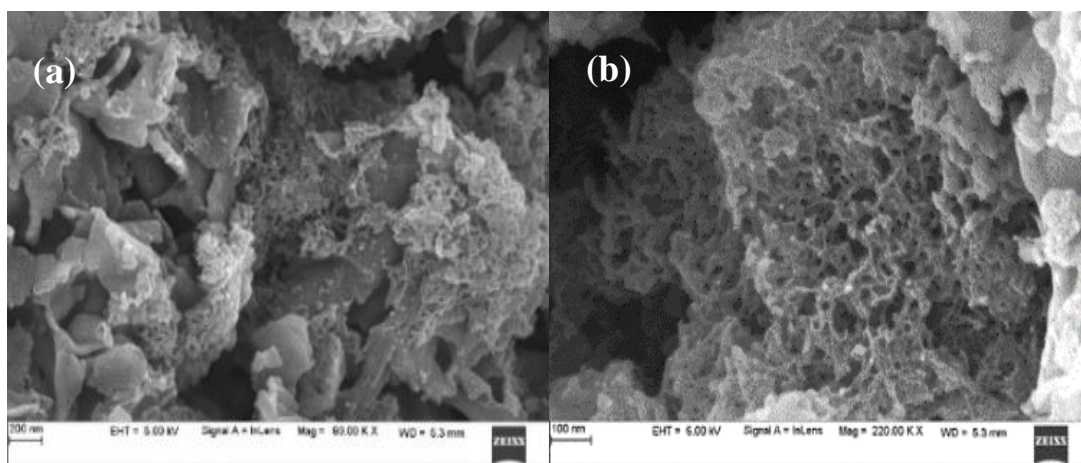


**Fig. 3.20** (a) and (b) The FE-SEM images of the GCP nanocomposites.

The FE-SEM images of GCP nanocomposite are given in Fig. 3.20a and 3.20b. As a general observation, it can be inferred that the PANI has formed a uniform porous layer on the rGO sheets in such a way that the restacking and agglomeration of them is effectively reduced, and there by PANI acting as a spacer. This interpretation is further corroborated by the Raman results indicating the conversion of multi rGO layers into few layered during the synthesis of the composite. The porous architecture, as depicted in Fig. 3.20b, enables the electrolyte to penetrate deep into the bulk of the composite material during energy storage and increases the surface area available for the formation of electrical double layers, enabling the channels for the accumulation of ions and in turn increasing the specific capacitance. The flexibility of the composite structure effectively relieves the material from undergoing failure by any sort of strain on the application of high currents. The distribution of copper and its oxides on rGO – PANI layers ensures the integrity of the constituents and connectivity for electron transfer.



### 3.2.2. Electrochemical characterizations

The GCP nanocomposites were synthesized by varying the weight percent of each of the constituent materials so as to achieve a best weight percentage of all the three constituents with better electrochemical properties. The nomenclatures used for the GCP composites of different composition and their respective percentages of the constituents are summarized in Table 3.6.

**Table 3.6** The nomenclature used for the GCP composites of different composition and their respective percentages of the constituents.

Component under study	Weight of constituents (mg)			Weight percentage (%)	Nomenclature of composite
	P	C	G		
PANI series	100	50	25	57.10	GCP57
	150	50	25	66.66	GCP67
	200	50	25	72.72	GCP73
	250	50	25	76.90	GCP78
	300	50	25	80.00	GCP80
	350	50	25	82.35	GCP82
Copper oxide series	300	100	25	23.52	GC24P
	300	150	25	31.57	GC32P
	300	200	25	38.09	GC38P
	300	250	25	43.47	GC43P
	300	300	25	48.00	GC48P
	300	350	25	51.85	GC51P
rGO series	300	250	50	8.30	G8CP
	300	250	75	12.00	G12CP
	300	250	100	15.38	G15CP
	300	250	125	18.51	G19CP
	300	250	150	21.42	G21CP

Eventually the nanocomposite G12CP was obtained to be the best composition with specific capacitance, as high as 684.93 F g<sup>-1</sup>. The discussions on the electrochemical studied are presented in the following sections.

## 3.2.2.1. CV studies

The CV curves of GCP and binary composites at a scan rate of  $5 \text{ mV s}^{-1}$  with  $0.4 \text{ M H}_2\text{SO}_4$  as electrolyte are shown in Fig. 3.21a. It is seen from Fig. 3.21a that the CV curves are not rectangular in shape, but are asymmetric with redox peaks which indicate the involvement of both faradaic process of PANI and oxides of copper and non-faradic process of rGO during the charge storage process. The peaks are attributed to the redox transitions of PANI (Han et al. 2014) and of copper oxide. Fig. 3.21a shows that the cyclic voltammogram of G12CP possesses more area, indicating the higher conductivity and lower internal resistance of the composite (Han et al. 2014). The area created under cathodic and anodic curves of a cyclic voltammogram is proportional to the effective charge stored, which in turn is proportional to the capacity of a composite electrode material. Thus, the higher area of G12CP is ascribed to the high specific capacitance.

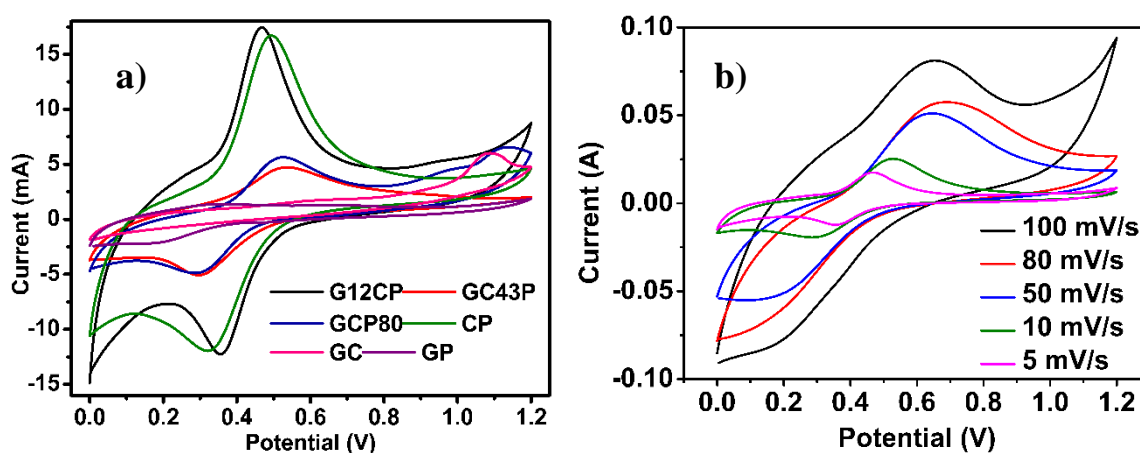


**Fig. 3.21** (a) Cyclic voltammograms of G12CP, GC43P, GCP80, CP, GC and GP at a scan rate of  $5 \text{ mV s}^{-1}$ ; (b) Cyclic voltammograms of composites G12CP at different scan rates.

The oxidation peak at  $0.46 \text{ V}$  is associated with the oxidation of semiconducting leucoemeraldine form of PANI to emeraldine and a reduction peaks at  $0.35 \text{ V}$  is due to reduction of emeraldine to pernigraniline form. As the composite G12CP yields more charge storage, the cyclic voltammograms of it at different scan rates are shown in Fig. 3.21b. It is seen from Fig. 3.21b that there is a shift of anodic and cathodic peak positions as the scan rate increases. This is due to the internal resistance of the electrode

material (Asen and Shahrokhian 2017a), and existence of polarization (Maitra et al. 2017). The decrease in the capacity of the electrode on increasing the scan rate is ascribed to the less electrolyte diffusion into the interior of the electrode material at high scan rates (Asen and Shahrokhian 2017a) as the electrolyte access is confined to the outer surface of the electroactive materials and the inner active sites are left unaccessed by electrolyte ions. At lower scan rates the electrolyte diffusion into the electroactive sites present at the interior of the electrode materials is made effective and hence the possible maximum redox reactions occur on the active sites yielding high specific capacitance (Dhibar and Das 2014).

#### 3.2.2.2. *GCD studies*

The general observations of GCD studies are as follows. All the CD curves obtained are quasi triangular in shape, which signifies that the obtained specific capacitance is a combined contribution of non-faradaic electrical double layer charge storage and faradaic pseudo capacitance (Mondal et al. 2017). The plateaus on the GCD curves are attributed to the fact that the synthesized composites exhibit reversible pseudo capacitance originated from the faradic redox reactions of PANI and copper oxide nano-particles that are dispersed over rGO layers (Wu et al. 2015a). All the nanocomposites showed longer time of discharge at lower current densities indicating better capacitance and the sufficient insertion of  $H^+$  ion on the polymer back bone of PANI and into the porous architecture developed in the composite (Han et al. 2014). The decrease in specific capacitance with the increase in current density in all the cases is due to the reason that at higher current densities the IR drop increases and all the electroactive sites present in the electrode materials do not undergo their characteristic redox reactions; and the available surface area in the porous architecture of nanolayers of rGO is not utilized to the fullest extent in storing the charges. On the contrary at low current density the better diffusivity of electrolyte ions into the three-dimensional porous architecture of the ternary composite allows the presence of maximum possible electroactive sites in the interior of the electrode materials to undergo their respective charge storing reactions efficiently. Also, the good diffusion of electrolyte in to composite material brings down the internal resistance offered by the materials, increasing the specific capacitance (Maitra et al. 2017; Asen and Shahrokhian 2017a).

The larger ohmic drop in all the composites might have aroused due to the reason that no conductivity enhancer like carbon black in acetylene are used and the lack of compact package of electrode material over the carbon cloth and between the stainless steel which are used as current collectors.

**Table 3.7.** The electrochemical parameters of different GCP composites synthesized at a current density of  $0.25 \text{ A g}^{-1}$ .

Constituent under study	Composite	$C_s$ ( $\text{F g}^{-1}$ )	$E$ ( $\text{W h kg}^{-1}$ )	$P$ ( $\text{W kg}^{-1}$ )
<b>PANI series</b>	GCP57	30.04	6.01	376.91
	GCP67	46.99	9.39	466.04
	GCP73	33.92	6.78	405.70
	GCP78	35.11	7.02	435.84
	GCP80	60.97	12.19	426.23
	GCP82	15.01	3.00	505.17
<b>Copper oxide series</b>	GC24P	75.30	15.06	382.34
	GC32P	88.65	17.73	374.57
	GC38P	81.43	16.28	360.59
	GC43P	129.53	25.90	391.21
	GC48P	78.86	15.77	342.47
	GC51P	47.52	9.50	373.58
<b>rGO series</b>	G8CP	130.89	26.17	266.96
	G12CP	171.23	34.24	328.94
	G15CP	98.42	19.68	354.68
	G19CP	82.23	16.44	319.02
	G21CP	78.12	15.62	367.64

As the current density increases, the ohmic drop also increases, which might be attributed to the resistance offered by the unutilized electrode materials due to the ineffective diffusion of electrolyte into the entire bulk of the electrode material at high current density. As the current density decreases the ohmic drop decreases as the unutilized electrode materials are reduced at low current density as the diffusion of electrolyte into the electro active materials increases. The electrochemical parameters of the GCP composites synthesized are given in Table 3.7.

### PANI series

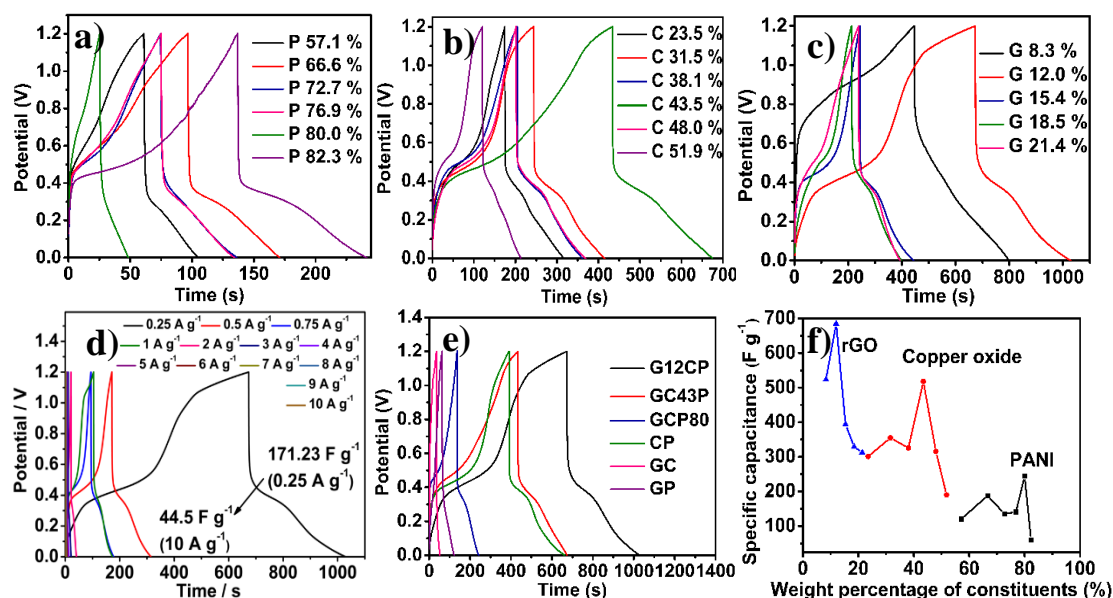


**Fig. 3.22.** GCD curves of composites (a) with different weight percentages of PANI at a current density of  $0.25 \text{ A g}^{-1}$ ; (b) with different weight percentages of copper oxide at a current density of  $0.25 \text{ A g}^{-1}$ ; (c) with different weight percentages of rGO at a current density of  $0.25 \text{ A g}^{-1}$ ; (d) GCD curves of composites G12CP at current densities ranging from  $0.25$  to  $10 \text{ A g}^{-1}$ ; (e) GCD curves of G12CP, GC43P, GCP80, CP, GC and GP at a current density of  $0.25 \text{ A g}^{-1}$ ; (f) Plot of specific capacitances of nanocomposites at a current density of  $0.25 \text{ A g}^{-1}$  vs weight percentages of rGO, copper oxide and PANI.

A series of composites were synthesized by varying the weight ratio of PANI and keeping the weight ratio of copper oxide, and reduced graphene oxide (rGO) as constant as  $50 \text{ mg}$  and  $25 \text{ mg}$ , respectively. The GCD curves of PANI series are shown

in Fig. 3.22a. It is seen from Fig. 3.22a and data in Table 3.7 that, as the polymer weight loading increases from 100 mg to 300 mg, there is an increase in specific capacitance from  $30.04 \text{ F g}^{-1}$  to  $60.97 \text{ F g}^{-1}$  and further increase in the weight of PANI decreases the specific capacitance to  $60.06 \text{ F g}^{-1}$  at a current density of  $0.25 \text{ A g}^{-1}$ .

The initial increase in the specific capacitance might be due to the increase in the redox active sites, surface area and conductivity of the composite as the weight of PANI increases. The later trend of diminishing of electrochemical properties is attributed to the nonuniform densification of PANI over rGO and around  $\text{Cu}_2\text{O}/\text{CuO}$ , tending to form agglomerates in a random manner which limits the access of electrolyte into the entire bulk of the composite, and its fullest utilization (Xu et al. 2010). Since the composite with 300 mg of PANI showed the better electrochemical properties, the weight percentages of the constituents in that particular composite was calculated and it was found to be rGO 6.6%:  $\text{Cu}_2\text{O}/\text{CuO}$  13.4%: PANI 80% and named to be GCP80.

#### *Copper oxide series*

In this series, the weight of copper oxide was varied keeping the weight of PANI at 300 mg, which corresponds to the maximum capacitance in the previous series and also keeping the weight of rGO constant. The GCD curves of the copper oxide series are shown in Fig. 3.22b. It is observed from Fig. 3.22b and Table 3.7 that the specific capacitance increases when the weight of copper oxide increases from 50 mg to 250 mg to give maximum capacitance of  $129.53 \text{ F g}^{-1}$  and decreases to  $78.86 \text{ F g}^{-1}$ , at a current density of  $0.25 \text{ A g}^{-1}$  on further increase in the weight. The initial increase in capacitance may be due to the increase in the extent of redox reactions of oxides of copper as the weight of copper oxide nanoparticles increases. The distribution of  $\text{Cu}_2\text{O}/\text{CuO}$  nanoparticles on and in-between the PANI covered rGO layers provide a charge carrier network. The decrease in capacitance at higher quantities of copper oxide could be accounted to the formation of micro-sized particles due to agglomeration when a large amount of particles are incorporated in PANI coated rGO layers and to the internal resistance created by them. In such micro-sized particles of copper oxide, due to their bigger size, the redox reaction takes place only on the superficial surface and not in the core of the particles. The weight percentage of nanocomposite with copper

oxide weight of 250 mg was determined to be rGO 4.3%: Cu<sub>2</sub>O/CuO 43.4%: PANI 52.3% and named to be GC43P.

#### *rGO series*

A series of composites was prepared by fixing the weight ratio of PANI and Cu<sub>2</sub>O/CuO as 300 mg and 250 mg, respectively, and the weight of rGO was varied. The GCD curves of rGO series are shown in Fig. 3.22c. When the rGO weight increases from 25 mg to 75 mg, the specific capacitance increases from 130.89 F g<sup>-1</sup> to 171.23 F g<sup>-1</sup> and on further increasing the weight of rGO, the supercapacitance decreases to 98.42 F g<sup>-1</sup>, at a current density of 0.25 A g<sup>-1</sup>. The initial increase in specific capacitance till 75 mg may be attributed to the fact that increasing the rGO content would allow PANI and copper oxide to disperse without agglomeration. Such a distribution would open up more redox active sites of PANI and copper oxide and create more porosities for charge accumulation by EDL capacitance. The decrease in specific capacitance at higher quantities of rGO is attributed to the spreading up of available PANI and copper oxide nanoparticles on rGO layers resulting in disconnection of three-dimensional charge carrying network and disturbing the continuous flow of charges. The weight percentage of composite with rGO weight of 75 mg was determined to be rGO 12%: Cu<sub>2</sub>O/CuO 40%: PANI 48% and named to be G12CP. The specific capacity (C g<sup>-1</sup>) of G12CP calculated using Equation. 2.5 (Brousse et al. 2015). The specific capacity of G12CP at a current density of 0.25 A/g is found to be 205.47 C g<sup>-1</sup>.

The Fig. 3.22d shows the CD curves of G12CP at different current densities ranging from 0.25 A g<sup>-1</sup> to 10 A g<sup>-1</sup>. It is seen from Fig. 3.22d, that the standardized composite (G12CP) has exhibited a maximum capacitance at a lower current density of 0.25 A g<sup>-1</sup> due to the better electrolyte diffusion into the interior nano-channels of the composite as discussed above. To establish the fact that the standardized composites supersedes binary composites, the binary combinations of afore-discussed three constituents with the same weight ratios as that of G12CP were synthesized and named as copper oxide/polyaniline (CP), reduced graphene oxide/copper oxide (GC), reduced graphene oxide/polyaniline (GP) binary composites. The GCD curves of GCP and corresponding binary composites at a current density of 0.25 A g<sup>-1</sup> are shown in Fig. 3.22e. The specific capacitance, energy densities and power densities, calculated at a current density of 0.25 A g<sup>-1</sup>, are listed in Table 3.8.

**Table 3.8** The electrochemical parameters of nanocomposites G12CP, CP, GC and GP at a current density of 0.25 A g<sup>-1</sup>.

Composite	C <sub>s</sub> (F g <sup>-1</sup> )	<i>E</i> (W h kg <sup>-1</sup> )	<i>P</i> (W kg <sup>-1</sup> )
G12CP	171.23	34.24	328.94
CP	133.69	26.73	355.71
GC	11.84	2.36	519.92
GP	34.48	6.89	443.35

It is seen from Fig. 3.22e that the ternary composites are ranking better than the binary composites. The plots of variation of specific capacitance with weight percent of PANI, copper oxide and rGO are shown in Fig. 3.22f. The binary composite CP shows a good electrochemical performance; and even better power density than G12CP. This is due to the fact that the pseudocapacitive materials, copper oxide and PANI, store large amount of charges by their reversible redox reactions which is more than that of energy stored by EDLC mechanism (Wang et al. 2012a). However, the composite has a limitation of lower cyclic stability. The limitation is due to the fact that the PANI undergoes volumetric expansion and contraction during charge and discharge process, which causes structural breakdown leading to poor capacity retention (Pan et al. 2016). On the other hand, copper oxide undergoes considerable strain during charge/discharge process causing crack in charge flowing networks and decreasing the cyclic stability (Zhi et al. 2013). The standardized composite G12CP has high discharge time signifying better capacitive ability than all other composites. This may be attributed to the positive effect obtained by integrating the constituent materials in a right proportion.

The IR drop in binary composites are high compared to that in ternary composites and among ternary composites the composite G12CP exhibits the least IR drop of 0.58 V. The observed IR drops for GC43P, GCP80, CP, GC and GP are 0.74 V, 0.77 V, 0.74V, 0.83 V and 0.66 V, respectively. The equivalent series resistance (ESR in Ω) of nanocomposites were calculated from discharge curves using Equation 2.4. The ESR values of G12CP, GC43P, and GCP80 are found to be 1.16 Ω, 1.48 Ω, and 1.54 Ω, respectively. The composite G12CP has the lowest ESR and better conductance, which is attributed to the low contact resistance between the active



electrode materials and current collector, low intrinsic resistance between electrode materials and the low ionic resistance of the electrolyte solution (Sahoo and Shim 2017).

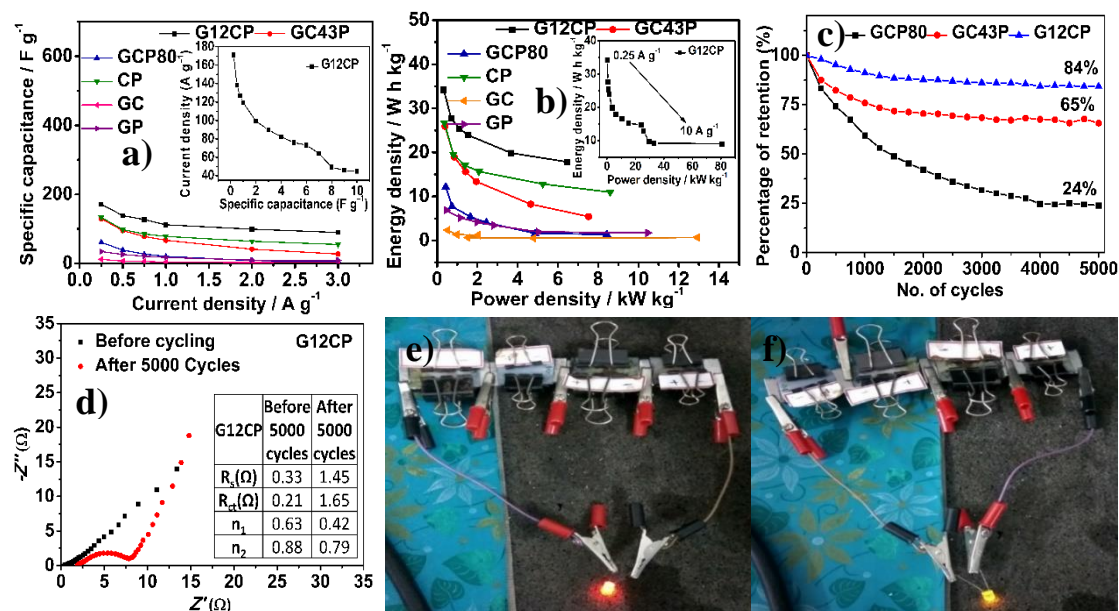


**Fig. 3.23.** (a) Plots of specific capacitance versus current densities of composites G12CP, GC43P, GCP80, CP, GC and GP (with the inset of same plot of G12CP till current density of 10 A g<sup>-1</sup>); (b) Ragone plots of composites G12CP, GC43P, GCP80, CP, GC and GP from current density from 0.25 to 3 A g<sup>-1</sup> (with the inset of same plot of G12CP at current densities from 0.25 to 10 A g<sup>-1</sup>); (c) Plots of retention of capacitance versus number of cycles of composites G12CP, GC43P, GCP80; (d) Nyquist plots before and after 5000 cycles (with the inset of a table of resistance values) (e and f) The as-fabricated supercapacitors energizing red and yellow light emitting diodes.

The plots of specific capacitance versus current density are shown Fig. 3.23a. It is seen from Fig. 3.23a that the composite G12CP shows the higher specific capacitance values than GC43P, GCP80, CP, GC and GP composites. The maximum specific capacitance shown at 0.25 A g<sup>-1</sup> is 171.23 F g<sup>-1</sup> and retains a value of 44.5 F g<sup>-1</sup> even when the current density is increased to 10 A g<sup>-1</sup>, indicating a good rate performance.

The better performance of the composite suggests that the three-dimensional architecture present in the composite provides more surface area for electrolytic ions to access, even at higher current densities (Pendashteh et al. 2015). The Ragone plots of the composites at different current densities are shown in Fig. 3.23b. The composite G12CP exhibits high energy density and high power density of  $34.24 \text{ W h kg}^{-1}$  and  $328.94 \text{ W kg}^{-1}$ , respectively, at  $0.25 \text{ A g}^{-1}$ . These values are higher than those exhibited by other composites. G12CP maintains an energy density and power density of  $8.98 \text{ W h kg}^{-1}$  and  $80.89 \text{ kW kg}^{-1}$ , respectively, even at a high current density of  $10 \text{ A g}^{-1}$ . This high energy behavior of the composite is due to the good interfacial contact between the PANI nanoparticles and rGO substrate through  $\pi$ - $\pi$  interactions, enabling the increased utilization of PANI and reducing the diffusion and migration paths for electrolyte ions during rapid redox reactions (Shen et al. 2013).

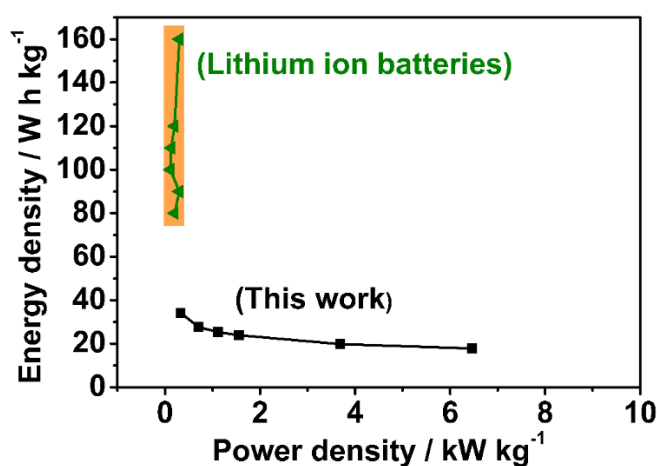


**Fig. 3.24.** Comparison of energy density and power density of G12CP with energy densities of lithium ion batteries.

The comparison of energy densities of G12CP at different current densities with the energy densities of lithium ion batteries is shown in Fig. 3.24 and it can be observed from Fig. 3.24 that G12CP exhibits energy densities lower than those of lithium ion batteries (Dunn et al. 2011) but higher than EDL supercapacitors ( $\sim 10 \text{ W h kg}^{-1}$ ). The cyclic stability of the composite G12CP was measured by reversible cyclic voltammetry at a high scan rate of  $700 \text{ mV s}^{-1}$  up to 5000 cycles and the plots of percentage capacitance retention versus number of cycles are shown in Fig. 3.23c.

The G12CP exhibited a retention of about 84.3% of its initial capacitance up to 5000 cycles. The deterioration of cyclic stability of G12CP is attributed to the development of internal resistance like solution resistance ( $R_s$ ) and charge transfer resistance ( $R_{ct}$ ), due to the constant evaporation of electrolyte during the cyclic process. The same is reflected in Fig. 3.23d and in table given at the inset of Fig. 3.23d. GCP80 and GC43P show relatively poor cyclic stability, which is attributed to the structural degradation of PANI due to the swelling and shrinkage on charge and discharge (Asen and Shahrokhian 2017a). In order to explore the realistic application of the composite material it was coated on four pairs of carbon clothes of dimension 2 cm  $\times$  3 cm following the aforementioned fabrication method and were connected in series. This set up was ample enough to light up red and yellow light emitting diodes of 1.7 V (the photographic images of the same are depicted in Fig. 3.23e and 3.23f), when charged with 9 V battery (EW high power 6F22) for 1 min. On removing the battery after one minute the LED continued to glow for the next 45 s, taking energy from the fabricated device, which shows the good energy density of the device and the ability to act as a secondary power source.

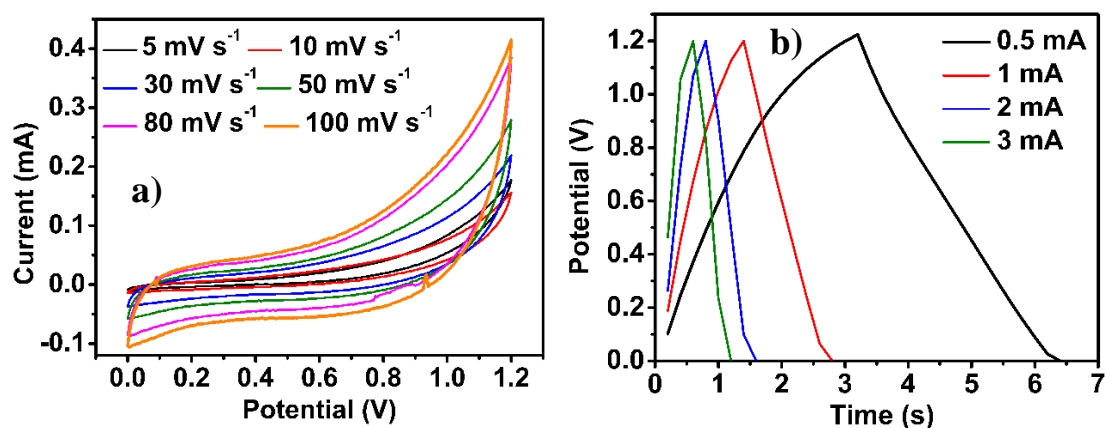


**Fig. 3.25** (a) Cyclic voltammograms of bare carbon cloths at scan rates of 100, 80, 50, 30, 10, 5  $\text{mV s}^{-1}$  (b) GCD curves of carbon cloths at applied currents of 0.5 mA, 1 mA, 2 mA, and 3 mA.

To evaluate the electrochemical properties contributed by the carbon cloth, CV and GCD studies were carried out on a pair of carbon cloths without coating with electroactive materials. The obtained CV and GCD curves are

shown in Fig. 3.25a and 3.25b, respectively. It is observed from the figures that the charge stored by bare carbon cloths is insignificantly small and hence the specific capacitance measured after coating with electroactive materials was only of the electrode material under study.

### 3.2.2.3. EIS studies

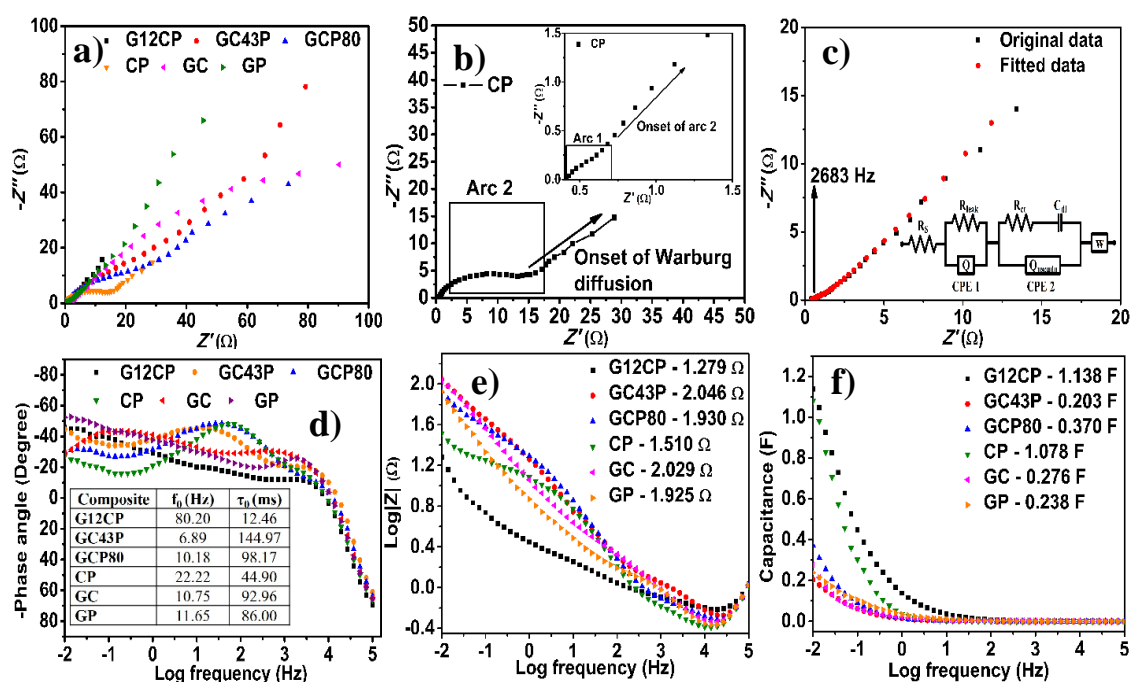


**Fig. 3.26** (a) Nyquist plots of G12CP, GC43P, GCP80, CP, GC and GP; (b) Nyquist plot of a nanocomposite CP with Arc 1 and Arc 2; (c) Equivalent circuit fitment of G12CP with the equivalent circuit (EC) at the inset; (d) Bode plots of G12CP, GC43P, GCP80, CP, GC and GP with the table of  $f_0$  and  $\tau_0$  values; (e) Bode magnitude plots of G12CP, GC43P, GCP80, CP, GC and GP; (f) Plots of capacitance versus log frequency of G12CP, GC43P, GCP80, CP, GC and GP.

The Nyquist plots of G12CP, GC43P, GCP80, CP, GC and GP are shown in Fig. 3.26a. The impedance spectra possess two semicircles in series one at the high frequency region and the other at the mid-frequency region. These two semicircles indicate the presence of two electrode-electrolyte interfaces produced by faradaic materials and non-faradaic material. The magnified images of the high frequency regions of the Nyquist plot is shown in Fig. 3.26b. The arc 1 at

high frequency is due to the interface produced by Cu<sub>2</sub>O/CuO and PANI with the electrolyte and the following arc 2 is due to the interface between electrolyte and rGO. The diameters of both the arcs decrease from binary composites to ternary composites and they are lowest in the case of G12CP, indicating the amplified charge transfer kinetics and fast redox reaction of PANI and Cu<sub>2</sub>O/CuO (Asen and Shahrokhian 2017a). The increased charge transfer across the electrode/electrolyte interfaces results from the lowering of charge transfer resistance ( $R_{ct}$ ) from binary to ternary composites. To determine the values of various electrical components involved, the impedance data were used for equivalent circuit (EC) fitting using the software Zsimpwin of version 3.21.

The equivalent circuit fitment curve and the EC (Masarapu et al. 2009; Li and Wei 2012) are shown in Fig. 3.26c; which is same as the one explained in section 3.1.2.3. The decrease in slope of the Warburg straight line from binary to G12CP composite indicate the rapid diffusion of the ions from electrolyte on to the electrode surface (Asen and Shahrokhian 2017a). The impedance parameters are summarized in Table 3.9.

**Table 3.9** Equivalent circuit fitment parameters of nanocomposites G12CP, GC43P, GCP80 and binary composites CP, GC and GP.

Composite	$R_s$ ( $\Omega$ )	$R_{ct}$ ( $\Omega$ )	$n_1$	$n_2$	$W$ ( $\Omega$ )
<b>G12CP</b>	0.33	0.21	0.63	0.88	0.26
<b>GC43P</b>	0.29	3.27	0.96	0.40	1.01
<b>GCP80</b>	0.35	11.69	0.77	0.41	8.23
<b>CP</b>	0.37	11.82	0.99	0.73	0.19
<b>GC</b>	0.37	1.53	0.55	0.65	8.37
<b>GP</b>	0.38	0.58	0.76	0.93	0.06

It is seen from Table 3.9 that G12CP exhibits low value of Warburg resistance (0.26  $\Omega$ ), indicating the fast-electrolytic diffusion into the electrode material. The roughness exponents ( $n$ ) of the composite G12CP corresponds to CPE 1 and CPE 2 are 0.63 and 0.88, respectively, showing the moderate capacitive behaviour of the material. The low solution resistance ( $R_s$ ) and low

charge transfer resistance ( $R_{ct}$ ) of G12CP suggest the consistent interfacial contact among the three-components facilitating continues electron transfer and better electrolyte accessibility on and into the electrode material surfaces, enabled by the three-dimensional architecture formed by the integration of the constituent materials. Also, the rGO provides a platform for PANI and oxides of copper, which results in the quick redox reactions helping to achieve high rate capability (Pendashteh et al. 2015; Miao et al. 2016). The knee frequencies of the composites G12CP, GC43P, GCP80, CP, GC and GP are 2683.0 Hz, 372.8Hz, 0.193 Hz, 0.139 Hz, 26.83 Hz, and 193.10 Hz, respectively. The composite G12CP shows the highest knee frequency demonstrating the faster energy storing ability (Miao et al. 2016).

Fig. 3.26d, depicts the phase angle Bode plots of the composites. At high frequency, the impedance is predominantly contributed by resistance and at low frequency it is predominantly contributed by capacitance (Zhang et al. 2006; Miller et al. 2010; Pan et al. 2014). At phase angle of  $-45^\circ$  the transition from resistance to capacitance occurs and at phase angle  $-90^\circ$  the device completely acts as a capacitor. So, the frequency corresponds to impedance phase angle of  $-45^\circ$  is a critical frequency to be considered to make the disparity. The consideration of  $-45^\circ$  is further substantiated by the fact that at  $-45^\circ$  the magnitude of resistance and the reactance of the capacitor are same (Sheng et al. 2012a; Pan et al. 2014). It is seen from the Table shown as the inset in Fig. 3.26d that G12CP has frequency ( $f_0$ ) of 80.20 Hz, which is clearly high in comparison with other composites, showing the enhanced and fast response of the supercapacitor. The relaxation time constant ( $\tau_0$ ) was calculated using Equation 2.9. The value of  $\tau_0$  is 12.4 ms for G12CP, is the least among all the composites, indicating the rapid discharge (Sheng et al. 2012a). The Bode magnitude plot (Fig. 3.26e) shows that the G12CP has an impedance of  $1.279 \Omega$  at low frequency, which is the lowest among all other ternary and binary composites synthesized, signifying in the high conductivity and high electrolytic diffusion in to G12CP (Senthilkumar et al. 2012). The variation of capacitance with the applied frequency is shown in Fig. 3.26f. The capacitance was calculated using Equation 2.10 (Wu et al. 2015b). The increase of capacitance with decrease in

frequency indicates that the higher capacitance is obtained at low frequency rather than at high frequency (Senthilkumar et al. 2012). The G12CP shows the highest capacitance of 1.136 F, which is the highest of all the ternary and binary composites synthesized. The capacitance values are in well agreement with the results obtained from galvanostatic charge/discharge method.

The results of the present work are compared with some of the recent research works on ternary nanocomposites and it is satisfactory to note that the present work is on par with or even better than the some of the reported works, listed in Table 3.10. The present work was carried out using two electrode system whereas the data present in the comparison table are of electrochemical performances of similar systems obtained in both two electrode and three electrode systems. The performances obtained with three electrode systems are four times higher than the actual performances exhibited by super capacitor cells (two electrode system) (Nyström et al. 2015).

**Table 3.10.** Comparison of obtained results of GCP-300 and G12CP with reported similar systems.

Composite	Electrolyte	E (V)	$C_s$ (F g <sup>-1</sup> )	$E$ (W h kg <sup>-1</sup> )	$P$ (W kg <sup>-1</sup> )	Cyclic stability	Ref.
<b>Two electrode systems</b>							
<b>GCP-300</b>	<b>2 M Na<sub>2</sub>SO<sub>4</sub></b>	<b>0.8 V</b>	<b>53.30 at 0.25 A g<sup>-1</sup></b>	<b>4.73</b>	<b>136.44</b>	<b>97.6% up to 5000 cycles</b>	-
CuO/PANI/ rGO hydrogel	1 M Na <sub>2</sub> SO <sub>4</sub>	1.2	634.4 at 1 A g <sup>-1</sup>	126.8 at 1 A g <sup>-1</sup>	114.2 At 1 A g <sup>-1</sup>	97.4% up to 10000 cycles	(Zhu et al. 2016)
rGO/PANI	1 M H <sub>2</sub> SO <sub>4</sub>	0.8	438.8 at 5 mV s <sup>-1</sup>	-	-	76.5% up to 2000 cycles	(Hong et al. 2017)

rGO/PANI	1 M H <sub>2</sub> SO <sub>4</sub> /catechol	1.2	409 at 1 A g <sup>-1</sup>	81.0	7.7	87% up to 5000 cycles	(Mousavi et al. 2017)
<b>G12CP</b>	<b>0.4 M H<sub>2</sub>SO<sub>4</sub></b>	<b>1.2</b>	<b>171.23 at 0.25 A g<sup>-1</sup></b>	<b>34.24</b>	<b>328.75</b>	<b>84% retention up to 5000 cycles at 700 mV s<sup>-1</sup></b>	
<b>Three electrode systems</b>							
rGO/PANI	1 M H <sub>2</sub> SO <sub>4</sub> / catechol	1.2	1967 F g <sup>-1</sup> at 1 A g <sup>-1</sup>	393	9.83	89.7% up to 5000 cycles	(Mousavi et al. 2017)
rGO/CuO	0.5 M K <sub>2</sub> SO <sub>4</sub>	1.2	326 at 0.5 A g <sup>-1</sup>	65.7	302	100% up to 1500	(Purushot haman et al. 2014)
rGO/Cu <sub>2</sub> O/Cu O	6 M KOH	0.8	173.4 at 1 A g <sup>-1</sup>	-	-	98.2% up to 100000 cycles	(Wang et al. 2015a)
CuO/N-rGO	6M KOH	1.4	340 at 0.5 A g <sup>-1</sup>	-	-	80% up to 500 cycles	(Li et al. 2014b)
rGO/CuO	0.1 M Na <sub>2</sub> SO <sub>4</sub>	1.1	227 at 1 A/g	-	-	86% up to 1000 cycles	(Majumda r et al. 2017)
CuO/PANI	1 M Na <sub>2</sub> SO <sub>4</sub>	1.1	185 at 5 mV s <sup>-1</sup>	-	-	72% up to 2000 cycles	(Gholivan d et al. 2015)
CuO/PANI	0.5 M H <sub>2</sub> SO <sub>4</sub>	0.8	286.35 at 20 mV s <sup>-1</sup>	-	-	81.82% up to 500 cycles	(Ates et al. 2015)



	0.1 M						(Sudhakar
rGO/CuO	H <sub>2</sub> SO <sub>4</sub> :H <sub>3</sub> P O <sub>4</sub> (9:1)	0.9	224	14	12	-	et al. 2017)
CuO/carbon nano fibers	3 M KOH	0.4	398.0 at 1 A g <sup>-1</sup>	3.4	10000	92% up to 2000 cycles at 2 A g <sup>-1</sup>	(Moosavif ard et al. 2014)
CuO/ rGO	1 M Na <sub>2</sub> SO <sub>4</sub>	1.0	80.0 at 10 mV s <sup>-1</sup>	-	-	-	(Bu and Huang 2017)
rGO/Cu <sub>2</sub> O/Cu	1 M KOH	1.0	98.5 at 1 A g <sup>-1</sup>	-	-	-	(Dong et al. 2014)
rGO/PANI	1 M H <sub>2</sub> SO <sub>4</sub>	1.1	250.0 at 10 mV s <sup>-1</sup>	-	-	-	(Kumar et al. 2012)
Cu <sub>2</sub> O/ rGO	1 M Na <sub>2</sub> SO <sub>4</sub>	1.6	195.0 at 2 A g <sup>-1</sup>	-	-	92% up to 1000 cycles at 6 A g <sup>-1</sup>	(Park and Han 2014)
PANI/f-rGO	2 M H <sub>2</sub> SO <sub>4</sub>	0.8	590.0 at 0.1 A g <sup>-1</sup>	-	-	91% up to 1000 cycles at 2 A g <sup>-1</sup>	(Wang et al. 2013)
PANI/rGO	-	1.0	367 at 0.3 A g <sup>-1</sup>	-	-	82% up to 1000 cycles	(Zhang and Zhao 2012)
PANI/rGO	1 M H <sub>2</sub> SO <sub>4</sub>	1.2	329.5 at 5 mA s <sup>-1</sup>	-	-	-	(Gao et al. 2012)

### 3.3. REDUCED GRAPHENE OXIDE, VANADIUM PENTOXIDE AND POLYANILINE TERNARY NANOCOMPOSITES

The vanadium pentoxide ( $V_2O_5$ ) is a semiconductor, facile to synthesis, low cost, and a layer structured faradaic metal oxide, which is capable of exhibiting multiple oxidation states of +2, +4, +5 and +6 during electrochemical redox reactions. These multiple oxidation states make  $V_2O_5$  unique in its redox capacitive behavior by storing more than one electron per unit formula and it possess a theoretic capacitance of  $\sim 400 \text{ mA h g}^{-1}$ . The layered structure of  $V_2O_5$  allows electrolytic ions to intercalate in between the layers and thereby enhances the electrolyte diffusion. Along with these merits  $V_2O_5$  possesses its own limitations. The bulk orthorhombic form of  $V_2O_5$  is less capacitive in nature, stores one electron per unit formula, exhibits low electrical conductivity of  $10^{-2} - 10^{-3} \text{ S cm}^{-1}$ , and hence needs to be embedded with a good conducting material. Also, it has limitations of slower electrolytic diffusion, and its possible dissolution in the presence of acid electrolytes. All these limitations fetch poor capacitance and lower cyclic stability (Perera et al. 2013; Augustyn et al. 2014). The theoretical specific capacitance of  $V_2O_5$  for a potential window of 1 V is  $\sim 2120 \text{ F g}^{-1}$  (Zhi et al. 2013). These limitations are expected to be overcome when  $V_2O_5$  is integrated with other classes of capacitive materials like carbonaceous material and conducting polymers. The ternary nanocomposite, containing rGO/ $V_2O_5$ /PANI (GVP) is expected to yield a better electrochemical performance. Therefore, a series of GVP nanocomposites were synthesized by varying the weight percentages of each of the constituents by following the synthetic route described in section 2.2.4. The structural and electrochemical characterizations are presented in the following sections.

#### 3.3.1. Structural characterizations

##### 3.3.1.1. X-ray diffraction studies

The X-ray diffraction pattern of GVP are depicted in Fig.3.26a. The GVP exhibits a broad peak at  $24.9^\circ$  indicating the formation of rGO (Wang et al. 2016a). The broad nature of the peak signifies the loose packing of rGO layers which is brought about by the intercalation of PANI in between the honeycomb lattices. The presence of PANI in GVP is confirmed by the peaks at  $19.41^\circ$  (110),  $23.07^\circ$  (200),  $25.66^\circ$  (003),  $28.77^\circ$

(202),  $31.67^\circ$  (031),  $38.79^\circ$  (213) and  $46.80^\circ$  (115) (JCPDS file No. -53-1717, 53-1891).

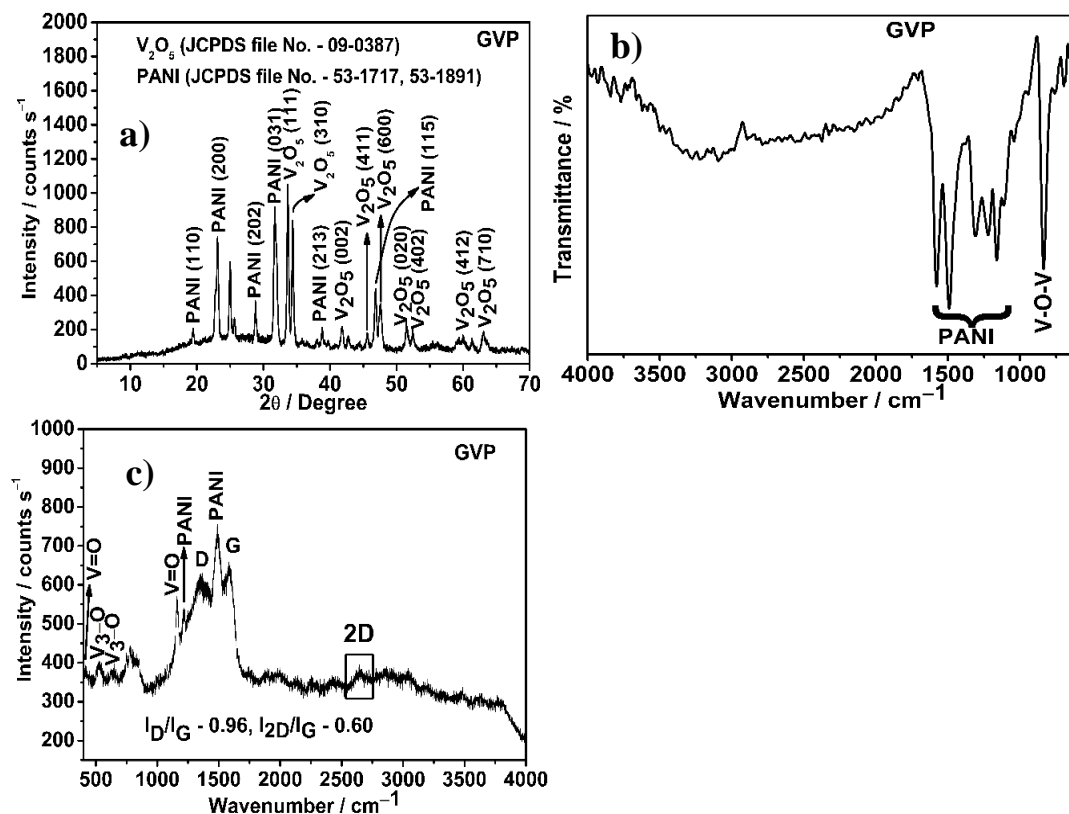


**Fig. 3.27** (a) X-ray diffraction pattern of GVP (b) FT-IR spectrum of GVP (c) Raman spectrum of GVP.

The presence of  $V_2O_5$  in GVP is confirmed by the peaks at  $33.62^\circ$  (111),  $34.37^\circ$  (310),  $41.80^\circ$  (002),  $45.80^\circ$  (411),  $47.51^\circ$  (600),  $51.36^\circ$  (020),  $52.36^\circ$  (402),  $59.26^\circ$  (412) and  $62.96^\circ$  (710) (JCPDS file No.- 09-0387). The crystalline size of PANI and  $V_2O_5$ , calculated from the most intense peaks of PANI and  $V_2O_5$  are 17.23 nm and 31.60 nm, respectively, which are proving the nano dimensions to the GVP composite.

### 3.3.1.2. FT-IR spectrum

Fig.3.27b shows the FT-IR spectrum of GVP. The peak at  $699\text{ cm}^{-1}$  is the stretching vibrations of doubly bonded oxygen (V=O), (Choudhury et al. 2015) peaks at  $621.62\text{ cm}^{-1}$  (Zhang et al. 2016b) and  $836.63\text{ cm}^{-1}$  (Asen and Shahrokhian 2017b) are pertaining to the symmetric and asymmetric vibrations of V-O-V bond. The peaks at  $1580.87\text{ cm}^{-1}$  and  $1498.18\text{ cm}^{-1}$  are assigned to C=C stretching vibrations of quinoid

and benzenoid ring (Pan et al. 2016). Peaks at  $1313.71\text{ cm}^{-1}$  and  $1222.11\text{ cm}^{-1}$  correspond to the stretching vibrations of C–N (Pan et al. 2016) and C=N (Jin and Jia 2015) bonds. The peaks at  $1163\text{ cm}^{-1}$  and  $1045\text{ cm}^{-1}$  are pertaining to the bending vibrations of C–H bond. (Hu et al. 2009; Feng et al. 2015; Pan et al. 2016)

### 3.3.1.3. Raman spectrum

The Raman spectrum of GVP is shown in Fig. 3.27c. The  $I_D/I_G$  ratio of GVP (0.96) is higher than that of graphene oxide (GO) (0.95), due to the reduction of GO to rGO and increase of defects in GVP. The  $I_{2D}/I_G$  ratio of GVP is 0.6, signifying the presence of few layers of rGO in GVP. The presence of PANI is confirmed by the peaks at  $751.26\text{ cm}^{-1}$ ,  $783.11\text{ cm}^{-1}$ ,  $1217.80\text{ cm}^{-1}$ , and  $1488.46\text{ cm}^{-1}$ , which are pertaining to the bending of quinoid ring, deformation of quinoid ring, (Trchová et al. 2014) C–N stretching vibrations of polaronic segments and C=N stretching vibrational modes of quinoid ring (Jin and Jia 2015), respectively. The peaks at  $413.54\text{ cm}^{-1}$ ,  $525.64\text{ cm}^{-1}$ ,  $630.21\text{ cm}^{-1}$  and  $1159.87\text{ cm}^{-1}$  are corresponding to V=O bending vibrations, V(III)–O stretching vibrations, V(III)–O bending vibrations (Foo et al. 2014) and  $V^{+5}=O$  stretching vibrations (Lee et al. 2003), respectively.

### 3.3.1.4. FE-SEM analyses

The FE-SEM images of GVP are presented in Fig. 3.28a, Fig. 3.28b, Fig.3.28c, Fig.3.28d, Fig.3.28e and Fig. 3.28f. It is seen from the images that all the three constituents are uniformly integrated and the  $V_2O_5$  is present as nanoparticles and dispersed on PANI nanofibrils and rGO sheets. The FE-SEM images with the labels of rGO layers, PANI nanofibers and the nanochannels are clearly shown in Fig. 3.28d, Fig. 3.28e and Fig. 3.28f. As it is seen from Fig. 3.28e and Fig. 3.28f, the diameters of  $V_2O_5$  nanoparticles coated PANI nanofibers are in the range of  $\sim 20\text{ nm}$  to  $\sim 35\text{ nm}$ ; and the diameters of the nanochannels are in the range of  $\sim 39\text{ nm}$  to  $\sim 111\text{ nm}$ , which facilitate the diffusion of electrolyte into the interior parts of the GVP electrode materials.

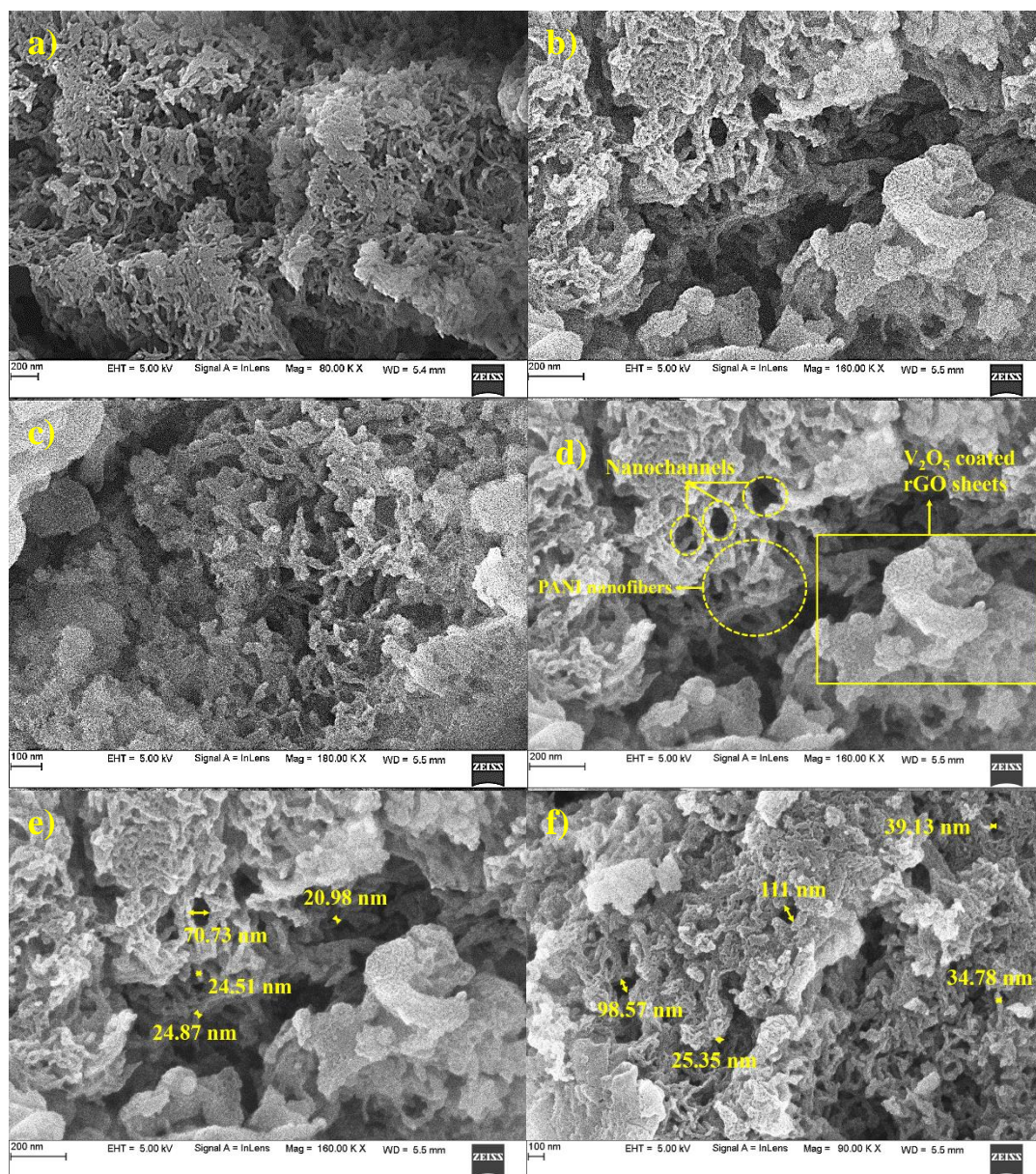


**Fig. 3.28** (a-c) FE-SEM images of GVP nanocomposites; and (e-f) with distinct labels of PANI, rGO,  $V_2O_5$  nanoparticles, nanochannels and their marked dimensions.

### 3.3.1.5. XPS analysis

The survey spectrum of GVP is shown in Fig. 3.29a. The presence of peaks pertaining to C, N, O and V confirm their presence in the composite. Fig. 3.29b shows the core level spectra of C 1s. The C 1s peak deconvolutes into four peaks at 284.77 eV, 285.07 eV, 286.95 eV and 289.34 eV. These peaks are corresponding to C=C bond present in rGO, C-N bond present in PANI, (Xia et al. 2012b) C-O and C=O bonds of



oxygen containing functional groups that are left unreduced on the surface of rGO, (Lin et al. 2016) respectively. The deconvoluted N 1s spectra are depicted in Fig. 3.29c. The N 1s peak is resolved into three peaks at 398.10 eV, 399.72 eV and 401.86 eV corresponding to =N– imine bond present in quinoid ring, –NH– amine bond present benzenoid ring and N<sup>+</sup> radical present in PANI salt, (Xia et al. 2012b) respectively.

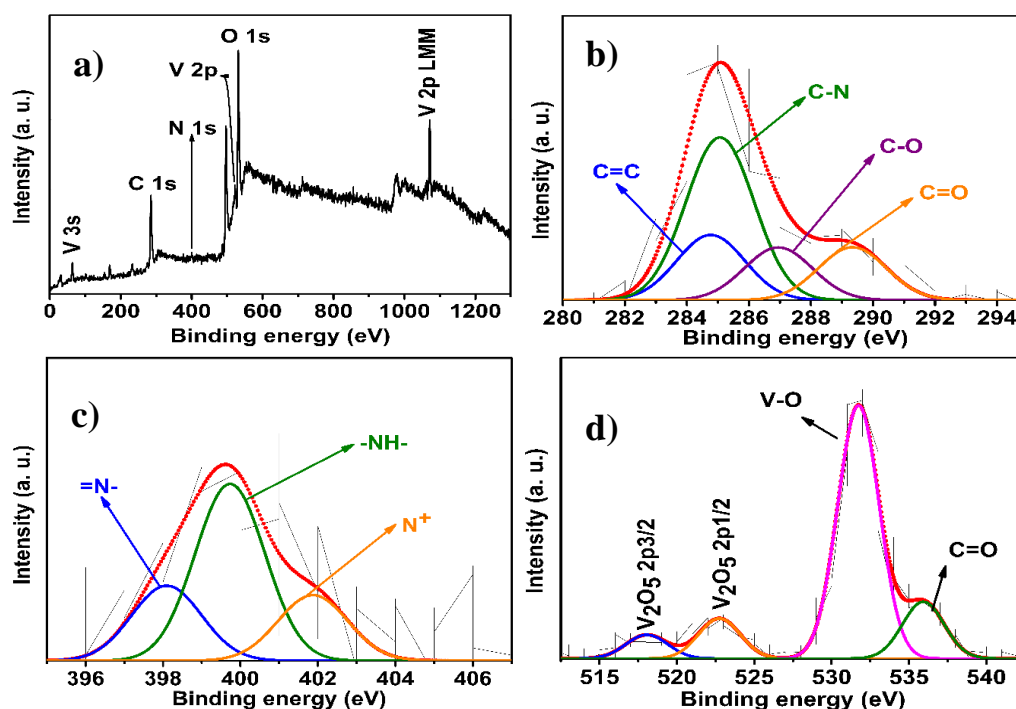


**Fig. 3.29** (a) The XPS survey spectrum of GVP, core level spectra of (b) C 1s (c) N 1s (d) O 1s and V 2p.

The core level spectra of O 1s and V 2p are shown in Fig. 3.29d. Peaks at 531.74 eV and 535.93 eV are corresponding to V–O bond present in V<sub>2</sub>O<sub>5</sub> and C=O bond of unreduced carboxylic group present on the surface of rGO, respectively. Peaks at 518.06 eV and 522.75 eV are corresponding to V<sub>2</sub>O<sub>5</sub> 2p<sub>3/2</sub> and V<sub>2</sub>O<sub>5</sub> 2p<sub>1/2</sub>, respectively. These peaks further confirm the +5 oxidation state of vanadium present (Choudhury et al. 2016; Wang et al. 2017; Zheng et al. 2017). The Auger L3M23V peak of V<sub>2</sub>O<sub>5</sub> is observed at a binding energy of 1072.62 eV (kinetic energy of 410.08 eV), (Kasperkiewicz et al. 1983) confirming the presence of V<sub>2</sub>O<sub>5</sub> in GVP nanocomposite.

### 3.3.2. Electrochemical characterizations

Three series of GVP composites were synthesized by varying the weight ratios of each of the constituents to optimize a weight ratio with higher electrochemical performance. Later the weight ratios were converted into weight percentages. A composite with a weight percentage of constituents, rGO5.88%: V11.76%: P82.36% (GVP82) exhibited the maximum electrochemical performance with a specific capacitance ( $C_s$ ) of  $1092 \text{ F g}^{-1}$  at a current density of  $1 \text{ A g}^{-1}$ . The entire processes are discussed in successive sections. The weight ratios and corresponding weight percentages of constituents and the nomenclatures of composites are summarized in Table. 3.11.

**Table 3.11.** The weight percentages of GVP composites and their nomenclature.

Component under study	Weight of constituents (mg)			Weight percentage (%)	Composite
	P	V	G		
PANI series	100	50	25	57.10	GVP57
	150	50	25	66.66	GVP67
	200	50	25	72.72	GVP73
	250	50	25	76.90	GVP78
	300	50	25	80.00	GVP80
	350	50	25	82.35	GVP82
	400	50	25	84.21	GVP84
	450	50	25	85.71	GVP86
$\text{V}_2\text{O}_5$ series	350	100	25	21.06	GV21P
	350	150	25	28.57	GV29P
	350	200	25	34.78	GV35P
	350	250	25	40.00	GV40P
	350	300	25	44.44	GV44P
	350	350	25	48.27	GV48P
rGO series	350	50	50	11.11	G11VP
	350	50	75	15.79	G16VP
	350	50	100	20.00	G20VP

## 3.3.2.1. CV studies

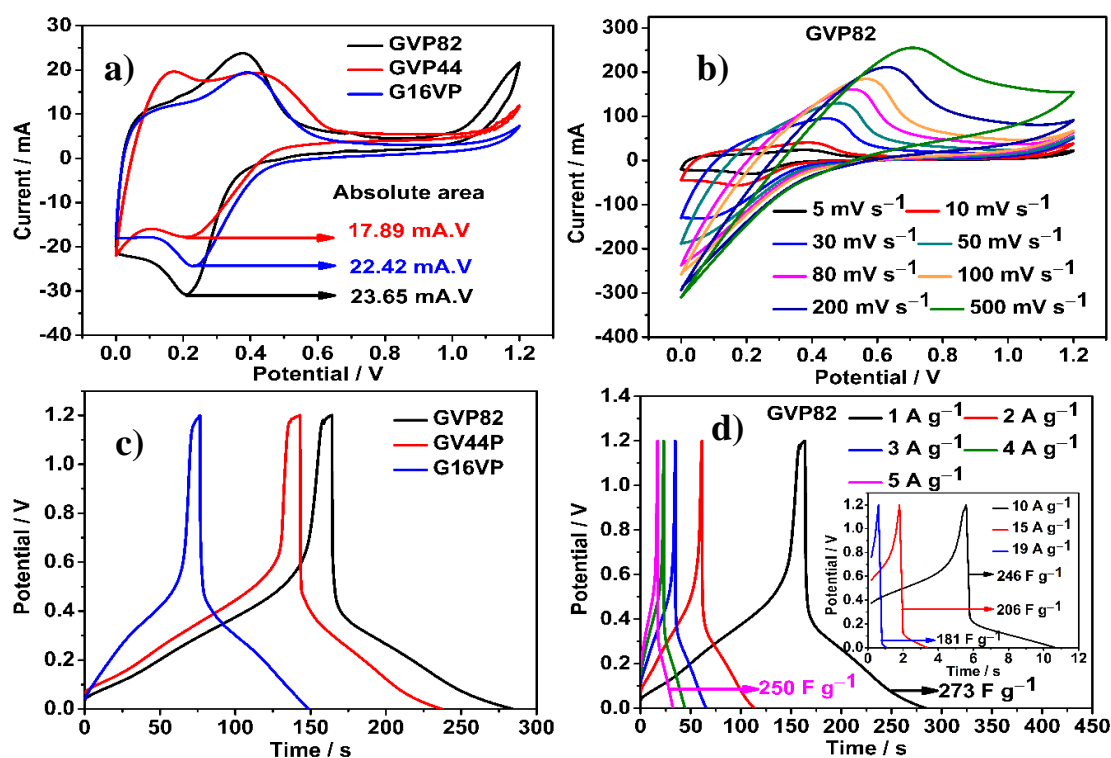


**Fig. 3.30** (a) CV curves of composites GVP82, GV44P and G16VP at a scan rate of  $5 \text{ mV s}^{-1}$  (b) CV curves of GVP82 at different scan rates (c) CD curves of composites GVP82, GV44P and G16VP at a current density of  $1 \text{ A g}^{-1}$  (d) CD curves of composite GVP82 at different current densities.

The CV curves of GVP composites are depicted in Fig.3.30a and Fig. 3.30b. The curves are not rectangular in shape but are with redox peaks indicating capacitive property of GVP and the combined role of faradaic and non-faradaic process of energy storage (Han et al. 2014). The CV curves of composites GVP82, GV44P and G16VP at a scan rate of  $5 \text{ mV s}^{-1}$  are depicted in Fig. 3.30a, these three composites are considered for comparison due to their high performance from each of their series synthesized. The area under the redox peaks is proportional to the quantity of charge stored by the electrode material. The maximum area is exhibited by GVP82 signifying its high charge storing ability as compared to those of other composites (Han et al. 2014). The redox peaks are the manifestation of redox transformation of PANI and  $\text{V}_2\text{O}_5$ . The CV curves of the composite GVP82 at different scan rates are shown in Fig. 3.30b. The GVP82 exhibits the capacitive behavior even up to high scan rate of 500



$\text{mV s}^{-1}$ , signifying its high rate capability. The shift of redox peaks on increasing the scan rate is attributed to the presence of polarity in the system (Maitra et al. 2017) caused by presence of polarons and bipolarons of PANI (Hu and Lin 2002; Wu et al. 2012).

### 3.3.2.2. GCD studies

The CD curves of GVP composites are shown in Fig. 3.30c and Fig. 3.30d. The curves are not triangular but are quasi triangular indicating the presence of pseudo capacitance in combination with electrical double layer capacitance. (Wu et al. 2015a) The composite GVP82 takes longer discharge time than GV44P and G16VP indicating its superior energy storage capacity (Han et al. 2014) than other composites (Fig. 3.30c). On varying the weight percentage of PANI by keeping the weight percentage of  $\text{V}_2\text{O}_5$  and rGO constants, increase in  $C_s$  was observed up to 82%, and beyond which the  $C_s$  decreases. The increase in  $C_s$  is attributed to the increase of redox reaction with the increase in PANI content. The decrease in  $C_s$  above 82% of PANI is due to the formation of aggregates of PANI, randomly, limiting the access of electrolyte into the entire electrode material. (Xu et al. 2010) In the subsequent series the weight percentages of PANI and rGO were kept constants and the weight percentage of  $\text{V}_2\text{O}_5$  was increased. The variation does not lead to an increase in the value of  $C_s$ , rather a decrease in  $C_s$  is observed. This is due to the increase in the weight percentage of  $\text{V}_2\text{O}_5$  nanoparticles producing a carpet effect, causing limited surface to interact with the electrolyte, which is an extrinsic capacitive behavior of  $\text{V}_2\text{O}_5$  (Augustyn et al. 2014). The similar decrease in  $C_s$  is observed on increasing the weight percentage of rGO beyond 6%, which corresponds to GVP80. This is due to the formation of  $\text{V}_2\text{O}_5$  nanoparticles on rGO and PANI, acting as a carpet and blocking the nano channels, thereby reducing the active surface area, redox sites and access of electrolyte into the interior of the electrode material (considering the synthetic route adopted). The obtained electrochemical parameters at a current density of  $1 \text{ A g}^{-1}$  are tabulated in Table. 3.12

The ESR values of GVP82, GV44P and G16VP are  $0.298 \Omega$ ,  $0.340 \Omega$  and  $0.275 \Omega$ , respectively; and the corresponding IR drops are  $0.597 \text{ V}$ ,  $0.680 \text{ V}$  and  $0.554 \text{ V}$ ,

respectively. The low ESR of GVP82 is indicating its low intrinsic resistance and low loss (IR drop) of potential during energy storage.

**Table 3.12.** The electrochemical parameters GVP composites.

Composite	$C_s$ (F g <sup>-1</sup> )	$E$ (W h kg <sup>-1</sup> )	$P$ (kW kg <sup>-1</sup> )	$\eta$ (%)
GVP57	87.03	17.4	1.91	95.34
GVP67	106.49	21.39	1.91	93.45
GVP73	154.80	30.95	1.92	84.79
GVP77	156.98	31.39	1.77	91.64
GVP80	144.50	28.90	1.71	88.88
GVP82	273.22	54.64	1.63	73.20
GVP84	135.50	27.10	1.82	86.40
GVP86	191.20	38.24	1.29	81.19
GV21P	143.47	28.69	1.71	82.92
GV28P	200.40	40.08	1.80	86.76
GV35P	101.62	20.32	1.87	91.98
GV40P	206.18	41.23	1.66	88.29
GV44P	206.61	41.32	1.57	65.87
GV48P	148.80	29.76	1.68	91.64
G11VP	120.91	24.18	1.70	95.86
G16VP	160.25	32.05	1.59	94.25
G20VP	147.49	29.49	1.70	94.24

The time constant ( $\tau$ ) is an imperative parameter of supercapacitors that gives the information of responsiveness and energy stored. The higher value of time constant ( $\tau$ ) signifies the higher accessible amount of energy stored (Yassine et al. 2017). Time constants of composites GVP82, GV44P and G16VP are 1.58 s, 1.05 s and 0.93 s,

respectively. The higher time constant ( $\tau$ ) of GVP82 signifies the higher accessible energy stored in it than those of GV44P and G16VP. The CD curves of GVP82 at different current densities are shown in Fig. 3.30d. The specific capacitance values ( $C_s$  in  $F g^{-1}$ ) of GVP composites are listed in Table. 3.12.

It is observed from Fig. 3.30d that GVP82 exhibits a  $C_s$  of  $273.22 F g^{-1}$  at a low current density of  $1 A g^{-1}$ . Even at a current density of  $19 A g^{-1}$  it exhibits the  $C_s$  of  $180.95 F g^{-1}$ , which is only 33.72% less than that exhibited at  $1 A g^{-1}$ . This fact signifies its remarkable rate capability, which is ascribed to the adequate diffusion of electrolytic ions ( $H^+$  and  $SO_4^{2-}$ ) even at high current densities as it is at low current densities (Pendashteh et al. 2015). The specific capacity ( $Q$  in  $C g^{-1}$ ) of GVP82 is  $328.5 C g^{-1}$ . The plots of specific capacitance versus current densities are shown Fig. 3.31a, which pictorially illustrate the high rate capability of GVP82. The energy density ( $E$  in  $W h kg^{-1}$ ) and power density ( $P$  in  $W kg^{-1}$ ) values of GVP composites are given in Table 3.12.

The Ragone plots of GVP composites are presented in Fig. 3.31b. The composite, GVP82 exhibits a high  $E$  of  $54.64 W h kg^{-1}$  and a  $P$  of  $1.63 kW kg^{-1}$  at  $1 A g^{-1}$  and maintains to exhibit a high  $E$  of  $36.19 W h kg^{-1}$  and a  $P$  of  $217.14 kW kg^{-1}$  at a high current density of  $19 A g^{-1}$ . Such an excellent  $E$  and  $P$  originate from the process of  $\pi$ - $\pi$  contact of rGO and PANI, and the dispersion of  $V_2O_5$  nanoparticles on them providing an intimate close contact of each constituents and reducing the path length for the ions and increasing the diffusion rates of electrolytic ions (Shen et al. 2013). The  $V_2O_5$  contributes to the high  $E$  by its faradaic reaction, which is considered to be 10 -100 times more than that of  $E$  exhibited by electrical double layer capacitance (EDLC) materials. The comparison of energy density and power densities of GVP82 with those of Li-ion batteries are depicted in Fig. 3.31c. The energy densities of GVP82 are lower than the energy densities of Li-ion batteries reported in the literature (Dunn et al. 2011), but higher than the energy densities of EDL supercapacitors ( $\sim 10 W h kg^{-1}$ ). The columbic efficiency ( $\eta$ ) of GVP composites were calculated using Equation 2.8 and listed in Table. 3.12. The high value of  $\eta$  at high current densities of GVP82 indicates the similar times taken for charging and discharging.

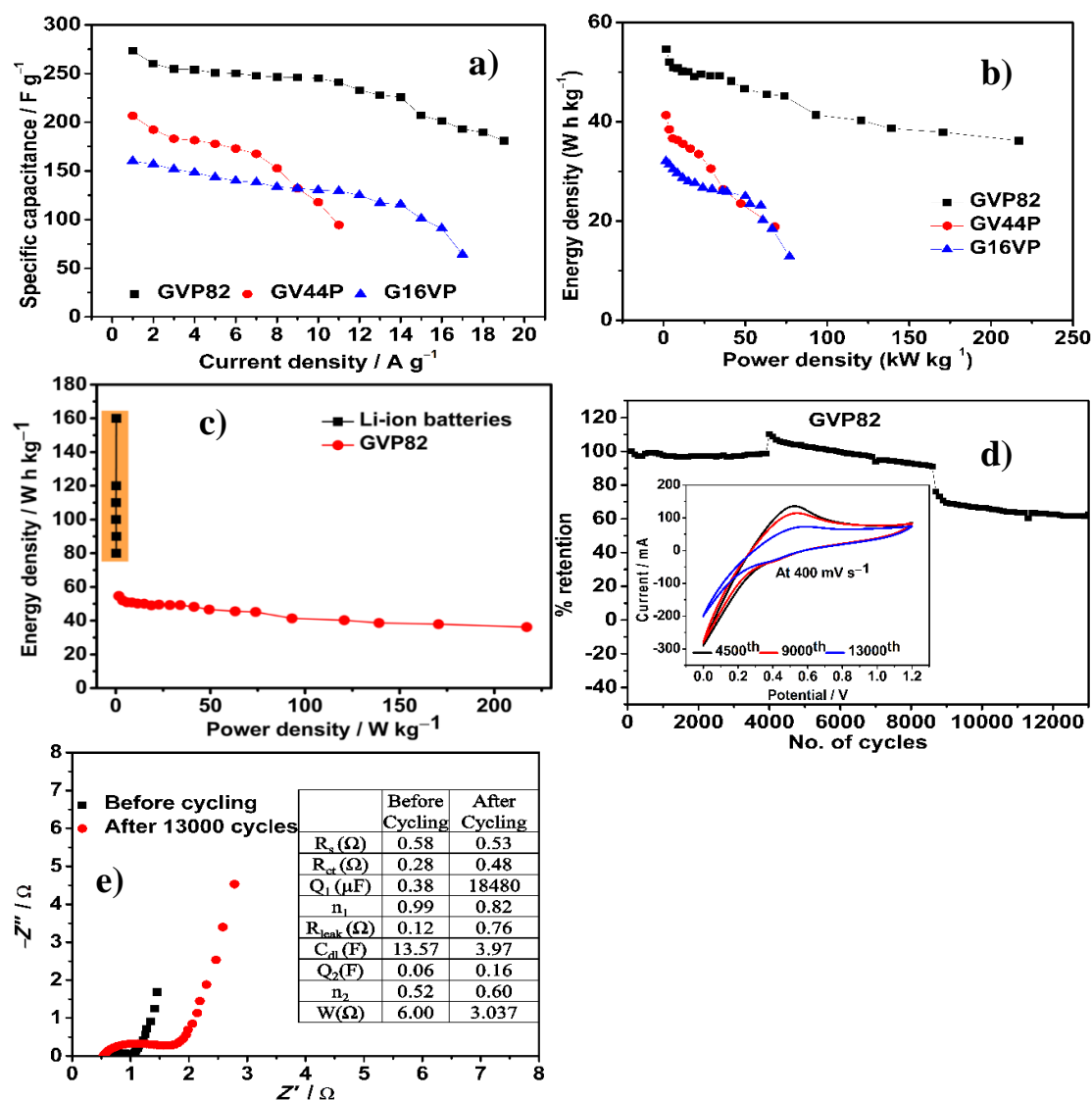


**Fig. 3.31** (a) Plots of specific capacitance versus current density (b) Ragone of plots composites GVP82, GV44P and G16VP (c) Comparison of energy densities of GVP82 with Li-ion batteries (d) Plots of percentage retention of specific capacitance versus number of cycles of composite GVP82 (CV curves obtained after 4500, 9000 and 1300 cycles at  $400 \text{ mV s}^{-1}$  at the inset) (e) Nyquist plots of GVP82 before and after 13000 cycles.

The cyclic stability study on GVP82 was carried out using CV technique at a scan rate of  $400 \text{ mV s}^{-1}$  (Fig.3.31d). The GVP82 exhibits a small increase in its performance after 4000 cycles, which is attributed to the opening of redox nano channels due to the continuous diffusion of electrolyte into the electrode material

(Pendashteh et al. 2015). Beyond 4000 cycles, the performance decreases steadily and at the end of the 13000 cycles GVP82 retains 61% of its initial capacitance, thereby exhibiting a good cycling stability. The Nyquist plots obtained pre and post cyclic stability studies are presented in Fig. 3.31e with the values of electrical parameters deduced by fitting the Nyquist plots for an equivalent circuit, at the inset. The slight increase in the capacitance after 4000 cycles is due to the decrease in Warburg diffusion resistance from  $6.00 \Omega$  to  $3.03 \Omega$ . The decrease in specific capacitance is due to the following changes that occurred in the system. The increases in the charge transfer resistance from  $0.28 \Omega$  to  $0.48 \Omega$  and leakage resistance from  $0.12 \Omega$  to  $0.76 \Omega$  cause the increase in the intrinsic resistance of the device. The decrease in roughness exponent  $n_1$  from 0.99 to 0.82 indicates the increase in the surface roughness of the electrode. Also, there is a decrease in the electrical double layer capacitance ( $C_{dl}$ ) from 13.57 F to 3.97 F. These factors rationalize the 61 % retention of  $C_s$  at the end of 13000 cycles.

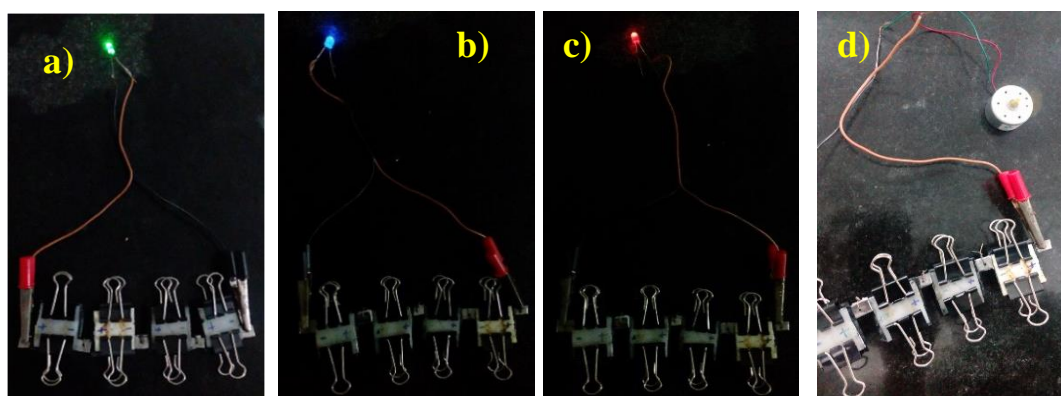


**Fig. 3.32** (a-d) GVP82 super capacitor device energizing green, blue, red color LEDs and a DC motor.

The realistic application of GVP82 was explored by connecting four devices in series. The devices could successfully energize LED of green, blue and red colors and a DC motor (Fig. 3.32a-d). To demonstrate the energy density of the device, it was charged using a Nippo 9 V battery for 2 min with a red color LED connected with it, and on cutting short the power from battery, the LED continued to glow for the next 40 s taking energy from the device. The same demonstration was carried out with a DC motor, in which the device was charged for 1 min and on disconnecting the power from

the battery, the motor continued to run for another 1 min. These observations confirm the high energy density of GVP82.

### 3.3.2.2.1. Application of GVP82 in DC-DC switch capacitor convertor (SCC)

DC-DC switch capacitor converters are used mainly for potential step-up and step-down purposes and is an inevitable component in voltage regulators, battery chargers, power management signal processors and in very large scale integrated (VLSI) circuits. The important function of SCC is to give different output potentials for a single input potential. In these capacitors, a series of capacitors acts as energy storing elements and deliver the energy required for step-up and step-down processes (Subburaj et al. 2016). In such a DC-DC SCC, GCP82 supercapacitor was included as one of the capacitors and checked for its practical application. The DC-DC SCC circuit is shown in Fig.3.33.

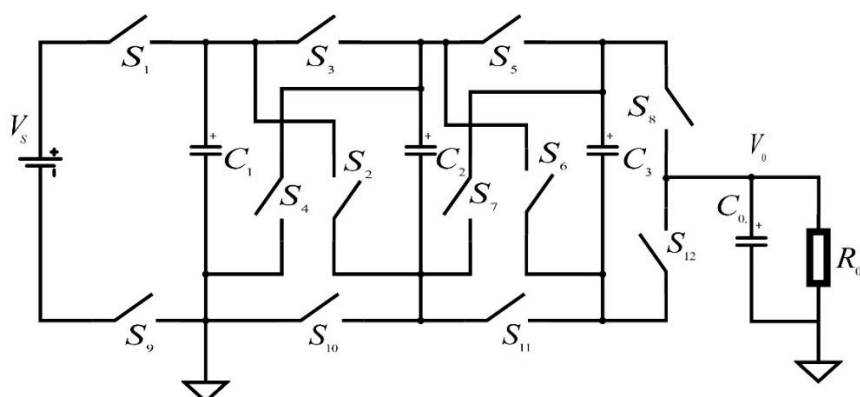


**Fig. 3.33** The circuit of DC-DC SCC.

In the circuit, the capacitors  $C_1$ ,  $C_2$ ,  $C_3$  and  $C_0$  are primarily made up of electrolytic capacitors. The capacitors  $C_1$ ,  $C_2$  and  $C_3$  act as flying capacitors to store the energy on simultaneous switch on and switch off mechanism that is programmed in the circuit. The capacitor  $C_0$  is the filter capacitor that gives the output potential. The Fibonacci series serves as the base for the various fractions with which each of the capacitors are charged and discharged (Subburaj et al. 2016).

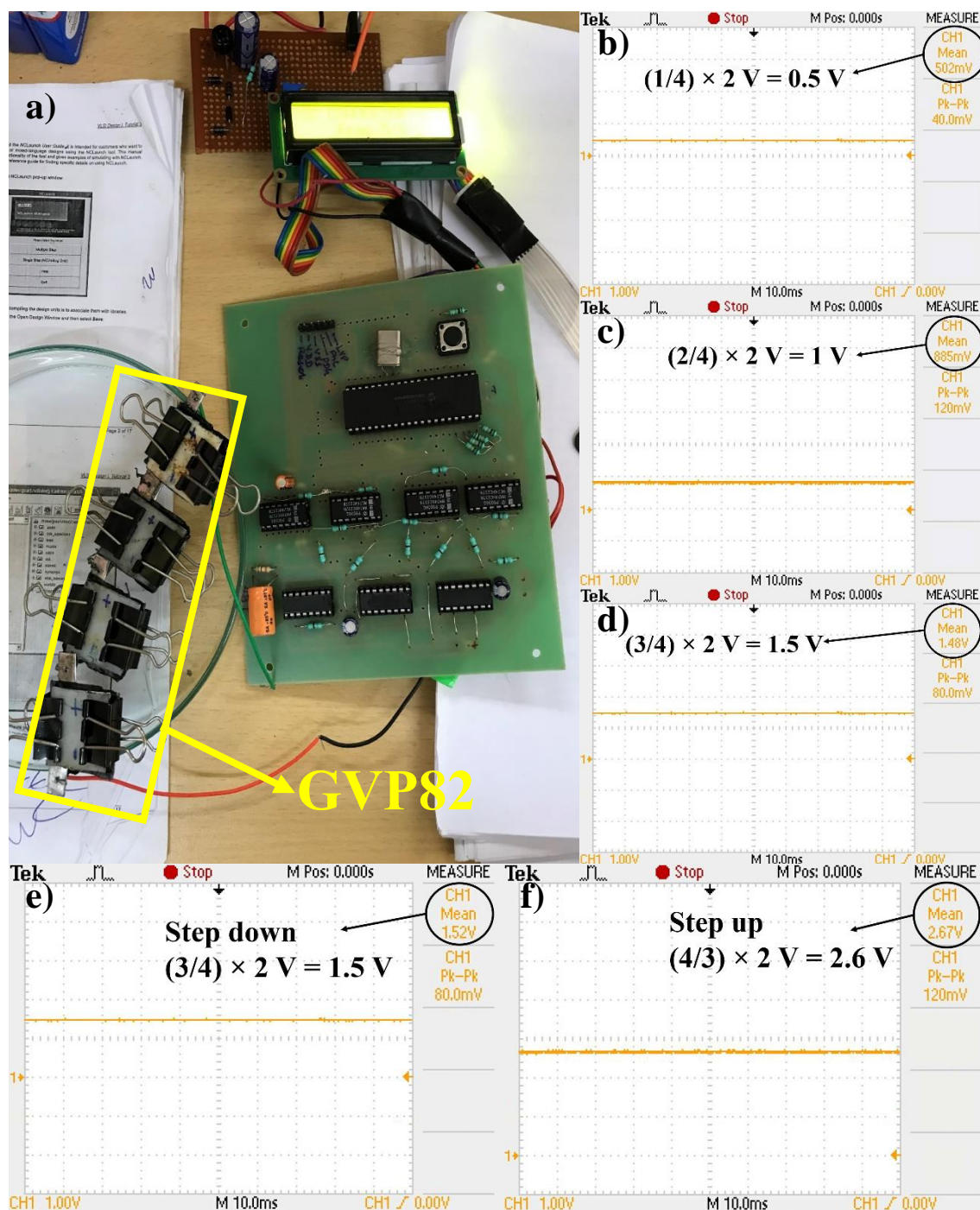


**Fig. 3.34** (a) The real time DC-DC SCC with GVP82 incorporated in the circuit (b – f) The digital oscilloscope reading of GVP82 on applying 2 V.

The fractions across  $C_1$ ,  $C_2$ , and  $C_3$  are  $1/4$ ,  $2/4$  and  $3/4$ . The fractions that were used for stepdown and stepup across  $C_0$  are  $3/4$  and  $4/3$ , respectively. The applied input potential across all the capacitors is 2V. Therefore, on applying 2 V to  $C_1$ ,  $C_2$  and  $C_3$ ,

the output potential supposed to be produced across them are 0.5 V, 1 V and 1.5 V, respectively (output potential = fraction  $\times$  input potential). The output potential supposed to be generated across  $C_0$  for stepdown (3/4) and stepup (4/3) are 1.5 V and 2.6 V, respectively. Each of these capacitors namely,  $C_1$ ,  $C_2$ ,  $C_3$  and  $C_0$  are individually replaced with GVP82 device one after the other and their potential step down and step up applications were experimented.

It was made sure that at a time only one of these four electrolyte capacitors is replaced with GVP82 supercapacitor and the other three capacitors are left to be electrolytic capacitors. The potential produced by the GVP82 for different fractions were measured using digital oscilloscope (Brand – Digiliet). On applying a potential of 2 V, GVP82 produced output potentials of 0.5 V, 0.85 and 1.43 V across  $C_1$ ,  $C_2$  and  $C_3$ , respectively. The loss of potential of 0.15 V in  $C_2$  is due to the possible loss of potential in the circuit. The potential produced across  $C_0$  during stepdown and step up are 1.53 V and 2.66 V, respectively. The obtained potentials match well with the theoretical values demonstrating the successful practical application of the device fabricated with GVP82. The Fig. 3.34a depicts the real time DC-DC SCC, with GVP82 incorporated in the circuit. Fig. 3.34b, 3.34c, 3.34d, 3.34e and 3.34f show the digital oscilloscope readings of GVP82 on applying a potential of 2 V.

### 3.3.2.3. EIS studies

The Nyquist plots of the composites GVP82, GV44P and G16VP are shown Fig. 3.35a. The Nyquist plots possess a semicircle at high frequency region and a linear Warburg diffusion portion at low frequency region indicating the capacitive nature of the GVP composites. It is seen from Fig. 3.35a, that GVP82 possesses least resistance among the three composites as evidenced from the diameters of the capacitive loops. The Nyquist plot of GVP82 is fitted with an equivalent circuit (mean error <1.23%) to obtain the magnitudes of the electrical elements involved in the system (Fig. 3.35b). The electrical elements involved in the equivalent circuit is described in section 3.1.23. the obtained resistance values are  $R_s = 0.58 \Omega$ ,  $R_{ct} = 0.28 \Omega$ ,  $R_{leak} = 0.12 \Omega$ ,  $W = 6.00 \Omega$ ,  $C_{dl} = 13.57 \text{ F}$ ,  $Q_1 = 0.38 \mu\text{F}$ ,  $Q_2 = 0.06 \text{ F}$ ,  $n_1 = 0.99$  and  $n_2 = 0.52$ .



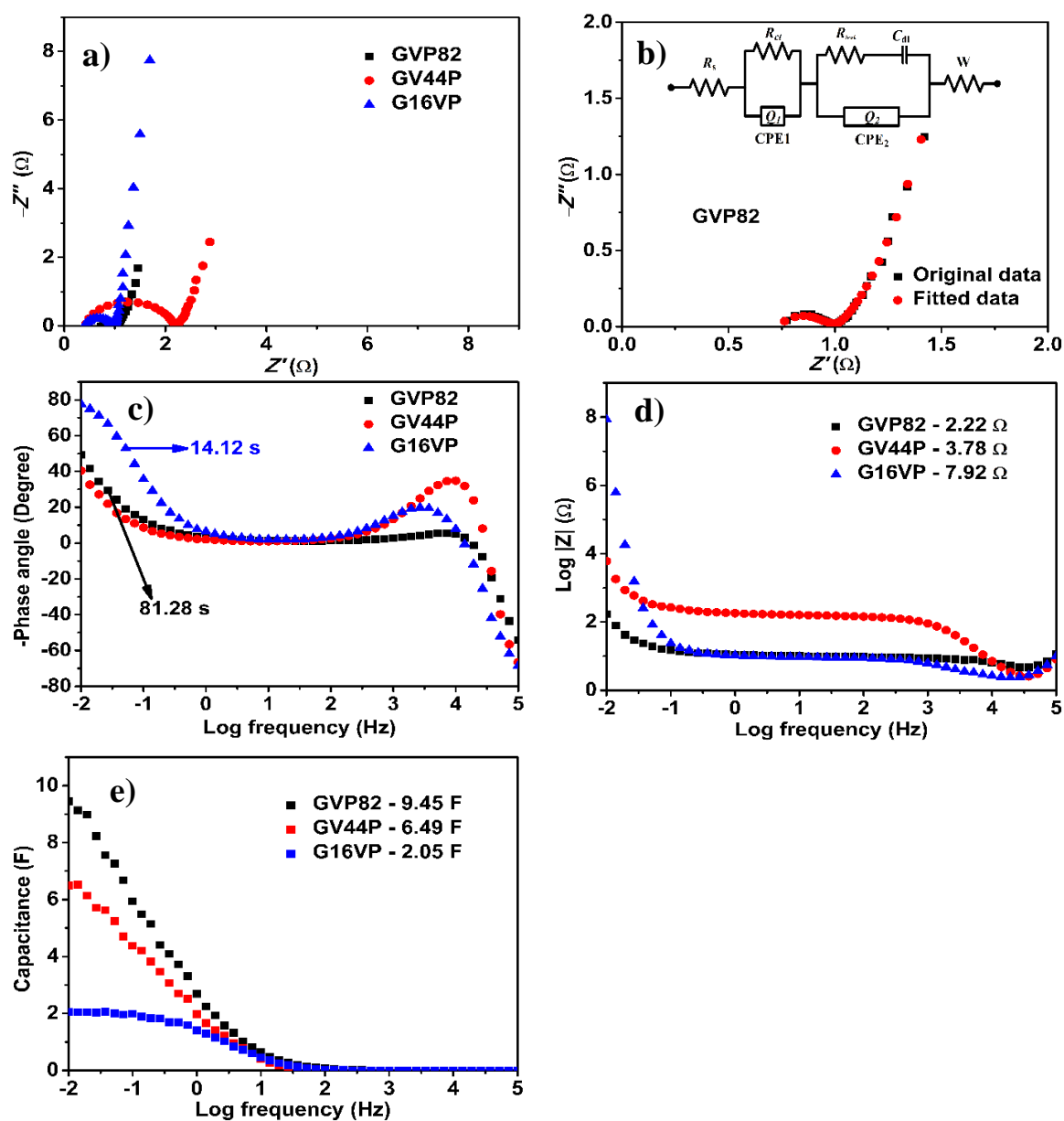


**Fig. 3.35** (a) Nyquist plots of composites GVP82, GV44P and G16VP (b) Equivalent circuit fitment for the Nyquist plot of GVP82 (c) Bode phase angle plots (d) Bode magnitude plots (e) Plots of capacitance versus log frequency of composites GVP82, GV44P and G16VP.

The use of constant phase element ( $Q_1$  and  $Q_2$ ) in place of the ideal capacitors  $C_1$  and  $C_2$  is substantiated by the relation given Equation 3.1 and the description is given in section 3.1.2.3. The knee frequency is the frequency below which the complete capacitive behavior of a device is obtained. (Zhang et al. 2010) The high knee frequency

offers a high energy to access (Li and Wei 2012). The knee frequency values are 13.90 Hz, 3.72 Hz and 5.17 Hz for composites GVP82, GV44P and G16VP, respectively. The higher knee frequency of GVP82 apprises the early onset of capacitive behavior as compared to those of other composites. The relaxation times ( $\tau_0$ ) of GVP82 and G16VP calculated from Bode phase angle plots (Fig. 3.35c) are 81.28 s and 14.12 s, indicating the slow discharge process and higher energy storage of GVP82 than those of other composites. As the Bode phase plot of GV44P did not reach  $-45^\circ$  its  $\tau_0$  value was not calculated. From the Bode magnitude plots (Fig. 3.35d), it is seen that the GVP82 exhibits a low impedance of 2.22  $\Omega$  at the low frequency region, indicating a lower intrinsic resistance and higher conductivity of GVP82 than those of other composites. The low impedance is positively reflected in the plot of specific capacitance versus log frequency of GVP82 (Fig. 3.35e), where it exhibits a maximum capacitance ( $C$ ) of 9.45 F, which is higher than those of the composites GV44P and G16VP.

The results of GVP82 are compared with some of the similar works reported and found to be better than those of reported. The comparison is given in Table 3.13.

**Table 3.13** Comparison electrochemical results of GVP82 with similar work.

Composite	Electrolyte	E (V)	$C_s$ (F g <sup>-1</sup> )	$E$ (W h kg <sup>-1</sup> )	$P$ (W kg <sup>-1</sup> )	Cyclic stability	Ref.
Two electrode systems							
rGO/V <sub>2</sub> O <sub>5</sub> , asymmetric capacitor	1 M KCl	1.6 V	635 at 1 A g <sup>-1</sup>	79.5	900	94% retention up to 3000 cycles	(H. Nagaraju et al. 2014)
PANI/V <sub>2</sub> O <sub>5</sub>	5 M LiCl/PVA gel	1.6 V	443 at 0.5 mA cm <sup>-2</sup>	69.2	720	92% retention up to 5000 cycles	(Bai et al. 2014)
V <sub>2</sub> O <sub>5</sub> /MWCNT	LiClO <sub>4</sub> / PVA Gel	1.8 V	160 at 1 A g <sup>-1</sup>	72	2300	96% retention up to 4000 cycles	(Pandit et al. 2017)

V <sub>2</sub> O <sub>5</sub> /MnO <sub>2</sub> , asymmetric capacitor	0.5 M K <sub>2</sub> SO <sub>4</sub>	1 V	61 at 0.5 A g <sup>-1</sup>	8.5	127	-	(Saravanaku mar et al. 2014)
V <sub>2</sub> O <sub>5</sub> /PPy/GO	0.5 M Na <sub>2</sub> SO <sub>4</sub>	0.8 V	345 at 5 A g <sup>-1</sup>	27.6	3600	-	(Asen and Shahrokhian 2017b)
V <sub>2</sub> O <sub>5</sub> /graphene	0.5 M K <sub>2</sub> SO <sub>4</sub>	0.65 V	195.4 at 1 A g <sup>-1</sup>	-	-	-	(Xu et al. 2014)
V <sub>2</sub> O <sub>5</sub> /CNF	2 M KCl	0.8 V	227 at 1 A g <sup>-1</sup>	63.6	4554.6	80% retention up to 1000 cycles	(Choudhury et al. 2016)
rGO/V <sub>2</sub> O <sub>5</sub> , asymmetric capacitor	0.5 M K <sub>2</sub> SO <sub>4</sub>	1 V	53 at 0.5 A g <sup>-1</sup>	7.4	127	85% retention up to 100 cycles	(Saravanaku mar et al. 2016)
V <sub>2</sub> O <sub>5</sub> /graphene, asymmetric capacitor	1 M LiTFSI in CAN	1.8 V	279 At 1 A g <sup>-1</sup>	37.2	3743	-	(Choudhury et al. 2015)
V <sub>2</sub> O <sub>5</sub> /CNT/ SAC	2 M NaNO <sub>3</sub>	0.8 V	357 at 10 A g <sup>-1</sup>	-	-	-	(Wang et al. 2016c)
V <sub>2</sub> O <sub>5</sub> /rGO	1 M Na <sub>2</sub> SO <sub>4</sub>	1 V	437 at 1 A g <sup>-1</sup>	-	-	96% retention up to 10000 cycles	(Ye et al. 2015)
<b>GVP82</b>	<b>1 M H<sub>2</sub>SO<sub>4</sub></b>	<b>1.2 V</b>	<b>273 at 1 A g<sup>-1</sup></b>	<b>54.62</b>	<b>1636.5</b>	<b>61% retention up to 13000 cycles</b>	
Three electrode systems							
rGO/V <sub>2</sub> O <sub>5</sub>	3 M KCl	0.8 V	129.7 at 0.1 A g <sup>-1</sup>	-	-	-	(Foo et al. 2014)
V <sub>2</sub> O <sub>5</sub> /PPy/GO	0.5 M Na <sub>2</sub> SO <sub>4</sub>	1 V	750 at 5 A g <sup>-1</sup>	-	-	83% retention up to 3000 cycles	(Asen and Shahrokhian 2017b)

rGO/V <sub>2</sub> O <sub>5</sub>	0.5 M K <sub>2</sub> SO <sub>4</sub>	1 V	484 at 0.5 A g <sup>-1</sup>	-	-	83% retention up to 1000 cycles	(Saravanaku mar et al. 2016)
V <sub>2</sub> O <sub>5</sub> /graphene nanoribbon	0.5 M Na <sub>2</sub> SO <sub>4</sub>	1 V	335.8 at 1 A g <sup>-1</sup>	42.09	475	95.2 % retention up to 10000 cycles	(Sahu et al. 2017)
Hydrated V <sub>2</sub> O <sub>5</sub> /graphene	2 M KCl	0.7 V	649 at 5 mV s <sup>-1</sup>	44	1100	93% retention up to 600 cycles	(Qian et al. 2016)
V <sub>2</sub> O <sub>5</sub> /CNT	1 M Na <sub>2</sub> SO <sub>4</sub>	1 V	553.33 at 5 mV s <sup>-1</sup>	-	-	83% retention up to 1000 cycles	(Wang et al. 2017)
V <sub>2</sub> O <sub>5</sub> microspheres	1 M LiNO <sub>3</sub>	1.2 V	308 at 1 A g <sup>-1</sup>	-	-	-	(Zhang et al. 2016b)

---

## REDUCED GRAPHENE OXIDE, NICKEL HYDROXIDE AND POLYANILINE NANOCOMPOSITES

The nickel hydroxide ( $\text{Ni}(\text{OH})_2$ ) is a semiconductor with a band gap of  $\sim 3$  eV (Hermet et al. 2011), easy to synthesize, highly abundant on earth and inexpensive. The theoretical capacitance of  $\text{Ni}(\text{OH})_2$  is  $2082 \text{ F g}^{-1}$  (Kong et al. 2011) with a potential window of 0.5 V (Kong et al. 2011). It is widely used in alkaline rechargeable batteries and supercapacitors (Tang et al. 2015). Nickel hydroxide along with carbonaceous materials is reported for its electrochemical reversibility, due to its high kinetic proton diffusion and better discharge property (Huang et al. 2007). The nanocomposite containing rGO,  $\text{Ni}(\text{OH})_2$  and PANI (GNP) is anticipated to exhibit promising electrochemical properties when fabricated as supercapacitor electrode material. The GNP nanocomposites were synthesized by varying the weight percentage of each of their constituents by following the synthetic route described in the section 2.2.5. The following sections present the structural and electrochemical characterizations of GNP nanocomposite.

### 3.4. GNP WITH GLACIAL ACETIC ACID AS DOPANT

#### 3.4.1. Structural characterizations

##### 3.4.1.1. X-ray diffraction analysis

The XRD pattern of reduced graphene oxide/ $\text{Ni}(\text{OH})_2$ /polyaniline (GNP) is shown in Fig. 3.36. The GNP possesses peaks at  $20.51^\circ$  and  $23.30^\circ$  which correspond to (020) and (112) planes of polyaniline (PANI) (JCPDS Card No. – 053-1717 and 053-1891), a peak at  $25.22^\circ$  corresponds to (002) plane of reduced graphene oxide (rGO) (Abdolhosseinzadeh et al. 2015); the peaks at  $33.77^\circ$ ,  $38.70^\circ$ ,  $59.64^\circ$  are corresponding to (101), (015) and (110) planes of  $\text{Ni}(\text{OH})_2$  (JCPDS card No. - 038 - 0715). The two peaks with low intensities at  $52.16^\circ$  and  $62.85^\circ$  are indicating the presence of (200) and (104) planes of Ni and NiO, respectively (JCPDS card No.- 004-0850 and 022-1189). The crystalline size of  $\text{Ni}(\text{OH})_2$ , calculated from the Scherrer's equation 2.1 is 5.64 nm, confirming the composite is a nanocomposite

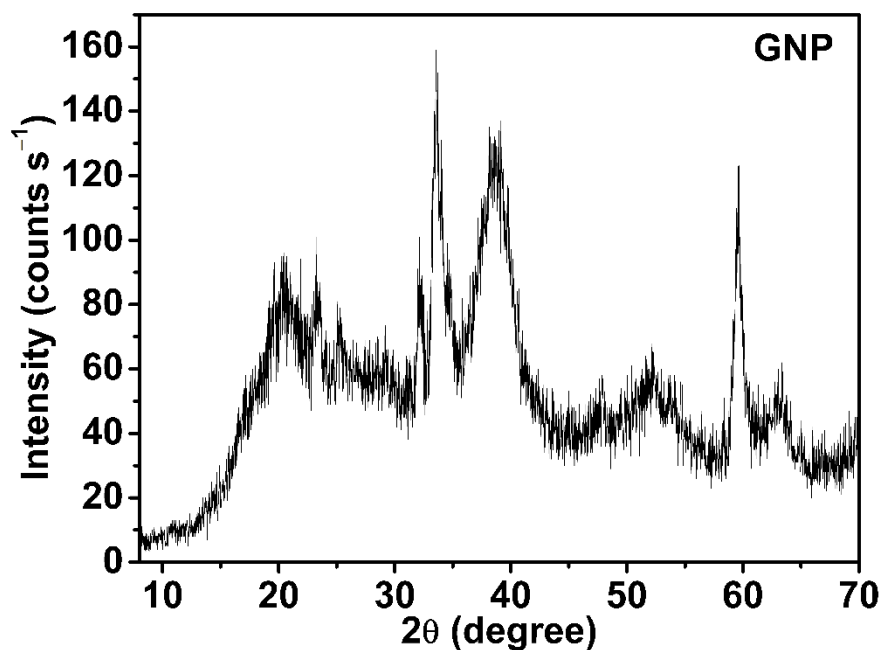


**Fig. 3.36** XRD pattern of GNP.

#### 3.4.1.2. FT-IR spectrum

The FT-IR spectrum of reduced graphene oxide/Ni(OH)<sub>2</sub>/polyaniline (GNP) is shown in Fig. 3.37.

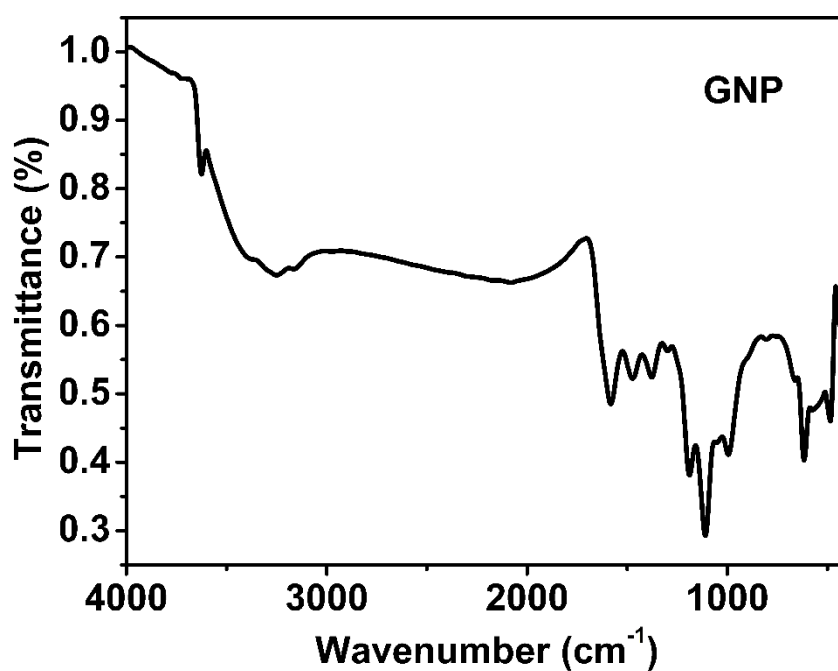


**Fig. 3.37** FT-IR spectrum of are reduced graphene oxide/Ni(OH)<sub>2</sub>/polyaniline (GNP).

The GNP nanocomposite exhibits peaks at  $1581\text{ cm}^{-1}$ ,  $1472\text{ cm}^{-1}$ ,  $1376\text{ cm}^{-1}$ ,  $1188\text{ cm}^{-1}$ ,  $1109\text{ cm}^{-1}$  and  $994\text{ cm}^{-1}$ , correspond to C=C stretching of quinoid and benzenoid ring, C-N stretching vibration, C=N stretching vibration, -C-H in plane bending (Pan et al. 2016) and -C-H out of plane bending (Feng et al. 2015), respectively. The peaks at  $616\text{ cm}^{-1}$  and  $485 - 439\text{ cm}^{-1}$  correspond to stretching vibrations of Ni-O-H, and Ni-O (Rahdar et al. 2015), respectively. These three different peaks of different forms of nickel are in support of the results obtained in XRD in the case of GNP.

### 3.4.1.3. Raman spectrum

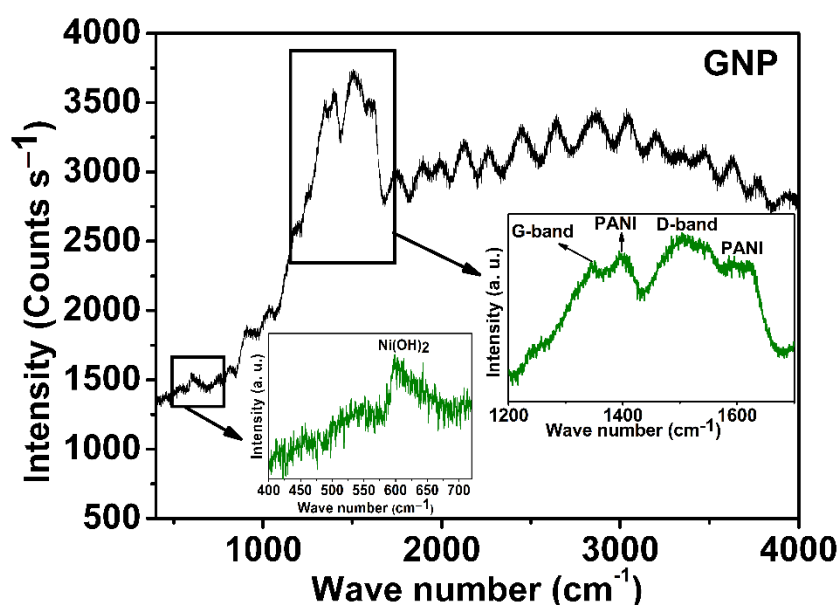


**Fig. 3.38.** Raman spectrum of reduced graphene oxide/Ni(OH)<sub>2</sub>/polyaniline (GNP).

Figure 3.38 shows the Raman spectra of GNP. The  $I_D/I_G$  ratio is 1.05 which is higher than those of GO (0.95), indicating the reduction of GO to rGO in GNP, and also the increase of defects in the composites. The  $I_{2D}/I_G$  ratio of GNP is 0.97, which corresponds to the double layer nature of the rGO present in the GNP composite (Akhavan et al. 2014). The higher value of  $I_{2D}/I_G$  ratio of GNP is attributed to the effective intercalation of PANI and Ni(OH)<sub>2</sub> in between rGO layers. This phenomenon helps to increase the effective specific surface area of the composite. The PANI in GNP nanocomposite is confirmed by peaks at  $531\text{ cm}^{-1}$ ,  $599.71\text{ cm}^{-1}$ ,  $816.50\text{ cm}^{-1}$ ,  $1193.02\text{ cm}^{-1}$ ,  $1401.30\text{ cm}^{-1}$  and  $1611.03\text{ cm}^{-1}$  associated with phenazine like

segments, stretching and bending of out of plane C–H bonds of quinoid rings, bending modes of C–H in benzenoid rings, stretching modes of –C–N in polaronic elements, vibrational semiquinone radicals, stretching vibrations of C=N in quinoid elements, and stretching modes of C=C in quinoid rings, respectively (Jin and Jia 2015). The peak at  $598\text{ cm}^{-1}$  confirms the presence of  $\text{Ni}(\text{OH})_2$ .

#### 3.4.1.4. XPS

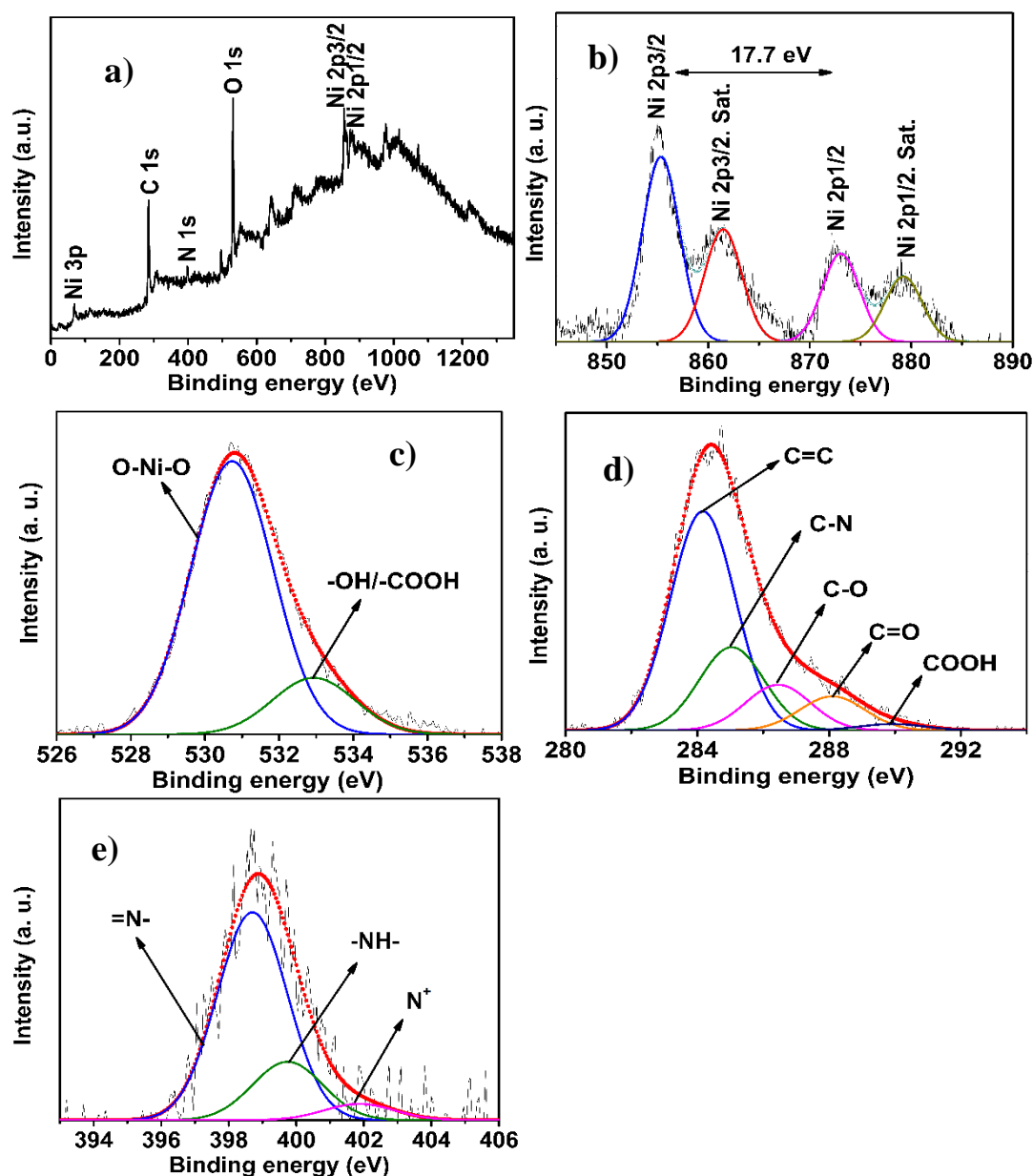


**Fig. 3.39** a) Survey spectrum of GNP; core level spectra of b) Ni 2p c) O 1s, d) C 1s and e) N 1s.



The survey spectrum of GNP, core level spectra of Ni 2p, O 1s, C 1s and N 1s are depicted in Fig. 3.39a, 3.39b, 3.39c, 3.39d and 3.39e, respectively. It is comprehended from the survey spectra that the elements present in the GNP are, C, N, O and Ni. The deconvoluted Ni 2p core level spectra consists of four peaks at binding energies (BEs) of 855.33 eV, 861.46 eV, 873.06 eV and 879.23 eV, which are associated to Ni 2p<sub>3/2</sub>, Ni 2p<sub>3/2</sub> Sat, Ni 2p<sub>1/2</sub> and Ni 2p<sub>1/2</sub> Sat of Ni(OH)<sub>2</sub> (Mansour 1994). The BE separation of 17.7 eV between Ni 2p<sub>3/2</sub> and Ni 2p<sub>1/2</sub> further confirms the presence of Ni(OH)<sub>2</sub> (Venezia et al. 1995). The peaks obtained at BEs of 530.87 eV and 532.93 eV on deconvoluting the O 1s core level spectra are corresponding to O-Ni-O bond (Shalvoy et al. 1979; Mansour 1994) and unreduced oxygen functional groups (-OH/-COOH) present in the rGO, acetic acid which was used as dopant for PANI and -OH present in Ni(OH)<sub>2</sub> (Li et al. 2013a). The C 1s core level spectrum is deconvoluted to five peaks at 284.17 eV, 285.04 eV, 286.45 eV, 288.10 eV and 289.92 eV, corresponding to C=C (sp<sup>2</sup> hybridized), C-N bond of PANI (Xia et al. 2012b), C-O, C=O and COOH present on rGO due to incomplete reduction process (Lin et al. 2016) and of dopant acetic acid (Hareesh et al. 2016), respectively. The N 1s core level spectra deconvoluted to three peaks at 398.70 eV, 399.74 eV and 401.87 eV are corresponding to benzenoid amine bond (=N-), quinoid imine bond (-NH-) and cationic nitrogens (N<sup>+</sup>) of PANI (Xia et al. 2012b), respectively.

#### 3.4.1.5. FE-SEM

The Fig. 3.40 shows the FE-SEM images of GNP nanocomposite. The uniform distribution of Ni(OH)<sub>2</sub> nanoparticles on PANI nanofibers, dispersed on rGO is observed. It is seen in Fig. 3.40b that the average size of Ni(OH)<sub>2</sub> is 15.38 nm, the average diameter of PANI nanofibers are in the range of 16 nm to 21 nm and the diameters of nano-channels created in the composites are in the range of 23 nm to 52 nm. The nanochannels created in the GNP composite enable the percolation of electrolytes deep into the electrode materials.

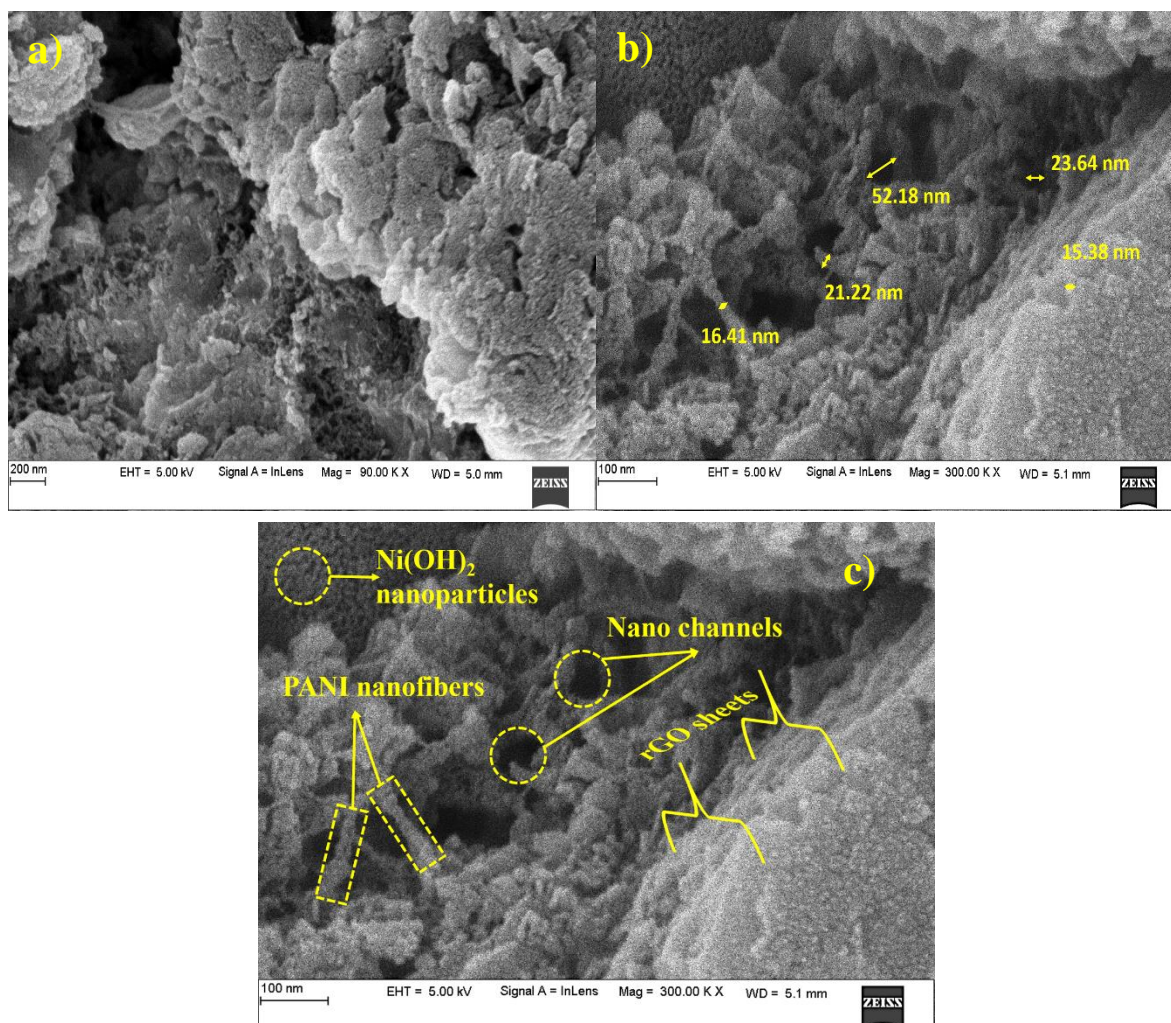


**Fig. 3.40** (a - c) FE-SEM images of GNP at different magnifications.

### 3.4.2. Electrochemical characterization

The reduced graphene oxide/Ni(OH)<sub>2</sub>/polyaniline (GNP) composites were synthesized by varying the weight percentages of each of the constituents namely, polyaniline, nickel hydroxide (Ni(OH)<sub>2</sub>) and reduced graphene oxide (rGO). The weight percentages of the GNP composite and the nomenclature used are listed in Table 3.14. When weight percentages of each one of the constituents were changed, the one composite with a weight percentages of constituents rGO 11.11%: Ni(OH)<sub>2</sub> 22.22%: P66.67% (G11NP) exhibited the promising electrochemical performance. The potential window used for the study is 1.2 V, which is the full potential window offered by the aqueous electrolyte 1 M H<sub>2</sub>SO<sub>4</sub>, even though the faradic reactions of Ni(OH)<sub>2</sub> (Balducci et al. 2017) occur in the potential range of 0 to 0.7 V. The substantiations for the use of

1.2 V are as follows (i) the GNP composite is constituted of both faradaic (PANI and Ni(OH)<sub>2</sub>) and Non faradaic (rGO) materials. Therefore the rGO present requires maximum potential window for its energy storage by electrical double layer (EDL) mechanism and (ii) the energy density of supercapacitor device is directly proportional to the potential window used (Chen et al. 2016a) and hence the highest possible potential window is favorable. The discussions for the entire studies are as follows.

**Table 3.14** The nomenclatures of the GNP composites

Component under study	Weight of constituents (mg)			Weight percentage (%)	Nomenclature
	P	N	G		
PANI series	100	50	25	57.10	GNP57
	150	50	25	66.66	GNP67
	200	50	25	72.72	GNP73
	250	50	25	76.90	GNP77
	300	50	25	80.00	GNP80
	350	50	25	82.35	GNP82
Ni(OH) <sub>2</sub> series	300	100	25	24.00	GN24P
	300	150	25	31.58	GN31P
	300	200	25	38.10	GN38P
	300	250	25	43.47	GN43P
	300	300	25	48.00	GN48P
	300	350	25	51.86	GN51P
rGO series	300	100	50	11.11	G11NP
	300	100	75	15.79	G16NP
	300	100	100	20.00	G20NP

#### 3.4.2.1. CV studies

Fig. 3.41a, depicts the CV curves of GNP composites at a scan rate of 5 mV s<sup>-1</sup>. It is seen from Fig. 3.41a that the CV curves are with redox peaks attributed to the obvious presence of pseudocapacitance and the capacitive behavior of the GNP composites. The redox peaks are caused by the faradaic transformations of pseudocapacitive PANI from leucoemeraldine to emeraldine and emeraldine to

pernigraniline (Xia et al.2012b); and of Ni(OH)<sub>2</sub> from Ni(OH)<sub>2</sub> to NiOOH (hydrous nickel oxide) and vice versa (Park et al. 2019) present in the GNP

composites. The area under the redox peaks are the measure of the charge storage by the electrode materials (Han et al. 2014). The composite G11NP exhibits the maximum area indicating high charge storage.

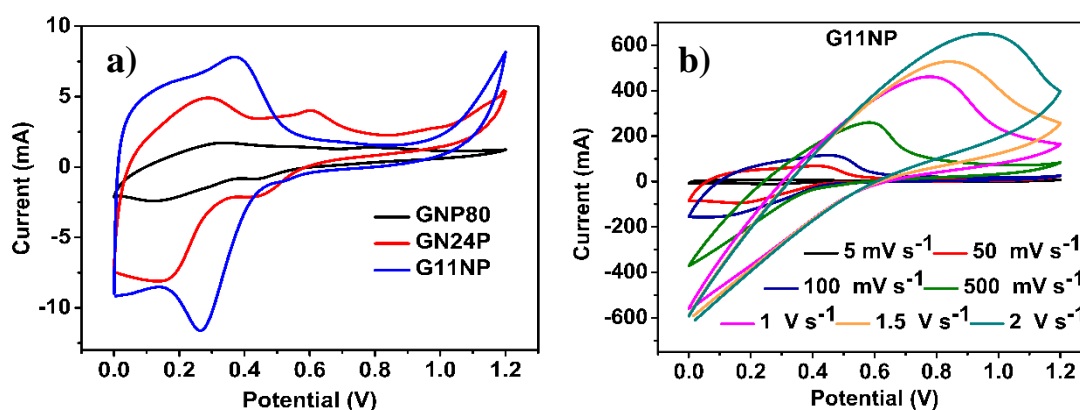


**Fig. 3.41** (a) Cyclic Voltammograms (CV curves) of composites GNP80, GN24P and G11NP at a scan rate of  $5 \text{ mV s}^{-1}$  (b) CV curves of G11NP at different scan rates.

The Fig. 3.41b depicts the CV curves of composite G11NP at different scan rates ranging from  $5 \text{ mV s}^{-1}$  to  $2 \text{ V s}^{-1}$ . The shift of redox peaks as the scan rate changes is attributed to the polarity present in the electrode material (Maitra et al. 2017). The G11NP composite exhibits capacitive behavior even at a high scan of  $2 \text{ V s}^{-1}$ , signifying the high rate capability of G11NP. This is caused by the effective electrolyte diffusion into the electrode materials even at a high scan rates, primarily caused by the enhanced surface area tailored in the electrode material by the intercalation of PANI and Ni(OH)<sub>2</sub> between rGO layers, effectively resisting them from restacking and making them to offer more specific surface area per unit mass for charge accumulation.

#### 3.4.2.2. GCD studies

The CD curves of composites GNP80, GN24P and G11NP at a current density of  $1 \text{ A g}^{-1}$  are shown in Fig. 3.42a. The composites do not exhibit triangular CD curves but quasi-triangular curves suggesting the capacitive behavior of the GNP composites and the presence of faradaic capacitance (Wu et al. 2015a). The composite G11NP shows a long discharge time, resulted by the adequate diffusion of electrolytic ions ( $\text{H}^+$

and  $\text{SO}_4^{2-}$ ) into the electrode material and the superior capacitive behavior (Han et al. 2014). Fig. 3.42b shows the CD curves of G11NP at different current densities ranging from 1 to 18  $\text{A g}^{-1}$ . The time taken for discharging is long at lower current density, which is attributed to the reason that at high current density the electrolyte diffusion is more confined to the super facial region and not into the interior of the electrode material where as at low current density the electrolyte diffuses well into interiors of the materials exhibiting better electrochemical performance (Dhibar and Das 2014; Asen and Shahrokhian 2017a). The ESRs of GNP80, GN24P and G11NP are 0.447  $\Omega$ , 0.364  $\Omega$  and 0.360  $\Omega$ , respectively and time constants are 0.051 s, 0.405 s and 0.632 s, respectively. The low *ESR* indicates the low intrinsic resistance and low IR loss in the case of G11NP. The high time constant of G11NP indicates the high energy stored in G11NP (Parlak et al. 2017; Yassine et al. 2017).

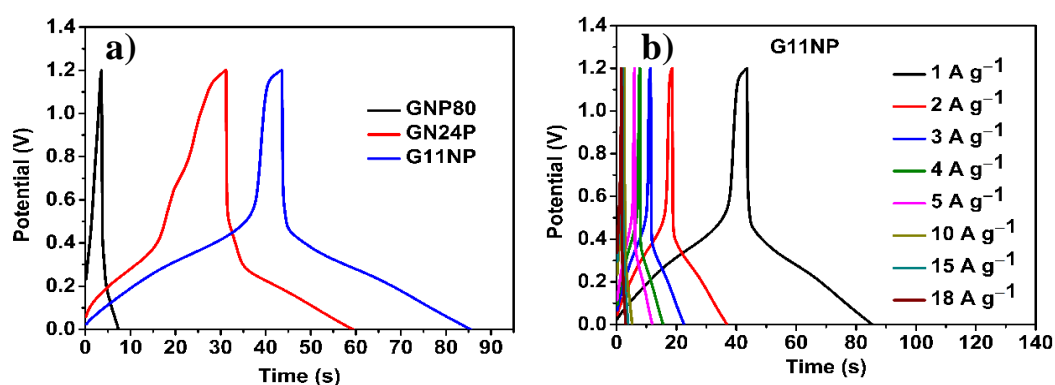


**Fig. 3.42** (a) CD curves of composites GNP80, GN24P and G11NP at a current density of 1  $\text{A g}^{-1}$  (b) CD curves of G11NP at different current densities.

The specific capacitances ( $C_s$ ), energy densities ( $E$ ), power densities ( $P$ ), columbic efficiencies ( $\eta$ ) of the GNP composites (electrochemical parameters) at a current density of 1  $\text{A g}^{-1}$  are listed in Table 3.15. As it is seen from the Table 3.15 that there is an increase in specific capacitance as the weight percent of PANI increases up to 80%, and beyond which the further increase causes decrease in specific capacitance, which is owing to the random aggregation of PANI causing the the electrolyte to confined to the superficial part of the composite; and hence the contact of electrolyte with the entire electrode material becomes ineffective resulting in the decrease in specific capacitance (Xu et al. 2010).

**Table 3.15** The electrochemical parameters of the composites at a current density of 1 A g<sup>-1</sup>

Composite	$C_s$ (F g <sup>-1</sup> )	$E$ (W h kg <sup>-1</sup> )	$P$ (kW kg <sup>-1</sup> )	$\eta$ (%)
GNP57	0.81	0.16	975	100.0
GNP66	3.05	0.61	2748	133.3
GNP72	3.49	0.69	1798	133.3
GNP76	5.39	1.07	2773	116.6
GNP80	10.67	2.13	2023	105.5
GNP82	9.91	1.98	1486	133.3
GN24P	74.34	14.86	1898	90.3
GN31P	3.89	0.77	2002	100.0
GN38P	1.53	0.30	1846	100.0
GN43P	0.92	0.18	1658	66.6
GN48P	22.16	4.43	1773	100.0
GN51P	27.97	5.59	1936	94.5
G11NP	92.42	18.48	1584	96.3
G15NP	87.07	17.41	1741	97.2
G20NP	73.20	14.64	1550	95.5

With the weight of the PANI being maintained as constant at 300 mg (GNP80) (corresponds to 80% in the PANI series), and on increasing the weights of Ni(OH)<sub>2</sub>, an enhancement in specific capacitance is observed up to a weight of 100 mg (24%) with a specific capacitance of 74.34 F g<sup>-1</sup> at 1 A g<sup>-1</sup>. Further increase in Ni(OH)<sub>2</sub> content decreases the specific capacitance. This is caused by the semiconductor nature of Ni(OH)<sub>2</sub> (~ 3 eV) (Hermet et al. 2011), reducing the conductivity of the composite, when its percentage further increases in the composite. Thus, the weight of Ni(OH)<sub>2</sub> was kept at a constant of 100 mg, corresponds to 24% in the Ni(OH)<sub>2</sub> series. Subsequently the weight of rGO was increased and a maximum specific capacitance of 92.42 F g<sup>-1</sup> was obtained at 1 A g<sup>-1</sup> at a weight of 50 mg (11.11%), beyond which the deterioration of properties were observed. This indicates the definite role of rGO in appropriate weight percentage, in increasing the energy storage. Since the GNP composites constituted of pseudocapacitive materials, particularly Ni(OH)<sub>2</sub> along with

non-faradaic material rGO; the weight percentage of  $\text{Ni}(\text{OH})_2$  is higher than the rGO and the proper practice of mentioning the energy storage of pseudocapacitive material is as specific capacity ( $\text{C g}^{-1}$ ) (Balducci et al. 2017) and the specific capacity of G11NP is  $110.90 \text{ C g}^{-1}$ .

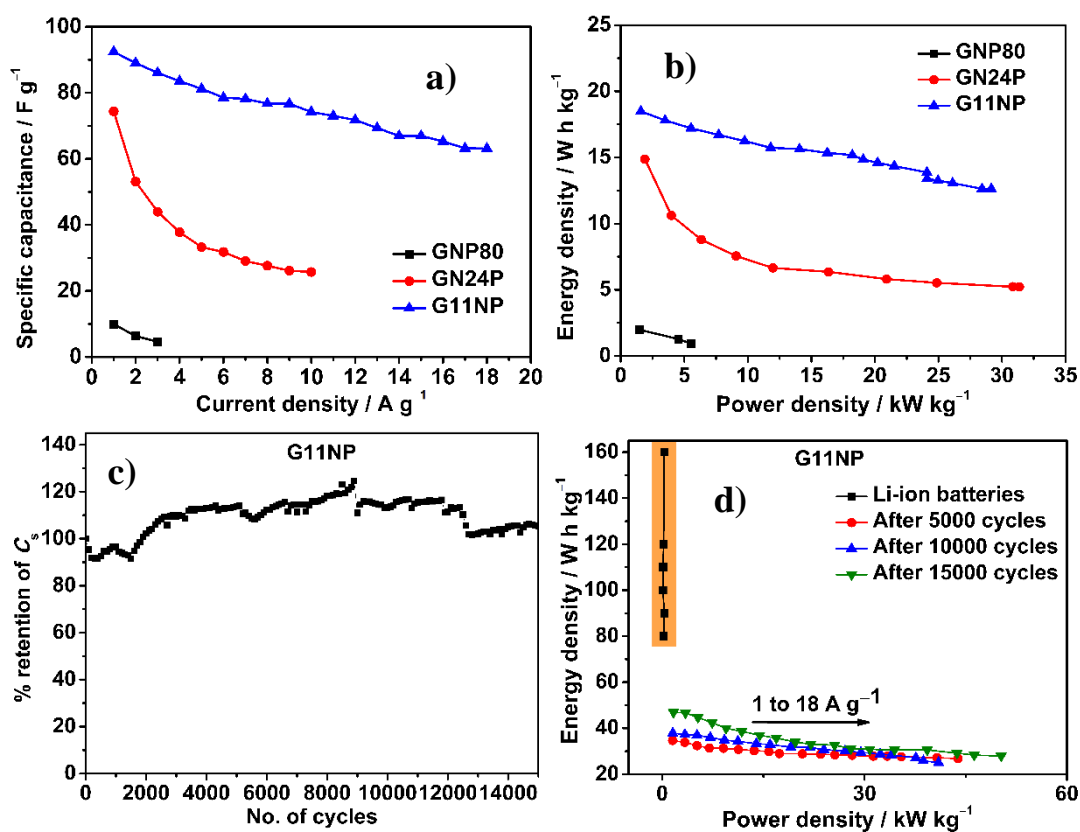


**Fig. 3.43** (a) Plots of specific capacitance versus current densities (b) Ragone plots of composites GNP80, GN24P, and G11NP (c) Plot of retention of specific capacitance versus number of cycles of G11NP (d) Comparison of energy density and power density of Li-ion batteries with energy density and power density of G11NP obtained after 5000, 10000 and 15000 cycles.

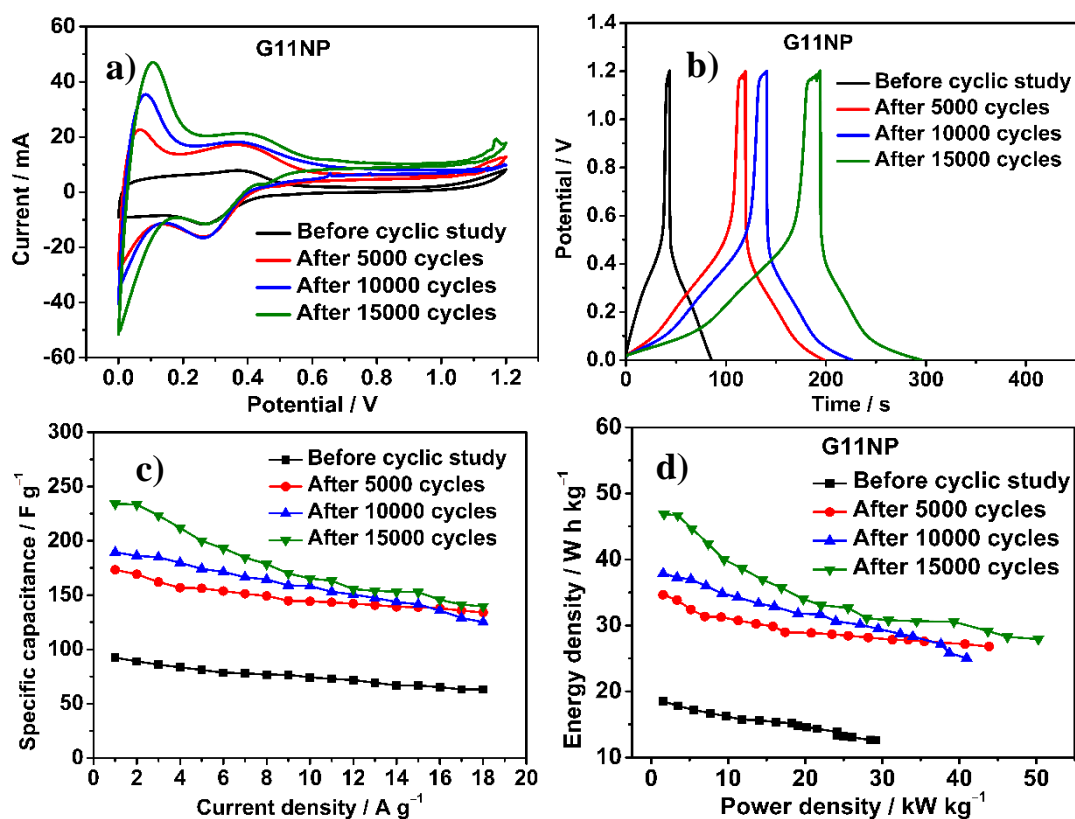
The plots of specific capacitance versus current density and Ragone plots are shown in Fig. 3.43 a and 3.43b. It is seen in Fig. 3.43a, that the composite G11NP exhibits high specific capacitance of  $63.14 \text{ F g}^{-1}$  at high current density of  $18 \text{ A g}^{-1}$ , unlike the composites GNP80 and GN24P, which indicates the higher charge transport in the composite G11NP and its lower intrinsic resistance. The Ragone plots (Fig. 3.43b) show the high energy densities and power densities exhibited by the G11NP

than those of GNP80 and GN24P. This is resulted by the good interfacial link between PANI and Ni(OH)<sub>2</sub> nano particles and rGO through  $\pi$ - $\pi$  interactions, enabling the increased utilization of PANI and reducing the diffusion and migration paths for electrolyte ions during rapid redox reactions (Shen et al. 2013). The cyclic stability of G11NP was carried out using CV technique at a scan rate of 400 mV s<sup>-1</sup> for 15000 cycles. The plot of retention of specific capacitance versus number of cycles are shown in Fig. 3.43c. After every 5000 cycles the electrochemical parameters were calculated. Towards the end of 15000 cycles, the time taken for charging by the composite was found to be increasing, giving raise to low coulombic efficiency of 52.16% and hence the reversible charge/ discharge cycle was stopped. The G11NP exhibits no deterioration in specific capacitance even after 15000 cycles; rather there is an increase in specific capacitance as the number of cycle increases. At the end of the 15000 cycles the G11NP composite exhibits a specific capacitance of 234.19 F g<sup>-1</sup>, energy density of 46.87 W h kg<sup>-1</sup> and power density of 1.66 kW kg<sup>-1</sup> at a current density of 1 A g<sup>-1</sup>, which are 253.39% enhancement of the values obtained before the onset of cyclic stability study. The time constant ( $\tau$ ) of G11NP after 5000, 10000 and 15000 cycles are 1.110 s, 1.224 s and 1.530 s, indicating the increase of energy storage with the increase in number of cycles. The comparisons are shown in Fig. 3.43d. The high energy density of 46.87 W h kg<sup>-1</sup> obtained after 15000 cycles, is higher than EDL supercapacitors (~10 W h kg<sup>-1</sup>) and approaching close to energy densities of Li-ion batteries (Fig. 3.43d). The electrochemical parameters obtained after every 5000 cycles upto 15000 cycles at a current density of 1 A g<sup>-1</sup> are listed in Table 3.16. The CV curves and CD curves of G11NP, obtained before cycling, after 5000, 10000 and 15000 cycles at a scan rate of 5 mV s<sup>-1</sup> and current density of 1 A g<sup>-1</sup>, respectively, are shown in Fig. 3.44a and 3.44b, respectively. The plots of specific capacitance versus current density and Ragone plots of G11NP, obtained before cycling, after 5000, 10000 and 15000 cycles are shown in Figs. 3.44c and 3.44d, respectively. It is seen from Fig. 3.44a that the area under the redox peaks increases as the number of cycles increases indicating an enhancement in energy storage by the G11NP as the number cycles increases. Fig. 3.44b shows that G11NP exhibits a long discharge time as the number of cycles increases, indicating an enhanced energy storage as the number of cycles increases.



**Table 3.16** Electrochemical parameters of G11NP before cycling, after 5000, 10000 and 15000 cycles.

No. of cycles	$C_s$ ( $F g^{-1}$ )	$E$ ( $W h kg^{-1}$ )	$P$ ( $kW kg^{-1}$ )	$\eta$ (%)
0	92.42	18.48	1584.36	96.33
5000	173.31	34.66	3354.39	80.51
10000	189.39	37.87	3375.33	76.80
15000	234.19	46.87	1664.02	52.16

**Fig. 3.44** (a) CV curves of G11NP at a scan rate of  $5 \text{ mV s}^{-1}$  (b) CD curves of G11NP at a current density of  $1 \text{ A g}^{-1}$  (c) Plots of specific capacitance versus current densities of G11NP (d) Ragone plots of G11NP, after subjecting into different number of cycles.

These observations are attributed to the structural activation and opening of nano pores on the composites surface (Pendashteh et al. 2015) exposing more surface redox sites for energy storage. The Figs. 3.44c and 3.44d show that high specific capacitances, energy densities and power densities are obtained even after 15000 of

cycles. The electrical changes that occur during the process of cyclization are followed by electrochemical impedance spectroscopy. The Nyquist plots of G11NP before and after subjecting into cycles are shown in Fig. 3.45a. They are fitted with an equivalent circuit using a software ZimpWin 3.21 to  $R_s(R_{ct}Q_1)((R_{leak}C_{dl})(Q_2))W$  and, the magnitudes of electrical parameters are listed in Table 3.17. It is seen from Table 3.17 that the solution resistance ( $R_s$ ) decreases from 0.28  $\Omega$  to 0.01  $\Omega$ , charge transfer resistance ( $R_{ct}$ ) reduces from 37.98  $\Omega$  to 0.23  $\Omega$  and there is an increase of electrical double layer capacitance from 1.87 F to 11.18 F by the end of the 5000 cycles. These observations substantiate the increase in the performance as the number of cycles increases. The trend of reduction in the overall resistances is corroborated by the Bode magnitude plots (Fig. 3.45b). It is seen in Fig. 3.45b that at low frequency region as the number of cycles increases the impedance decreases.

**Table 3.17** The electrical parameters of G11NP after subjecting into different number of cycles.

No. of cycles	$R_s$ ( $\Omega$ )	$R_{ct}$ ( $\Omega$ )	$Q_1$ (F)	$n_1$	$R_{leak}$ ( $\Omega$ )	$C_{dl}$ (F)	$Q_2$ ( $\mu$ F)	$n_2$	$W$ ( $\Omega$ )
0	0.28	37.98	2.72	0.99	0.25	1.87	1138.00	0.75	3.60
5000	0.01	0.23	$29 \times 10^{-4}$	0.67	0.27	11.18	$1.70 \times 10^{-9}$	0.63	7.88
10000	0.30	0.05	0.71	0.61	0.18	13.28	517.20	0.86	12.50
15000	0.33	0.08	0.37	0.50	0.17	20.44	452.80	0.88	14.71

The trend of decrease in  $R_{ct}$  and  $R_{leak}$  and increase of  $C_{dl}$  as the number of cycles increases rationalizes the increase in the electrochemical performance along with the number of cycles. This is supported by the plots of capacitance versus log frequency, showing high capacitance at low frequency region as the number of cycles increases (Fig. 3.45c). On the other hand, the slight increase in  $R_s$  and significant increase of Warburg diffusion resistance ( $W$ ) (3.60  $\Omega$  to 14.71  $\Omega$ ) rationalizes the increase of charging time ( $t_c$ ) as the number of cycles increases, which is supported by the Bode phase angle plots (Fig. 3.45d). The value of  $\tau_o$  increases with the number of cycles apprising slow diffusion of electrolyte and long discharge time confirming high energy storage (Han et al. 2014).

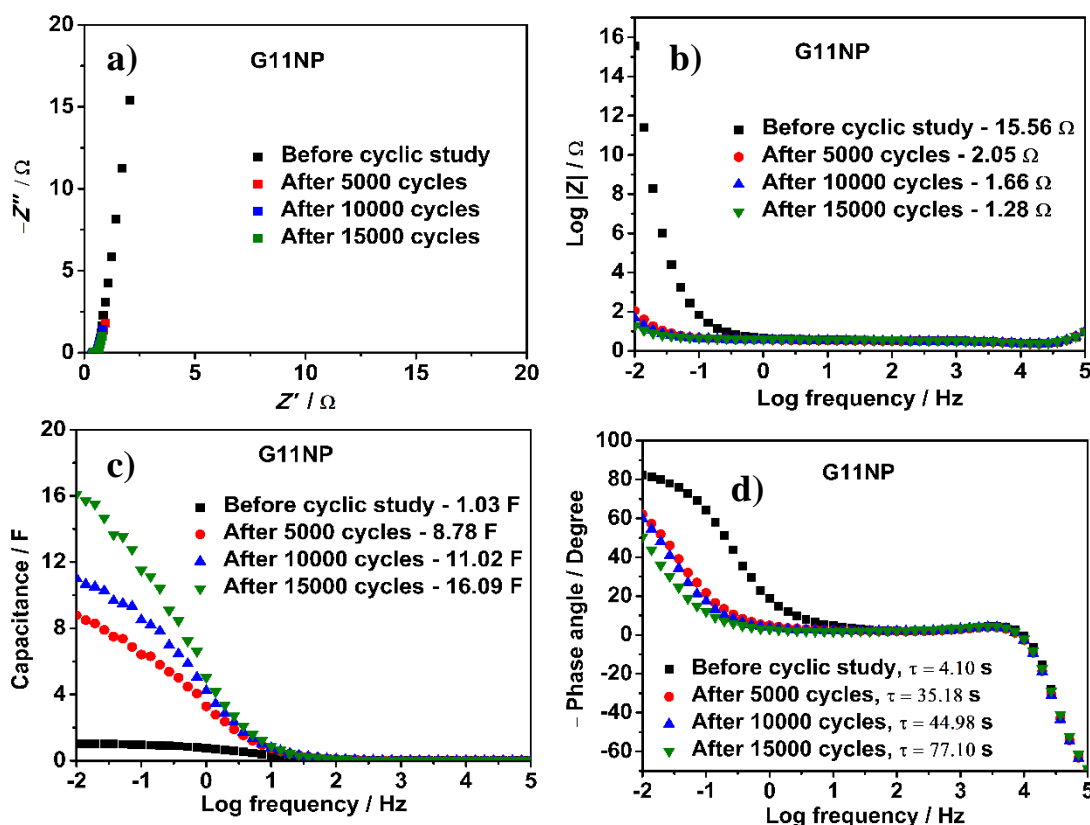


**Fig. 3.45** (a) Nyquist plots (b) Bode magnitude plots (c) Plots of capacitance versus log frequency plots (d) Bode phase angle plots, of G11NP after subjecting into different number of cycles.

Four G11NP composite supercapacitor devices, fabricated as explained in section 2.3, were connected in series and their practical application was explored by using them as an energy sources to light up light emitting diodes (LED) of colors blue (working potential  $\sim 3 \text{ V}$ ), green ( $\sim 2 \text{ V}$ ), orange ( $\sim 1.7 \text{ V}$ ) and red ( $\sim 1.7 \text{ V}$ ). The as fabricated GNP device could successfully light them up (Fig. 3.46). The ability of G11NP composite to act as a power backup device is demonstrated by charging them for 1 min with 9V Nippo heavy duty battery while a red color LED is connected, on cutting short the power from battery the LED continued to glow for next 50 s taking energy from supercapacitor. The same procedure repeated with green color LED, which gave a 30 s of for 1 min of charging. This experiment confirms the real time ability of G11NP to act as secondary power source.

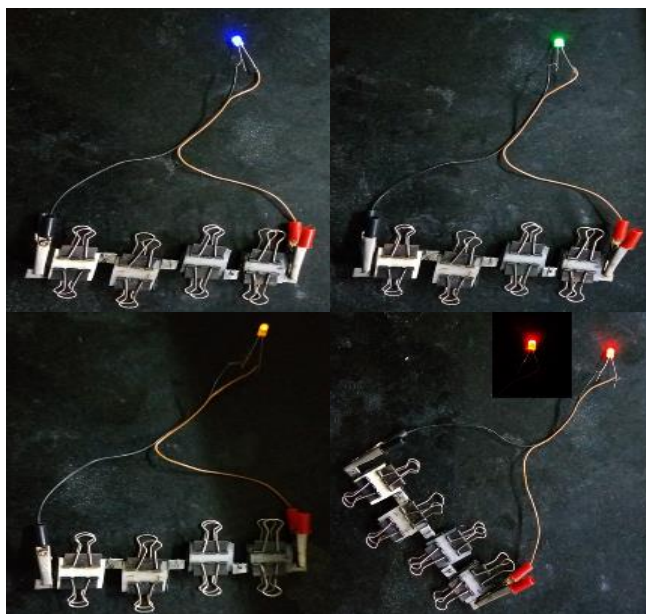


**Fig. 3.46** The as-fabricated GNP composite device lighting up blue, green, orange, and red LEDs.

#### 3.4.2.3. EIS studies

The Fig. 3.47a depicts the Nyquist plots of composites GNP80, GN24P and G11NP. All the Nyquist plots possess a semicircle at high frequency region and a Warburg diffusion at the low frequency region indicating the capacitive behavior of the composites. As it is seen in the Fig. 3.47a, the composite G11NP has the lowest resistance along the real axis, suggesting the low intrinsic resistance of the G11NP. Figure 3.47b depicts the equivalent circuit fitment of the composite G11NP with the equivalent circuit at the inset. The obtained equivalent circuit (<1.96 % mean error) possesses a solution resistance ( $R_s$ ) (0.28  $\Omega$ ), charge transfer resistance ( $R_{ct}$ ) (37.98  $\Omega$ ), Warburg resistance ( $W$ ) (3.60  $\Omega$ ), leakage resistance ( $R_{leak}$ ) (0.25  $\Omega$ ) (which causes the loss of potential when the device is not connected with an external load), electrical double layer capacitance ( $C_{dl}$ ) (1.87 F), and the constant phase elements  $Q_1$  and  $Q_2$ . The inclusion of constant phase elements (CPE)  $Q_1$  and  $Q_2$  (2.72 F and 1138  $\mu$ F) instead of ideal capacitances  $C_1$  and  $C_2$  are substantiated by relation 3.1 and the explanation is given in section 3.1.2.3.

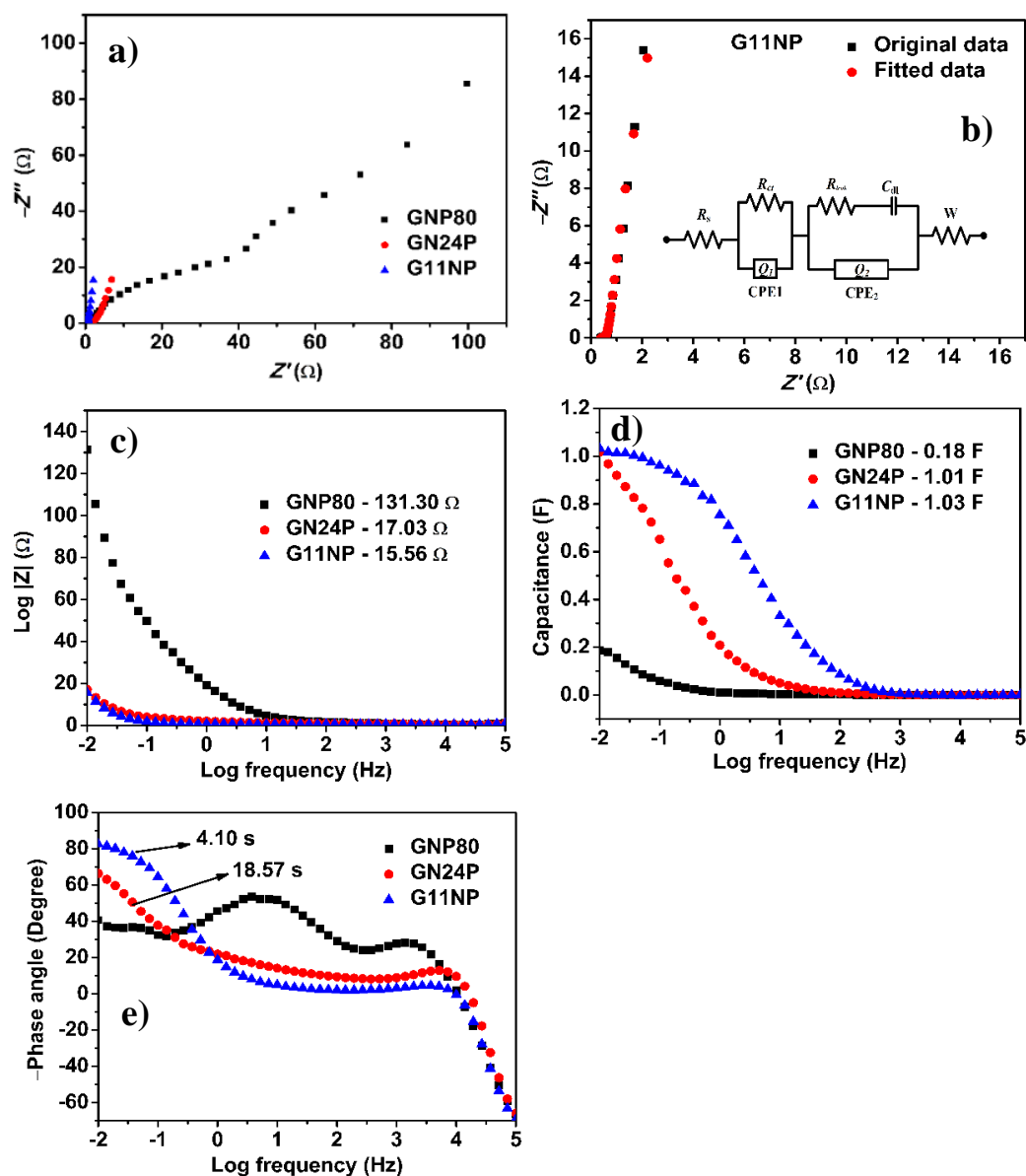


**Fig. 3.47** (a) Nyquist plots of composites GNP80, GN24P and G11NP; (b) Equivalent circuit fitment of G11NP with the equivalent circuit in the inset; (c) Bode magnitude plots; (d) Plots capacitance versus log frequency; (e) Bode phase angle plots, of composites GNP80, GN24P and G11NP.

The obtained roughness factors are 0.99 and 0.75 indicating the moderate capacitive behavior of the electrode material. From the Bode magnitude plots (Fig. 3.47c) it could be noted that the composite G11NP exhibits lower resistance in the low frequency region (15.56  $\Omega$ ) than that of composites GNP80 and GN24P, signifying the low intrinsic resistance and high conductivity of G11NP. The Fig. 3.47d shows the plots

of capacitance versus log frequency. The value of capacitance exhibited (1.03 F) at low frequency by G11NP is higher than those of other composites.

The Bode phase angle plots are shown in Fig. 3.47e. The composite G11NP shows the low relaxation time of 4.10 s, indicating rapid diffusion of electrolyte. The phase angle approaches close to  $90^\circ$  indicating a behavior close to that of an ideal capacitor. Other composites largely deviate from ideality of the capacitors.

---

### 3.5. EFFECT OF MAGNETIC FIELD IN ELECTROCHEMICAL PERFORMANCES OF REDUCED GRAPHENE OXIDE, NICKEL HYDROXIDE, AND POLYANILINE NANOCOMPOSITE

Nickel hydroxide ( $\text{Ni(OH)}_2$ ) is a pseudo capacitive material, one of the most recognized electrode material used in batteries (Hermet et al. 2011), symmetric and asymmetric supercapacitors (Patil et al. 2009; Wang et al. 2010), whose theoretical capacitance is  $2082 \text{ F g}^{-1}$  (Yan et al. 2012). The  $\text{Ni(OH)}_2$  is an antiferromagnetic semiconducting material (Hermet et al. 2011), whose antiferromagnetic nature can be changed to ferromagnetic by applying magnetic field (Zhang et al. 2017). Such conversion is expected to bring about changes in electrochemical performances of  $\text{Ni(OH)}_2$ . Since,  $\text{Ni(OH)}_2$ , a known semiconductor and is capable of exhibiting ferromagnetic nature on applying magnetic field, their band gap would change (Tanaka et al. 2014) to result better electrochemical performance.  $\text{Ni(OH)}_2$  with applied magnetic field has also found its applicability in novel field called spintronics (Tang et al. 2015). The notion of applying the magnetic field is also strengthened by following factors (1) the permittivity of the dielectric used in the fabrication of capacitor is important due to the role of break down voltage and the manufacturability of the capacitors. The application of magnetic field is found to increase the permittivity of the dielectric medium and thereby imparting high specific capacitance, energy storage and high energy density to the supercapacitors (Hong and Lee 2017). (2) The motion of charge carriers, electron polarization and transportation would be different under the magnetic field, in comparison with normal conditions, and it is already mentioned in literatures that the magnetic field would affect the resistance exerted by the graphene as well. Therefore, the applied magnetic field would affect the capacitive behavior of the system (Zhu et al. 2013). (3) The dispersion of magnetic nanoparticle on reduced graphene oxide results in the encapsulation nanoparticle in the graphitic shell, thereby limiting the aggregation and provide stability against environmental degradation in many organic and inorganic media (Vermisoglou et al. 2014). The synthesis of the nanocomposites with the combination versatile  $\text{Ni(OH)}_2$  with rGO (possesses higher surface area) and PANI (exhibits high pseudo capacitance) under the influence of magnetic field and their electrochemical results are discussed in the following sections.

### 3.5.1. Electrochemical characterizations

A series of six GNP composites were synthesized with different weight percentages of Ni(OH)<sub>2</sub> of 24% , 31%, 38%, 43%, 48% and 51%, while the amounts of rGO and PANI were maintained constant. The corresponding composites were designated to be GN24P, GN31P, GN38P, GN43P, GN48P and GN51P and their magnetic susceptibilities were measured to be 340, 512, 454, 438, 850 and 628, respectively. The composite GN48P exhibited high magnetization in the presence of applied magnetic field and the magnetic susceptibility of 850 exhibited by it was the highest of all the composites. Electrochemical analyses revealed that; no composites other than GN48P showed any significant improvement in their electrochemical behavior on the application of magnetic fields of different strengths. The electrochemical analyses of composites except that of GN48P in the presence and in the absence of applied magnetic fields are discussed as follows:

#### *GN24P*

The CV curves at a scan rate of 5 mV s<sup>-1</sup>, CD curves at a current density of 0.25 A g<sup>-1</sup> and Nyquist plots of GN24P are shown in Fig. 3.48a, Fig. 3.48b and Fig. 3.48c, respectively. It is observed from the figures that the GN24P exhibits a low redox area, less discharge time and high resistance along the real axis of the Nyquist plots, indicating the low energy storage in the presence of applied magnetic field of 625 μT. The specific capacitance obtained without magnetic field is 33.60 F g<sup>-1</sup> which is 31.8% higher than the specific capacitance obtained on applying a magnetic field of 625 μT (22.91 F g<sup>-1</sup>). Thus, the composite GN24P did not show any increase in energy storage properties with applied magnetic field which is attributed to the low magnetic susceptibility(340) of GN24P.



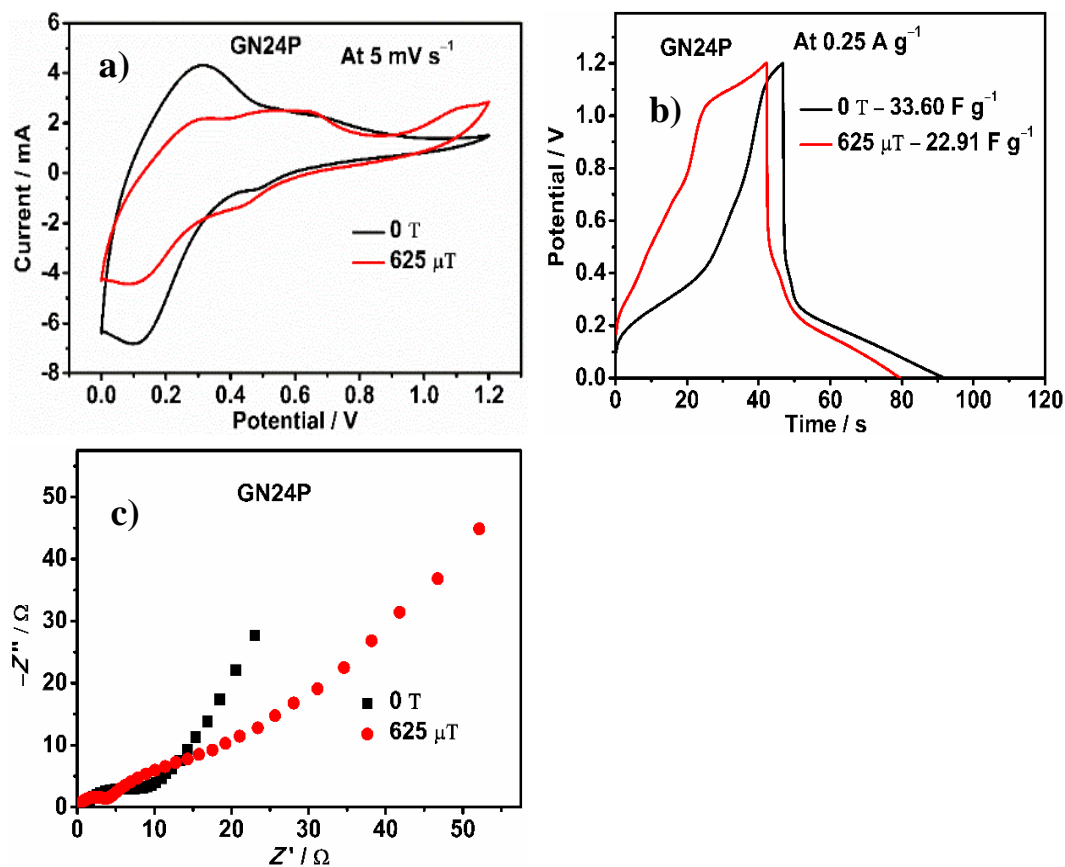


**Fig. 3.48** (a) CV curves at a scan rate of 5 mV s<sup>-1</sup> (b) CD curves at a current density of 0.25 A g<sup>-1</sup> (c) Nyquist plots, of GN24P.

### GN31P

The CV curves at a scan rate of 5 mV s<sup>-1</sup>, CD curves at a current density of 0.25 A g<sup>-1</sup> and Nyquist plots of GN31P are shown in Fig. 3.49a, Fig. 3.49b and Fig. 3.49c, respectively. It is observed from the figures that the nanocomposite GN31P exhibits an high redox area, long discharge time and low resistance along the real axis of the Nyquist plots, indicating the high energy storage by GN31P in the presence of magnetic field of 625 μT. The specific capacitance obtained without magnetic field is 2.57 F g<sup>-1</sup> which is 105% lower than the specific capacitance (5.28 F g<sup>-1</sup>) obtained in the presence of magnetic field of 625 μT. However, the 105% increase in specific capacitance did not provide a substantial magnitude of specific capacitance.

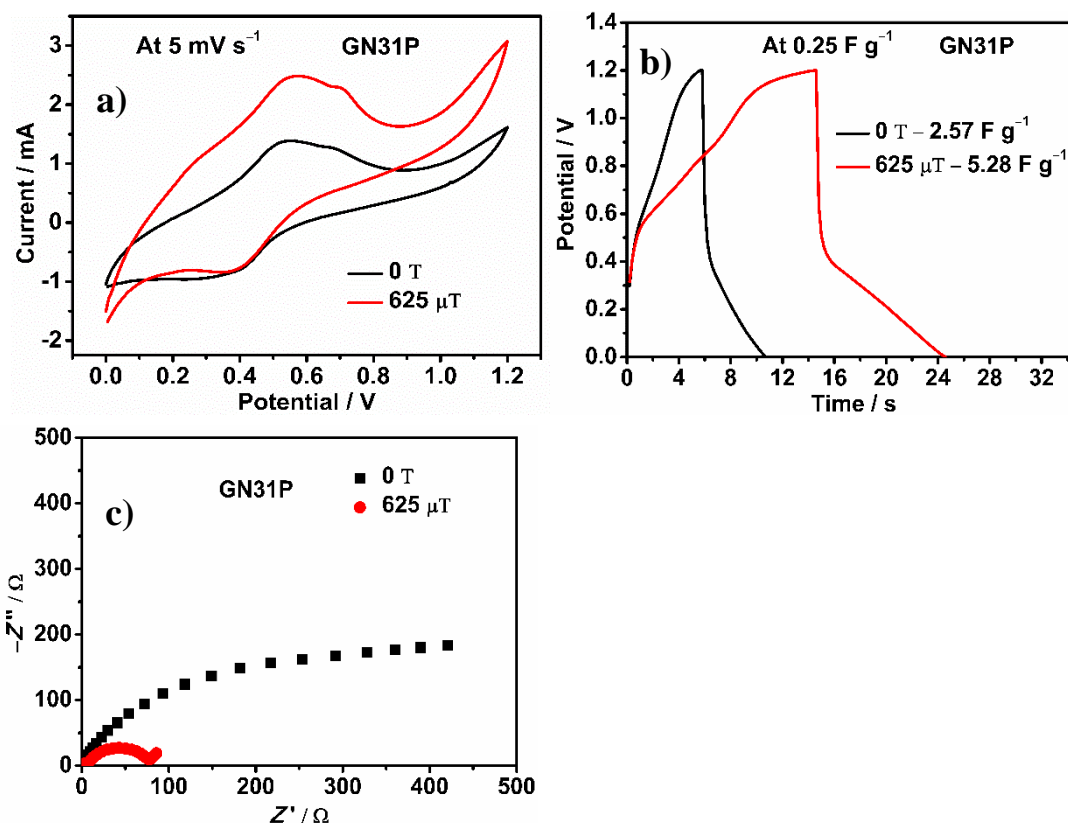


**Fig. 3.49** (a) CV curves at a scan rate of  $5 \text{ mV s}^{-1}$  (b) CD curves at a current density of  $0.25 \text{ A g}^{-1}$  (c) Nyquist plots, of GN31P.

### GN38P

The CV curves at a scan rate of  $5 \text{ mV s}^{-1}$ , CD curves at a current density of  $0.25 \text{ A g}^{-1}$  and Nyquist plots of GN38P are shown in Fig. 3.50a, Fig. 3.50b and Fig. 3.50c, respectively. It is observed from the figures that the nanocomposite GN38P exhibits a high redox area, longer discharge time and lower resistance along the real axis of the Nyquist plots indicating the high energy storage by GN38P in the presence of magnetic field of  $625 \text{ μT}$ . The specific capacitance obtained without magnetic field is  $5.04 \text{ F g}^{-1}$  which is 301% lower than the specific capacitance ( $20.25 \text{ F g}^{-1}$ ) obtained in the presence of magnetic field of  $625 \text{ μT}$ . However, the 301% increase in specific capacitance did not provide a substantial magnitude of specific capacitance. On the other hand, the coulombic efficiency of GN38P in the presence of  $625 \text{ μT}$  is reduced to a low value of 47.2%, while the coulombic efficiency obtained with out magnetic field is 85.45%.

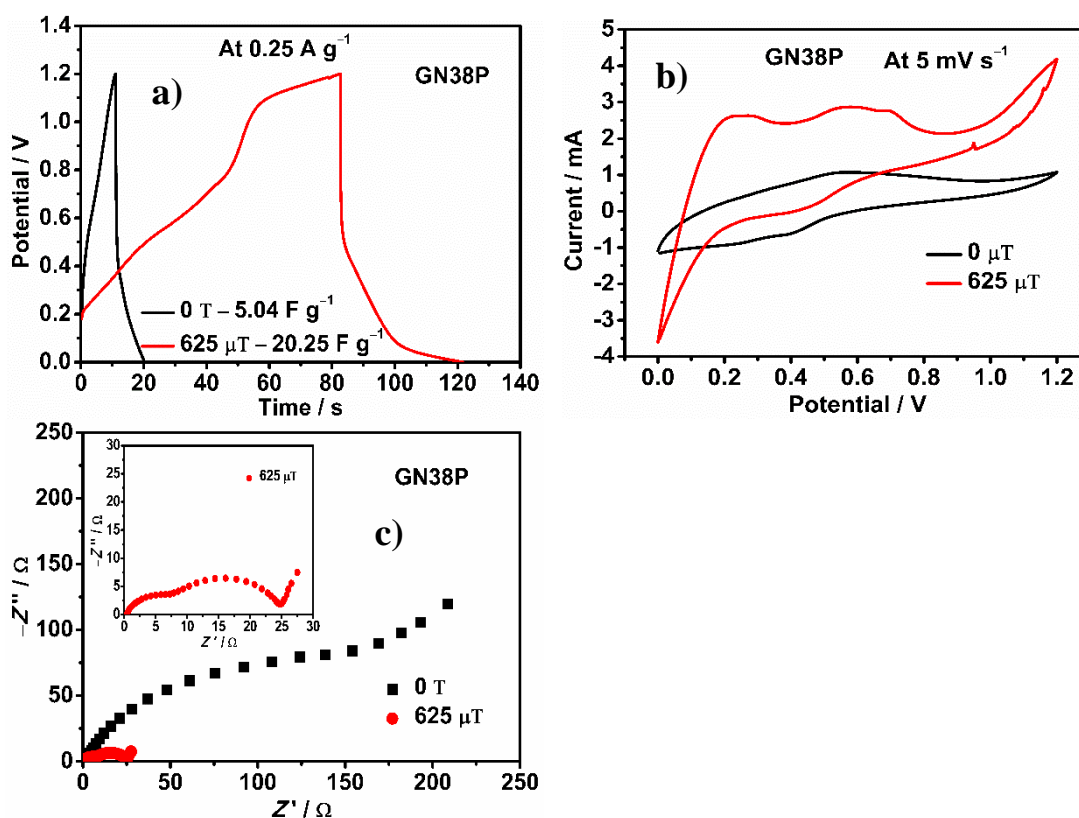


**Fig. 3.50** (a) CV curves at a scan rate of 5 mV s<sup>-1</sup> (b) CD curves at a current density of 0.25 A g<sup>-1</sup> (c) Nyquist plots, of GN38P.

#### GN43P

The CV curves at a scan rate of 5 mV s<sup>-1</sup>, CD curves at a current density of 0.25 A g<sup>-1</sup> and Nyquist plots of GN43P are shown in Fig. 3.51a, Fig. 3.51b and Fig. 3.51c, respectively. It is observed from the figures that the nanocomposite GN43P exhibit less redox area, lesser discharge time and higher resistance along the real axis of the Nyquist plots, indicating the low energy storage by GN43P in the presence of magnetic field of 625 μT. The specific capacitance obtained without magnetic field is 0.9398 F g<sup>-1</sup> which is 12.82% higher than the specific capacitance (0.8330 F g<sup>-1</sup>) obtained in the presence of magnetic field of 625 μT. The decrease in specific capacitance in the presence of the magnetic field is attributed to the low magnetic susceptibility (438) of GN43P.

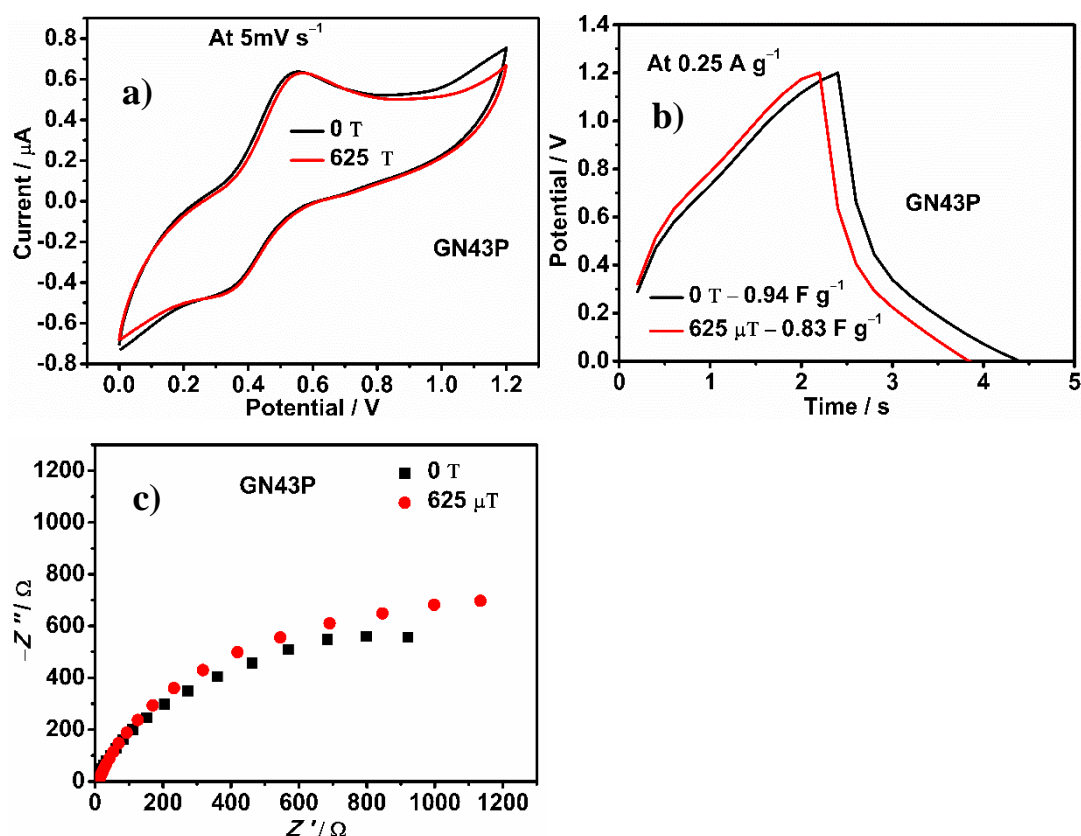


**Fig. 3.51** (a) CV curves at a scan rate of 5 mV s<sup>-1</sup> (b) CD curves at a current density of 0.25 A g<sup>-1</sup> (c) Nyquist plots, of GN43P.

### GN51P

The CV curves at a scan rate of 5 mV s<sup>-1</sup>, CD curves at a current density of 0.25 A g<sup>-1</sup> and Nyquist plots of GN51P are shown in Fig. 3.52a, Fig. 3.52b and Fig. 3.52c, respectively. It is observed from the figures that the nanocomposite GN451P exhibit less redox area, lesser discharge time and higher resistance along the real axis of the Nyquist plots indicating the low energy storage by GN51P in the presence of magnetic field of 625 μT. The specific capacitance obtained without magnetic field is 23.25 F g<sup>-1</sup> which is 44.86% higher than the specific capacitance (12.82 F g<sup>-1</sup>) obtained in the presence of magnetic field of 625 μT. This decrease in specific capacitance despite of high magnetic susceptibility (628) is attributed to the low conductivity of GN51P, which is well seen from the Nyquist plots as the GN51P exhibit a very high resistance along real axis of the Nyquist plot. The low conductivity is due to the presence of high amount of semiconducting Ni(OH)<sub>2</sub> with the band gap of 3 eV (Hermet et al. 2011).

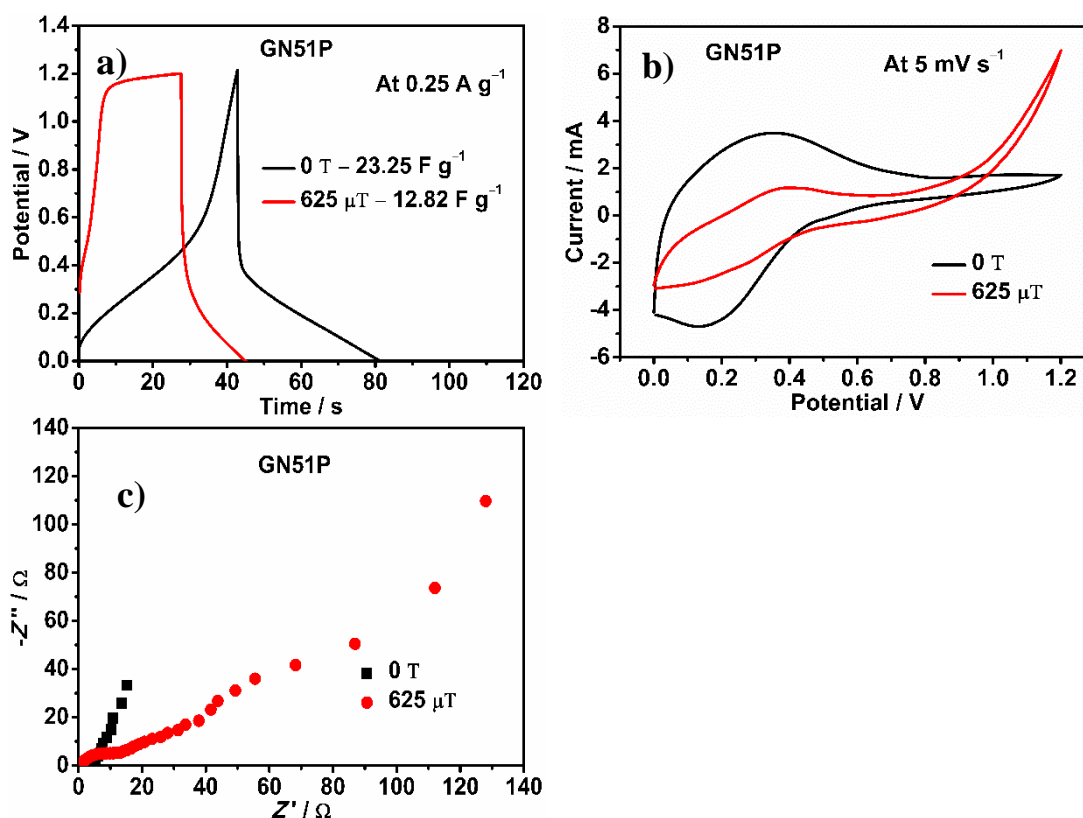


**Fig. 3.52** (a) CV curves at a scan rate of 5 mV s<sup>-1</sup> (b) CD curves at a current density of 0.25 A g<sup>-1</sup> (c) Nyquist plots, of GN51P.

It is clear from the above observations that the redox area and discharge time varies with the change in the weight percentage of Ni(OH)<sub>2</sub>, indicating its role in storing energy. It is important to note that in the absence of magnetic field the composite with the least amount of Ni(OH)<sub>2</sub> (24%) (GN24P), exhibits a highest specific capacitance of 33.60 F g<sup>-1</sup> at a current density of 0.25 A g<sup>-1</sup>. The further increase in the percentage of Ni(OH)<sub>2</sub>, beyond 24% leads to the decrease in specific capacitance. This observation is due to the decrease in the conductivity of the composite as a whole, as the weight percentage of semiconducting Ni(OH)<sub>2</sub> (3 eV) (Hermet et al. 2011) increases. On the other hand as the weight percentage of Ni(OH)<sub>2</sub> increases the magnetic susceptibility increases (Fig. 3.53), up to 48 wt %, which is due to the higher magnetic response provided by the higher amount of Ni(OH)<sub>2</sub>. This increase in magnetic susceptibility in turn transcends the limitation of low conductivity of composites when Ni(OH)<sub>2</sub> present in the composite is higher enough to produce poor electrochemical performance.

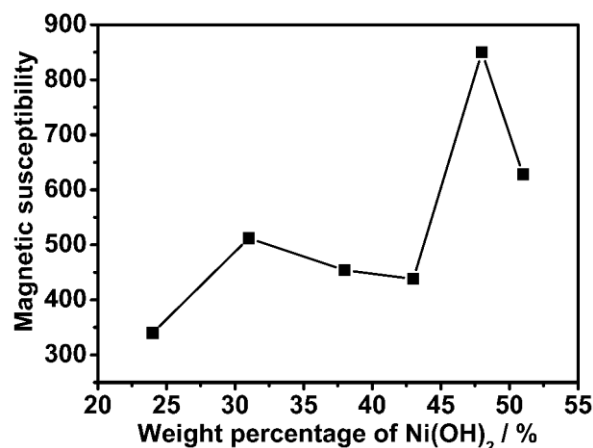


**Fig. 3.53** Plot of magnetic susceptibility versus weight percentage of Ni(OH)<sub>2</sub>.

The higher electrochemical performance of GN48P is attributed to its higher response to the applied magnetic field as compared to that of other composites. Therefore, further studies were carried out only for GN48P at different applied magnetic fields (0T, 415  $\mu$ T, 551  $\mu$ T, 625  $\mu$ T, 657  $\mu$ T, 676  $\mu$ T, and 682  $\mu$ T). The obtained electrochemical performances of GN48P are discussed in successive sections.

#### 3.5.1.1. CV studies

The CV curves of GN48P at different magnetic fields at a scan rate of 5  $\text{mV s}^{-1}$  shown in Fig. 3.54a. The CV curves are not rectangular in shape but are with redox peaks, indicating the capacitance results from redox process of Ni(OH)<sub>2</sub> and PANI along with the EDL capacitance of rGO (Han et al. 2014). The redox transformations of PANI leucoemeraldine to emeraldine and emeraldine to pernigraniline (Xia et al. 2012b) and that of Ni(OH)<sub>2</sub> is transformation from Ni(OH)<sub>2</sub> to Ni(OOH) and vice versa (Park et al. 2019). These redox peaks are shifted in their positions on altering the magnetic field, signifying the change of polarity (Maitra et al. 2017) on every increase in the magnetic field. The area under the redox peaks is the measure of charge stored (Asen and Shahrokhian 2017c) in the electrode materials. As the magnetic field increases, the redox area also increases which evidently confirms the effect of magnetic field in increasing the charge storage in the electrode material. The increase in absolute area (redox area) with the increase in magnetic field, is attributed to the decreased intrinsic resistance and increased conductance of the electrode. It is evident that, the magnetic field of 625  $\mu$ T gives the highest redox area of 18.81 mA.V, signifying its

highest capacitance. The CV curves of GN48P composite at a magnetic field of 625  $\mu\text{T}$  and at different scan rates are shown in Fig. 3.54b. The composite does not deviate from its capacitive behavior even at a scan rate of  $2 \text{ V s}^{-1}$ , apprising its high rate capability and better diffusion of electrolyte at high scan rates (Pendashteh et al. 2015).

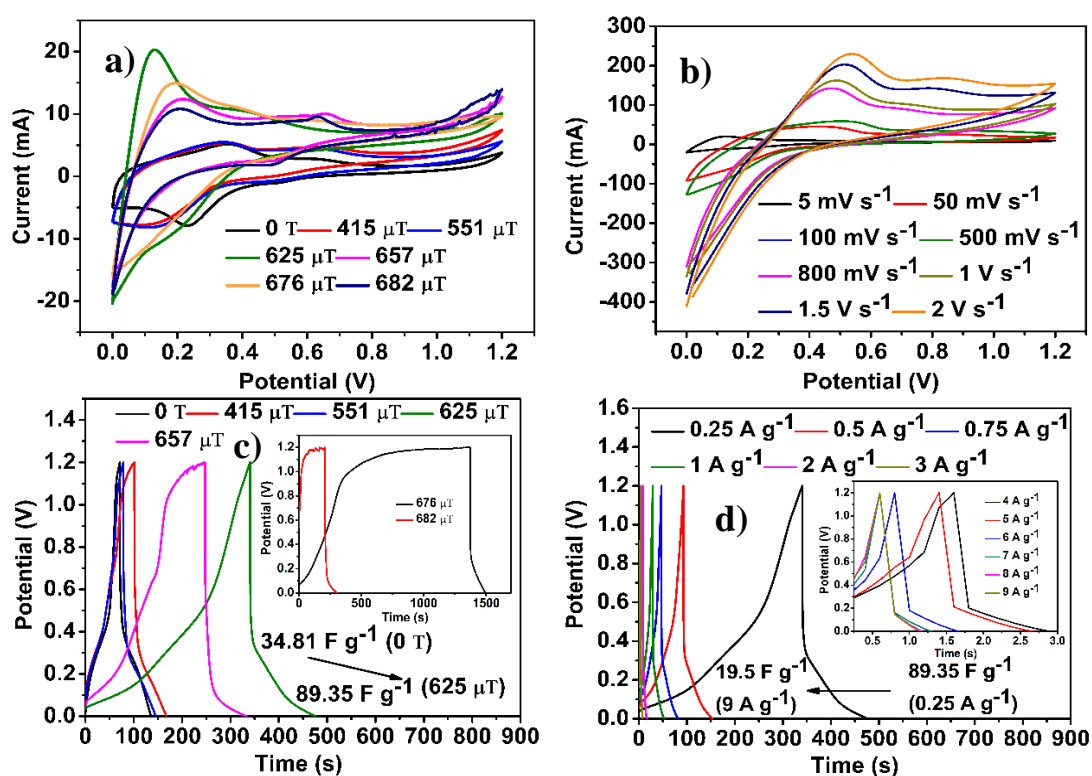


**Fig. 3.54** (a) CV curves of GN48P at different magnetic fields at a scan rate of  $5 \text{ mV s}^{-1}$  (b) CV curves of GN48P at a magnetic field of  $625 \mu\text{T}$  at different scan rates (c) CD curves of GN48P at different magnetic fields at a current density of  $0.25 \text{ A g}^{-1}$  (d) CD curves of GN48P at a magnetic field of  $625 \mu\text{T}$  and at different current densities.

### 3.5.1.2. GCD studies

The charge discharge (CD) curves of GN48P at different magnetic fields at a current density of  $0.25 \text{ A g}^{-1}$  are depicted in Fig. 3.54c. The curves are quasi-triangular, indicating the combination of both faradaic and non-faradaic processes in storing the energy (Mondal et al. 2017). The discharge time is the measure of the energy stored by a material (Jin and Jia 2015) and it is observed that as the magnetic field changes the discharge time of the electrode material changes. This is attributed to the alteration of

intrinsic resistance of the material by the magnetic field, majorly caused by the presence of antiferromagnetic material  $\text{Ni}(\text{OH})_2$  in the electrode material. GN48P takes the longest discharge time at a magnetic field of 625  $\mu\text{T}$ , implying a highest energy storage at a magnetic field of 625  $\mu\text{T}$ . The electrochemical parameters obtained for GN48P at different applied magnetic fields and at a current density of 0.25  $\text{A g}^{-1}$  are listed in Table 3.18.

**Table 3.18** The electrochemical parameters of GN48P at different magnetic fields at 0.25  $\text{A g}^{-1}$ .

Magnetic field applied to GN48P ( $\mu\text{T}$ )	$C_s$ ( $\text{F g}^{-1}$ )	$E$ ( $\text{W h kg}^{-1}$ )	$P$ ( $\text{W kg}^{-1}$ )	$\eta$ (%)
0	34.81	6.96	388.00	90.73
415	39.80	7.96	430.36	66.33
551	40.71	8.14	436.24	85.71
625	89.35	17.87	471.99	39.90
657	90.33	18.06	758.04	34.65
676	97.27	19.45	560.31	9.10
682	89.82	17.96	666.70	9.70

As seen from Table 3.18, the specific capacitance ( $C_s$ ) of GN48P increases with the increase in magnetic field up to 676  $\mu\text{T}$ . But, the further increase in current density at the applied magnetic fields of 657  $\mu\text{T}$  and 676  $\mu\text{T}$  causes a sudden loss of capacitive behavior beyond 1  $\text{A g}^{-1}$ . Therefore, these magnetic fields were not considered for the further study. At an applied magnetic field of 625  $\mu\text{T}$ , GN48P not only yields a high  $C_s$  (89.45  $\text{F g}^{-1}$ ) at 0.25  $\text{A g}^{-1}$  but also it maintains to yield moderate  $C_s$  values even at higher current densities. Therefore, the magnetic field of 625  $\mu\text{T}$  was considered as an effective magnetic field for further studies. The CD curves of GN48P at a magnetic field of 625  $\mu\text{T}$  at different current densities ranging from 0.25 to 9  $\text{A g}^{-1}$  are shown in Fig. 3.54d. The  $C_s$  decreases as the current density increases, as a result of the effective ingress of electrolyte ions into the electrode, covering maximum bulk at low current densities; and the poor electrolytic diffusion at high current densities as the electrolyte fails to cover whole of the electrode material effectively.



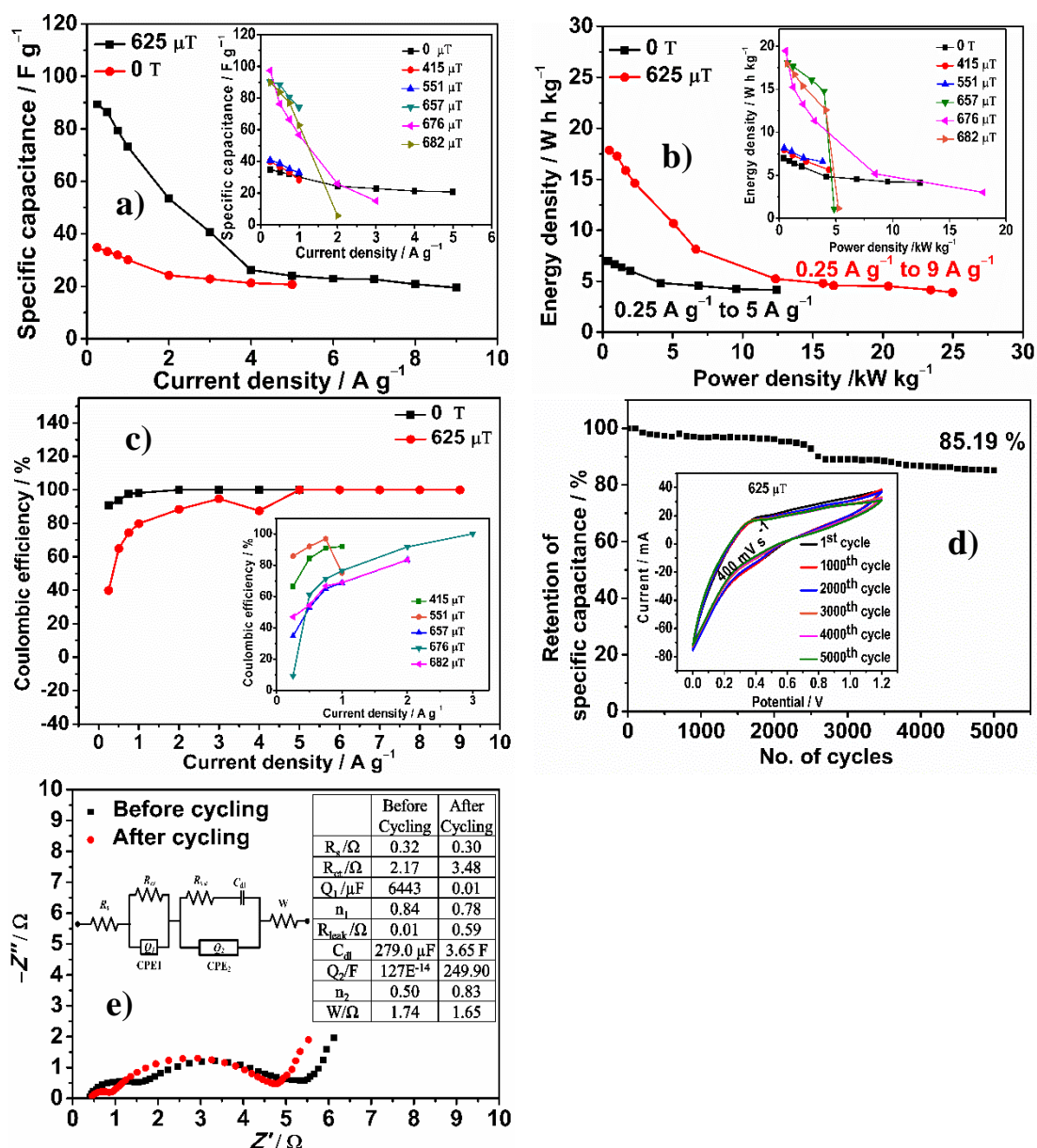


**Fig. 3.55** (a) Plots of specific capacitance versus current densities (b) Ragone plots and (c) Plots of coulombic efficiency versus current densities of GN48P at different applied magnetic fields (d) Plots of percentage retention of capacitance versus number of cycles of GN48P at an applied magnetic field of 625 μT with an inset of CV curves obtained after every 1000 cycles upto 5000 cycles (e) Comparison of Nyquist plots obtained before and after the cyclic studies with an inset of table showing the equivalent circuit parameters values.

Fig. 3.55a shows the plots of  $C_s$  as a function of current densities. The composite GN48P continues to exhibit moderate  $C_s$  (19.51 F g<sup>-1</sup>) up to 9 A g<sup>-1</sup>. This is attributed

to the high rate capability of GN48P at the applied magnetic field of 625  $\mu\text{T}$ , caused by the nanochannels present in the composites enabling the electrolytic ions to penetrate deep into the electrode materials effectively even at higher current densities. The specific capacitance obtained with the magnetic field of 657  $\mu\text{T}$  at current densities of 0.25  $\text{A g}^{-1}$  and 2  $\text{A g}^{-1}$  are 90.33  $\text{F g}^{-1}$  and 5.49  $\text{F g}^{-1}$ , respectively. The specific capacitance obtained with the magnetic field of 676  $\mu\text{T}$  at current densities of 0.25  $\text{A g}^{-1}$  and 2  $\text{A g}^{-1}$  are 97.27  $\text{F g}^{-1}$  and 25.84  $\text{F g}^{-1}$ , respectively. The specific capacitance obtained with the magnetic field of 682  $\mu\text{T}$  at current densities of 0.25  $\text{A g}^{-1}$  and 2  $\text{A g}^{-1}$  are 89.82  $\text{F g}^{-1}$  and 5.72  $\text{F g}^{-1}$ , respectively. These observations suggest that at the high magnetic field the GN48P could deliver high specific capacitance at low current density, but lacks the sustainability at higher current densities beyond 1  $\text{A g}^{-1}$ . The specific capacity ( $Q$  in  $\text{C g}^{-1}$ ) of GN48P at a current density of 0.25  $\text{A g}^{-1}$  is calculated using Equation 2.5 is 107.05  $\text{C g}^{-1}$ . The time constant ( $\tau$ ), which gives a measure of responsiveness of the device and energy stored, (Parlak et al. 2017; Yassine et al. 2017) was calculated for GN48P at different magnetic fields. The time constant of GN48P at magnetic fields of 0 T, 415  $\mu\text{T}$ , 551  $\mu\text{T}$ , 625  $\mu\text{T}$ , 657  $\mu\text{T}$ , 676  $\mu\text{T}$ , and 682  $\mu\text{T}$ , at a current density of 0.25  $\text{A g}^{-1}$  are 1.1469 s, 1.3280 s, 1.3509 s, 3.7392 s, 2.3598 s, 4.3774 s and 2.6946 s, respectively. The  $\tau$  of 3.7392 s at 625  $\mu\text{T}$  is the second highest time constant in the series, indicating the high energy stored in it. Fig. 3.55b shows the Ragone plots at different applied magnetic fields. GN48P exhibits an energy density ( $E$ ) of 17.85  $\text{W h kg}^{-1}$  and power density ( $P$ ) of 471.99  $\text{W kg}^{-1}$  at a current density of 0.25  $\text{A g}^{-1}$  and exhibits an  $E$  of 3.9  $\text{W h kg}^{-1}$  and  $P$  of 23414.63  $\text{W kg}^{-1}$ , even at a high current density of 9  $\text{A g}^{-1}$ . These values are 156.86% higher than that of the results obtained in the absence of a magnetic field. Fig. 3.55c depicts the plots of coulombic efficiency ( $\eta$ ) versus current density. It is seen that, at an applied magnetic field of 625  $\mu\text{T}$ , GN48P exhibits lower coulombic efficiencies at lower current densities due to the slow diffusion of electrolyte into the electrode material, causing a delay in charging. With the increasing current density,  $\eta$  also increases due to the rapid diffusion of electrolyte, causing fast charging and discharging, Thus the value of  $\eta$  increases to 100% at higher current densities.

The cyclic stability studies on GN48P was carried out with an applied magnetic field of 625  $\mu\text{T}$  and at a scan rate of 400  $\text{mV s}^{-1}$ , for 5000 cycles. The plot of retention of specific capacitance versus number of cycles is shown in Fig. 3.55d. The composite retains 85.14 % of its initial capacitance till 5000 cycles. The CV curves obtained after every 1000 cycles upto 5000 cycles are depicted at the inset of Fig. 3.55d, from which it is observed that the redox area decreases as the number of cycles increases. The deterioration is due to the increase in charge transfer resistance ( $R_{\text{ct}}$ ) from 2.17  $\Omega$  to 3.48  $\Omega$  and leakage resistance from 0.01  $\Omega$  to 0.59  $\Omega$ . On the other hand, the solution resistance ( $R_s$ ) is changing insignificantly and Warburg diffusion resistance decreases from 1.74  $\Omega$  to 1.65  $\Omega$ , respectively. The electrical double layer capacitance ( $C_{\text{dl}}$ ) increases from 279.0  $\mu\text{F}$  to 3.65 F. These factors are responsible for the retention of initial capacitance despite of high  $R_{\text{ct}}$ . These resistance values are obtained by fitting the Nyquist plots (Fig. 3.55e) with an equivalent circuit of  $R_s(R_{\text{ct}}Q_1)((R_{\text{leak}}C_{\text{dl}})(Q_2))W$  (inset of Fig. 3.55e) using the software ZsimpWin 3.21. The Nyquist plots obtained before and after cyclic studies are shown in Fig.3.55e. The values of impedance parameters obtained from the equivalent circuit fitment are listed in the table presented at the inset of Fig. 3.55e.

### 3.5.1.3.EIS studies

Figure 3.56a presents the Nyquist plots of GN48P at different magnetic fields. The Nyquist plots comprise of semicircles at the high frequency region and Warburg diffusion components at the low frequency region, indicating the capacitive behavior of the composite GN48P. Fig. 3.56b depicts the circuit fitment for the Nyquist plot of GN48P at an applied magnetic field of 625 $\mu\text{T}$ , with the equivalent circuit (mean error < 3%) at the inset. The electrical elements present in the equivalent circuit are, solution resistance ( $R_s$ ) (0.32  $\Omega$ ), charge transfer resistance ( $R_{\text{ct}}$ ) (2.17  $\Omega$ ), leakage resistance ( $R_{\text{leak}}$ ) (0.01  $\Omega$ ), War-burg resistance ( $W$ ) (1.74  $\Omega$ ), electrical double layer capacitance ( $C_{\text{dl}}$ ) (279  $\mu\text{F}$ ) and constant phase elements  $Q_1$  and  $Q_2$ . The constant phase elements (CPE)  $Q_1$  and  $Q_2$  (6443  $\mu\text{F}$  and  $127 \times 10^{-8}$   $\mu\text{F}$ ) are used instead of ideal capacitances  $C_1$  and  $C_2$  to account for the roughness present in the electrode material, as explained in section 3.1.2.3. The obtained roughness factors are 0.84 and 0.50, signifying the

moderate capacitive behavior of GN48P. The electrical changes that take place on the device, on applying magnetic field of 625  $\mu\text{T}$ , are ascertained by comparing the equivalent circuit fitment data of Nyquist plots obtained in absence and in the presence of the magnetic field and the data are listed in Table 3.19.

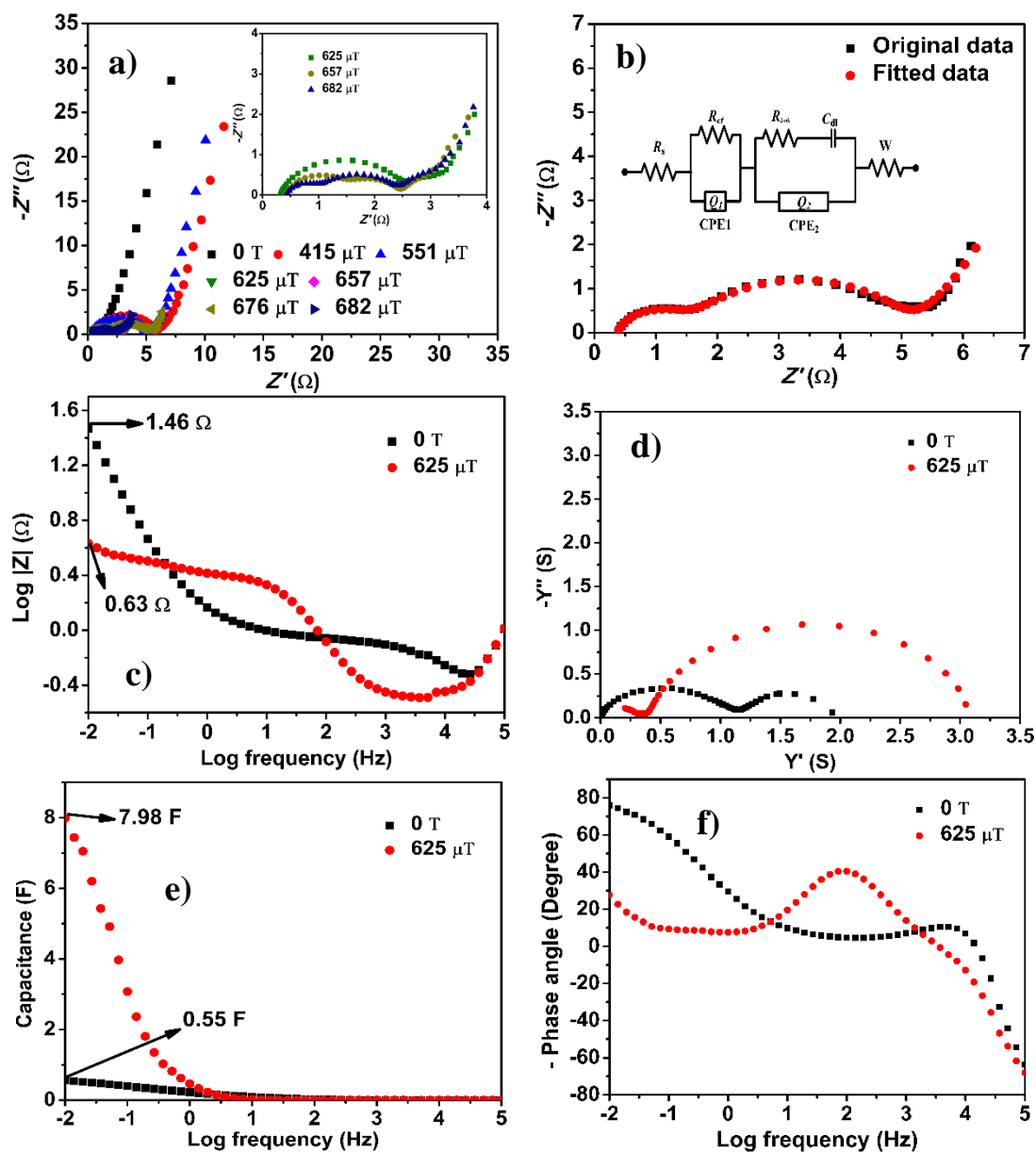


**Fig. 3.56** (a) Nyquist plots of GN48P at different magnetic fields (b) Circuit fitment of GN48P with the equivalent circuit in the inset (c) Bode magnitude plots of GN48P at 0 T and 625  $\mu\text{T}$  (d) Admittance plots of GN48P at 0 T and 625  $\mu\text{T}$  (e) Plots of capacitance versus log frequency of GN48P at 0 T and 625  $\mu\text{T}$  (f) Bode phase angle plots of GN48P at 0 T and 625  $\mu\text{T}$ .

It is seen from Table 3.19 that  $R_s$ ,  $R_{ct}$ , and  $R_{leak}$  are reduced in the presence of the applied magnetic field, rationalizing the increase in the performance on applying the magnetic field. The increase in Warburg resistance causes the slow diffusion of electrolyte into the electrode materials, decreasing the coulombic efficiency and  $C_{dl}$  in the presence of magnetic field. The decrease in roughness factor causes more depressed semicircle rather than a perfect semicircle, causing the device to slightly deviate from its ideality with low CPEs ( $Q_1$  and  $Q_2$ ).

**Table 3.19** The impedance parameters in the absence and in the presence of magnetic field.

Magnetic field	$R_s$ ( $\Omega$ )	$R_{ct}$ ( $\Omega$ )	$Q_1$ ( $\mu F$ )	$n_1$	$R_{leak}$ ( $\Omega$ )	$C_{dl}$	$Q_2$ ( $\mu F$ )	$n_2$	$W$ ( $\Omega$ )
0 T	0.38	515.70	615700.00	0.96	0.45	2.779 F	775.10	0.75	0.63
625 $\mu T$	0.32	2.17	6443.00	0.84	0.01	279 $\mu F$	$127 \times 10^{-14}$	0.50	1.74

It is seen from the Bode magnitude plots in Fig. 3.56c that GN48P exhibits lower impedance (0.63  $\Omega$ ) in the presence of the magnetic field than in the absence (1.46  $\Omega$ ) in the low frequency region. Fig. 3.56d shows the admittance plots of GN48P. It is observed that GN48P exhibits high conductance at an applied magnetic field of 625  $\mu T$ , which is higher than the conductance exhibited in the absence of the magnetic field. The low impedance and high conductance result in high capacitance, which is shown in Fig. 3.56e. GN48P exhibits the capacitance of 7.98 F at low frequency in the presence of the magnetic field, which is higher than the capacitance (0.55 F) exhibited in the absence of the magnetic field. The capacitance ( $C$ ) values were calculated using Equation 2.10 (Wu et al. 2015b). Fig. 3.56f depicts Bode phase angle plots of GN48P in the absence and in the presence of magnetic fields. At low frequency, in the absence of the magnetic field, the phase angle reaches close to  $-90^\circ$ , signifying the fast diffusion of electrolyte and thus fast charging and discharging (Warburg diffusional resistance = 0.63  $\Omega$ ). In the presence of the magnetic field, the phase angle reaches to a low value of  $-27.77^\circ$ , signifying the slow diffusion of electrolyte (Warburg diffusional resistance = 1.74  $\Omega$ ) in to the electrode material causing long charging time. The relaxation time

( $\tau_0$ ) is the minimum time that is required by the device to discharge (discharge time) its stored energy with an efficiency more than 50% of its maximum value (Sheng et al. 2012b; Wu et al. 2015b) and the discharge time is directly proportional to the amount of energy stored (Jin and Jia 2015). The relaxation time calculated for GN48P at magnetic field strengths of 0 T, 415  $\mu$ T and 551  $\mu$ T are 3.2847 s, 29.9433 s and 32.4339 s, indicating the increase in the relaxation time with increase in magnetic field strength, and in turn indicating the increase of energy storage with the increase in magnetic field strength. Since the Bode phase plot of GN48P at 625  $\mu$ T, 657  $\mu$ T, 676  $\mu$ T and 682  $\mu$ T did not reach  $-45^\circ$  their  $\tau_0$  value were not calculated.

The comparison of the performance of the composite, GN48P, with a few of the similar studies are shown in Table 3.20. An observation on the previously reported literatures, on the effect of magnetic field in improving the energy storage properties of magnetic nanoparticles and the composites made of ferromagnetic materials like NiO, Fe<sub>2</sub>O<sub>3</sub>, Co<sub>3</sub>O<sub>4</sub>, etc., discloses that the studies carried out were not with the practical supercapacitor cells, but with three electrode system with an electromagnet used to provide the magnetic fields. The magnetic fields used for the composites were as follows: 9.5 mT (NiO/nickel foam) (Lu et al. 2015) , 0.072 T (graphene/nickel foam) (Zhu et al. 2013), 0.072 T graphene/Fe<sub>2</sub>O<sub>3</sub>/nickel foam (Zhu et al. 2013) and 0.072 T (carbon/Co<sub>3</sub>O<sub>4</sub>/nickel foam) (Zhu et al. 2014). The present work involves the practical supercapacitor cell (two electrode system) and permanent magnets to supply magnetic fields. The permanent magnets provide magnetic fields in the unit of micro tesla ( $\mu$ T) which are far less than the magnetic field strengths that are reported. A low applied magnetic field of 625  $\mu$ T resulted in the 156% enhancement in electrochemical performances compared to the electrochemical performance obtained in the absence of applied magnetic field.

**Table 3.20.** Comparison of obtained results of GN48P under a magnetic field 625  $\mu$ T with reported similar systems.

Composite	Electrolyte	E (V)	$C_s$ (F g <sup>-1</sup> )		$E$ (W h kg <sup>-1</sup> )		$P$ (W kg <sup>-1</sup> )		Enhancement (%)	Cyclic stability (with magnetic field)	Ref.
			Without Magnetic field	With magnetic field	Without Magnetic field	With magnetic field	Without Magnetic field	With magnetic field			
<b>Two electrode systems</b>											
Present work rGO/Ni(OH) <sub>2</sub> /PANI	1 M H <sub>2</sub> SO <sub>4</sub>	1.2	34.81	89.43 at 0.25 A g <sup>-1</sup> at 625 $\mu$ T	6.96	17.85	388.00	471.99	156	85.19 % retention up to 5000 cycles at 400 mV s <sup>-1</sup>	
<b>Three electrode systems</b>											
NiO/nickel foam	3M KOH	0.4		932.1 at 0.5 A g <sup>-1</sup> at 9.5 mT	-		-	-	-	91.9% retention for 1000 cycles at 2 A g <sup>-1</sup>	(Lu et al. 2015)
Graphene/nickel foam	1 M Na <sub>2</sub> SO <sub>4</sub>	0.8	24.7 at 2 mV s <sup>-1</sup>	41.24 at 2 mV s <sup>-1</sup>					67.1 at 2 mV s <sup>-1</sup>		(Zhu et al. 2013)
Graphene/Fe <sub>2</sub> O <sub>3</sub> /nickel foam	1 M Na <sub>2</sub> SO <sub>4</sub>	0.8	<10	-	-	-	-	-	154.6 at 2 mV s <sup>-1</sup>	96.1 % retention after 500 cycles	(Zhu et al. 2013)
Carbon/cobalt/nickel foam	1M KOH			100 at 5 mV s <sup>-1</sup> at 0.072 T							(Zhu et al. 2014)

### 3.6.GNP WITH METHANE SULPHONIC ACID AS DOPANT

#### 3.6.1. Structural characterization

The structural characterizations are similar to the details explained in section 3.2.1., except for the change in morphology and particle size.

##### 3.6.1.1. XRD studies

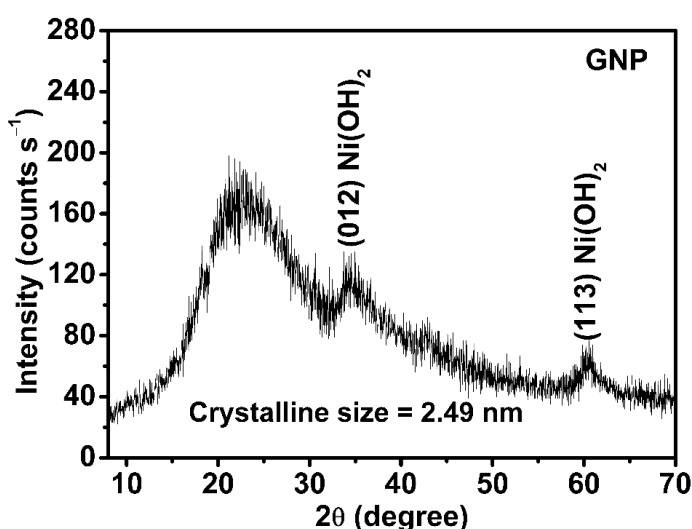


**Fig. 3.57** XRD pattern of GNP synthesized using MSA as dopant.

The XRD pattern of GNP synthesized using MSA as a dopant is shown in Fig. 3.57. The broad peak starting from  $2\theta$  of  $17^\circ$  to near  $30^\circ$  is due to PANI (020) and rGO (002) (Mu et al. 2014; Wang et al. 2016a). The broad nature of the peak signifies the intimate intercalation of PANI in between rGO layers (Han et al. 2014). The peaks at  $34.35^\circ$  and  $60.18^\circ$  are due to (012) and (113) planes of  $\text{Ni(OH)}_2$  (JCDPS No. – 38-0715). The crystalline size of  $\text{Ni(OH)}_2$  present is from the most intense peak to be 2.49 nm which is less than the crystalline size of  $\text{Ni(OH)}_2$  (5.64 nm) obtained when synthesized using glacial acetic acid as dopant.

##### 3.6.1.2. FE-SEM analyses

The FE-SEM images of GNP are shown in Fig. 3.58 a, Fig. 3.58b, Fig. 3.58c and Fig.3.58d. The rGO, PANI and  $\text{Ni(OH)}_2$  have layered, fibril and particle morphology, respectively. The usage of MSA as dopant has resulted in enhanced formation of nanochannels for electrolyte percolation and reduction of overall sizes of



nickel hydroxide nanoparticles, leading to the formation of particles with more surface area for redox reaction to occur. The reduction in particle size was confirmed from the XRD results.

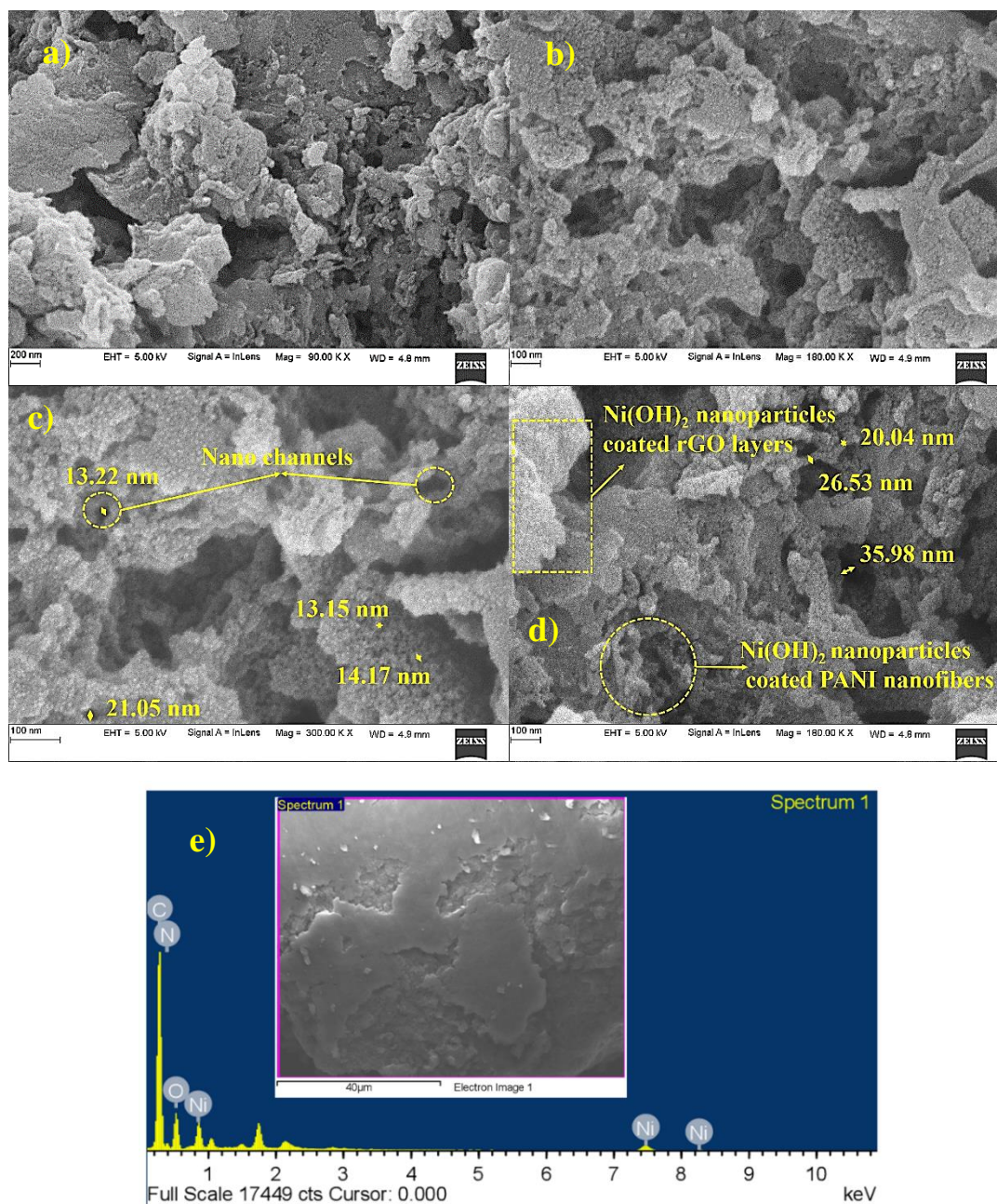


**Fig. 3.58** (a-d) FE-SEM images of GNP synthesized using MSA as dopant (e) EDS of GNP with a spot from which the spectrum was recorded.

The average particle size of Ni(OH)<sub>2</sub> nanoparticles are in the range of ~13 nm to ~14 nm ( Fig.3.58c), the average diameters of nanochannels are in the range of ~13

nm to ~36 nm (Fig. 3.58c and Fig. 3.58d) and the average diameter of Ni(OH)<sub>2</sub> nanoparticles coated PANI nanofibers is in the range of ~20 nm to ~27 nm (Fig. 3.58d). The surface elemental composition of the composite was confirmed by EDS analyses (Fig.3.58e) and results are listed in Table 3.21.

**Table 3.21** The elements present with corresponding weight and atomic percentages.

Elements	Weight %	Atomic %
C	5.73	12.89
N	3.33	51.73
O	15.28	9.51
Ni	10.31	25.87

### 3.6.2. Electrochemical characterizations

**Table 3.22** The nomenclatures of the GNP composites

Component under study	Weight of constituents (mg)			Weight percentage (%)	Nomenclature
	P	N	G		
PANI series	100	50	25	57.10	GNP57
	150	50	25	66.66	GNP67
	200	50	25	72.72	GNP73
	250	50	25	76.90	GNP77
	300	50	25	80.00	GNP80
Ni(OH) <sub>2</sub> series	250	100	25	26.67	GN27P
	250	150	25	35.30	GN35P
	250	200	25	42.11	GN42P
	250	250	25	47.62	GN48P
	250	300	25	52.17	GN52P
rGO series	250	150	50	14.29	G14NP
	250	150	75	20.00	G20NP
	250	150	100	25.00	G25NP

The rGO/Ni(OH)<sub>2</sub>/PANI (GNP) composites were synthesized by varying the weight percentages of each of the constituents namely, polyaniline, nickel hydroxide and reduced graphene oxide (rGO). The weight percentages of the GNP composite and

the nomenclature used are listed in Table 3.22. The composite with a weight percentages of constituents rGO 14%: Ni(OH)<sub>2</sub> 14%: P 72% exhibited the promising electrochemical performance with 1 M H<sub>2</sub>SO<sub>4</sub> as electrolyte. The discussion for the entire studies is presented in following sections.

### 3.6.2.1. CV studies

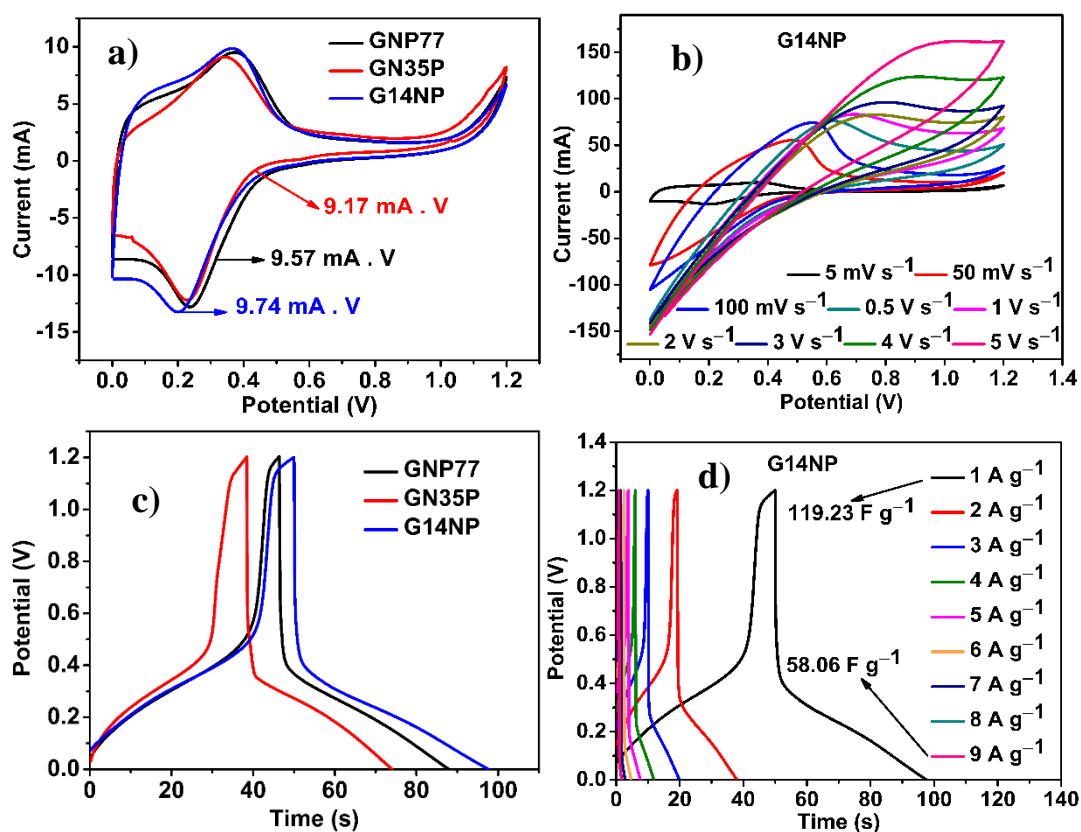


**Fig. 3.59** The CV curves of (a) GNP73, GN35P and G14NP at a scan rate of 5 mV s<sup>-1</sup>, (b) G14NP at different scan rates, CD curves of (c) GNP73, GN35P and G14NP at a current density of 1 A g<sup>-1</sup>, (d) G14NP at different current densities.

The CV curves of GNP composites at a scan rate of 5 mV s<sup>-1</sup> are shown in Fig. 3.59a. The curves are not rectangular in shape, but are with redox peaks indicating the role of faradaic and non-faradaic processes in storing the energy. The redox peaks are due to the redox reaction of Ni(OH)<sub>2</sub> and redox transition of PANI between leucoemeraldine and polaronic emeraldine forms (Xia et al. 2012b) during energy storage. The redox area exhibited by the composite is directly proportional to the amount of energy stored (Han et al. 2014). As it is seen from Fig. 3.59a, the composite

G14NP has the highest area of 9.74 mA.V indicating the high energy storage amongst the composites under study. The three composites namely GNP77, GN35P and G14NP are considered for comparison, due to the high electrochemical performances of these, in comparison with other composites that were studied in each of the series. The CV curves of G14NP at different scan rates ranging from 5 mV s<sup>-1</sup> to 5 V s<sup>-1</sup> are shown in Fig. 3.59b. It is seen from Fig. 3.59b that the G14NP does not deviate from exhibiting capacitive behavior even up to a high scan rate of 5 V s<sup>-1</sup>, signifying its sustainability to high potential and in turn its high rate capability.

### 3.6.2.2. GCD studies

The GCD curves of GNP composites are depicted in Fig. 3.59c. The quasi triangular curves indicate the operation of both faradaic (Wu et al. 2015a) and non-faradaic processes in storing energy. The longest time taken for discharging by G14NP indicates its high energy storage ability (Han et al. 2014). The GCD curves of G14NP at different current densities are shown in Fig. 3.59d. It is seen from the Fig. 3.59d that G14NP exhibits a specific capacitance of 118.34 F g<sup>-1</sup> at a low current density of 1 A g<sup>-1</sup> and maintains to exhibit a moderate specific capacitance of 58.06 F g<sup>-1</sup> at 9 A g<sup>-1</sup>, which is about 50% lower than the specific capacitance obtained at 1 A g<sup>-1</sup>, signifying its good rate capability. The specific capacitances ( $C_s$ ), energy densities ( $E$ ), power densities ( $P$ ) and coulombic efficiencies ( $\eta$ ) of all the composites synthesized by varying the weight percentage of each of constituents are listed in Table 3.23. It is seen from Table 3.23 that on increasing the weight percentages of PANI, the specific capacitance increases up to a weight of 250 mg, corresponding to the weight percentage of 77% (GNP77); and beyond which the specific capacitances decrease. This is due to the formation of random aggregates of PANI, when it is present in excess quantities that cannot be accommodated by the surface area available on the other constituent materials present in the composite. This leads to the ineffective utilization of whole of the electrode material for energy storage (Xu et al. 2010). On increasing the weight of Ni(OH)<sub>2</sub>, there is no increase in electrochemical properties beyond the performance exhibited by GNP77.

**Table 3.23** The electrochemical parameters of GNP composites at a current density of 1 A g<sup>-1</sup>.

Composite	$C_s$ (F g <sup>-1</sup> )	$E$ (W h kg <sup>-1</sup> )	$P$ (kW kg <sup>-1</sup> )	$\eta$ (%)
GNP57	2.54	0.50	1320.93	100.00
GNP67	86.35	17.46	2058.81	88.30
GNP73	88.49	17.69	1685.62	90.43
GNP77	106.60	21.32	4022.81	89.65
GNP80	95.23	19.04	1833.46	84.61
GN27P	44.48	8.89	1929.42	96.57
GN35P	96.99	19.39	1950.70	93.22
GN42P	31.37	6.27	1914.55	98.33
GN48P	44.64	8.92	1805.77	87.25
GN52P	11.66	2.33	1999.63	95.45
G14NP	118.34	23.66	1790.06	95.20
G20NP	100.52	20.10	1659.67	96.46
G25NP	50.58	10.11	1686.05	87.09

This is due to the fact that, the increase of semiconducting Ni(OH)<sub>2</sub> (band gap ~3 eV) decreases the conductivity of the composites leading to the poor performance (Hermet et al. 2011). Therefore, the weight of Ni(OH)<sub>2</sub> was maintained as low as 50 mg (15.38%), which corresponds to GNP77. Eventually on increasing the weight of rGO the increase in specific capacitance is observed up to 50 mg (14.29% corresponds to G14NP) and beyond which the decrease in specific capacitance is observed. This is due to the increase of rGO beyond 50 mg produces more surface area in such a way that the PANI and Ni(OH)<sub>2</sub> are dispersed on them are disconnected leading to the inefficient flow of charge carriers and there by hampering the energy storage. The composite with a weight percentages of constituents of rGO 14%: Ni(OH)<sub>2</sub> 14%: P72% (G14NP) is with the best electrochemical performances among the composites synthesized. The *ESRs* of GNP77, GN35P and G14NP at a current density of 1 A g<sup>-1</sup> are 0.391 Ω, 0.395 Ω and 0.348 Ω, respectively. The specific capacities of GNP77, GN35P and G14NP at a current density of 1 A g<sup>-1</sup> are 127.93 C g<sup>-1</sup>, 116.28 C g<sup>-1</sup> and 142.01 C g<sup>-1</sup>, respectively.

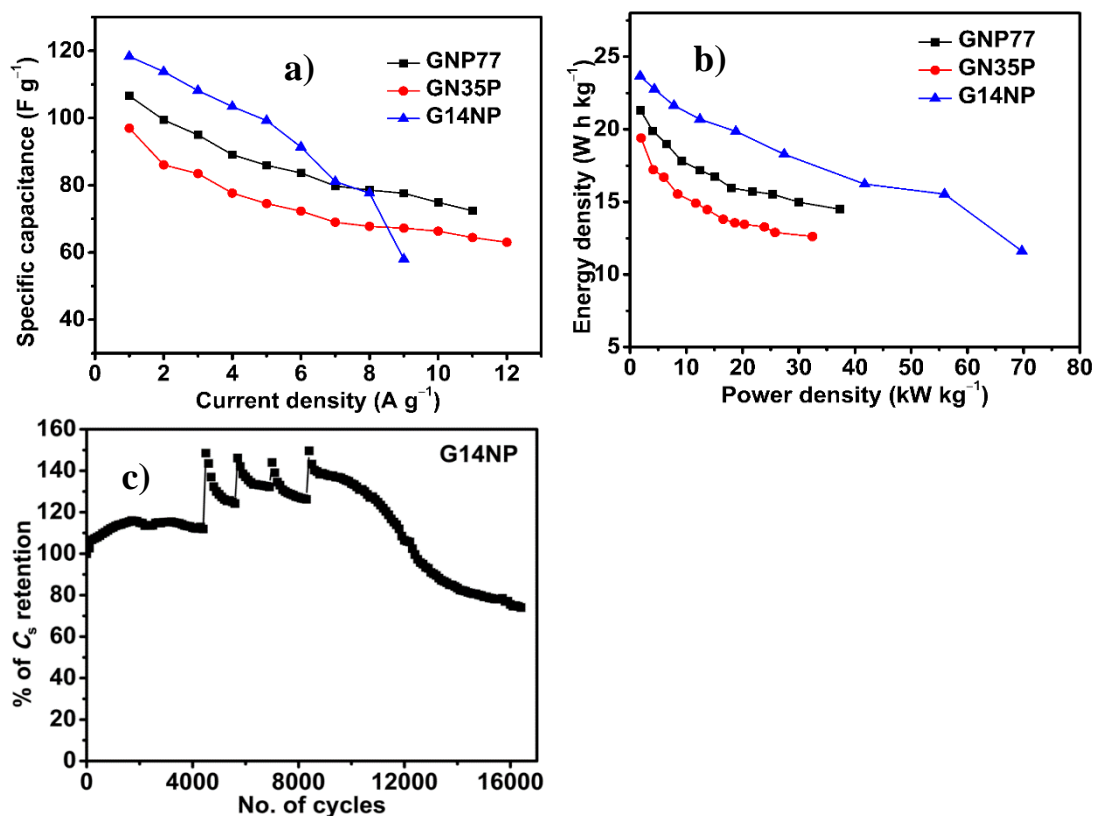


**Fig. 3.60** (a) Plots of specific capacitance versus current density of GNP77, GN35P and G14NP; (b) Ragone plots of GNP77, GN35P and G14NP; (c) Plot of retention of specific capacitance versus number of cycles of cycles.

The energy densities and power densities of GNP composites are listed in Table 3.23. The plot of specific capacitance versus current density and Ragone plots are shown in Fig. 3.60a and 3.60b, respectively. It is seen from the figures that the G14NP possesses high specific capacitance and high energy density, due to the low intrinsic resistance and high conductivity. The cyclic stability of G14NP was studied using CV technique at a scan rate of 400 mV s<sup>-1</sup> (Fig. 3.60c). The G14NP did not lose its initial specific capacitance, rather the specific capacitance increased with the increase in the number of cycles up to 12500 cycles and reached a maximum specific capacitance. The subsequent increase in cycles accompany the reduction of specific capacitance till 16500 cycles. But, even at the end of the 16500 cycles, the G14NP still retains 75% of the maximum specific capacitance obtained after 12500 cycles. To study the electrochemical changes that take place with the increase in the number of cycles the

electrochemical performance studies were carried out after 4500, 7000, 11500 and 16500 cycles.

**Table 3.24** Electrochemical parameters of G14NP after different number of cycles.

Number of cycles	$C_s$ (F g <sup>-1</sup> )	$E$ (W h kg <sup>-1</sup> )	$P$ (kW kg <sup>-1</sup> )	$\eta$ (%)
0	118.34	23.66	1790.06	95.20
4500	280.11	56.02	2307.55	64.64
7000	276.75	55.29	1564.06	62.12
11500	602.40	120.48	2584.83	66.37
16500	289.01	57.80	2550.15	72.72

The CV curves, CD curves, plots of specific capacitance versus current density, Ragone plots and plots of coulombic efficiency versus current density, obtained after different number of cycles are shown in Fig. 3.61a-e. The specific capacitances ( $C_s$ ), energy densities ( $E$ ), power densities ( $P$ ) and coulombic efficiencies ( $\eta$ ) obtained after different number of cycles are listed in Table 3.24.

It is seen from Fig. 3.61a that with the increase in number of CV cycles the area under the redox peaks increases and there is appearance of two new pairs of redox peaks at middle and high end of the potential range. The redox pairs at 0.39 V and 0.55 V are corresponding to the redox transition between benzoquinone and hydroquinone. The later redox pair at 0.86 V and 0.75 V are corresponding to the redox transition between polaronic emeraldine and bipolaronic pernigraniline structure of PANI (Wang et al. 2008; Zhao et al. 2009). These new sets of redox peaks of PANI indicate the fruitful utilization of electrode material by the electrolyte, makes PANI to undergo its maximum redox transition and in turn to yield high amount of energy storage. When the number of cycles reaches 12500, the redox area decreases, indicating the reduced energy storage by the materials, which implies the onset of possible degradation of electrode materials and reduced access of electrolyte into the electrode material. The similar observation is evident from Fig. 3.61b that the time taken for discharging increases with the increase in the number of cycles; and when the cycle number reaches



16500 the time taken by the G14NP to discharge is decreasing indicating its low energy storage.

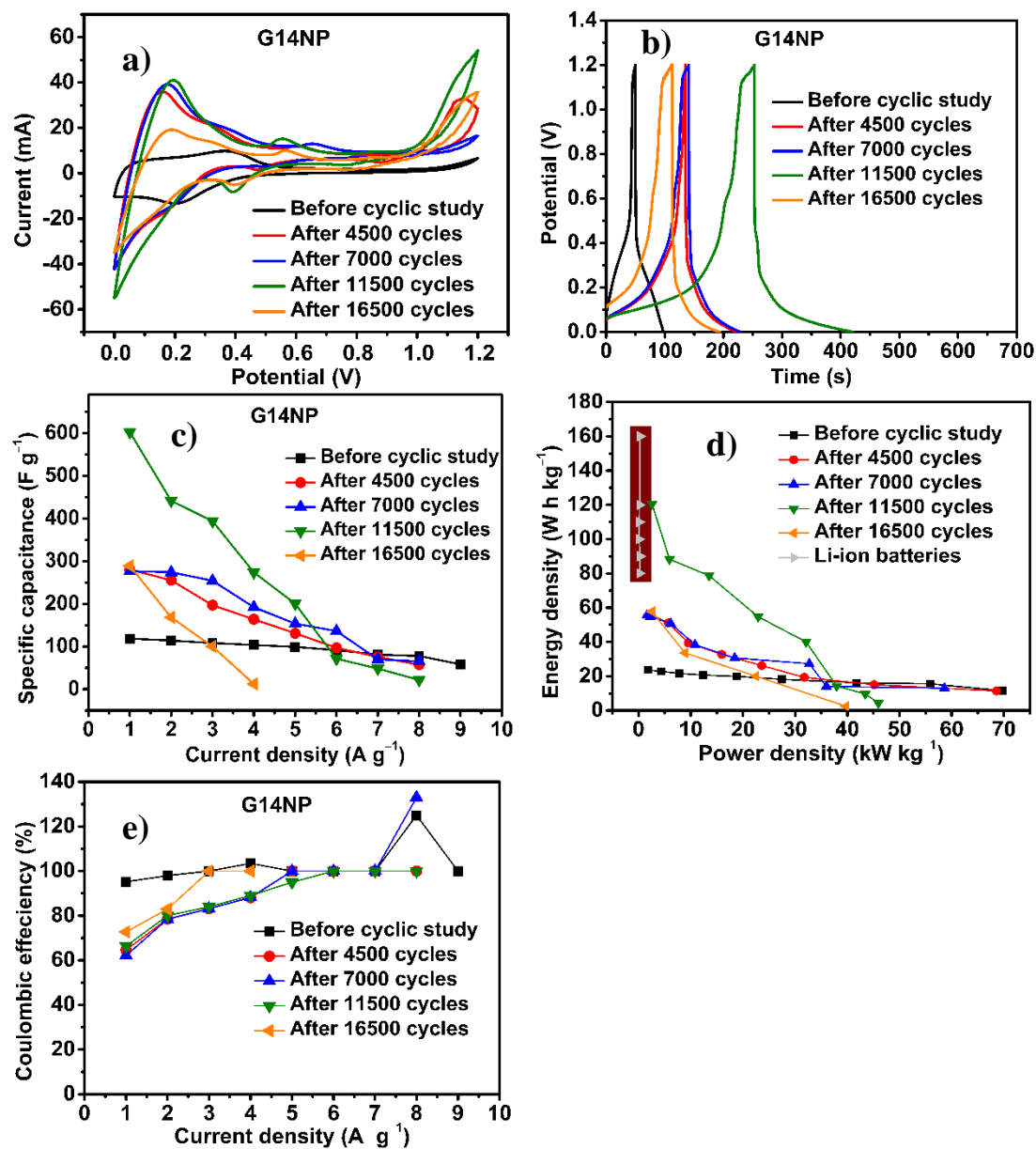


**Fig. 3.61** (a) CV curves (b) CD curves (c) Plots of specific capacitance versus current density (d) Ragone plot (e) Plots of coulombic efficiency versus current density, of G14NP after different number of cycles

The plots of specific capacitance versus current density is shown in Fig.3.61c. It is seen that the enhancement in specific capacitance with the increase in the number of cycles; and the maximum specific capacitance obtained is 602.40  $F g^{-1}$  after 11500



cycles at a current density of  $1 \text{ A g}^{-1}$  (Table 3.24), which is 409.03% enhancement compared to that of specific capacitance obtained before the composite is subjected to cyclic studies. The knee frequencies of G14NP before and after 4500, 7000, 11500 and 16500 cycles are 5.17 Hz, 1.39 Hz, 1.39 Hz, 1.00 Hz and 0.71 Hz, respectively. The low knee frequency of G14NP after 16500 cycles indicates a poor rate capability (Brun et al. 2012). It is seen from the Ragone plots of G14NP before and after number of cycles (Fig. 3.61d), that the maximum energy density of  $120.48 \text{ W h kg}^{-1}$  is obtained after 11500 cycles, which is comparable with the energy densities of Li-ion batteries (Dunn et al. 2011). The enhancement of specific capacitance and energy density on cyclization is due to the structural activation of the composite materials caused by the continuous diffusion of electrolyte, which is believed to open up the nano channels present in the electrode material enabling the most active surface available for the process of formation of electrical double layer and redox reaction (Pendashteh et al. 2015). The high energy density is also due to the promising  $\pi$ - $\pi$  interaction between PANI and rGO causing the migration of charges faster by shortening the charge carrier path caused by good electrolyte percolation (Shen et al. 2013). It is seen from the plots of coulombic efficiency versus current density (Fig. 3.61e) that at low current density, the G14NP exhibits coulombic efficiencies close to 100% before cyclic study, and as the number of cycles increases, the coulombic efficiencies are decreasing close to 70% and as the current density increases it reaches 100% and more. The low coulombic efficiency at low current density is due to the low kinetic interaction of electrolytic ions with the electrode material, causing longer time for charging. At high current densities the faster kinetic interaction of the electrolytic ions with the electrode materials gives rise to faster charging and discharging, in turn higher coulombic efficiency. The exceptionally high stability of the G14NP up to 16500 cycles is due to the sustainability of electrode materials without degradation and effective retardation of the possible volumetric swelling and shrinkage of PANI by the fellow constituent materials rGO and  $\text{Ni(OH)}_2$  (Mu et al. 2014). In order to comprehend the electrochemical changes that the electrode material (G14NP) undergoes with cyclization, the EIS studies were carried out after certain number of cycles. The Nyquist plots, plots of series resistance versus log frequency, Bode magnitude plots, Bode phase angle plots and plots of capacitance versus log frequency are shown in Fig 3.62a-e.

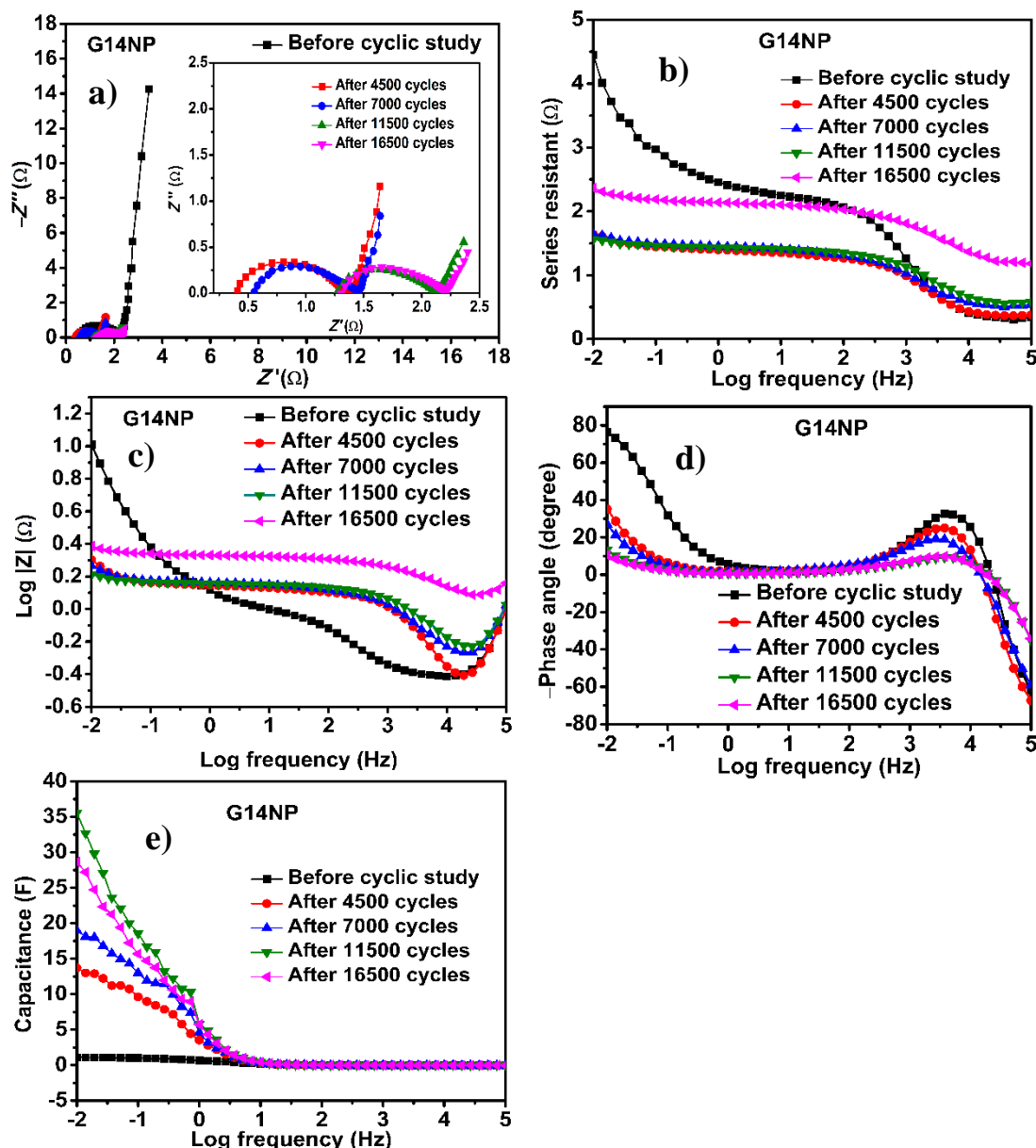


**Fig. 3.62** (a) Nyquist plots, (b) Plots of series resistance versus log frequency, (c) Bode magnitude plot, (d) Bode phase angel plots, (e) Plots of capacitance versus log frequency, of G14NP before and after 4500, 7000, 11500 and 16500 cycles.

It is seen from Fig. 3.62a that the overall resistance of G14NP along real axis reduces with the increase in the number of cycles, which is further confirmed by the plots of series resistance versus log frequency (Fig. 3.62b). The least series resistance of  $1.55 \Omega$  is exhibited by G14NP after 11500 cycles. The decrease in the impedance of G14NP with cycle number is depicted in Bode impedance plots (Fig. 3.62c); and G14NP exhibits the least impedance of  $0.21 \Omega$  after 11500 cycles. The bode phase angle

plots show that as the cycle number increases, the plots reach low phase angles at low frequency range (Fig. 3.62d), which indicates the enhanced energy storage by the G14NP. The above fact also suggests the transition from low energy storing ideal conventional capacitors to the high energy storing supercapacitors, which are believed to be the bridge between conventional capacitors and high energy batteries. The capacitance versus log frequency plots also show the enhancement of capacitance as the number of cycles increases. It is seen in Fig. 3.62e that G14NP exhibits a high capacitance of 35.58 F at low frequency after 11500 cycles. The decrease of intrinsic resistance and increase of conductivity with the increase in number of cycles are the reasons for the enhancement in electrochemical performance. The changes taking place in the electrical elements with the cycle number were quantified by fitting the Nyquist plots obtained at different points of the cyclic stability experiment to an equivalent circuit. The best fitted equivalent circuit is  $R_s(R_{ct}Q_1)((R_{leak}C_{dl})(Q_2))W$  (mean error <1.2%). The magnitude of electrical elements involved are listed in Table 3.25.

**Table 3.25** The electrical parameters of G14NP after subjecting into different number of cycles.

No. of cycles	$R_s$ ( $\Omega$ )	$R_{ct}$ ( $\Omega$ )	$Q_1$ ( $\mu F$ )	$n_1$	$R_{leak}$ ( $\Omega$ )	$C_{dl}$ (F)	$Q_2$ ( $\mu F$ )	$n_2$	$W$ ( $\Omega$ )
0	0.42	1.75	161.70	0.86	0.12	0.7930	356300	0.95	3.68
4500	0.34	1.74	120600	0.62	0.85	17.45	324900	0.86	11.55
7000	0.48	0.75	563200	0.82	0.19	24.48	847500	0.66	14.97
11500	0.01	0.89	942300	0.73	0.39	53.93	6.672 E-11	0.45	18.08
16500	1.27	1.03	203900	0.62	1.07	50.7	827300	0.82	12.04

It is seen from Table 3.25 that there is decrease in solution resistance ( $R_s$ ) and charge transfer resistance ( $R_{ct}$ ), increase in  $Q_1$  and a significant increase in double layer capacitance ( $C_{dl}$ ) with the increase in cycle number up to 11500 cycles, which are the reasons for the enhancement of electrochemical performances. A sudden increase of  $R_s$  to 1.27  $\Omega$ ,  $R_{ct}$  to 1.03  $\Omega$ , leakage resistance ( $R_{leak}$ ) to 1.07  $\Omega$ , a decrease in  $Q_1$  and  $C_{dl}$  after 16500 cycles are the reasons for decrease of electrochemical performance after 16500 cycles.

The energy density of G14NP, was experimented by connecting four supercapacitors fabricated with G14NP, in series and using it to energize LEDs of different colors and DC motors. The commercial Nippo (9V) battery was used for charging the supercapacitor at high current loading. As it is seen in Fig. 3.63a and 3.63b, the G14NP could energize two LED bulbs of blue (~2 V) and green (~1.7 V) color at a time and two DC motors at a time. The power backup application of G14NP was experimented by charging it for 1 min with a 9V Nippo battery at high current loading rate while a DC motor connected with it. On disconnecting the battery power source after 1 min, the motor continued to run for another 1 min. A similar experiment was carried out with a LED which is capable of emitting blue and red light alternatively. On disconnecting the battery power source after 1 min, the alternative switch pattern of blue and red continued to glow for next 5 s and the red color continued to glow for next 30 s. The failure of blue color is due to the reduction in energy available in the supercapacitor to less than 2 V, but red light could glow as it required less energy (1.7 V). Similar observations were made when another experiment was carried out with two individual LEDs of green and blue color connected with a supercapacitor at the same time.

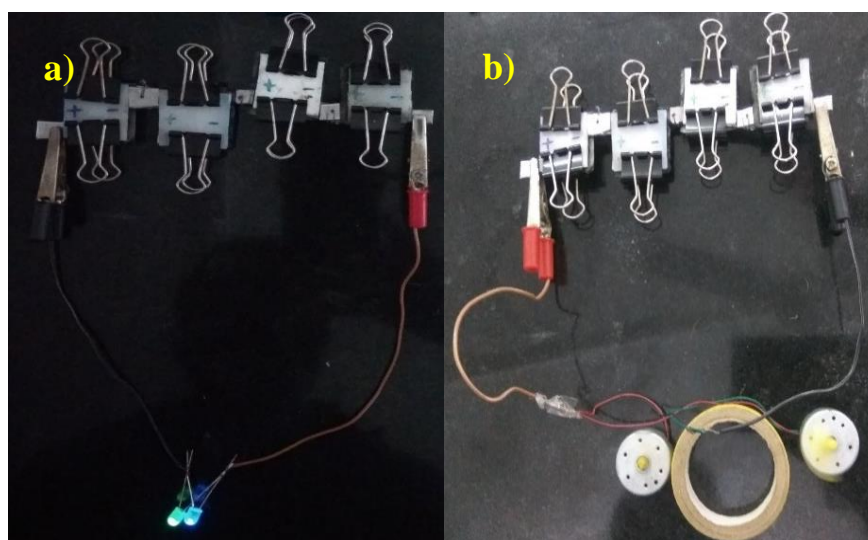


**Fig. 3.63** The G14NP energizing (a) LED of blue (~2 V) and green (~1.7 V) color at a time (b) Two DC motors at a time.

## 3.6.2.3. EIS studies

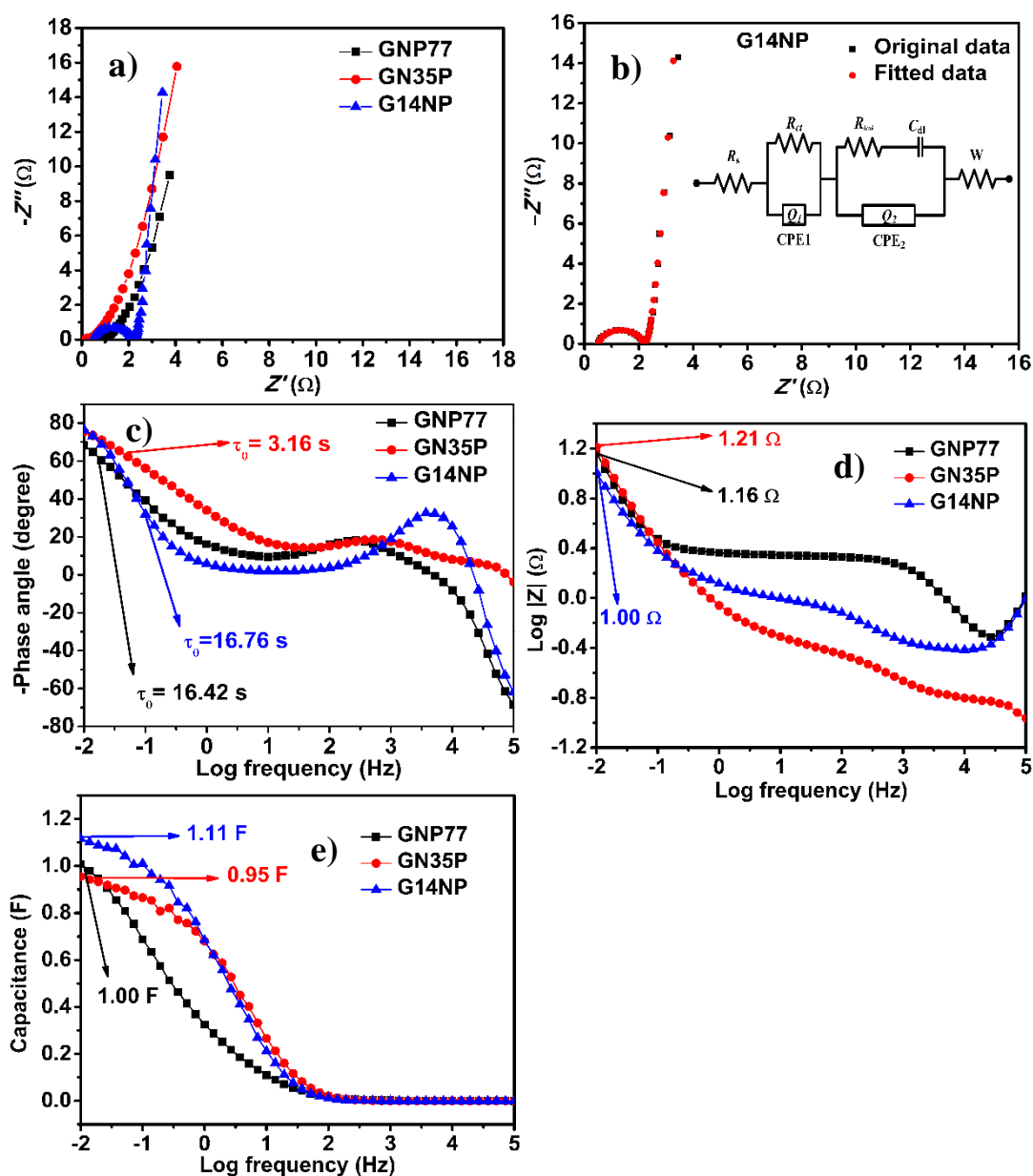


**Fig. 3.64** (a) Nyquist plots (b) Equivalent circuit fitment on Nyquist plot of G14NP (c) Bode phase angle plots (d) Bode magnitude plots (e) Plots of capacitance versus log of frequency, of nanocomposites GNP77, GN35P and G14NP.

The Nyquist plots of nanocomposites GNP77, GN35P and G14NP are shown in Fig. 3.64a. Nyquist plots possess semicircles at high frequency region and linear Warburg portions at low frequency region, indicating capacitive behavior of the GNP composites. It is seen in Fig. 3.64a that the G14NP possesses low resistance along the

real axis, indicating the low intrinsic resistance and high conductivity of G14NP. The equivalent circuit fitment of G14NP and the equivalent circuit are presented in Fig. 3.64b. G14NP exhibited  $R_s$ ,  $R_{ct}$ ,  $Q_1$ ,  $R_{leak}$ ,  $C_{dl}$ ,  $Q_2$  and  $W$  of  $0.42 \Omega$ ,  $1.74 \Omega$ ,  $161.7 \mu F$ ,  $0.12 \Omega$ ,  $0.79 \Omega$ ,  $0.35 F$  and  $3.68 \Omega$ , respectively. The magnitudes of roughness factors  $n_1$  and  $n_2$  are 0.86 and 0.95, indicating the moderate capacitive behavior of G14NP (Dinodi and Shetty 2014).

It seen from the Bode phase angle plots (Fig.3.64c) that the phase angle for G14NP approaches close to  $-90^\circ$ , indicating its capacitive behavior close to an ideal capacitor. The relaxation time calculated is 16.76 s which is higher than those of the GNP77 and GN35P, indicating high energy storage of G14NP. It is seen from the Bode magnitude plots (Fig. 3.64d) that the G14NP possesses lowest impedance of  $1.00 \Omega$  at low frequency region indicating the high conductivity and low intrinsic resistance of the G14NP. The plots of capacitance versus log frequency (Fig. 3.64e) show that G14NP exhibits the high capacitance of 1.11 F at low frequency, which is higher than those of GNP77 and GN35P. The results of EIS studies matches well with GCD studies. The comparison of electrochemical performance exhibited by G11NP and G14NP with similar reported materials are presented in Table 3.26.

**Table 3.26** Comparison of the results of G11NP and G14NP supercapacitor with the reported similar systems.

Composite	Electrolyte	E (V)	$C_s$ (F g <sup>-1</sup> )	$E$ (W h kg <sup>-1</sup> )	$P$ (W kg <sup>-1</sup> )	Cyclic stability	Ref.
<b>Two electrode systems</b>							
<b>Previous work</b> rGO/Ni(OH) <sub>2</sub> / PANI (G11NP)	1 M H <sub>2</sub> SO <sub>4</sub>	1.2	234.19	46.87	1664.02	No deterioration up to 15000 cycles at a scan rate of 400 mV s <sup>-1</sup>	
<b>Present work</b> rGO/Ni(OH) <sub>2</sub> / PANI (G14NP)	1 M H <sub>2</sub> SO <sub>4</sub>	1.2	602.40	120.48	2584.83	No deterioration up to 16500 cycles at a scan rate of 400 mV s <sup>-1</sup>	
<b>Three electrode systems</b>							

NiS/rGO/nickel foam	2 M KOH	0.65	1169.1 at 5 A g <sup>-1</sup>	-	-	77.9% retention for 1000 cycles at 10 A g <sup>-1</sup>	(Xing et al. 2013)
Ni(OH) <sub>2</sub> /rGO/nickel foam	1 M KOH	0.6	1667 at 3.3 A g <sup>-1</sup>	-	-	92.5 % retention for 1000 cycles at 10mA	(Min et al. 2014)
NiS/rGO/nickel foam	2 M KOH	0.6	1424 at 0.75 A g <sup>-1</sup>	-	-	89.6% retention for 3000 cycles at 15 A g <sup>-1</sup>	(Zhang et al. 2013)
Carbon coated NiS/rGO/ nickel foam	3 M KOH	0.5	860.1 at 5 mV s <sup>-1</sup>	-	-	98.6 % retention for 500 cycles at 5 A g <sup>-1</sup>	(Ma et al. 2014)
PANI/NiO	1 M H <sub>2</sub> SO <sub>4</sub>	0.6	353 at 0.8 A g <sup>-1</sup>	17.6	590.3	64 % retention for 1000 cycles at 0.8 A g <sup>-1</sup>	(Singu et al. 2016)
rGO/NiO/PANI/nickel foam	1 M KOH	1	638 1 at 1 mV s <sup>-1</sup>	-	-	91% % retention for 5000 cycles at 300 mA	(Bai et al. 2017)
PANI/NiO	0.05 M KI	0.4	2122.75 at 0.1 A g <sup>-1</sup>	-	-	86% retention for 1000 cycles at 1.5 A g <sup>-1</sup>	(Cai et al. 2017)
PANI/NiO/nickel foam	2 M KOH	0.55	2565 at 1 A g <sup>-1</sup>	-	-	100% retention for 5000 cycles at 1 A g <sup>-1</sup>	(Sun et al. 2016)
Graphene/NiO/PANMA	1 M H <sub>2</sub> SO <sub>4</sub>	0.8	562 at 0.5 A g <sup>-1</sup>	-	-	76.3 retention for 800 cycles at 2 A g <sup>-1</sup>	(Ji et al. 2016)
Graphene/PANI	1 M H <sub>2</sub> SO <sub>4</sub>	1	257 at 0.1 A g <sup>-1</sup>	-	-	-	(Li et al. 2013b)

### **3.7. COMPARISON OF ELECTROCHEMICAL PERFORMANCES OF GCP-300, G12CP, GVP80, G11NP AND G14NP**

A comparison was made between the nanocomposites that resulted in promising electrochemical performances from the three varieties of composites synthesized, namely GCP, GVP and GNP. The composites GCP-300, G12CP, GVP80, G11NP and G14NP belong to GCP, GVP, GNP family, respectively, exhibited promising performances. Among these four nanocomposites G14NP stands out to be the best composites with highest the electrochemical properties ( $C_s$ ,  $E$ ,  $P$ ,  $\eta$  and cyclic stability). The comparison is presented in Table 3.27. The results obtained for as GN48P composite at an applied magnetic field of 625  $\mu$ T and without magnetic field is presented in Table 3.28.



**Table 3.27** The comparison of electrochemical performances of GCP-300, G12CP, GVP80, G11NP and G14NP.

Composite	Electrolyte	E (V)	$C_s$ ( $F g^{-1}$ )	$E$ ( $W h kg^{-1}$ )	$P$ ( $W kg^{-1}$ )	Cyclic stability
rGO 6.6%: Cu <sub>2</sub> O/CuO 13.40%: PANI 80% (GCP-300)	2 M Na <sub>2</sub> SO <sub>4</sub>	0.8 V	53.3 at 0.25 A g <sup>-1</sup>	4.73	136.44	97.6% up to 5000 cycles at 200 mV s <sup>-1</sup>
rGO 12%: Cu <sub>2</sub> O/ CuO 40%: PANI 48% (G12CP)	0.4 M H <sub>2</sub> SO <sub>4</sub>	1.2	119.47 at 1 A g <sup>-1</sup>	23.89	1552.5	84% retention up to 5000 cycles at 700 mV s <sup>-1</sup>
rGO 5.88%: V <sub>2</sub> O <sub>5</sub> 11.76%: PANI 82.36% (GVP82)	1 M H <sub>2</sub> SO <sub>4</sub>	1.2 V	273 at 1 A g <sup>-1</sup>	54.62	1636.5	61% retention up to 13000 cycles at 400 mV s <sup>-1</sup>
rGO 11.11%: Ni(OH) <sub>2</sub> 22.22%: PANI 66.66% (G11NP)	1 M H <sub>2</sub> SO <sub>4</sub>	1.2	234.19 at 1 A g <sup>-1</sup>	46.87	1664.77	No deterioration up to 15000 cycles at a scan rate of 400 mV s <sup>-1</sup>
rGO 14%: Ni(OH) <sub>2</sub> 14%: PANI 72% (G14NP)	1 M H <sub>2</sub> SO <sub>4</sub>	1.2	602.40 at 1 A g <sup>-1</sup>	120.48	2584.83	No deterioration up to 16500 cycles at a scan rate of 400 mV s <sup>-1</sup>

**Table 3.28** The results obtained for as GN48P composite at an applied magnetic field of 625  $\mu$ T and without magnetic field.

Composite	Electrolyte	E (V)	Magnetic field	$C_s$ (F g <sup>-1</sup> )	$E$ (W h kg <sup>-1</sup> )	$P$ (W kg <sup>-1</sup> )	Performance enhancement (%)	Cyclic stability
rGO 4%: Ni(OH) <sub>2</sub> 48%: PANI 48% (GN48P)	1 M H <sub>2</sub> SO <sub>4</sub>	1.2	0 T	34.81 (0.25 A g <sup>-1</sup> )	6.96	388.00	156	-
			625 $\mu$ T	89.43 (0.25 A g <sup>-1</sup> )	17.85	471.99		85.19 % retention up to 5000 cycles at 400 mV s <sup>-1</sup>

---

## CHAPTER – 4

### SUMMARY AND CONCLUSIONS

#### 4.1. SUMMARY

Three series of nanocomposites, namely, reduced graphene oxide/copper oxide/polyaniline (GCP), reduced graphene oxide/vanadium pentoxide/polyaniline (GVP) and reduced graphene oxide/nickel hydroxide/polyaniline (GNP) were synthesized by facile insitu single step chemical methods in series by varying the weight percentages of each of the constituent materials to achieve a standard composition, which would exhibit promising electrochemical performances. The structures of synthesized nanocomposites were confirmed by XRD, FT-IR spectra, XPS, Raman spectra and FE-SEM analyses. The electrochemical performances of the nanocomposites were analyzed by CV, GCD and EIS using practical two electrode system and using aqueous electrolytes. As nickel hydroxide is antiferromagnetic in nature, the composite containing of Ni(OH)<sub>2</sub>, was studied for its electrochemical performance enhancement under different applied magnetic fields.

The standardized weight percentages of nanocomposites are rGO 12%: Cu<sub>2</sub>O/ CuO 40%: PANI 48% (G12CP), rGO 5.88%: V<sub>2</sub>O<sub>5</sub> 11.76%: PANI 82.36% (GVP82), rGO 11.11%: Ni(OH)<sub>2</sub> 22.22%: PANI 66.66% (G11NP) and rGO 14%: Ni(OH)<sub>2</sub> 14%: PANI 72% (G14NP) for GCP, GVP and GNP, respectively. The GNP with a weight percentages of rGO 4%: Ni(OH)<sub>2</sub> 48%: PANI 48% (GN48P) with a magnetic susceptibility of 850 exhibited an enhancement of 156 % in its electrochemical performances over the performance obtained in the absence of magnetic field. The Energy densities of G14NP are comparable with those of the Li-ion batteries and exhibited outstanding cyclic stability. The best performance among all the nanocomposites synthesized was exhibited by the G14NP composite. The results of all standardized compositions were compared with similar works reported and it was found that the result obtained are comparable and superior than most of the works. The merits of ternary composites over binary composites are also compared by synthesizing few of the binary composites with similar weight percentages as those of ternary nanocomposites and the comparison were also made with the some of the reported

performances of binary nanocomposites. Practical applicability of these composites as secondary power backup sources was satisfactorily demonstrated.

## **4.2. CONCLUSIONS**

The major conclusions drawn from the entire research work reported in thesis are

- The synthetic approach of single step insitu chemical synthesis is an efficient method to synthesis composite with qualities of high surface area and possible least agglomeration of nanoparticles.
- The ternary composites synthesized by insitu single step chemical method is capable of producing double layer graphene sheets and effectively avoid their restacking.
- The synthetic method is useful for the production of high energy density supercapacitor electrode materials.
- The integrity of reduced graphene oxide, metal oxide/hydroxide and conducting polymers are very effective in improving the energy density of the supercapacitors than those of binary combinations of them.
- The application of magnetic field to the nanocomposite containing antiferromagnetic nickel hydroxide is highly effective in ameliorating the electrochemical performances.
- Among all the composites synthesized the G14NP exhibited a highest performance with maximum specific capacitance of  $602.40 \text{ F g}^{-1}$ , specific capacity of  $722.88 \text{ C g}^{-1}$ , energy density of  $120.48 \text{ W h kg}^{-1}$ , and a power density of  $2584.83 \text{ W kg}^{-1}$  at a current density of  $1 \text{ A g}^{-1}$ . The G14NP retains 75% of its initial specific capacitance up to 16500 cycles.
- The synthesized nanocomposites are suitable for fabricating high energy storage devices.

## **4.3. SCOPE FOR FUTURE WORK**

- Similar ternary composites can be synthesized using other transition metal oxides, hydroxide and sulfides, which are not reported in this research thesis.
- Similar composites can be synthesized using other conducting polymers, which are not reported in this research thesis.

---

**REFERENCES**

- Abdolhosseinzadeh, S., Asgharzadeh, H., and Seop Kim, H. (2015). "Fast and fully-scalable synthesis of reduced graphene oxide." *Sci. Rep.*, 5, 10160.
- Adeyemo, A., Hunter, G., and Dutta, P. K. (2011). "Interaction of CO with hydrous ruthenium oxide and development of a chemoresistive ambient CO sensor." *Sens. Actuators B Chem.*, 152(2), 307–315.
- Akhavan, O., Ghaderi, E., Hashemi, E., and Rahighi, R. (2014). "Ultra-sensitive detection of leukemia by graphene." *Nanoscale*, 6(24), 14810–14819.
- Arezzo, F., Severini, E., and Zacchetti, N. (1994). "An XPS study of diamond films grown on differently pretreated silicon substrates." *Surf. Interface Anal.*, 22(1-12), 218–223.
- Asen, P., and Shahrokhian, S. (2017a). "A high performance supercapacitor based on graphene/polypyrrole/Cu<sub>2</sub>O–Cu(OH)<sub>2</sub> ternary nanocomposite coated on nickel foam." *J. Phys. Chem. C*, 121(12), 6508–6519.
- Asen, P., and Shahrokhian, S. (2017b). "One step electrodeposition of V<sub>2</sub>O<sub>5</sub>/polypyrrole/graphene oxide ternary nanocomposite for preparation of a high performance supercapacitor." *Int. J. Hydrog. Energy*, 42(33), 21073–21085.
- Asen, P., and Shahrokhian, S. (2017c). "A High Performance Supercapacitor Based on Graphene/Polypyrrole/Cu<sub>2</sub>O–Cu(OH)<sub>2</sub> Ternary Nanocomposite Coated on Nickel Foam." *J. Phys. Chem. C*, 121(12), 6508–6519.
- Ates, M. (2016). "Graphene and its nanocomposites used as an active materials for supercapacitors." *J. Solid State Electrochem.*, 20(6), 1509–1526.
- Ates, M., Serin, M. A., Ekmen, I., and Ertas, Y. N. (2015). "Supercapacitor behaviors of polyaniline/CuO, polypyrrole/CuO and PEDOT/CuO nanocomposites." *Polym. Bull.*, 72(10), 2573–2589.

- Augustyn, V., Simon, P., and Dunn, B. (2014). “Pseudocapacitive oxide materials for high-rate electrochemical energy storage.” *Energy Environ. Sci.*, 7(5), 1597–1614.
- Bai, M. H., Liu, T. Y., Luan, F., Li, Y., and Liu, X. X. (2014). “Electrodeposition of vanadium oxide–polyaniline composite nanowire electrodes for high energy density supercapacitors.” *J. Mater. Chem. A*, 2(28), 10882–10888.
- Bai, Y., Sun, G., Chen, S., Lu, L., and Bao, J. (2017). “Reduced graphene oxide/nickel oxide/polyaniline: preparation and properties investigation as supercapacitor electrode material.” *Int J Electrochem Sci*, 12, 652–662.
- Balducci, A., Belanger, D., Brousse, T., Long, J. W., and Sugimoto, W. (2017). “Perspective—a guideline for reporting performance metrics with electrochemical capacitors: from electrode materials to full devices.” *J. Electrochem. Soc.*, 164(7), A1487–A1488.
- Barreca, D., Gasparotto, A., and Tondello, E. (2007). “CVD Cu<sub>2</sub>O and CuO nanosystems characterized by XPS.” *Surf. Sci. Spectra*, 14(1), 41–51.
- Bélanger, D., Brousse, L., and Long, J. W. (2008). “Manganese oxides: battery materials make the leap to electrochemical capacitors.” *Electrochem. Soc. Interface*, 17(1), 49.
- Bhuyan, M. S. A., Uddin, M. N., Islam, M. M., Bipasha, F. A., and Hossain, S. S. (2016). “Synthesis of graphene.” *Int. Nano Lett.*, 6(2), 65–83.
- Bianco, A., Cheng, H.-M., Enoki, T., Gogotsi, Y., Hurt, R. H., Koratkar, N., Kyotani, T., Monthieux, M., Park, C. R., Tascon, J. M. D., and Zhang, J. (2013). “All in the graphene family – A recommended nomenclature for two-dimensional carbon materials.” *Carbon*, 65, 1–6.
- Bournel, F., Laffon, C., Parent, P., and Tourillon, G. (1996). “Adsorption of some substituted ethylene molecules on Pt (111) at 95 K Part 1: NEXAFS , XPS and UPS studies.” *Surf. Sci.*, 350, 60–78.

- Brousse, T., Bélanger, D., and Long, J. W. (2015). “To Be or Not To Be Pseudocapacitive?” *J. Electrochem. Soc.*, 162(5), A5185–A5189.
- Brun, N., Prabakaran, S. R. S., Surcin, C., Morcrette, M., Deleuze, H., Birot, M., Babot, O., Achard, M. F., and Backov, R. (2012). “Design of hierarchical porous carbonaceous foams from a dual-template approach and their use as electrochemical capacitor and Li ion battery negative electrodes.” *J. Phys. Chem. C*, 116(1), 1408–1421.
- Bu, I. Y. Y., and Huang, R. (2017). “Fabrication of CuO-decorated reduced graphene oxide nanosheets for supercapacitor applications.” *Ceram. Int.*, 43(1), 45–50.
- Cai, X., Cui, X., Zu, L., Zhang, Y., Gao, X., Lian, H., Liu, Y., and Wang, X. (2017). “Ultra high electrical performance of nano nickel oxide and polyaniline composite materials.” *Polymers*, 9(7), 288.
- Chen, C., Yu, D., Zhao, G., Du, B., Tang, W., Sun, L., Sun, Y., Besenbacher, F., and Yu, M. (2016a). “Three-dimensional scaffolding framework of porous carbon nanosheets derived from plant wastes for high-performance supercapacitors.” *Nano Energy*, 27, 377–389.
- Chen, S. M., Ramachandran, R., Mani, V., and Saraswathi, R. (2014). “Recent advancements in electrode materials for the high-performance electrochemical supercapacitors: a review.” *Int J Electrochem Sci*, 9(8), 4072–4085.
- Chen, W., Tao, X., Wei, D., Wang, H., Yu, Q., and Li, Y. (2016b). “High-performance supercapacitor based on activated carbon–MnO<sub>2</sub>–polyaniline composite.” *J. Mater. Sci. Mater. Electron.*, 27(2), 1357–1362.
- Chen, X. K., Irwin, J. C., and Franck, J. P. (1995). “Evidence for a strong spin-phonon interaction in cupric oxide.” *Phys. Rev. B*, 52(18), R13130–R13133.
- Choudhury, A., Bonso, J. S., Wunch, M., Yang, K. S., Ferraris, J. P., and Yang, D. J. (2015). “In-situ synthesis of vanadium pentoxide nanofibre/exfoliated graphene nanohybrid and its supercapacitor applications.” *J. Power Sources*, 287, 283–290.

Choudhury, A., Kim, J. H., Yang, K. S., and Yang, D. J. (2016). “Facile synthesis of self-standing binder-free vanadium pentoxide-carbon nanofiber composites for high-performance supercapacitors.” *Electrochim. Acta*, 213, 400–407.

Compton, O. C., and Nguyen, S. T. (2010). “Graphene oxide, highly reduced graphene oxide, and graphene: versatile building blocks for carbon-based materials.” *Small*, 6(6), 711–723.

Conte, M. C. (2010). “Supercapacitors technical requirements for new applications.” *Fuel Cells*, 5(10), 806–818.

Das, A. K., Karan, S. K., and Khatua, B. B. (2015). “High energy density ternary composite electrode material based on polyaniline (pani), molybdenum trioxide (MoO<sub>3</sub>) and graphene nanoplatelets (gnp) prepared by sono-chemical method and their synergistic contributions in superior supercapacitive performance.” *Electrochimica Acta*, 180, 1–15.

Deng, Y., Handoko, A. D., Du, Y., Xi, S., and Yeo, B. S. (2016). “In situ raman spectroscopy of copper and copper oxide surfaces during electrochemical oxygen evolution reaction: identification of Cu<sup>III</sup> oxides as catalytically active species.” *ACS Catal.*, 6(4), 2473–2481.

Dhibar, S., and Das, C. K. (2014). “Silver nanoparticles decorated polyaniline /multiwalled carbon nanotubes nanocomposite for high-performance supercapacitor electrode.” *Ind. Eng. Chem. Res.* 53, 3495–3508.

Dinodi, N., and Shetty, A. N. (2014). “Alkyl carboxylates as efficient and green inhibitors of magnesium alloy ZE41 corrosion in aqueous salt solution.” *Corros. Sci.*, 85, 411–427.

Dong, X., Wang, K., Zhao, C., Qian, X., Chen, S., Li, Z., Liu, H., and Dou, S. (2014). “Direct synthesis of RGO/Cu<sub>2</sub>O composite films on Cu foil for supercapacitors.” *J. Alloys Compd.*, 586, 745–753.



Dunn, B., Dunn, B., Kamath, H., and Tarascon, J. (2011). "Electrical energy storage for the grid for the Grid : A Battery of choices." *Sci. Mag.*, 334(6058), 928–936.

Ertl, G., Hierl, R., Knözinger, H., Thiele, N., and Urbach, H. P. (1980). "XPS study of copper aluminate catalysts." *Appl. Surf. Sci.*, 5(1), 49–64.

Feng, X. ., Chen, N. ., Zhou, J. ., Li, Y. ., Huang, Z. ., Zhang, L. ., Ma, Y. ., Wang, L. ., and Yan, X. . (2015). "Facile synthesis of shape-controlled graphene-polyaniline composites for high performance supercapacitor electrode materials." *New J. Chem.*, 39(3), 2261–2268.

Foo, C. Y., Sumboja, A., Tan, D. J. H., Wang, J., and Lee, P. S. (2014). "Flexible and Highly Scalable V<sub>2</sub>O<sub>5</sub>-rGO Electrodes in an Organic Electrolyte for Supercapacitor Devices." *Adv. Energy Mater.*, 4(12), 1400236.

Gao, Z., Yang, W., Wang, J., Wang, B., Li, Z., Liu, Q., Zhang, M., and Liu, L. (2012). "A new partially reduced graphene oxide nanosheet/polyaniline nanowafer hybrid as supercapacitor electrode material." *Energy Fuels*, 27(1), 568–575.

Ghijsen, J., Tjeng, L., Elp, J. van, Eskes, H., Westerink, J., Sawatzky, G., and Czyzyk, M. (1988). "Electronic structure of Cu<sub>2</sub>O and CuO." *Phys. Rev. B*, 38(16), 11322–11330.

Gholivand, M. B., Heydari, H., Abdolmaleki, A., and Hosseini, H. (2015). "Nanostructured CuO/PANI composite as supercapacitor electrode material." *Mater. Sci. Semicond. Process.*, 30, 157–161.

Gidwani, M., Bhagwani, A., and Rohra, N. (2014). "Supercapacitors: the near Future of Batteries." *Int. J. Eng. Invent.*, 4(5), 22–2.

Gopalakrishnan, K., Ramesh, C., Elango, M., and Thamilselvan, M. (2014). "Optical and magnetic studies on Cu<sub>2</sub>O/PANI nanocomposite prepared by chemical polymerization method." *ISRN Mater. Sci.*, 2014.

Hamdani, M., Singh, R. N., and Chartier, P. (2010). “Co<sub>3</sub>O<sub>4</sub> and Co-based spinel oxides bifunctional oxygen electrodes.” *Int J Electrochem Sci*, 5(4), 556–577.

Han, G., Liu, Y., Zhang, L., Kan, E., Zhang, S., Tang, J., and Tang, W. (2014). “MnO<sub>2</sub> nanorods intercalating graphene oxide/polyaniline ternary composites for robust high-performance supercapacitors.” *Sci. Rep.*, 4, 4824.

Han, G., Liu, Y., Zhang, L., Kan, E., Zhang, S., Tang, J., and Tang, W. (2015). “MnO<sub>2</sub> Nanorods Intercalating Graphene Oxide/Polyaniline Ternary Composites for Robust High-Performance Supercapacitors.” *Sci. Rep.*, 4(1), 4824.

Hareesh, K., Shateesh, B., Joshi, R. P., Dahiwal, S. S., Bhoraskar, V. N., Haram, S. K., and Dhole, S. D. (2016). “PEDOT:PSS wrapped NiFe<sub>2</sub>O<sub>4</sub>/rGO tertiary nanocomposite for the super-capacitor applications.” *Electrochim. Acta*, 201, 106–116.

Hawaldar, R., Merino, P., Correia, M. R., Bdikin, I., Gracio, J., Mendez, J., Martin-Gago, J. a, and Singh, M. K. (2012). “Large-area high-throughput synthesis of monolayer graphene sheet by hot filament thermal chemical vapor deposition.” *Sci. Rep.*, 2, 682.

Hermet, P., Gourrier, L., Bantignies, J.-L., Ravot, D., Michel, T., Deabate, S., Boulet, P., and Henn, F. (2011). “Dielectric, magnetic, and phonon properties of nickel hydroxide.” *Phys. Rev. B*, 84(23), 235211.

H. Nagaraju, D., Wang, Q., Beaujuge, P., and N. Alshareef, H. (2014). “Two-dimensional heterostructures of V<sub>2</sub>O<sub>5</sub> and reduced graphene oxide as electrodes for high energy density asymmetric supercapacitors.” *J. Mater. Chem. A*, 2(40), 17146–17152.

Hong, X., Zhang, B., Murphy, E., Zou, J., and Kim, F. (2017). “Three-dimensional reduced graphene oxide/polyaniline nanocomposite film prepared by diffusion driven layer-by-layer assembly for high-performance supercapacitors.” *J. Power Sources*, 343, 60–66.

Hong, Y. K., and Lee, J. J. (2017). *Magnetic supercapacitors*. Google Patents.

- Hu, C. C., Chen, W. C., and Chang, K. H. (2004). "How to achieve maximum utilization of hydrous ruthenium oxide for supercapacitors." *J. Electrochem. Soc.*, 151(2), A281–A290.
- Hu, C. C., and Lin, J. Y. (2002). "Effects of the loading and polymerization temperature on the capacitive performance of polyaniline in  $\text{NaNO}_3$ ." *Electrochim. Acta*, 47(25), 4055–4067.
- Hu, Z. A., Xie, Y. L., Wang, Y. X., Mo, L. P., Yang, Y. Y., and Zhang, Z. Y. (2009). "Polyaniline/ $\text{SnO}_2$  nanocomposite for supercapacitor applications." *Mater. Chem. Phys.*, 114(2), 990–995.
- Huang, Q., Wang, X., Li, J., Dai, C., Gamboa, S., and Sebastian, P. J. (2007). "Nickel hydroxide/activated carbon composite electrodes for electrochemical capacitors." *J. Power Sources*, 164(1), 425–429.
- Hummers, W. S., and Offeman, R. E. (1958). "Preparation of graphitic oxide." *J. Am. Chem. Soc.*, 80(6), 1339–1339.
- Jaidev, Jafri, R. I., Mishra, A. K., and Ramaprabhu, S. (2011). "Polyaniline– $\text{MnO}_2$  nanotube hybrid nanocomposite as supercapacitor electrode material in acidic electrolyte." *J. Mater. Chem.*, 21, 17601.
- Ji, X., Xu, Q., Zhou, T., Wang, X., Xu, H., Yao, X., and Lan, W. (2016). "Synthesis of poly ( aniline- co - m -aminophenol )/ graphene / NiO nanocomposite and its application in supercapacitors." 211, 14–18.
- Jin, Y., and Jia, M. (2015). "Design and synthesis of nanostructured graphene- $\text{SnO}_2$ - polyaniline ternary composite and their excellent supercapacitor performance." *Colloids Surf. Physicochem. Eng. Asp.*, 464, 17–25.
- Johra, F. T., and Jung, W. G. (2015). "Hydrothermally reduced graphene oxide as a supercapacitor." *Appl. Surf. Sci.*, 357, 1911–1914.

Jolley, J. G., Geesey, G. G., Hankins, M. R., Wright, R. B., and Wichlacz, P. L. (1989). "Auger electron and X-ray photoelectron spectroscopic study of the biocorrosion of copper by alginic acid polysaccharide." *Appl. Surf. Sci.*, 37(4), 469–480.

Juttner, K. (1990). "Electrochemical impedance spectroscopy (EIS) of corrosion processes on inhomogeneous surfaces." *Electrochim. Acta*, 35(10), 1501–1508.

Kang, E. T., Neoh, K. G., Zhang, X., Tan, K. L., and Liaw, D. J. (1996). "Surface modification of electroactive polymer films by ozone treatment." *Surf. Interface Anal. Int. J. Devoted Dev. Appl. Tech. Anal. Surf. Interfaces Thin Films*, 24(1), 51–58.

Kannappan, S., Kaliyappan, K., Manian, R. K., Pandian, A. S., Yang, H., Lee, Y. S., Jang, J. H., and Lu, W. (2013). "Graphene based supercapacitors with improved specific capacitance and fast charging time at high current density." *ArXiv Prepr. ArXiv13111548*.

Kasperkiewicz, J., Kovacich, J. A., and Lichtman, D. (1983). "XPS studies of vanadium and vanadium oxides." *J. Electron Spectrosc. Relat. Phenom.*, 32(2), 123–132.

Kong, D. S., Wang, J. M., Shao, H. B., Zhang, J. Q., and Cao, C. (2011). "Electrochemical fabrication of a porous nanostructured nickel hydroxide film electrode with superior pseudocapacitive performance." *J. Alloys Compd.*, 509(18), 5611–5616.

Kotal, M., Thakur, A. K., and Bhowmick, A. K. (2013). "Polyaniline-carbon nanofiber composite by a chemical grafting approach and its supercapacitor application." *ACS Appl. Mater. Interfaces*, 5(17), 8374–8386.

Kötz, R., and Carlen, M. (2000). "Principles and applications of electrochemical capacitors." *Electrochim. Acta*, 45(15), 2483–2498.

Krause, M. O., and Oliver, J. H. (1979). "Natural widths of atomic K and L levels, Ka X-ray lines and several kit auger lines." *J. Chem. Phys. Ref. Data*, 8(2), 329–337.

Kumar, N. A., and Baek, J. B. (2014). “Electrochemical supercapacitors from conducting polyaniline–graphene platforms.” *Chem. Commun.*, 50(48), 6298–6308.

Kumar, N. A., Choi, H. J., Shin, Y. R., Chang, D. W., Dai, L., and Baek, J. B. (2012). “Polyaniline-grafted reduced graphene oxide for efficient electrochemical supercapacitors.” *ACS Nano*, 6(2), 1715–1723.

Kumar, S. N., Bouyssoux, G., and Gaillard, F. (1990). “Electronic and structural characterization of electrochemically synthesized conducting polyaniline from XPS studies.” *Surf. Interface Anal.*, 15(9), 531–536.

Lee, S. H., Cheong, H. M., Seong, M. J., Liu, P., Tracy, C. E., Mascarenhas, A., Pitts, J. R., and Deb, S. K. (2003). “Raman spectroscopic studies of amorphous vanadium oxide thin films.” *Solid State Ion.*, Fifth International Meeting on Electrochromism, 165(1), 111–116.

Li, D., Liu, Y., Lin, B., Lai, C., Sun, Y., Yang, H., and Zhang, X. (2015a). “Synthesis of ternary graphene/molybdenum oxide/poly (p -phenylenediamine) nanocomposites for symmetric supercapacitors.” *RSC Adv.*, 5(119), 98278–98287.

Li, D., Liu, Y., Lin, B., Lai, C., Sun, Y., Yang, H., and Zhang, X. (2015b). “One-pot synthesis and electrochemical properties of graphene/SnO<sub>2</sub>/poly (p-phenylenediamine) ternary nanocomposites.” *J. Alloys Compd.*, 652, 9–17.

Li, H. B., Yu, M. H., Wang, F. X., Liu, P., Liang, Y., Xiao, J., Wang, C. X., Tong, Y. X., and Yang, G. W. (2013a). “Amorphous nickel hydroxide nanospheres with ultrahigh capacitance and energy density as electrochemical pseudocapacitor materials.” *Nat. Commun.*, 4, 1894.

Li, S. K., Pan, Y. Y., Wu, M., Huang, F. Z., Li, C. H., and Shen, Y. H. (2014a). “Large-scale and green synthesis of octahedral flower-like cupric oxide nanocrystals with enhanced photochemical properties.” *Appl. Surf. Sci.*, 315(1), 169–177.

Li, X., and Wei, B. (2012). “Facile synthesis and super capacitive behavior of SWNT/MnO<sub>2</sub> hybrid films.” *Nano Energy*, 1(3), 479–487.

Li, Y., Wang, G., Wei, T., Fan, Z., and Yan, P. (2016). “Nitrogen and sulfur co-doped porous carbon nanosheets derived from willow catkin for supercapacitors.” *Nano Energy*, 19, 165–175.

Li, Y., Ye, K., Cheng, K., Cao, D., Pan, Y., Kong, S., Zhang, X., and Wang, G. (2014b). “Anchoring CuO nanoparticles on nitrogen-doped reduced graphene oxide nanosheets as electrode material for supercapacitors.” *J. Electroanal. Chem.*, 727, 154–162.

Li, Z. F., Zhang, H., Liu, Q., Sun, L., Stanciu, L., and Xie, J. (2013b). “Fabrication of high-surface-area graphene/polyaniline nanocomposites and their application in supercapacitors.” *ACS Appl. Mater. Interfaces*, 5(7), 2685–2691.

Li, Z., Wang, J., Liu, X., Liu, S., Ou, J., and Yang, S. (2011). “Electrostatic layer-by-layer self-assembly multilayer films based on graphene and manganese dioxide sheets as novel electrode materials for supercapacitors.” *J. Mater. Chem.*, 21(10), 3397.

Lin, H., Huang, Q., Wang, J., Jiang, J., Liu, F., Chen, Y., Wang, C., Lu, D., and Han, S. (2016). “Self-assembled graphene/polyaniline/Co<sub>3</sub>O<sub>4</sub> ternary hybrid aerogels for supercapacitors.” *Electrochim. Acta*, 191, 444–451.

Lu, Y., Zhu, T., Zhang, G., He, Z., Lin, C., Chen, Y., and Guo, H. (2015). “Influence of magnetic fields on the morphology and pseudocapacitive properties of NiO on nickel foam.” *RSC Adv*, 5(121), 99745–99753.

Ma, L., Shen, X., Ji, Z., Wang, S., Zhou, H., and Zhu, G. (2014). “Carbon coated nickel sulfide/reduced graphene oxide nanocomposites: Facile synthesis and excellent supercapacitor performance.” *Electrochim. Acta*, 146, 525–532.

Maitra, A., Das, A. K., Bera, R., Karan, S. K., Paria, S., Si, S. K., and Khatua, B. B. (2017). “An approach to fabricate PDMS encapsulated all-solid-state advanced asymmetric supercapacitor device with vertically aligned hierarchical Zn-Fe-Co ternary oxide nanowire and nitrogen doped graphene nanosheet for high power device applications.” *ACS Appl. Mater. Interfaces*, 9(7), 5947–5958.

- Majumdar, D., Baugh, N., and Bhattacharya, S. K. (2017). "Ultrasound assisted formation of reduced graphene oxide-copper (II) oxide nanocomposite for energy storage applications." *Colloids Surf. Physicochem. Eng. Asp.*, 512(Ii), 158–170.
- Mansour, A. N. (1994). "Characterization of  $\beta$ -Ni(OH)<sub>2</sub> by XPS." *Surf. Sci. Spectra*, 3(3), 239–246.
- Marcano, D. C., Kosynkin, D. V., Berlin, J. M., Sinitskii, A., Sun, Z., Slesarev, A., Alemany, L. B., Lu, W., and Tour, J. M. (2010). "Improved synthesis of graphene oxide." *ACS Nano*, 4(8), 4806–4814.
- Masarapu, C., Zeng, H. F., Hung, K. H., and Wei, B. (2009). "Effect of temperature on the capacitance of carbon nanotube supercapacitors." *ACS Nano*, 3(8), 2199–2206.
- McIntyre, N. S. (1981). "Chemical information from XPS—applications to the analysis of electrode surfaces." *J. Vac. Sci. Technol.*, 18(1981), 714.
- McIntyre, N. S., and Cook, M. G. (1975). "X-Ray Photoelectron Studies on Some Oxides and Hydroxides of Cobalt, Nickel, and Copper." *Anal. Chem.*, 47(13), 2208–2213.
- Miao, F., Shao, C., Li, X., Wang, K., Lu, N., and Liu, Y. (2016). "Electrospun carbon nanofibers/carbon nanotubes/polyaniline ternary composites with enhanced electrochemical performance for flexible solid-state supercapacitors." *ACS Sustain. Chem. Eng.*, 4(3), 1689–1696.
- Midander, K., Cronholm, P., Karlsson, H. L., Elihn, K., Möller, L., Leygraf, C., and Wallinder, I. O. (2009). "Surface characteristics, copper release, and toxicity of nano- and micrometer-sized copper and copper(II) oxide particles: A cross-disciplinary study." *Small*, 5(3), 389–399.
- Miller, J. R., Outlaw, R. A., and Holloway, B. C. (2010). "Graphene double-layer capacitor with ac line-filtering performance." *Science*, 329(5999), 1637–1639.

- Min, S., Zhao, C., Chen, G., and Qian, X. (2014). "One-pot hydrothermal synthesis of reduced graphene oxide/Ni(OH)<sub>2</sub> films on nickel foam for high performance supercapacitors." *Electrochim. Acta*, 115, 155–164.
- Mondal, S., Rana, U., and Malik, S. (2017). "Reduced graphene oxide/Fe<sub>3</sub>O<sub>4</sub>/polyaniline nanostructures as electrode materials for an all-solid-state hybrid supercapacitor." *J. Phys. Chem. C*, 121(14), 7573–7583.
- Moosavifard, S. E., Shamsi, J., Fani, S., and Kadkhodazade, S. (2014). "Facile synthesis of hierarchical CuO nanorod arrays on carbon nanofibers for high-performance supercapacitors." *Ceram. Int.*, 40(10), 15973–15979.
- Mousavi, M. F., Hashemi, M., Rahmanifar, M. S., and Noori, A. (2017). "Synergistic effect between redox additive electrolyte and PANI-rGO nanocomposite electrode for high energy and high power supercapacitor." *Electrochim. Acta*, 228, 290–298.
- Mu, B., Zhang, W., Shao, S., and Wang, A. (2014). "Glycol assisted synthesis of graphene–MnO<sub>2</sub>–polyaniline ternary composites for high performance supercapacitor electrodes." *Phys. Chem. Chem. Phys.*, 16(17), 7872.
- Mugwang'a, F. K., Karimi, P. K., Njoroge, W. K., Omayio, O., and Waita, S. (2013). "Optical characterization of copper oxide thin films prepared by reactive dc magnetron sputtering for solar cell applications." *Int. J. Thin Film Sci. Tec.* 2 No. 1, 15-24.
- Nandy, S., Maiti, U. N., Ghosh, C. K., and Chattopadhyay, K. K. (2009). "Enhanced p-type conductivity and band gap narrowing in heavily Al doped NiO thin films deposited by RF magnetron sputtering." *J. Phys. Condens. Matter*, 21(11), 115804.
- Nguyen, V. H. . b, and Shim, J.-J. . (2015). "Ultrasmall SnO<sub>2</sub> nanoparticle-intercalated graphene@polyaniline composites as an active electrode material for supercapacitors in different electrolytes." *Synth. Met.*, 207, 110–115.
- Nyström, G., Marais, A., Karabulut, E., Wågberg, L., Cui, Y., and Hamed, M. M. (2015). "Self-assembled three-dimensional and compressible interdigitated thin-film supercapacitors and batteries." *Nat. Commun.*, 6, 7259.



- Pan, C., Gu, H., and Dong, L. (2016). "Synthesis and electrochemical performance of polyaniline @MnO<sub>2</sub>/graphene ternary composites for electrochemical supercapacitors." *J. Power Sources*, 303, 175–181.
- Pan, X., Ren, G., Hoque, M. N. F., Bayne, S., Zhu, K., and Fan, Z. (2014). "Fast supercapacitors based on graphene-bridged V<sub>2</sub>O<sub>3</sub>/VO<sub>x</sub> core-shell nanostructure electrodes with a power density of 1 MW kg<sup>-1</sup>." *Adv. Mater. Interfaces*, 1(9), 1–9.
- Pandit, B., Dubal, D. P., Gómez-Romero, P., Kale, B. B., and Sankapal, B. R. (2017). "V<sub>2</sub>O<sub>5</sub> encapsulated MWCNTs in 2D surface architecture: Complete solid-state bendable highly stabilized energy efficient supercapacitor device." *Sci. Rep.*, 7, 43430.
- Park, H., and Han, T. H. (2014). "Facile hybridization of graphene oxide and Cu<sub>2</sub>O for high-performance electrochemical supercapacitors." *Macromol. Res.*, 22(8), 809–812.
- Park, S., Khan, Z., Joo Shin, T., Kim, Y., and Ko, H. (2019). "Rechargeable Na/Ni batteries based on the Ni(OH)<sub>2</sub> /NiOOH redox couple with high energy density and good cycling performance." *J. Mater. Chem. A*, 7, 1564-1573.
- Parlak, O., Kumar Mishra, Y., Grigoriev, A., Mecklenburg, M., Luo, W., Keene, S., Salleo, A., Schulte, K., Ahuja, R., Adelung, R., Turner, A. P. F., and Tiwari, A. (2017). "Hierarchical aerographite nano-microtubular tetrapodal networks based electrodes as lightweight supercapacitor." *Nano Energy*, 34, 570–577.
- Patil, U. M., Gurav, K. V., Fulari, V. J., Lokhande, C. D., and Joo, O. S. (2009). "Characterization of honeycomb-like 'β-Ni(OH)<sub>2</sub>' thin films synthesized by chemical bath deposition method and their supercapacitor application." *J. Power Sources*, 188(1), 338–342.
- Pendashteh, A., Moosavifard, S. E., Rahmanifar, M. S., Wang, Y., El-Kady, M. F., Kaner, R. B., and Mousavi, M. F. (2015). "Highly Ordered Mesoporous CuCo<sub>2</sub>O<sub>4</sub> Nanowires, a Promising Solution for High-Performance Supercapacitors." *Chem. Mater.*, 27(11), 3919–3926.

Peng, X. Y., Liu, X. X., Diamond, D., and Lau, K. T. (2011). "Synthesis of electrochemically-reduced graphene oxide film with controllable size and thickness and its use in supercapacitor." *Carbon*, 49(11), 3488–3496.

Perera, S. D., Liyanage, A. D., Nijem, N., Ferraris, J. P., Chabal, Y. J., and Balkus, K. J. (2013). "Vanadium oxide nanowire – Graphene binder free nanocomposite paper electrodes for supercapacitors: A facile green approach." *J. Power Sources*, 230, 130–137.

Poulston, S., Parlett, P. M., Stone, P., and Bowker, M. (1996). "Surface oxidation and reduction of CuO and Cu<sub>2</sub>O studied using XPS and XAES." *Surf. Interface Anal.*, 24(12), 811–820.

Purushothaman, K. K., Saravanakumar, B., Babu, I. M., Sethuraman, B., and Muralidharan, G. (2014). "Nanostructured CuO/reduced graphene oxide composite for hybrid supercapacitors." *RSC Adv.*, 4(45), 23485.

Qian, A., Zhuo, K., Choi, B. N., Lee, S. J., Bae, J. W., Yoo, P. J., and Chung, C.-H. (2016). "Capacitance enhancement in supercapacitors by incorporating ultra-long hydrated vanadium-oxide nanobelts into graphene." *J. Alloys Compd.*, 688, 814–821.

Rahdar, A., Aliahmad, M., and Azizi, Y. (2015). "NiO Nanoparticles: Synthesis and Characterization." *J. Nanostructures*, 5(2), 145–151.

Rakhi, R. B., Chen, W., Cha, D., and Alshareef, H. N. (2012). "Substrate dependent self-organization of mesoporous cobalt oxide nanowires with remarkable pseudocapacitance." *Nano Lett.*, 12(5), 2559–2567.

Rana, U., and Malik, S. (2012). "Graphene oxide/polyaniline nanostructures: transformation of 2D sheet to 1D nanotube and in situ reduction." *Chem. Commun.*, 48(88), 10862.

Reitz, J. B., and Solomon, E. I. (1998). "Propylene oxidation on copper oxide surfaces: Electronic and geometric contributions to reactivity and selectivity." *J. Am. Chem. Soc.*, 120(44), 11467–11478.

- Ren, P. G., Yan, D. X., Ji, X., Chen, T., and Li, Z. M. (2011). "Temperature dependence of graphene oxide reduced by hydrazine hydrate." *Nanotechnology*, 22(5), 55705.
- Robert, T., and Offergeld, G. (1972). "Spectres de photoelectrons X de composites solides de cuivre Relation entre la presence de raies satellites et l'etat deoxydation du cuivre." *Phys. Status Solidi A*, 14(1), 277–282.
- Sahoo, S., and Shim, J. J. (2017). "Facile Synthesis of Three-Dimensional Ternary ZnCo<sub>2</sub>O<sub>4</sub>/Reduced Graphene Oxide/NiO Composite Film on Nickel Foam for Next Generation Supercapacitor Electrodes." *ACS Sustain. Chem. Eng.*, 5(1), 241–251.
- Sahu, V., Goel, S., Kumar Tomar, A., Singh, G., and Sharma, R. K. (2017). "Graphene nanoribbons @ vanadium oxide nanostrips for supercapacitive energy storage." *Electrochim. Acta*, 230, 255–264.
- Salavati-Niasari, M., and Davar, F. (2009). "Synthesis of copper and copper(I) oxide nanoparticles by thermal decomposition of a new precursor." *Mater. Lett.*, 63(3–4), 441–443.
- Saravanakumar, B., Kamaraj Purushothaman, K., and Muralidharan, G. (2014). "MnO<sub>2</sub> grafted V<sub>2</sub>O<sub>5</sub> nanostructures: formation mechanism, morphology and supercapacitive features." *CrystEngComm*, 16(46), 10711–10720.
- Saravanakumar, B., Purushothaman, K. K., and Muralidharan, G. (2016). "Fabrication of two-dimensional reduced graphene oxide supported V<sub>2</sub>O<sub>5</sub> networks and their application in supercapacitors." *Mater. Chem. Phys.*, 170, 266–275.
- Schön, G. (1972). "High resolution Auger electron spectroscopy of metallic copper." *J. Electron Spectrosc. Relat. Phenom.*, 1(4), 377–387.
- Senthilkumar, S. T., Selvan, R. K., Ponpandian, N., and Melo, J. S. (2012). "Redox additive aqueous polymer gel electrolyte for an electric double layer capacitor." *RSC Adv*, 2(24), 8937–8940.

- Shalvoy, R. B., Reucroft, P. J., and Davis, B. H. (1979). "Characterization of coprecipitated nickel on silica methanation catalysts by X-ray photoelectron spectroscopy." *J. Catal.*, 56(3), 336–348.
- Shen, J., Yang, C., Li, X., and Wang, G. (2013). "High-performance asymmetric supercapacitor based on nanoarchitected polyaniline/graphene/carbon nanotube and activated graphene electrodes." *ACS Appl. Mater. Interfaces*, 5(17), 8467–8476.
- Sheng, K., Sun, Y., Li, C., Yuan, W., and Shi, G. (2012a). "Ultrahigh-rate supercapacitors based on electrochemically reduced graphene oxide for ac line-filtering." *Sci. Rep.*, 2(250 mL), 247.
- Sheng, K., Sun, Y., Li, C., Yuan, W., and Shi, G. (2012b). "Ultrahigh-rate supercapacitors based on electrochemically reduced graphene oxide for ac line-filtering." *Sci. Rep.*, 2, 247.
- Simon, P., Gogotsi, Y., and Dunn, B. (2014). "Where Do Batteries End and Supercapacitors Begin?" *Science*, 343(6176), 1210–1211.
- Singu, B. S., Palaniappan, S., and Yoon, K. R. (2016). "Polyaniline–nickel oxide nanocomposites for supercapacitor." *J. Appl. Electrochem.*, 46(10), 1039–1047.
- Stoller, M. D., and Ruoff, R. S. (2010). "Best practice methods for determining an electrode material's performance for ultracapacitors." *Energy Environ. Sci.*, 3(9), 1294.
- Subburaj, V., Jena, D., Kumar, R., Deshmukh, A. V., Nayak, B., and Bansal, H. (2016). "Design of series,  $F_i = F_i \times 2^{2i-1} + F_i \times 2^{2i-3}$  for the denominators (1, 2,  $\dots$ ; 6) of switched capacitor converter." *2016 IEEE 1st Int. Conf. Power Electron. Intell. Control Energy Syst. ICPEICES*, 1–5.
- Sudhakar, Y. N., Hemant, H., Nitinkumar, S. S., Poornesh, P., and Selvakumar, M. (2017). "Green synthesis and electrochemical characterization of rGO–CuO nanocomposites for supercapacitor applications." *Ionics*, 23(5), 1267–1276.

Sun, B., He, X., Leng, X., Jiang, Y., Zhao, Y., Suo, H., and Zhao, C. (2016). “Flower-like polyaniline–NiO structures: a high specific capacity supercapacitor electrode material with remarkable cycling stability.” *RSC Adv.*, 6(50), 43959–43963.

Tanaka, M., Ohya, S., and Nam Hai, P. (2014). “Recent progress in III-V based ferromagnetic semiconductors: Band structure, Fermi level, and tunneling transport.” *Appl. Phys. Rev.*, 1(1), 11102.

Tang, Z. K., Liu, W. W., Zhang, D. Y., Lau, W. M., and Liu, L. M. (2015). “Tunable band gap and magnetism of the two-dimensional nickel hydroxide.” *RSC Adv.*, 5(94), 77154–77158.

Toupin, M., Brousse, T., and Bélanger, D. (2004). “Charge Storage Mechanism of MnO<sub>2</sub> Electrode Used in Aqueous Electrochemical Capacitor.” *Chem. Mater.*, 16(16), 3184–3190.

Trchová, M., Morávková, Z., Bláha, M., and Stejskal, J. (2014). “Raman spectroscopy of polyaniline and oligoaniline thin films.” *Electrochim. Acta*, 122, 28–38.

Trivich, D., Wang, E. Y., and Richard, J. K. (1978). “Cuprous oxide photovoltaic cells.” *Conf. IEEE Photovolt. Spec. Conf.*, (1).

Usman, M., Pan, L., Asif, M., Mahmood, Z., Khan, M. A., and Fu, X. (2016). “Enhanced electrochemical supercapacitor properties with synergistic effect of polyaniline, graphene and Ag<sub>2</sub>O.” *Appl. Surf. Sci.*, 370, 297–305.

Vangari, M., Pryor, T., and Jiang, L. (2012). “Supercapacitors: review of materials and fabrication methods.” *J. Energy Eng.*, 139(2), 72–79.

Veerendra, B., and Sathyanarayana, D. N. (2005). “Synthesis and characterization of polyaniline salts with phenoxy acetic acids by emulsion polymerization.” *Indian J. Chem. Sect. Inorg. Phys. Theor. Anal. Chem.*, 44(6), 1133–1138.

Venezia, A. M., Bertocello, R., and Deganello, G. (1995). “X-ray photoelectron spectroscopy investigation of pumice-supported nickel catalysts.” *Surf. Interface Anal.*, 23(4), 239–247.

Vermisoglou, E. C., Devlin, E., Giannakopoulou, T., Romanos, G., Boukos, N., Psycharis, V., Lei, C., Lekakou, C., Petridis, D., and Trapalis, C. (2014). “Reduced graphene oxide/iron carbide nanocomposites for magnetic and supercapacitor applications.” *J. Alloys Compd.*, 590, 102–109.

Vidhyadharan, B., Izwan Misnon, I., Abd Aziz, R., P. Padmasree, K., M. Yusoff, M., and Jose, R. (2014). “Superior supercapacitive performance in electrospun copper oxide nanowire electrodes.” *J. Mater. Chem. A*, 2(18), 6578–6588.

Viswanathan, A., and Shetty, A. N. (2017). “Facile in-situ single step chemical synthesis of reduced graphene oxide-copper oxide-polyaniline nanocomposite and its electrochemical performance for supercapacitor application.” *Electrochim. Acta*, 257, 483–493.

Viswanathan, A., and Shetty, A. N. (2018). “Single step synthesis of rGO, copper oxide and polyaniline nanocomposites for high energy supercapacitors.” *Electrochim. Acta*, 289, 204–217.

Wan, C., Jiao, Y., and Li, J. (2017). “Multilayer core–shell structured composite paper electrode consisting of copper, cuprous oxide and graphite assembled on cellulose fibers for asymmetric supercapacitors.” *J. Power Sources*, 361, 122–132.

Wang, G., Zhang, L., and Zhang, J. (2012a). “A review of electrode materials for electrochemical supercapacitors.” *Chem Soc Rev Chem Soc Rev*, 41(41), 797–828.

Wang, H., Casalongue, H. S., Liang, Y., and Dai, H. (2010). “Ni(OH)<sub>2</sub> nanoplates grown on graphene as advanced electrochemical pseudocapacitor materials.” *J. Am. Chem. Soc.*, 132(21), 7472–7477.

Wang, H., Ma, L., Gan, M., Zhou, T., Sun, X., Dai, W., Wang, H., and Wang, S. (2016a). “Design and assembly of reduced graphene oxide/polyaniline/urchin-like

mesoporous TiO<sub>2</sub> spheres ternary composite and its application in supercapacitors.” *Compos. Part B Eng.*, 92, 405–412.

Wang, K., Dong, X., Zhao, C., Qian, X., and Xu, Y. (2015a). “Facile synthesis of Cu<sub>2</sub>O/CuO/RGO nanocomposite and its superior cyclability in supercapacitor.” *Electrochim. Acta*, 152, 433–442.

Wang, L., Wu, T., Du, S., Pei, M., Guo, W., and Wei, S. (2016b). “High performance supercapacitors based on ternary graphene/Au/polyaniline (PANI) hierarchical nanocomposites.” *RSC Adv.*, 6(2), 1004–1011.

Wang, L., Ye, Y., Lu, X., Wen, Z., Li, Z., Hou, H., and Song, Y. (2013). “Hierarchical Nanocomposites of Polyaniline Nanowire Arrays on Reduced Graphene Oxide Sheets for Supercapacitors.” *Sci. Rep.*, 3, 1–9.

Wang, Q., Li, J., Gao, F., Li, W., Wu, K., and Wang, X. (2008). “Activated carbon coated with polyaniline as an electrode material in supercapacitors.” *New Carbon Mater.*, 23(3), 275–280.

Wang, Q., Zhu, L., Sun, L., Liu, Y., and Jiao, L. (2015b). “Facile synthesis of hierarchical porous ZnCo<sub>2</sub>O<sub>4</sub> microspheres for high-performance supercapacitors.” *J Mater Chem A*, 3(3), 982–985.

Wang, Q., Zou, Y., Xiang, C., Chu, H., Zhang, H., Xu, F., Sun, L., and Tang, C. (2016c). “High-performance supercapacitor based on V<sub>2</sub>O<sub>5</sub>/carbon nanotubes-super activated carbon ternary composite.” *Ceram. Int.*, 42(10), 12129–12135.

Wang, W., Hao, Q., Lei, W., Xia, X., and Wang, X. (2012b). “Graphene/SnO<sub>2</sub>/polypyrrole ternary nanocomposites as supercapacitor electrode materials.” *RSC Adv.*, 2(27), 10268–10274.

Wang, W., Liu, Z., Liu, Y., Xu, C., Zheng, C., and Wang, G. (2003). “A simple wet-chemical synthesis and characterization of CuO nanorods.” *Appl. Phys. A*, 76(3), 417–420.

Wang, X., Zuo, C., Jia, L., Liu, Q., Guo, X., Jing, X., and Wang, J. (2017). “Synthesis of sandwich-like vanadium pentoxide/carbon nanotubes composites for high performance supercapacitor electrodes.” *J. Alloys Compd.*, 708, 134–140.

Winter, M., and Brodd, R. J. (2004). “What Are Batteries, Fuel Cells, and Supercapacitors?” *Chem. Rev.*, 10(104), 4245–4270.

Wu, C., Cai, J., Zhang, Q., Zhou, X., Zhu, Y., Shen, P. K., and Zhang, K. (2015a). “Hierarchical mesoporous zinc-nickel-cobalt ternary oxide nanowire arrays on nickel foam as high-performance electrodes for supercapacitors.” *ACS Appl. Mater. Interfaces*, 7(48), 26512–26521.

Wu, C., Wang, X., Ju, B., Zhang, X., Jiang, L., and Wu, H. (2012). “Supercapacitive behaviors of activated mesocarbon microbeads coated with polyaniline.” *Int. J. Hydrog. Energy*, HYFUSEN, 37(19), 14365–14372.

Wu, Z. S., Liu, Z., Parvez, K., Feng, X., and Mullen, K. (2015b). “Ultrathin Printable Graphene Supercapacitors with AC Line-Filtering Performance.” *Adv. Mater.*, 27(24), 3669–3675.

Xia, X., Hao, Q., Lei, W., Wang, W., Sun, D., and Wang, X. (2012a). “Nanostructured ternary composites of graphene/Fe<sub>2</sub>O<sub>3</sub>/polyaniline for high-performance supercapacitors.” *J. Mater. Chem.*, 22(33), 16844–16850.

Xia, X., Hao, Q., Lei, W., Wang, W., Wang, H., and Wang, X. (2012b). “Reduced-graphene oxide/molybdenum oxide/polyaniline ternary composite for high energy density supercapacitors: Synthesis and properties.” *J. Mater. Chem.*, 22(17), 8314.

Xing, Z., Chu, Q., Ren, X., Tian, J., Asiri, A. M., Alamry, K. A., Al Youbi, A. O., and Sun, X. (2013). “Biomolecule-assisted synthesis of nickel sulfides/reduced graphene oxide nanocomposites as electrode materials for supercapacitors.” *Electrochem. Commun.*, 32, 9–13.



Xiong, P., Hu, C., Fan, Y., Zhang, W., Zhu, J., and Wang, X. (2014a). “Ternary manganese ferrite/graphene/polyaniline nanostructure with enhanced electrochemical capacitance performance.” *J. Power Sources*, 266, 384–392.

Xiong, P., Huang, H., and Wang, X. (2014b). “Design and synthesis of ternary cobalt ferrite/graphene/polyaniline hierarchical nanocomposites for high-performance supercapacitors This work is dedicated to Professor MIN Enze on the occasion of his 90th birthday.” *J. Power Sources*, 245, 937–946.

Xu, J., Sun, H., Li, Z., Lu, S., Zhang, X., Jiang, S., Zhu, Q., and Zakharova, G. S. (2014). “Synthesis and electrochemical properties of graphene/V<sub>2</sub>O<sub>5</sub> xerogels nanocomposites as supercapacitor electrodes.” *Solid State Ion.*, Solid State Ionics 19 Proceedings of the 19th International Conference on Solid State Ionics, 262, 234–237.

Xu, J., Wang, K., Zu, S.-Z., Han, B.-H., and Wei, Z. (2010). “Hierarchical nanocomposites of polyaniline nanowire arrays on graphene oxide sheets with synergistic effect for energy storage.” *ACS Nano*, 4(9), 5019–5026.

Yan, J., Fan, Z., Sun, W., Ning, G., Wei, T., Zhang, Q., Zhang, R., Zhi, L., and Wei, F. (2012). “Advanced asymmetric supercapacitors based on Ni(OH)<sub>2</sub>/graphene and porous graphene electrodes with high energy density.” *Adv. Funct. Mater.*, 22(12), 2632–2641.

Yassine, M., Fabris, D., Yassine, M., and Fabris, D. (2017). “Performance of Commercially Available Supercapacitors.” *Energies*, 10(9), 1340.

Ye, G., Gong, Y., Keyshar, K., Husain, E. A., Brunetto, G., Yang, S., Vajtai, R., and Ajayan, P. M. (2015). “3D Reduced graphene oxide coated V<sub>2</sub>O<sub>5</sub> nanoribbon scaffolds for high-capacity supercapacitor electrodes.” *Part. Part. Syst. Charact.*, 32(8), 817–821.

Yuan, C., Yang, L., Hou, L., Shen, L., Zhang, X., and Lou, X. W. (David). (2012). “Growth of ultrathin mesoporous Co<sub>3</sub>O<sub>4</sub> nanosheet arrays on Ni foam for high-performance electrochemical capacitors.” *Energy Environ. Sci.*, 5(7), 7883–7887.

Yuan, L., Lu, X.-H., Xiao, X., Zhai, T., Dai, J., Zhang, F., Hu, B., Wang, X., Gong, L., and Chen, J. (2011). “Flexible solid-state supercapacitors based on carbon nanoparticles/MnO<sub>2</sub> nanorods hybrid structure.” *ACS Nano*, 6(1), 656–661.

Zhang, G. Q., Zhao, Y. Q., Tao, F., and Li, H. L. (2006). “Electrochemical characteristics and impedance spectroscopy studies of nano-cobalt silicate hydroxide for supercapacitor.” *J. Power Sources*, 161(1), 723–729.

Zhang, H., Yu, X., Guo, D., Qu, B., Zhang, M., Li, Q., and Wang, T. (2013). “Synthesis of bacteria promoted reduced graphene oxide-nickel sulfide networks for advanced supercapacitors.” *ACS Appl. Mater. Interfaces*, 5(15), 7335–7340.

Zhang, J., and Zhao, X. S. (2012). “Conducting Polymers Directly Coated on Reduced Graphene Oxide Sheets as High-Performance Supercapacitor Electrodes.” *J. Phys. Chem. C*, 116(9), 5420–5426.

Zhang, L., Ma, S., Ge, Q., Liu, K., Jiang, Q., Han, X., Yang, S., Yu, K., and Zhong, Z. (2017). “A systematic study of the antiferromagnetic-ferromagnetic conversion and competition in MnNiGe:Fe ribbon systems.” *J. Mater. Sci. Technol.*, 33(11), 1362–1370.

Zhang, S., Peng, C., Ng, K. C., and Chen, G. Z. (2010). “Nanocomposites of manganese oxides and carbon nanotubes for aqueous supercapacitor stacks.” *Electrochim. Acta*, 55(25), 7447–7453.

Zhang, Y., Si, L., Zhou, B., Zhao, B., Zhu, Y., Zhu, L., and Jiang, X. (2016a). “Synthesis of novel graphene oxide/pristine graphene/polyaniline ternary composites and application to supercapacitor.” *Chem. Eng. J.*, 288, 689–700.

Zhang, Y., Zheng, J., Zhao, Y., Hu, T., Gao, Z., and Meng, C. (2016b). “Fabrication of V<sub>2</sub>O<sub>5</sub> with various morphologies for high-performance electrochemical capacitor.” *Appl. Surf. Sci.*, 377, 385–393.

Zhang, Z., Wei, Z., and Wan, M. (2002). “Nanostructures of polyaniline doped with inorganic acids.” *Macromolecules*, 35(15), 5937–5942.

- Zhao, B., Liu, P., Jiang, Y., Pan, D., Tao, H., Song, J., Fang, T., and Xu, W. (2012). "Supercapacitor performances of thermally reduced graphene oxide." *J. Power Sources*, 198, 423–427.
- Zhao, W., Fu, W., Yang, H., Tian, C., Li, M., Li, Y., Zhang, L., Sui, Y., Zhou, X., Chen, H., and Zou, G. (2011). "Electrodeposition of Cu<sub>2</sub>O films and their photoelectrochemical properties." *CrystEngComm*, 13(8), 2871.
- Zhao, X. Y., Zang, J. B., Wang, Y. H., Bian, L. Y., and Yu, J. K. (2009). "Electropolymerizing polyaniline on undoped 100nm diamond powder and its electrochemical characteristics." *Electrochem. Commun.*, 11(6), 1297–1300.
- Zheng, J., Zhang, Y., Jing, X., Wang, Q., Hu, T., Xing, N., and Meng, C. (2017). "Improvement of the specific capacitance of V<sub>2</sub>O<sub>5</sub> nanobelts as supercapacitor electrode by tungsten doping." *Mater. Chem. Phys.*, 186, 5–10.
- Zhi, M., Xiang, C., Li, J., Li, M., and Wu, N. (2013). "Nanostructured carbon-metal oxide composite electrodes for supercapacitors: a review." *Nanoscale*, 5(1), 72–88.
- Zhu, J., Chen, M., Qu, H., Luo, Z., Wu, S., A. Colorado, H., Wei, S., and Guo, Z. (2013). "Magnetic field induced capacitance enhancement in graphene and magnetic graphene nanocomposites." *Energy Environ. Sci.*, 6(1), 194–204.
- Zhu, J., Chen, M., Wei, H., Yerra, N., Haldolaarachchige, N., Luo, Z., Young, D. P., Ho, T. C., Wei, S., and Guo, Z. (2014). "Magnetocapacitance in magnetic microtubular carbon nanocomposites under external magnetic field." *Nano Energy*, 6, 180–192.
- Zhu, S., Wu, M., Ge, M. H., Zhang, H., Li, S. K., and Li, C. H. (2016). "Design and construction of three-dimensional CuO/polyaniline/rGO ternary hierarchical architectures for high performance supercapacitors." *J. Power Sources*, 306, 593–601.



## LIST OF PUBLICATIONS

### Research Article published in international Journals

- 1) Aranganathan Viswanathan and A. Nityananda Shetty, (2017) “Facile in-situ single step chemical synthesis of reduced graphene oxide-copper oxide-polyaniline nanocomposite and its electrochemical performance for supercapacitor application” *Electrochim Acta*, 257, 483-493.
- 2) Aranganathan Viswanathan and Nityananda Shetty, (2018) “Single step synthesis of rGO, copper oxide and polyaniline nanocomposites for high energy supercapacitors” *Electrochim Acta*, 289, 204-217.
- 3) Aranganathan Viswanathan, B.G. Prakashaiah, V. Subburaj, A.N. Shetty, (2019) “High energy reduced graphene oxide/vanadium Pentoxide/polyaniline hybrid supercapacitor for power backup and switched capacitor converters”, *J. Colloid Interface Sci.* 545, 82–93.
- 4) Aranganathan Viswanathan and Nityananda Shetty, (2019) “Real Time Magnetic Supercapacitor with Antiferromagnetic Nickel Hydroxide Based Nanocomposite” *Electrochim Acta*, 309, 187-196.

### Research works presented in national and international conferences

- 1) Aranganathan Viswanathan and A. Nityananda Shetty, (2017) “Reduced graphene oxide, copper oxide, and polyaniline ternary nanocomposite as an electrode material for super capacitors “presented in National seminar on current trends in chemistry (CITRIC 2017) held during 3 - 4<sup>th</sup> February, 2017 at Cochin university of science and technology, Cochin, Kerala.
- 2) Aranganathan Viswanathan and A. Nityananda Shetty, (2017) “Facile insitu single step chemical synthesis of reduced graphene oxide, Cu<sub>2</sub>O/CuO and polyaniline ternary nanocomposite and its application in supercapacitor” presented in national conference on research advances in science and technology held during 26-27<sup>th</sup> May, 2017 at CSI college of engineering, Ooty, Tamil Nadu.

- 3) Aranganathan Viswanathan and A. Nityananda Shetty, (2017) “Amelioration of electrochemical Performances of the Reduced Graphene Oxide/ Nickel Oxide/ Polyaniline Nanocomposite by Combination of Electrolytes” presented in International conference on emerging trends in chemical sciences (ICETCS-2017) held during 14-16<sup>th</sup> September 2017, at Manipal institute of technology, Manipal, Karnataka.
- 4) Aranganathan Viswanathan, Vivekanandan Subburaj and A. Nityananda Shetty, (2017) “Nanocomposite supercapacitor electrode and its application in switch capacitor convertors (SCC)” presented in International conference on Sustainable Chemistry for Health Environment and Materials (Su-Chem 2018) held during 05<sup>th</sup> – 08<sup>th</sup> August, 2018 at CSIR-IICT, Hyderabad, Telangana, India.
- 5) Aranganathan Viswanathan and A. Nityananda Shetty (2019) “Single step synthesis and characterizations of reduced graphene oxide/V<sub>2</sub>O<sub>5</sub>/polyaniline nanocomposite for supercapacitors applications” presented in International conference on Nanoscience and Nanotechnology (ICONN-2019) held during 28<sup>th</sup> – 30<sup>th</sup> January 2019 at SRM university, Chennai, Tamil Nadu, India.
- 6) Aranganathan Viswanathan and A. Nityananda Shetty (2019) “Long Lasting High Energy Supercapacitance of rGO/Ni(OH)<sub>2</sub> Nanocomposite” presented in International conference on Material for Millennium (MATCON-2019) held during 13<sup>th</sup> – 16<sup>th</sup> March 2019 at CUSAT, Kochi, Kerala, India.

## CURRICULUM VITAE

**ARANGANATHAN V**  
9591959720  
Email id: [ranguchemist@gmail.com](mailto:ranguchemist@gmail.com)

**Permanent address:**  
433, Mariamman Kovil Street,  
Seruthankuzi, sorathur-(post),  
Panruti-(TK), via Perperiyankuppam,  
Cuddalore-607805, Tamilnadu.

### Academic profile:

Degree	Institute	Year of completion	Aggregate
B.Sc Chemistry	Jawahar Science College, Neyveli	April, 2010	73%
M.sc Chemistry	Madras Christian College, Chennai	April, 2012	66%
Ph.D.	National Institute of Technology Karnataka	December, 2018 (2014-2018)	Course work 80%

### Professional experience:

Position	Institute	Years
Guest lecturer	Madras Christian College, Chennai	Two (2012-2014)

### Research Article published in international Journals

- 1) Aranganathan V and A. Nityananda Shetty, (2018) "Synthesis and characterization of reduced graphene oxide/ nickel oxide/ polyaniline ternary nanocomposites for their supercapacitive behavior" *Materials Today: Proceedings*, 5, 8857-8861.
- 2) Aranganathan Viswanathan and A. Nityananda Shetty, (2017) "Facile in-situ single step chemical synthesis of reduced graphene oxide-copper oxide-polyaniline nanocomposite and its electrochemical performance for supercapacitor application" *Electrochim Acta*, 257, 483-493.
- 3) Aranganathan Viswanathan and Nityananda Shetty, (2018) "Electrochemical comparison of nickel and nickel hydroxide composited with reduced graphene oxide and polyaniline for their supercapacitor application" *AIP conference proceeding*, 1943, 020066.

- 4) Aranganathan Viswanathan and Nityananda Shetty, (2018) “Single step synthesis of rGO, copper oxide and polyaniline nanocomposites for high energy supercapacitors” *Electrochim Acta*, 289, 204-217.
- 5) Aranganathan Viswanathan, B.G. Prakashaiah, V. Subburaj, A.N. Shetty, (2019) “High energy reduced graphene oxide/vanadium Pentoxide/polyaniline hybrid supercapacitor for power backup and switched capacitor converters”, *J. Colloid Interface Sci.* 545, 82–93.
- 6) Aranganathan Viswanathan and Nityananda Shetty, (2019) “Real Time Magnetic Supercapacitor with Antiferromagnetic Nickel Hydroxide Based Nanocomposite” *Electrochim Acta*, 309, 187-196.
- 7) Aranganathan Viswanathan and A. Nityananda Shetty, (2019) “Amelioration of Supercapacitance of Mixed Metal Oxide Dispersed Reduced Graphene Oxide and Polyaniline Nanocomposites Using  $\text{CH}_3\text{SO}_3\text{H}$  as Supporting Electrolyte in  $\text{H}_2\text{SO}_4$ ” *Materials today: proceedings* (accepted).

#### **Research works presented in national and international conferences**

- 1) Aranganathan Viswanathan and A. Nityananda Shetty, (2017) “Reduced graphene oxide, copper oxide, and polyaniline ternary nanocomposite as an electrode material for super capacitors “presented in National seminar on current trends in chemistry (CITRIC 2017) held during 3 - 4<sup>th</sup> February, 2017 at Cochin university of science and technology, Cochin, Kerala.
- 2) Aranganathan Viswanathan and A. Nityananda Shetty, (2017) “Synthesis and characterization of reduced graphene oxide/ nickel oxide/ polyaniline ternary nanocomposites for their supercapacitive behavior” presented in the international conference on recent advances in material chemistry (ICRAMC-2017) held during 15-17<sup>th</sup> February at SRM university, Chennai, Tamil nadu.
- 3) Dilip. H. N, Aranganathan Viswanathan and A. Nityananda Shetty (2017) “Synthesis and characterization of copper nanofluids” presented in national conference on chemistry of sustainable future (NCCSF-2017) held on 27<sup>th</sup> and 28<sup>th</sup>, January at Sri dharmasthala manjunadheshwara college, Ujire.



- 4) Swetha K V, Aranganathan Viswanathan and A. Nityananda Shetty, (2017) “Hydrazine hydrate as corrosion inhibitor for mild steel in NaCl” presented in national conference on chemistry of sustainable future (NCCSF-2017) held on 27<sup>th</sup> and 28<sup>th</sup>, January at Sri dharmasthala manjunadheshwara college, Ujire.
- 5) Swetha K V, Aranganathan Viswanathan and A. Nityananda Shetty, (2017) “Hydrazine hydrate as corrosion inhibitor in NaCl” presented in national conference on research advances in science and technology held on 26<sup>th</sup> and 27<sup>th</sup> May, at CSI college of engineering, Ooty.
- 6) Aranganathan Viswanathan and A. Nityananda Shetty, (2017) “Facile insitu single step chemical synthesis of reduced graphene oxide, Cu<sub>2</sub>O/CuO and polyaniline ternary nanocomposite and its application in supercapacitor” presented in national conference on research advances in science and technology held during 26-27<sup>th</sup> May, 2017 at CSI college of engineering, Ooty, Tamil Nadu.
- 7) Aranganathan Viswanathan and A. Nityananda Shetty, (2017) “Amelioration of electrochemical Performances of the Reduced Graphene Oxide/ Nickel Oxide/ Polyaniline Nanocomposite by Combination of Electrolytes” presented in International conference on emerging trends in chemical sciences (ICETCS-2017) held during 14-16<sup>th</sup> September 2017, at Manipal institute of technology, Manipal, Karnataka.
- 8) Aranganathan Viswanathan and A. Nityananda Shetty, (2018) “Electrochemical comparison of nickel and nickel hydroxide composited with reduced graphene oxide and polyaniline for their supercapacitor application” presented in International conference on design, materials and manufacturing (IcDeM 2018) held during 29 – 30<sup>th</sup> January, 2018 at National Institute of Technology, Surathkal, Mangalore, Karnataka.
- 9) Aranganathan Viswanathan and A. Nityananda Shetty, (2018) “Amelioration of Supercapacitance of Mixed Metal Oxide Dispersed Reduced Graphene Oxide and Polyaniline Nanocomposites Using CH<sub>3</sub>SO<sub>3</sub>H as Supporting Electrolyte in H<sub>2</sub>SO<sub>4</sub>” presented in International conference on recent advances in material chemistry (ICRAMC-2018) held during 14 - 16<sup>th</sup> February, 2018, at SRM university, Chennai, Tamil Nadu.

- 10) Aranganathan Viswanathan, Vivekanandan Subburaj and A. Nityananda Shetty, (2017) “Nanocomposite supercapacitor electrode and its application in switch capacitor convertors (SCC)” presented in International conference on Sustainable Chemistry for Health Environment and Materials (Su-Chem 2018) held during 05<sup>th</sup> – 08<sup>th</sup> August, 2018 at CSIR-IICT, Hyderabad, Telangana, India.
  - 11) Aranganathan Viswanathan and A. Nityananda Shetty (2019) “Single step synthesis and characterizations of reduced graphene oxide/V<sub>2</sub>O<sub>5</sub>/polyaniline nanocomposite for supercapacitors applications” presented in International conference on Nanoscience and Nanotechnology (ICONN-2019) held during 28<sup>th</sup> – 30<sup>th</sup> January 2019 at SRM university, Chennai, Tamil Nadu, India.
  - 12) Aranganathan Viswanathan and A. Nityananda Shetty (2019) “Long Lasting High Energy Supercapacitance of rGO/Ni(OH)<sub>2</sub> Nanocomposite” presented in International conference on Material for Millennium (MATCON-2019) held during 13<sup>th</sup> – 16<sup>th</sup> March 2019 at CUSAT, Kochi, Kerala, India.
-